frontiers | Research Topics

Cancer and central nervous system disease diagnosis and treatment

Edited by
Youmei Bao, Chao Zheng, Lu Wang, Jian Yang and Zikai He

Published in
Frontiers in Bioengineering and Biotechnology
Frontiers in Neurology

ISSN 1664-8714
ISBN 978-2-8325-2308-7
DOI 10.3389/978-2-8325-2308-7

About Frontiers

Frontiers is more than just an open access publisher of scholarly articles: it is a pioneering approach to the world of academia, radically improving the way scholarly research is managed. The grand vision of Frontiers is a world where all people have an equal opportunity to seek, share and generate knowledge. Frontiers provides immediate and permanent online open access to all its publications, but this alone is not enough to realize our grand goals.

Frontiers journal series

The Frontiers journal series is a multi-tier and interdisciplinary set of open-access, online journals, promising a paradigm shift from the current review, selection and dissemination processes in academic publishing. All Frontiers journals are driven by researchers for researchers; therefore, they constitute a service to the scholarly community. At the same time, the *Frontiers journal series* operates on a revolutionary invention, the tiered publishing system, initially addressing specific communities of scholars, and gradually climbing up to broader public understanding, thus serving the interests of the lay society, too.

Dedication to quality

Each Frontiers article is a landmark of the highest quality, thanks to genuinely collaborative interactions between authors and review editors, who include some of the world's best academicians. Research must be certified by peers before entering a stream of knowledge that may eventually reach the public - and shape society; therefore, Frontiers only applies the most rigorous and unbiased reviews. Frontiers revolutionizes research publishing by freely delivering the most outstanding research, evaluated with no bias from both the academic and social point of view. By applying the most advanced information technologies, Frontiers is catapulting scholarly publishing into a new generation.

What are Frontiers Research Topics?

Frontiers Research Topics are very popular trademarks of the *Frontiers journals series*: they are collections of at least ten articles, all centered on a particular subject. With their unique mix of varied contributions from Original Research to Review Articles, Frontiers Research Topics unify the most influential researchers, the latest key findings and historical advances in a hot research area.

Find out more on how to host your own Frontiers Research Topic or contribute to one as an author by contacting the Frontiers editorial office: frontiersin.org/about/contact

Cancer and central nervous system disease diagnosis and treatment

Topic editors

Youmei Bao — Yale University, United States
Chao Zheng — Yale University, United States
Lu Wang — First Affiliated Hospital of Jinan University, China
Jian Yang — Shanghai University, China
Zikai He — Harbin Institute of Technology, Shenzhen, China

Citation

Bao, Y., Zheng, C., Wang, L., Yang, J., He, Z., eds. (2023). *Cancer and central nervous system disease diagnosis and treatment*. Lausanne: Frontiers Media SA. doi: 10.3389/978-2-8325-2308-7

Table of contents

frontiers in Bioengineering and Biotechnology

ORIGINAL RESEARCH
published: 05 January 2022
doi: 10.3389/fbioe.2021.810890

Localizing Epileptic Foci Before Surgery in Patients With MRI-Negative Refractory Epilepsy Using Statistical Parameter Mapping and Three-Dimensional Stereotactic Surface Projection Based on ^{18}F-FDG PET

Hailing Zhou[1†], Wei Zhang[2†], Zhiqiang Tan[1†], Ziqing Zhou[1], Ying Li[1], Shaojuan Zhang[1], Lingling Zhang[1], Jiefeng Gan[1], Huanhua Wu[1], Yongjin Tang[1], Yong Cheng[1], Xueying Ling[1], Qiang Guo[2]* and Hao Xu[1]**

[1]Department of Nuclear Medicine, PET/CT-MRI Center, Center of Cyclotron and PET Radiopharmaceuticals, The First Affiliated Hospital of Jinan University, Guangzhou, China, [2]Epilepsy Center, Guangdong 999 Brain Hospital, Affiliated Brain Hospital of Jinan University, Guangzhou, China

OPEN ACCESS

Edited by:
Chao Zheng,
Yale University, United States

Reviewed by:
Jie Lu,
Capital Medical University, China
Xiaona Lu,
Yale University, United States
YingZhu Chen,
Yangzhou University, China
Jian Yang,
Shanghai University, China

***Correspondence:**
Hao Xu
txh@jnu.edu.cn
Qiang Guo
guoqiang999brain@163.com
Xueying Ling
lingxuey@163.com

†These authors have contributed equally to this work

Specialty section:
This article was submitted to Nanobiotechnology, a section of the journal Frontiers in Bioengineering and Biotechnology

Received: 08 November 2021
Accepted: 13 December 2021
Published: 05 January 2022

Citation:
Zhou H, Zhang W, Tan Z, Zhou Z, Li Y, Zhang S, Zhang L, Gan J, Wu H, Tang Y, Cheng Y, Ling X, Guo Q and Xu H (2022) Localizing Epileptic Foci Before Surgery in Patients With MRI-Negative Refractory Epilepsy Using Statistical Parameter Mapping and Three-Dimensional Stereotactic Surface Projection Based on ^{18}F-FDG PET. Front. Bioeng. Biotechnol. 9:810890. doi: 10.3389/fbioe.2021.810890

Patients with refractory epilepsy are not only free of seizures after resecting epileptic foci, but also experience significantly improved quality of life. Fluorine-18-fluorodeoxyglucose positron-emission tomography (^{18}F-FDG PET) is a promising avenue for detecting epileptic foci in patients with magnetic resonance imaging (MRI)-negative refractory epilepsy. However, the detection of epileptic foci by visual assessment based on ^{18}F-FDG PET is often complicated by a variety of factors in clinical practice. Easy imaging methods based on ^{18}F-FDG PET images, such as statistical parameter mapping (SPM) and three-dimensional stereotactic surface projection (3D-SSP), can objectively detect epileptic foci. In this study, the regions of surgical resection of patients with over 1 year follow-up and no seizures were defined as standard epileptic foci. We retrospectively analyzed the sensitivity of visual assessment, SPM and 3D-SSP based on ^{18}F-FDG PET to detect epileptic foci in MRI-negative refractory epilepsy patients and obtained the sensitivities of visual assessment, SPM and 3D-SSP are 57, 70 and 60% respectively. Visual assessment combined with SPM or 3D-SSP can improve the sensitivity of detecting epileptic foci. The sensitivity was highest when the three methods were combined, but decreased consistency, in localizing epileptic foci. We conclude that SPM and 3D-SSP can be used as objective methods to detect epileptic foci before surgery in patients with MRI-negative refractory epilepsy. Visual assessment is the preferred method for PET image analysis in MRI-negative refractory epilepsy. When the visual assessment is inconsistent with the patient's electroclinical information, SPM or 3D-SSP was further selected to assess the epileptic foci. If the combination of the two methods still fails to accurately locate the epileptic foci, comprehensive evaluation can be performed by combining the three methods.

Keywords: MRI-negative refractory epilepsy, epileptic foci, fluorine-18-fluorodeoxyglucose positron-emission tomography, statistical parameter mapping, three-dimensional stereotactic surface projection

INTRODUCTION

According to results released by the World Health Organization (WHO), approximately 50 million people suffer from epilepsy worldwide (World Health Organization, 2019). Approximately one-third of epilepsy patients, called refractory epilepsy patients, continue to have seizures even after receiving medication (Kwan et al., 2010). Studies have shown that patients with refractory epilepsy are not only free of seizures after surgery, but also experience significantly improved quality of life (Dwivedi et al., 2017; Engel et al., 2012).

At present, there is no unified standard for the location of epileptic foci, and evaluations are performed by a multidisciplinary team. Magnetic resonance imaging (MRI) can be used to identify the direct cause of seizures (Bernasconi et al., 2019). However, MRI results are negative in about 20–30% patients with refractory epilepsy, meaning that they cannot be directly treated with surgery and other methods are needed to assist in locating the epileptic foci (Muhlhofer et al., 2017; von Oertzen et al., 2002). Fluorine-18-fluorodeoxyglucose positron-emission tomography (^{18}F-FDG PET) is a promising avenue for detecting epileptic foci (Duncan et al., 2016; Jones and Cascino, 2016). Studies have shown that ^{18}F-FDG PET can not only guide a second MRI reading to find hidden lesions, but also provide surgeons with potential epileptic foci areas related to seizures (Chassoux et al., 2010; Rathore et al., 2014). At present, detection of abnormal metabolic areas from ^{18}F-FDG PET is mainly performed by visual assessment; however, the detection of epileptic foci by visual assessment is often complicated by a variety of factors in clinical practice.

Several easy imaging methods already exist for objective analysis of ^{18}F-FDG PET images. Statistical parameter mapping (SPM) is a voxel-based brain mapping software that has been used in detecting epileptic foci for more than 10 years. Studies have shown that the sensitivity of SPM is higher than that of visual assessment (Archambaud et al., 2013; Kim et al., 2002; Kumar et al., 2010; Wang et al., 2016). However, there are no articles assessing the ability of SPM to localize epileptic foci in patients with MRI-negative refractory epilepsy. Three-dimensional stereotactic surface projection (3D-SSP) is another voxel-based brain mapping software that uses a method similar to SPM. Only one article to date has applied 3D-SSP based on ^{18}F-FDG PET data to localize epileptic foci in patients with refractory epilepsy; even so, this study did not include patients with MRI-negative epilepsy, and the localization of epileptic foci was based on preoperative multidisciplinary evaluation rather than postoperative results (Wang et al., 2016). At present, no reports have simultaneously used SPM and 3D-SSP to detect epileptic foci before surgery in patients with MRI-negative refractory epilepsy.

In our study, we used the regions of surgical resection of patients with over 1 year follow-up and no seizures as standard epileptic foci, and then evaluated SPM and 3D-SSP based on ^{18}F-FDG PET images to detect epileptic foci before surgery in patients with MRI-negative refractory epilepsy.

MATERIALS AND METHODS

Patients

We retrospectively analyzed 643 patients who received ^{18}F-FDG PET examination at the PET CT/MRI center of the First Affiliated Hospital of Jinan University between January 1, 2014 and June 30, 2020 and who were followed-up for more than 1 year after surgical resection. Inclusion criteria: 1) Patients diagnosed with refractory epilepsy according to the standards of the International League Against Epilepsy (ILAE); 2) No structural lesions causing seizures were found at 3.0 T epilepsy-protocol; 3) Age≥5 years; 4) Patients underwent surgical resection and were followed-up for at least 1 year; 5) The postoperative outcomes of patients met Engel's Class I standards of ILAE. Exclusion criteria: 1) 3.0 T MRI epilepsy-protocol could detect structural lesions causing seizures; 2) The postoperative outcomes of patients did not meet Engel's Class I standards of ILAE; 3) Incomplete clinical data of patients; 4) Age < 5 years. A total of 91 patients were ultimately included. A total of 91 patients underwent preoperative multidisciplinary evaluation to locate the epileptic foci, 70 of whom underwent stereoelectroencephalography (SEEG) examination before treatment. All 91 patients underwent surgical treatment and were followed-up for more than 1 year.

For SPM analysis, we collected 27 age- and gender-matched controls of relatively normal health, which excluded malignant tumors, lymphomas, and hematological diseases. Subjects underwent full-body ^{18}F-FDG PET/CT scans and exhibited no ^{18}F-FDG PET abnormalities in the head, as well as no history of neurological disease, psychiatric disease, radiation, chemotherapy, or psychiatric medication.

MRI Epilepsy-Protocol

MRI was conducted on a 3.0 T MRI scanner (GE Discovery 750, Milwaukee, United States). The MRI epilepsy-protocol used for epilepsy patients at our center consists of an axial three-dimensional brain volume imaging (3D BRAVO) T1-weighted sequence (TR/TE 8.2/3.2, TI 450, matrix 256 × 256, 1.0 mm thickness), a T2-weighted axial sequence (TR/TE 12001/91.1, matrix 512 × 512, 1.0 mm thickness), and a 3D Cube T2 fluid attenuation inversion recovery (FLAIR) coronal sequence (TR/TE 5000/126.4, TI 1615.0, matrix 256 × 256, 1.0 mm thickness). MRI was classified as negative when no structural lesions causing seizures were detected (Bernasconi et al., 2019).

^{18}F-FDG PET Imaging

Interictal ^{18}F-FDG PET scans for all patients were conducted using a GE Discovery PET/CT 690 system (300 mm field of view (FOV), matrix 192 × 192, and 3.3 mm slice thickness). Patients were injected with ^{18}F-FDG, and ^{18}F-FDG PET images were acquired after a 60 min uptake time. The mean dose of ^{18}F-FDG administered was 0.1 mCi/kg body weight (3.7 MBq/kg). The injection of ^{18}F-FDG and subsequent ^{18}F-FDG PET examination were performed under quiet conditions. Patients were scanned while in a standard awake resting state, closing their eyes and unplugging their ears. All participants fasted for at least 6 h before PET (Hwang et al., 2001).

Visual Assessment

^{18}F-FDG PET images were assessed by two experienced nuclear physicians using the GE AW 4.6 workstation, and we used a colorized scale to detect metabolic changes. The nuclear physicians were blinded to patients' information, and divided the left and right hemispheres into ten lobes (frontal, parietal, occipital, temporal and insula lobe). Abnormal metabolic regions occurred when one hemisphere was metabolically altered from the opposite hemisphere. The presence of at least one abnormal metabolic region in ^{18}F-FDG PET images was considered indicative of potential epileptic foci (Spencer, 1994).

SPM Analysis

^{18}F-FDG PET images were analyzed by SPM12 (Institute of Neurology, University College London) using the Matlab platform (2020a, MathWorks, United StatesA). ^{18}F-FDG PET images of epilepsy patients and control subjects were imported into SPM12 in NIFTI format and preprocessed, including the application of spatial standardization and smoothing (FWHM = $8 \times 8 \times 8$ mm^3). On SPM12, we compared ^{18}F-FDG PET images of epilepsy patients to the control group using two independent sample T tests with age and gender as covariates. We set SPM threshold values of $p < 0.05$ (matching K > 0, corrected), $p < 0.005$ (matching K > 200, uncorrected), $p < 0.001$ (matching K > 100, uncorrected), and $p < 0.0001$ (matching K > 50, uncorrected). Areas of abnormal metabolism indicated by SPM were considered to be potential epileptic foci (Mayoral et al., 2016).

3D-SSP Analysis

3D-SSP analysis based on ^{18}F-FDG PET was conducted using Cortex ID software (University of Washington, Minoshima, United States). The ^{18}F-FDG PET images were imported into Cortex ID software in DICOM format, and anatomic standardization was performed through rotational correction and stereotactic realignment. The ^{18}F-FDG PET image metabolism data was extracted to the brain surface (3D-SSP images) automatically using the Cortex ID software. The Z value represents the degree of metabolic difference between the patient ^{18}F-FDG PET image and healthy controls in the database based on four different reference regions (global, pons, cerebellar, thalamus). Z= (μ_{normal} -patients)/ δ_{normal}. We set Z values of 1.96, 1.64, and 1.28. When the absolute value of a patient result was greater than the set Z values, this was considered as evidence of potential epileptic foci (Minoshima et al., 2020; Mizumura and Kumita, 2006).

Statistical Analysis

Surgical outcomes were based on the guidelines recommended by ILAE (Wieser et al., 2001). Engel's Class I: Free of disabling seizures. We considered results of Engel's Class I as good outcomes. Standard epileptic foci were defined as areas of surgical resection. Abnormal metabolic regions were obtained by the three methods. Correct detection was defined by abnormal metabolic zones is large but including surgical resection site. Correct localization was defined as abnormal metabolic zones is localized and consistent with the surgical resection site. Sensitivity is defined as the ratio of the number of patients correctly detected to the total number of patients. For clinical data before and after surgery, we reported medians (Inter-Quartile Range [IQR]) for continuous variables and percentages (numbers) for categorical variables. The sensitivities of different methods were expressed as percentages. SPM analysis was performed using two independent sample T tests. The sensitivities of different methods were compared using a paired Chi-square test. The above results were analyzed by SPSS26 (IBM SPSS Inc, Chicago, IL, United States), $p < 0.05$ was considered statistically significant.

TABLE 1 | Demographics and Clinical Data of participants.

Variable	
Gender	
Male	70% (n = 64)
Female	30% (n = 27)
Age at epilepsy onset, y (IQR)	8 (5–14)
Duration of epilepsy, y (IQR)	10 (4–15)
Age at epilepsy surgery, y (IQR)	21 (14–26)
Auras	37% (n = 34)
Seizure type	
Focal onset	69% (n = 63)
Generalized onset	31% (n = 28)
Seizure frequency	
Daily	34% (n = 31)
Weekly	15% (n = 14)
Monthly	43% (n = 39)
Yearly	8% (n = 7)
Follow up, y (IQR)	2 (2–3)

% (n), percent (number); y, year; IQR, Inter-Quartile Range.

RESULTS

Clinical Data

A total of 91 patients were included, including 64 males and 27 females, with an age range of 5–55 years and a median age of 21 (14–26) years. Other information is shown in **Table 1**. A total of 27 control subjects were subjected to SPM analysis, including 17 males and 10 females, ranged in age from 10 to 51 years, with a median age of 23 (19–27) years. There were no statistically significant differences in age or sex between the epilepsy and control groups.

Sensitivities of Visual Assessment, SPM, 3D-SSP in Detecting Epileptic Foci

Of 91 patients, epileptic foci were correctly detected for 52 patients, while epileptic foci were incorrectly detected by visual assessment for 39 patients. Among the 52 patients with epileptic foci detected correctly by visual assessment, 45 patients had epileptic foci detected by SPM and 38 patients by 3D-SSP. Among the 39 patients whose visual assessment were incorrect, SPM correctly detected foci in 19 patients, and 3D-SSP correctly detected foci in 17 patients. The abilities of these three methods to detect epileptic foci are shown in **Figure 1**.

Visual assessment, SPM and 3D-SSP were respectively able to detect 52, 64 and 55 patients with respective sensitivities of 57, 70

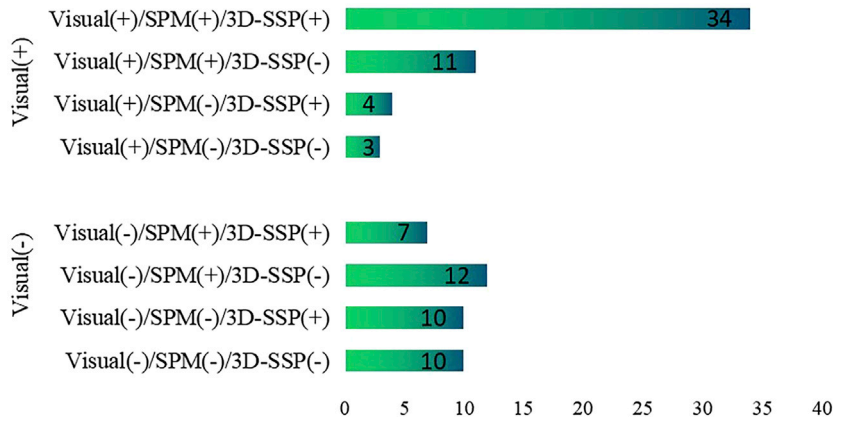

FIGURE 1 | The ability of visual assessment, SPM, 3D-SSP to detect epileptic foci based on postoperative results. Visual, visual assessment; SPM, statistical parameter mapping; 3D-SSP, three-dimensional stereotactic surface projection. (+) = epileptic foci are correctly detected, (–) = epileptic foci are incorrectly detected.

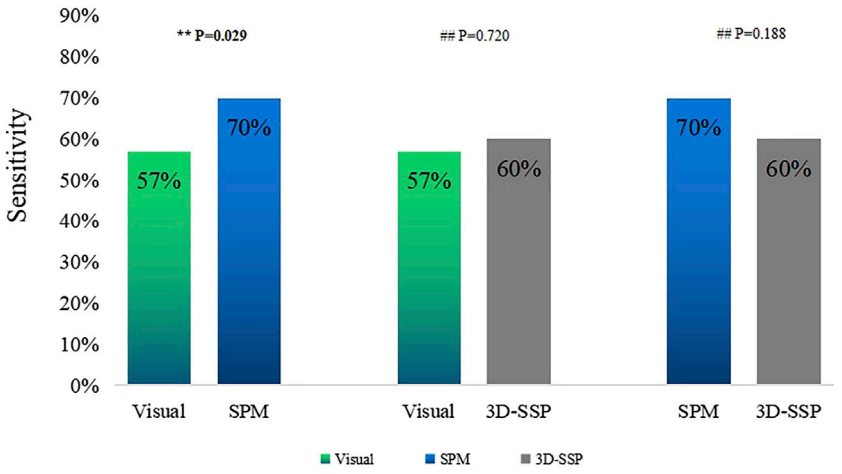

FIGURE 2 | Comparison of the sensitivities of visual assessment, SPM, 3D-SSP in detecting epileptic foci (**P < 0.05, ##P > 0.05).

and 60%. For the three methods respectively, 23, 24 and 27 patients exhibited localized abnormal metabolic regions consistent with surgical resection sites. There was a statistically significant difference between SPM and visual assessment, but there was no statistically significant difference between SPM and 3D-SSP. The sensitivity of visual assessment was similar to that of 3D-SSP, and there was no statistically significant difference detected between them (**Figure 2**).

Sensitivity of Two Combined Methods

Visual assessment combined with SPM (Visual/SPM) and visual assessment combined with 3D-SSP (Visual/3D-SSP) were able to detect 71 and 69 patients, respectively, with sensitivities of 78 and 76%. For 8 and 11 patients, respectively, abnormal metabolic regions were localized and consistent with surgical resection sites.

The sensitivity of Visual/SPM or Visual/3D-SSP was significantly higher than those of visual assessment alone or of 3D-SSP, and there was a statistically significant difference between them. Although the sensitivities of Visual/SPM and Visual/3D-SSP were higher than that of SPM, there was a statistical difference between Visual/SPM and SPM and no statistical difference between Visual/SPM and 3D-SSP. The sensitivity of Visual/SPM was similar to that of Visual/3D-SSP, and there was no statistically significant difference between the two (**Figure 3**).

Sensitivity of Three Combined Methods

Visual assessment combined with SPM and 3D-SSP (Visual/SPM/3D-SSP) could detect epileptic foci in 81 patients with a sensitivity of 89%, and 2 patients had abnormal focal metabolic areas consistent with the surgical resection site.

The sensitivity of three methods combined was significantly higher than any single method or two-method combination, and the comparison between them was statistically significant (**Figure 4**).

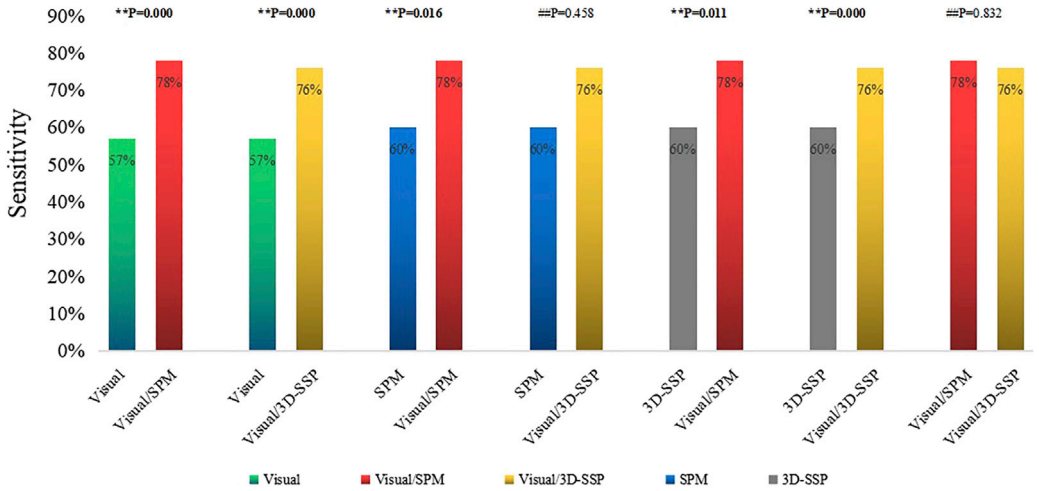

FIGURE 3 | Comparison of the sensitivities of single method, two combined methods (**P < 0.05, ##P > 0.05). Visual/SPM, Visual assessment combined with SPM; Visual/3D-SSP, Visual assessment combined with 3D-SSP.

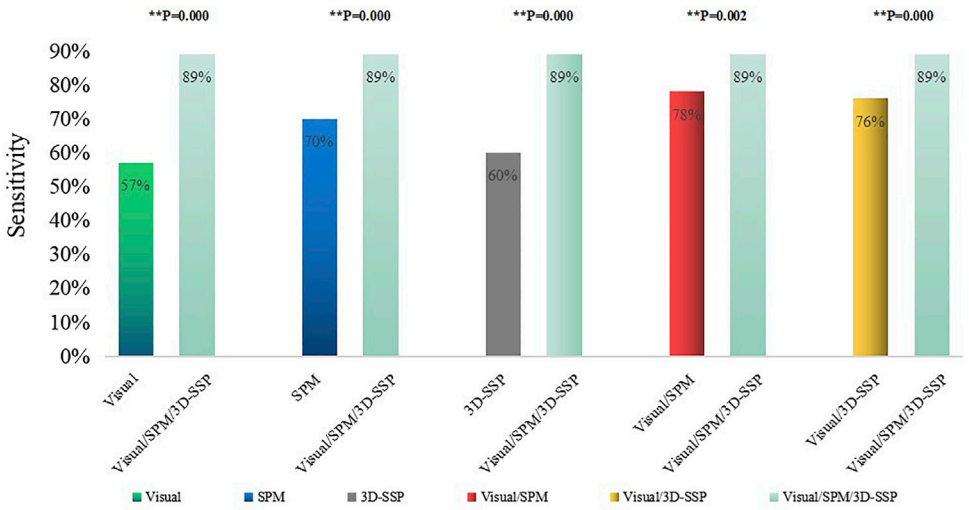

FIGURE 4 | Comparison of the sensitivities of single method, two combined methods, three combined methods (**p < 0.05, ##p > 0.05). Visual/SPM/3D-SSP, Visual assessment combined SPM and 3D-SSP.

DISCUSSION

In previous studies, when judging the ability of different methods to detect epileptic foci, localization of epileptic foci was based on multidisciplinary comprehensive evaluation or SEEG localization results (Gonzalez-Martinez et al., 2013). However, both approaches are susceptible to subjective errors and are not sufficient for the most accurate location of epileptic foci. We used the regions of surgical resection of patients with over 1 year follow-up and no seizures as standard epileptic foci, allowing us to assess the true efficacies of different methods. Due to the immature brain development and the boundary between white and gray matter is unclear of people under 5 years old, so we did not include people under 5 years old in this study.

Previous researches have shown that, although ^{18}F-FDG PET is highly sensitive in detecting epileptic foci, the abnormal metabolic regions detected by ^{18}F-FDG PET are often larger than the real epileptic foci (Rathore et al., 2014; Uijl et al., 2007). The main function of ^{18}F-FDG PET is to detect potential epileptic foci, after which epileptic foci can be comprehensively located in combination with other examinations. Previous studies have shown that the sensitivity of visual assessment based on ^{18}F-FDG PET in detecting epileptic foci in patients with refractory epilepsy ranges from 36 to 78.2% (Spencer, 1994; Kim et al., 2002; Desai et al., 2013; Wang et al., 2016;

Jayalakshmi et al., 2019; Rossi Sebastiano et al., 2020), while the sensitivity of visual assessment based on ^{18}F-FDG PET to detect epileptic foci in patients with MRI-negative refractory epilepsy ranges from 36 to 75% (Kim et al., 2002; Rossi Sebastiano et al., 2020). Our study showed that visual assessment correctly detected 52 out of 91 patients, with a sensitivity of 57%. Although a previous study found that the sensitivity of visual assessment based on ^{18}F-FDG PET was 75% in MRI-negative refractory epilepsy, SEEG results were used as the reference criteria for localization of epileptic foci (Rossi Sebastiano et al., 2020). Another study found that the sensitivity of visual assessment based on ^{18}F-FDG PET in MRI-negative frontal lobe patients was only 36%, although postoperative results were used as the standard for localization of epileptic foci (Kim et al., 2002). These differences are due to the complex functional changes observed in patients with frontal lobe epilepsy, which can lead to inaccurate localization of ^{18}F-FDG PET. Our study included patients with MRI-negative epilepsy and postoperative compliance with Engel's Class I criteria, and our results demonstrate the true clinical value of visual assessment based on ^{18}F-FDG PET in MRI-negative refractory epilepsy. Although our study was based on postoperative follow-up results, the sensitivity of visual assessment in our study was within the range of previous results.

Previous studies have shown that the sensitivity of SPM in detecting epileptic foci in patients with refractory epilepsy ranges from 40 to 83% (Archambaud et al., 2013; Kim et al., 2002; Kumar et al., 2010; Mayoral et al., 2016; Wang et al., 2016). No papers about the sensitivity of SPM in detecting epileptic foci in patients with MRI-negative refractory epilepsy have been previously published. Most studies have reported that the sensitivity of SPM is higher than that of visual assessment. There have been two studies reporting the sensitivity of SPM as 83 and 79%, respectively (Archambaud et al., 2013; Wang et al., 2016). However, the definition of epileptic foci was based on the results of preoperative assessment in these two studies. Kumar et al. showed that the sensitivity of SPM is 71% in detecting epileptic foci in patients with refractory epilepsy based on a lack of seizures after surgery (Kumar et al., 2010). In our study, the sensitivity of SPM in MRI-negative epilepsy patients was 70% based on lack of post-surgery seizures, and our results were similar to those of Kumar et al. (2010). Although most of the previous results reported a high sensitivity of SPM in detecting refractory epileptic foci, one study, which included patients that were ^{18}F-FDG PET-negative, determined that the sensitivity of SPM was only 40% (Mayoral et al., 2016). SPM results were based on ^{18}F-FDG PET images, so a study based on ^{18}F-FDG PET-negative patients will suggest reduced sensitivity of SPM.

The sensitivity of SPM in detecting epileptic foci is not only related to the localization standard of epileptic foci, but also to the setting results of threshold (P) and voxel (K), for which there are still no unified setting standards. High p-value matching big voxel and low p-value matching small voxel were the most common threshold settings in previous studies. In our analysis of previous studies (Archambaud et al., 2013; Kim et al., 2002; Kumar et al., 2010; Mayoral et al., 2016; Wang et al., 2016), we found that $p < 0.005$ was most sensitive when both children and adults were included in the study, while $p < 0.001$ was more sensitive when only children were included in the study. The patients in our study included children and adults, and we concluded that the sensitivity of SPM in detecting epileptic foci was highest when $p < 0.005$ (uncorrected), in agreement with two previous studies (Kim et al., 2002; Mayoral et al., 2016). We established an optimized scheme for SPM. First, ^{18}F-FDG PET images of all patients with MRI-negative refractory epilepsy were analyzed with $p < 0.005$, K > 200 and obtained abnormal metabolic regions were defined as potential epileptic foci. For patients without abnormal metabolic regions, further analysis was performed with $p < 0.005$, K > 100. For patients who still exhibited no abnormal metabolic zones after the previous threshold analysis, we continued the analysis with $p < 0.005$, K > 50. By keeping the p-value unchanged and gradually reducing the K value, we were able to identify more areas with minor metabolic abnormalities, which could be easily ignored with larger K values or using visual evaluation (**Figure 5**). We found that correction would reduce the sensitivity of SPM. Preoperative localization of epileptic foci is the result of multidisciplinary evaluation rather than a single examination. The high sensitivity of ^{18}F-FDG PET ensures that potential epileptic foci leading to seizures will not be missed, while SPM correction will limit this function to some extent. We conclude that SPM could play a beneficial role in the detection of epileptic foci when appropriate thresholds and voxels are chosen without correction.

3D-SSP has been used previously to detect abnormal metabolism in the brains of patients with early Alzheimer's disease (AD) (Imabayashi et al., 2004; Kaneko et al., 2004; Kirino, 2017; Lehman et al., 2012; Minoshima et al., 2020; Tang et al., 2004). Since the Cortex ID database contains ^{18}F-FDG PET images of normal subjects, a 3D-SSP method based on the Cortex ID database has recently been used to detect epileptic foci in patients with refractory epilepsy. Our study showed that the sensitivity of 3D-SSP to detect epileptic foci was 60%. So far, only one paper has applied 3D-SSP to the localization of epileptic foci (Wang et al., 2016). The study concluded that the sensitivity of 3D-SSP in detecting epileptic foci (71%) was higher than that reported in our study (60%). In their study, the localization of epileptic foci was based on preoperative comprehensive evaluation, while all the patients in our study met Engel's Class I criteria after surgery. Additionally, all patients in our study were MRI-negative. These differences contributed to the differences in results between the two studies. Previous studies have suggested that Z-values greater than 1.96 or 1.5 for 3D-SSP analysis based on SPECT images were useful for diagnosing AD patients (Kaneko et al., 2004; Wang et al., 2016; Kirino, 2017). However, the optimal Z threshold for 3D-SSP analysis based on ^{18}F-FDG PET image for the detection of epileptic foci in patients with refractory epilepsy has not yet been determined. The previous study did not report a specific Z-value (Wang et al., 2016). In our study, thresholds were set according to confidence intervals, and we concluded not only that the sensitivity of 3D-SSP was high, but also that the number of abnormal metabolic regions aligned with epileptic foci was similar to visual assessment at a Z-value of 1.28.

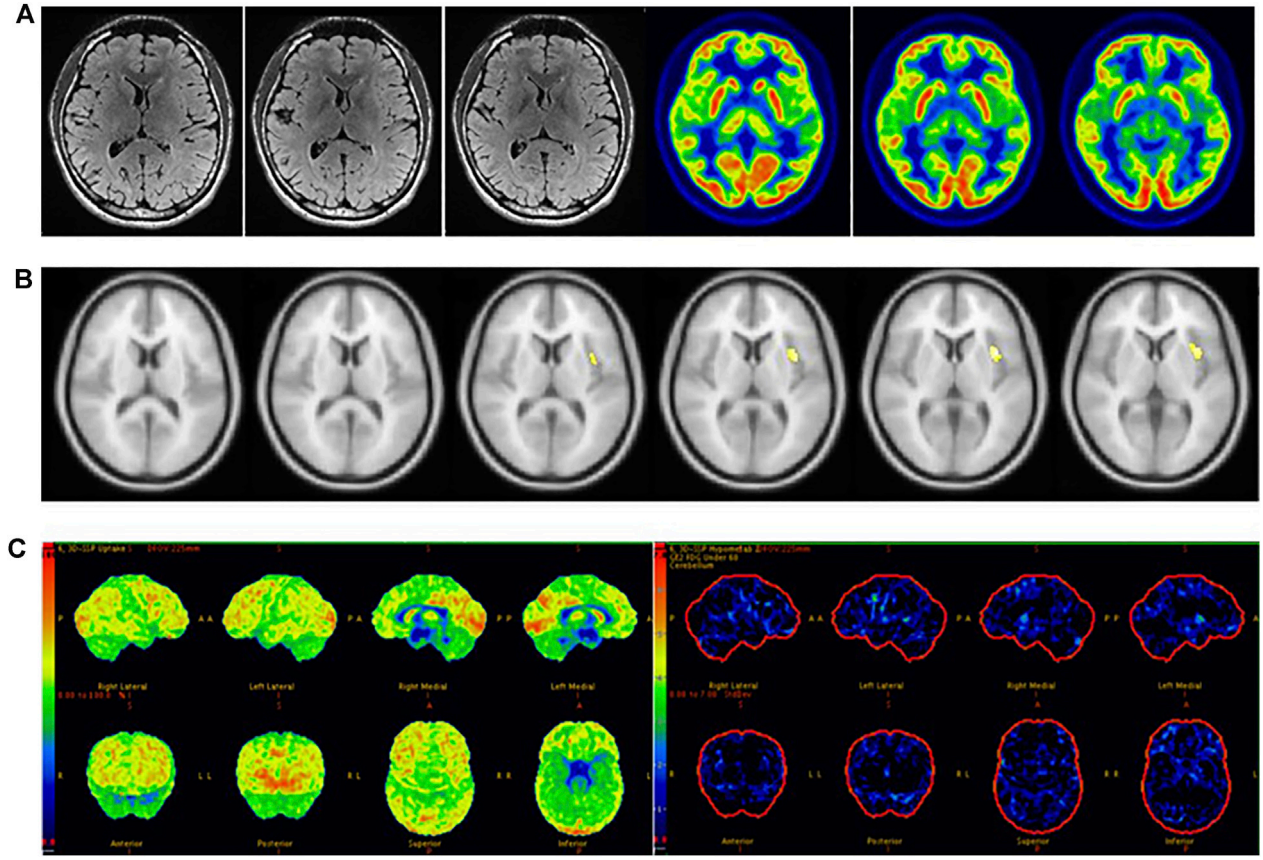

FIGURE 5 | Male, 22 years old, left insula epilepsy. **(A)** No structural lesions causing seizures were found at MRI 3.0 T epilepsy-protocol. ^{18}F-FDG PET showed doubtful abnormal decreased metabolism in the left insula lobe. **(B)** SPM did not find abnormal metabolic regions whlie $p < 0.005$ and $K > 200$ but obtain abnormal metabolism in left insula while $p < 0.005$ and $K > 50$. **(C)** 3D-SSP did not obtain abnormal metabolic regions. The left insula was surgically resected and lack of seizures for 2 years follow-up.

Visual assessment, SPM and 3D-SSP based on ^{18}F-FDG PET had high sensitivity in detecting epileptic foci, but their ability to correctly locate epileptic foci was low. This was due to the low specificity of ^{18}F-FDG PET (Rathore et al., 2014; Uijl et al., 2007), meaning that the abnormal metabolic regions detected by SPM and 3D-SSP based on ^{18}F-FDG PET were often larger than the real epileptic foci. Previous articles did not indicate the specificities of SPM and 3D-SSP in locating epileptic foci (Archambaud et al., 2013; Kim et al., 2002; Kumar et al., 2010; Mayoral et al., 2016; Wang et al., 2016). In our study, the specificities of SPM or 3D-SSP analysis based on ^{18}F-FDG PET were not significantly improved.

In clinical work, visual assessment based on ^{18}F-FDG PET images has many uncertain factors, and SPM and 3D-SSP can reduce human factors to allow the objective detection of epileptic foci. We found that the sensitivity of SPM was significantly higher than that of visual assessment, and there was a statistically significant difference between the two methods. SPM correctly detected 19 of the 39 patients incorrectly detected by visual assessment, with epileptic foci mainly located in small areas with low resolution that could be easily overlooked by visual analysis. We found that patients with abnormal metabolic regions located in the insula were more often identified by SPM than in visual assessment; because the insula is small in size and located at the junction of several brain lobes, it is difficult to assess visually (**Figure 5**). Ajay Kumar et al. also concluded that SPM is more useful for in cases of medial epilepsy, because medial abnormal metabolic foci are more likely to be missed by visual assessment (Kumar et al., 2010). Although there was no statistically significant difference between 3D-SSP and visual assessment, 3D-SSP was able to detect an additional 17 of the 39 patients who were incorrectly detected by visual assessment. 3D-SSP was not as good as SPM at detecting medial epileptic foci, but it was still able to detect microscopic abnormal metabolic areas of the cortex. In 10 patients, we found that neither visual assessment nor SPM correctly detected epileptic foci, but 3D-SSP correctly detected the foci (**Figure 6**). Although there was no statistically significant difference between the sensitivities of the two tests, 3D-SSP detected fewer epileptic foci than SPM, mainly because it failed to correctly detect epileptic foci in 14 of the 52 patients who were correctly detected by visual assessment. 3D-SSP software can be used to diagnose degenerative diseases in the elderly by analyzing metabolic changes of ^{18}F-FDG PET.

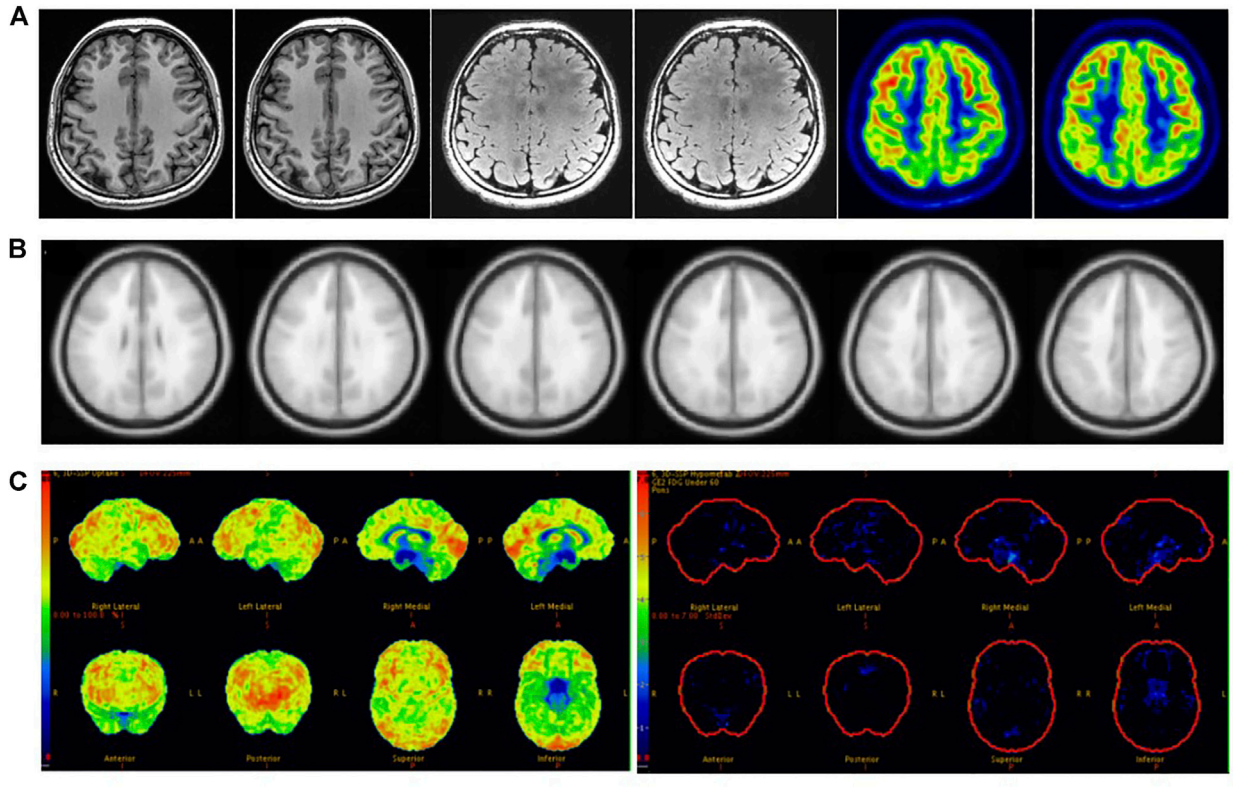

FIGURE 6 | Female, 21 years old, right frontal lobe epilepsy. **(A)** No structural lesions causing seizures were found at MRI 3.0 T epilepsy-protocol. ^{18}F-FDG PET obtained abnormal decreased metabolism in the left frontal, parietal and temporal lobes. **(B)** SPM obtained abnormal metabolism in left temporal lobe while $p < 0.005$ and $K > 100$. **(C)** 3D-SSP obtained abnormal metabolism in right frontal, double parietal and double occipital lobes. Further SEEG examination obtained the epilepsy foci originated from right frontal lobe. There had been no seizures for 3 years after surgical resection.

The age of control group in 3D-SSP database is >40 years old, and the age of the control group we selected (40–60 years old) is older than the average age of epilepsy group (21 years old), so there will be some deviation in the results obtained. If the 3D-SSP software database adds a young control population, it will provide more help for patients with refractory epilepsy.

While Visual/3D-SSP did not significantly improve sensitivity compared with SPM, visual assessment combined with either method did significantly improve sensitivity compared with visual assessment, SPM or 3D-SSP alone. SPM and 3D-SSP can objectively detect microscopic lesions overlooked in visual assessment, while visual assessment can identify lesions below the threshold settings of SPM or 3D-SSP. Therefore, the combination of the two methods can significantly improve sensitivity. Wang et al. also concluded that the combined sensitivity of the two tests is higher than that of the single test (Wang et al., 2016). There was no statistically significant difference between the sensitivities of Visual/SPM and Visual/3D-SSP, suggesting that similar sensitivity can be achieved in clinical application by combining visual assessment with either of the two objective methods.

Sensitivity reached 89% when visual assessment was combined with SPM and 3D-SSP, higher than for either method. A study has reported that the sensitivity of ^{18}F-FDG PET combined with three other methods to detect epileptic foci in patients with MRI-negative refractory epilepsy can reach 80% (Rossi Sebastiano et al., 2020), and another paper concluded that the sensitivity of Visual/SPM/3D-SSP can reach 97% (Wang et al., 2016). Our study is the first to simultaneously combine visual assessment, SPM and 3D-SSP based on ^{18}F-FDG PET to detect epileptic foci in MRI-negative epilepsy patients. We found that the combination of the three methods can significantly improve sensitivity, but reduces consistency due to the complementary detection capacities of the three methods, resulting in a larger range of detected abnormal lesions than actual epileptic foci. Therefore, in clinical work, we choose methods according to different situations. When the visual assessment is consistent with the electroclinical information of patients with MRI-negative refractory epilepsy, additional objective testing methods may not be accepted. When visual assessment is inconsistent with the patient's electroclinical information, we need to further accept objective testing methods and even combine visual assessment with multiple objective testing methods to prevent missing epileptogenic foci. When receiving multiple methods, judgments must be made based on different results. Attention should be paid to cases in which different methods indicate the same lesion, as it is the most likely potential epileptic focus (**Figure 7**). If multiple methods are inconsistent and cannot be

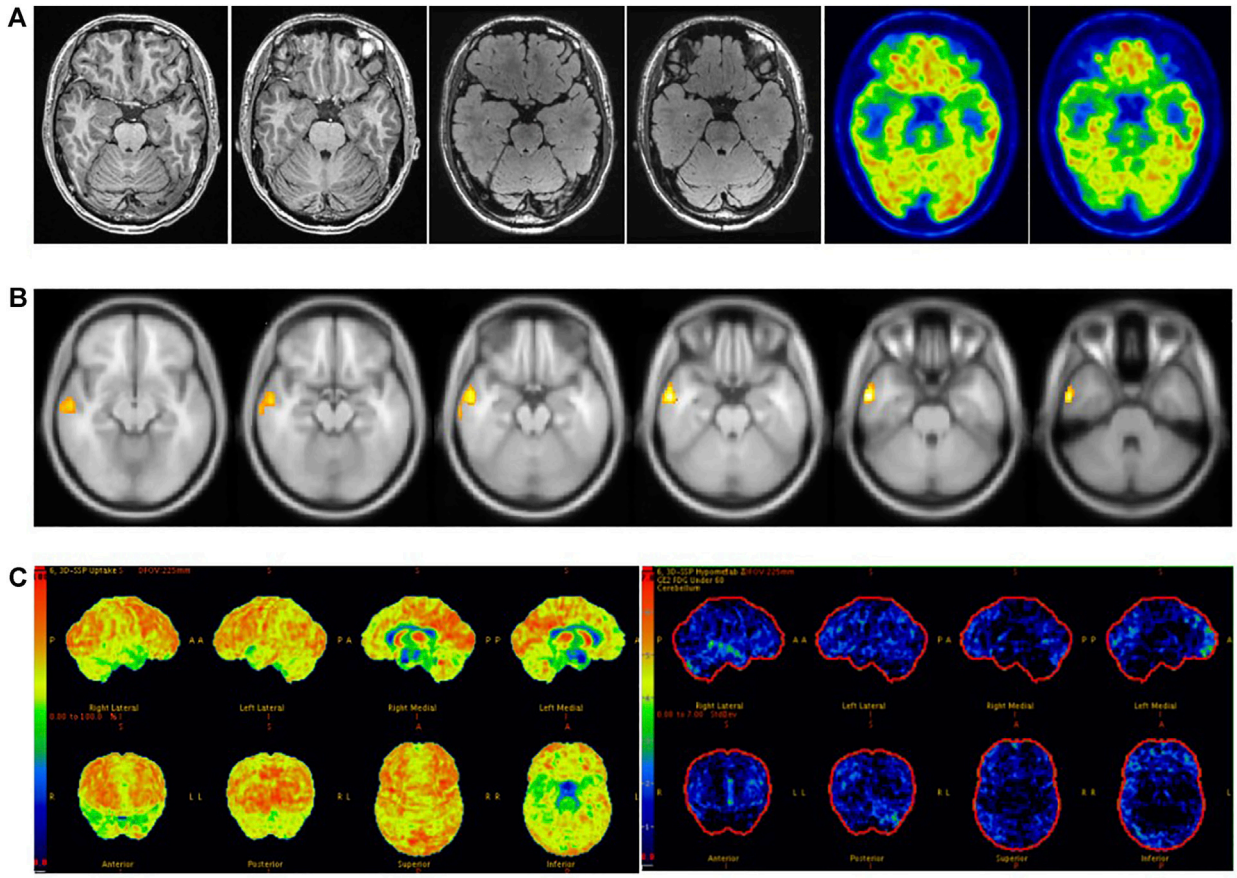

FIGURE 7 | Male, 37 years old, right temporal lobe epilepsy. **(A)** No structural lesions causing seizures were found at 3.0 T epilepsy-protocol. ^{18}F-FDG PET obtained abnormal decreased metabolism in the right temporal lobe. **(B)** SPM showed decreased metabolism in right temporal lobe while $p < 0.005$ and $K > 200$. **(C)** Abnormal metabolism in the right temporal lobe was found by 3D-SSP. The right anterior temporal lobe was surgically resected and remained seizure-free for 2 years follow-up.

used for localization, however, further evaluation should be performed by combining clinical symptoms with video-EEG or even SEEG (**Figure 6**).

SPM and 3D-SSP can be used as objective methods to detect epileptic foci before surgery in patients with MRI-negative refractory epilepsy. Clinical routine visual assessment of PET images is preferred in patients with MRI-negative refractory epilepsy. When visual assessment is consistent with electroclinical information of patients with epilepsy, additional objective testing methods are not acceptable. When the visual assessment is inconsistent with the patient's electroclinical information, SPM or 3D-SSP was further selected to assess the epileptic foci. If the combination of the two methods still fails to accurately locate the epileptic foci, comprehensive evaluation can be performed by combining the three methods.

DATA AVAILABILITY STATEMENT

The raw data supporting the conclusions of this article will be made available by the authors, without undue reservation.

ETHICS STATEMENT

The studies involving human participants were reviewed and approved by the First Affiliated Hospital of Jinan University Research Ethics Committee. Written informed consent to participate in this study was provided by the participants' legal guardian/next of kin. Written informed consent was obtained from the individual(s), and minor(s)' legal guardian/next of kin, for the publication of any potentially identifiable images or data included in this article.

AUTHOR CONTRIBUTIONS

HZ, WZ, and ZT contributed to the writing of the manuscript. HZ, ZZ, YL, SZ, LZ, JG, and HW collected the original data. HZ contributed to the statistical analysis of the data and constructed the figures and tables. XL, YT, YC, and ZT contributed to the analysis of imaging information. QG and HX conceived the paper layout and modified the paper. All authors had read and approved the final version of the manuscript.

FUNDING

This work was financially supported by the National Natural Science Foundation of China (No. 81871383), Basic and Applied Basic Research Foundation of Guangdong (2020A1515011192).

ACKNOWLEDGMENTS

We gratefully acknowledge the support of K.C. Wong Education Foundation (China), and the Project of Innovative Team for the Guangdong Universities (2018KCXTD001, China). We thank Boston Professional Group (BPG) Editing for editing the paper.

REFERENCES

Archambaud, F., Bouilleret, V., Hertz-Pannier, L., Chaumet-Riffaud, P., Rodrigo, S., Dulac, O., et al. (2013). Optimizing Statistical Parametric Mapping Analysis of 18F-FDG PET in Children. *EJNMMI Res.* 3, 2. doi:10.1186/2191-219X-3-2

Bernasconi, A., Cendes, F., Theodore, W. H., Gill, R. S., Koepp, M. J., Hogan, R. E., et al. (2019). Recommendations for the Use of Structural Magnetic Resonance Imaging in the Care of Patients with Epilepsy: A Consensus Report from the International League against Epilepsy Neuroimaging Task Force. *Epilepsia* 60, 1054–1068. doi:10.1111/epi.15612

Chassoux, F., Rodrigo, S., Semah, F., Beuvon, F., Landre, E., Devaux, B., et al. (2010). FDG-PET Improves Surgical Outcome in Negative MRI Taylor-type Focal Cortical Dysplasias. *Neurology* 75, 2168–2175. doi:10.1212/WNL.0b013e31820203a9

Desai, A., Bekelis, K., Thadani, V. M., Roberts, D. W., Jobst, B. C., Duhaime, A.-C., et al. (2013). Interictal PET and Ictal Subtraction SPECT: Sensitivity in the Detection of Seizure Foci in Patients with Medically Intractable Epilepsy. *Epilepsia* 54, 341–350. doi:10.1111/j.1528-1167.2012.03686.x

Duncan, J. S., Winston, G. P., Koepp, M. J., and Ourselin, S. (2016). Brain Imaging in the Assessment for Epilepsy Surgery. *Lancet Neurol.* 15, 420–433. doi:10.1016/s1474-4422(15)00383-x

Dwivedi, R., Ramanujam, B., Chandra, P. S., Sapra, S., Gulati, S., Kalaivani, M., et al. (2017). Surgery for Drug-Resistant Epilepsy in Children. *N. Engl. J. Med.* 377, 1639–1647. doi:10.1056/NEJMoa1615335

Engel, J., Jr., McDermott, M. P., Wiebe, S., Langfitt, J. T., Stern, J. M., Dewar, S., et al. (2012). Early Surgical Therapy for Drug-Resistant Temporal Lobe Epilepsy. *JAMA* 307, 922–930. doi:10.1001/jama.2012.220

Gonzalez-Martinez, J., Bulacio, J., Alexopoulos, A., Jehi, L., Bingaman, W., and Najm, I. (2013). Stereoelectroencephalography in the "difficult to Localize" Refractory Focal Epilepsy: Early Experience from a North American Epilepsy center. *Epilepsia* 54, 323–330. doi:10.1111/j.1528-1167.2012.03672.x

Hwang, S. I., Kim, J. H., Park, S. W., Han, M. H., Yu, I. K., Lee, S. H., et al. (2001). Comparative Analysis of MR Imaging, Positron Emission Tomography, and Ictal Single-Photon Emission CT in Patients with Neocortical Epilepsy. *AJNR Am. J. Neuroradiol* 22, 937–946. doi:10.1016/S0925-4927(01)00075-0

Imabayashi, E., Matsuda, H., Asada, T., Ohnishi, T., Sakamoto, S., Nakano, S., et al. (2004). Superiority of 3-dimensional Stereotactic Surface Projection Analysis over Visual Inspection in Discrimination of Patients with Very Early Alzheimer's Disease from Controls Using Brain Perfusion SPECT. *J. Nucl. Med.* 45, 1450–1457.

Jayalakshmi, S., Nanda, S. K., Vooturi, S., Vadapalli, R., Sudhakar, P., Madigubba, S., et al. (2019). Focal Cortical Dysplasia and Refractory Epilepsy: Role of Multimodality Imaging and Outcome of Surgery. *AJNR Am. J. Neuroradiol* 40, 892–898. doi:10.3174/ajnr.A6041

Jones, A. L., and Cascino, G. D. (2016). Evidence on Use of Neuroimaging for Surgical Treatment of Temporal Lobe Epilepsy. *JAMA Neurol.* 73, 464–470. doi:10.1001/jamaneurol.2015.4996

Kaneko, K., Kuwabara, Y., Sasaki, M., Ogomori, K., Ichimiya, A., Koga, H., et al. (2004). Posterior Cingulate Hypoperfusion in Alzheimer's Disease, Senile Dementia of Alzheimer Type, and Other Dementias Evaluated by Three-Dimensional Stereotactic Surface Projections Using Tc-99m HMPAO SPECT. *Clin. Nucl. Med.* 29, 362–366. doi:10.1097/01.rlu.0000127091.43180.92

Kim, Y. K., Lee, D. S., Lee, S. K., Chung, C. K., Chung, J. K., and Lee, M. C. (2002). (18)F-FDG PET in Localization of Frontal Lobe Epilepsy: Comparison of Visual and SPM analysisF-FDG PET in Localization of Frontal Lobe Epilepsy: Comparison of Visual and SPM Analysis. *J. Nucl. Med.* 43, 1167–1174. doi:10.1590/S1517-86922003000400006

Kirino, E. (2017). Three-dimensional Stereotactic Surface Projection in the Statistical Analysis of Single Photon Emission Computed Tomography Data for Distinguishing between Alzheimer's Disease and Depression. *Wjp* 7, 121–127. doi:10.5498/wjp.v7.i2.121

Kumar, A., Juhász, C., Asano, E., Sood, S., Muzik, O., and Chugani, H. T. (2010). Objective Detection of Epileptic Foci by 18F-FDG PET in Children Undergoing Epilepsy Surgery. *J. Nucl. Med.* 51, 1901–1907. doi:10.2967/jnumed.110.075390

Kwan, P., Arzimanoglou, A., Berg, A. T., Brodie, M. J., Allen Hauser, W., Mathern, G., et al. (2010). Definition of Drug Resistant Epilepsy: Consensus Proposal by the Ad Hoc Task Force of the ILAE Commission on Therapeutic Strategies. *Epilepsia* 51, 1069–1077. doi:10.1111/j.1528-1167.2009.02397.x

Lehman, V. T., Carter, R. E., Claassen, D. O., Murphy, R. C., Lowe, V., Petersen, R. C., et al. (2012). Visual Assessment versus Quantitative Three-Dimensional Stereotactic Surface Projection Fluorodeoxyglucose Positron Emission Tomography for Detection of Mild Cognitive Impairment and Alzheimer Disease. *Clin. Nucl. Med.* 37, 721–726. doi:10.1097/RLU.0b013e3182478d89

Mayoral, M., Marti-Fuster, B., Carreño, M., Carrasco, J. L., Bargalló, N., Donaire, A., et al. (2016). Seizure-onset Zone Localization by Statistical Parametric Mapping in Visually normal18F-FDG PET Studies. *Epilepsia* 57, 1236–1244. doi:10.1111/epi.13427

Minoshima, S., Frey, K. A., Koeppe, R. A., Foster, N. L., and Kuhl, D. E. (2020). A Diagnostic Approach in Alzheimer's Disease Using Three-Dimensional Stereotactic Surface Projections of Fluorine-18-FDG PET. *J. Nucl. Med.* 61, 142s–152s. doi:10.2967/jnumed.120.252510a

Mizumura, S., and Kumita, S.-i. (2006). Stereotactic Statistical Imaging Analysis of the Brain Using the Easy Z-Score Imaging System for Sharing a normal Database. *Radiat. Med.* 24, 545–552. doi:10.1007/s11604-006-0056-8

Muhlhofer, W., Tan, Y. L., Mueller, S. G., and Knowlton, R. (2017). MRI -negative Temporal Lobe Epilepsy-What Do We Know? *Epilepsia* 58, 727–742. doi:10.1111/epi.13699

Rathore, C., Dickson, J. C., Teotónio, R., Ell, P., and Duncan, J. S. (2014). The Utility of 18F-Fluorodeoxyglucose PET (FDG PET) in Epilepsy Surgery. *Epilepsy Res.* 108, 1306–1314. doi:10.1016/j.eplepsyres.2014.06.012

Rossi Sebastiano, D., Tassi, L., Duran, D., Visani, E., Gozzo, F., Cardinale, F., et al. (2020). Identifying the Epileptogenic Zone by Four Non-invasive Imaging Techniques versus Stereo-EEG in MRI-Negative Pre-surgery Epilepsy Patients. *Clin. Neurophysiol.* 131, 1815–1823. doi:10.1016/j.clinph.2020.05.015

Spencer, S. S. (1994). The Relative Contributions of MRI, SPECT, and PET Imaging in Epilepsy. *Epilepsia* 35 (Suppl. 6), S72–S89. doi:10.1111/j.1528-1157.1994.tb05990.x

Tang, B.-N. -T., Minoshima, S., George, J., Robert, A., Swine, C., Laloux, P., et al. (2004). Diagnosis of Suspected Alzheimers? Disease Is Improved by Automated Analysis of Regional Cerebral Blood Flow. *Eur. J. Nucl. Med. Mol. Imaging* 31, 1487–1494. doi:10.1007/s00259-004-1597-7

Uijl, S. G., Leijten, F. S. S., Arends, J. B. A. M., Parra, J., van Huffelen, A. C., and Moons, K. G. M. (2007). The Added Value of [18F]-Fluoro-D-Deoxyglucose Positron Emission Tomography in Screening for Temporal Lobe Epilepsy Surgery. *Epilepsia* 48, 2121–2129. doi:10.1111/j.1528-1167.2007.01197.x

von Oertzen, J., Urbach, H., Jungbluth, S., Kurthen, M., Reuber, M., Fernandez, G., et al. (2002). Standard Magnetic Resonance Imaging Is Inadequate for Patients with Refractory Focal Epilepsy. *J. Neurol. Neurosurg. Psychiatry* 73, 643–647. doi:10.1136/jnnp.73.6.643

Wang, K., Liu, T., Zhao, X., Xia, X., Zhang, K., Qiao, H., et al. (2016). Comparative Study of Voxel-Based Epileptic Foci Localization Accuracy between Statistical Parametric Mapping and Three-Dimensional Stereotactic Surface Projection. *Front. Neurol.* 7, 164. doi:10.3389/fneur.2016.00164

Wieser, H. G., Blume, W. T., Fish, D., Goldensohn, E., Hufnagel, A., King, D., et al. (2001). ILAE Commission Report. Proposal for a New Classification of Outcome with Respect to Epileptic Seizures Following Epilepsy Surgery. *Epilepsia* 42, 282–286. doi:10.1046/j.1528-1157.2001.35100.x

World Health Organization (2019). Epilepsy. Available at: https://www.who.int/zh/news-room/fact-sheets/detail/epilepsy (Accessed June 20, 2019).

Conflict of Interest: The authors declare that the research was conducted in the absence of any commercial or financial relationships that could be construed as a potential conflict of interest.

Publisher's Note: All claims expressed in this article are solely those of the authors and do not necessarily represent those of their affiliated organizations, or those of the publisher, the editors and the reviewers. Any product that may be evaluated in this article, or claim that may be made by its manufacturer, is not guaranteed or endorsed by the publisher.

frontiers in Bioengineering and Biotechnology

CASE REPORT
published: 07 January 2022
doi: 10.3389/fbioe.2021.803868

Case Report: Primary Pulmonary Angiosarcoma With Brain Metastasis

Xiangjun Tang[1†], Jing Zhu[2†], Fangcheng Zhu[3†], Hanjun Tu[1], Aiping Deng[1], Junti Lu[1], Minghuan Yang[1], Longjun Dai[1], Kuanming Huang[1] and Li Zhang[1]**

[1]Department of Neurosurgery, Taihe Hospital, Hubei University of Medicine, Shiyan, China, [2]Department of Respiratory and Critical Care Medicine, The Central Hospital of Wuhan, Tongji Medical College, Huazhong University of Science and Technology, Wuhan, China, [3]School of Basic Medical Sciences, Hubei University of Medicine, Shiyan, China

Primary pulmonary angiosarcoma (PPA) is a rare malignant vascular tumor, of which early diagnosis is challenging due to lack of specific clinical manifestations and a low level of suspicion. Here, we report a case of PPA presented with advanced brain metastasis. A 21-year-old patient with 1 week history of headache and mild cough was hospitalized for a head injury. Head MRI showed multiple intracranial lesions with brain edema. Chest CT displayed bilateral pulmonary infiltrates with mediastinal lymph node enlargement. After 2 months of anti-tuberculosis treatment, the patient was readmitted for persistent headache and cough with occasional hemosputum along with worsening pulmonary and intracranial lesions. Despite seizure prophylaxis and control of intracranial pressure and brain edema, his symptoms progressively aggravated, accompanied by cough with bloody sputum, frequent epileptic seizures, and hypotension. He eventually developed coma and died within 3 months of onset of symptoms. An autopsy confirmed PPA with brain metastasis.

Keywords: primary pulmonary angiosarcoma, brain metastasis, autopsy, diagnose, treatment

OPEN ACCESS

Edited by:
Youmei Bao,
Yale University, United States

Reviewed by:
Longbo Zhang,
Yale University, United States
Huiguo Liu,
Huazhong University of Science and Technology, China
Bin Peng,
Wuhan University, China

****Correspondence:***
Li Zhang
zhanglith@163.com
Kuanming Huang
hkm1111@sina.com

[†]These authors have contributed equally to this work

Specialty section:
This article was submitted to Nanobiotechnology, a section of the journal Frontiers in Bioengineering and Biotechnology

Received: *28 October 2021*
Accepted: *13 December 2021*
Published: *07 January 2022*

Citation:
Tang X, Zhu J, Zhu F, Tu H, Deng A, Lu J, Yang M, Dai L, Huang K and Zhang L (2022) Case Report: Primary Pulmonary Angiosarcoma With Brain Metastasis. Front. Bioeng. Biotechnol. 9:803868. doi: 10.3389/fbioe.2021.803868

INTRODUCTION

Angiosarcoma is an uncommon malignant endothelial tumor originated from blood or lymphatic vessels, accounting for about 2% of all soft tissue sarcomas. The tumor can arise in any organ, most often in the head and neck cutaneous tissue (Young et al., 2010). It is aggressive and often multicentric, with a high rate of local recurrence and distant metastasis associated with an overall poor prognosis. The lung is usually the major metastatic site of angiosarcoma, while primary pulmonary angiosarcoma (PPA) is extremely rare (Chen et al., 2010; ObesoCarillo et al., 2013). Patients with PPA may present with various degree of respiratory symptoms, however, definite diagnosis is difficult to make based on imaging or bronchoscopy, and often requires biopsy through surgical resection. We report here an uncommon case of PPA presented with advanced brain metastasis.

CASE REPORT

The patient was a 21-year-old male non-smoker without significant past medical history other than alcohol drinking (150 g/day). One week before admission, the patient developed a swelling headache without obvious inducement. The headache progressively intensified, accompanied by minor coughs

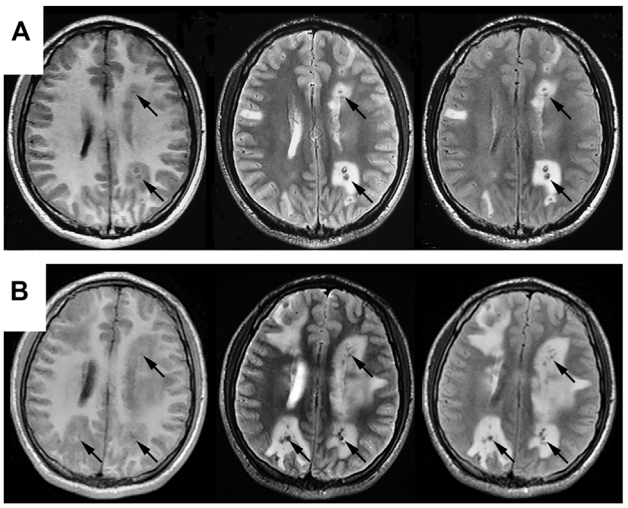

FIGURE 1 | Comparisons of cranial MRI results before **(A)** and after **(B)** admission. Both **(A,B)** reveal multiple nodular abnormal signals in bilateral cerebral and cerebellar hemispheres, mainly in the cortical and cortical medullary junctions, with lesions series **(B)** significantly larger than that in series **(A)**. T2WI and T2flair are mainly low signals, with high signals in some lesions. T1flair shows equal and low signals, with obvious edema around the lesions.

without hemoptysis or other neurological symptoms. Two days before admission, the patient was admitted to a local hospital for head trauma and found to have multiple intracranial space-occupying lesions on a head CT scan. He was transferred to our hospital for further diagnosis and treatment.

On admission, the patient's vital signs were stable, mental status normal and physical examinations unremarkable. Laboratory tests showed WBC 11.42 × 10^9/L, neutrophil 8.18 × 10^9/L and eosinophil 0.51 × 10^9/L, normal coagulation tests, normal tumor markers (CEA and AFP), and negative PPD test. Plain and enhanced head MRI revealed bilateral multiple intracranial lesions suggesting tuberculosis or possible metastatic tumors (**Figure 1A**). An enhanced CT scan of the chest showed bilateral pulmonary patchy infiltrates, most prominent in the left lower lobe dorsal segment, and an enlarged mediastinal lymph node (about 2.5 × 1.6 cm) without pleural effusion (**Figure 2A**). The patient was treated with intracranial pressure lowering agents and seizure prophylaxis as well as anti-tuberculosis agents and other antibiotics. One month later, patient's headache and cough remained unchanged, while repeat CT scan showed that both intracranial and pulmonary lesions had progressed significantly. The patient then underwent a bronchoscopy, which displayed bronchial inflammation and hemorrhage in the left lower lobe basal segment, as were consistent with bronchial biopsy results. No cancer cells were detected in the lavage. Considering the duration of treatment, the patient was advised to continue anti-tuberculosis and seizures prophylaxis as an outpatient.

The patient continued suffering from intermittent headache, cough with phlegm and occasional hemosputum. When he returned for follow-up 1 month later, his head MRI showed bilateral lesions wider than those of the previous one (**Figure 1B**). Chest CT indicated bilateral scattered lesions, with the lesion in the left lower lobe and the mediastinal lymph node larger than before and associated with high density lesions in the lower left oblique fissure (**Figure 2B**). Additionally, spinal tap was performed, and examination of cerebrospinal fluid revealed colorless, transparent fluid without clots, negative for Pan's test, total protein 0.55 g/L, glucose 4.12 mmol/L, and no cells or acid-fast bacilli found. While the patient continued to receive treatment for brain edema, anti-infection and seizure prophylaxis, his condition deteriorated progressively with worsening headache, frequent convulsions, hypotension, leading to coma and death. With the consent of the patient's family, an autopsy was performed, and it revealed multiple nodular lesions in the lungs and brain (**Figure 3**), no tumor in other organs. Immunohistochemistry of the lungs and brain displayed CK (-), Ki-67 (-), CD31 (+), CD34 (+), EMA (-) and GFAP (-). Histopathology of the lesions confirmed the diagnosis of PPA with brain metastasis (**Figure 4**).

DISCUSSION

PPA is a malignant tumor originating from pulmonary vascular endothelial cells and is a type of deep soft tissue angiosarcoma. The occurrence of the disease is extremely rare (Maglaras et al., 2004; Campione et al., 2009; Chen et al., 2010; ObesoCarillo et al., 2013). The average age of onset is 47.9 years-old (ranging 2–79 years) with occurrences more common in men (Drosos et al., 2019). The clinical manifestations of PPA are not specific. The most common symptoms of the disease reported so far are hemoptysis or hemosputum, cough, dyspnea, chest pain, and other non-specific symptoms such as fatigue, weight loss and fever (Ren et al., 2016). However, some patients may be asymptomatic during the course of the disease. In this case, the patient was younger than most reported patients (Drosos et al., 2019; Virarkar et al., 2019), and showed only minor coughs with occasional hemosputum, while headache due to metastasis was prominent. These factors contributed the misdiagnosis as tuberculosis.

Imaging is important in the diagnosis of pulmonary angiosarcoma, however, chest X-ray usually fails to detect fine changes of pulmonary angiosarcoma. PPA may present as multifocal or solitary nodular lesions on CT scans, with or without ground-glass changes, or with solidity changes (Ozcelik et al., 2006; Chen et al., 2010; Weissferdt and Moran, 2010). It is essential to differentiate pulmonary angiosarcoma from infectious diseases such as pneumonia and tuberculosis. Atasoy *et al.* reported a solitary PPA with large soft tissue masses in the left upper lobe, with mediastinal invasion and left parabronchial lymph node enlargement on the CT (Atasoy et al., 2001). At admission, our patient had pulmonary CT findings of patches in the dorsal segment of the left lower lobe, associated with ground-glass changes and enlargement of mediastinal lymph nodes, as well as multiple intracranial nodules on the cranial MRI. On the other hand, laboratory test suggested presence of infection, and bronchoscopy showed no intratracheal

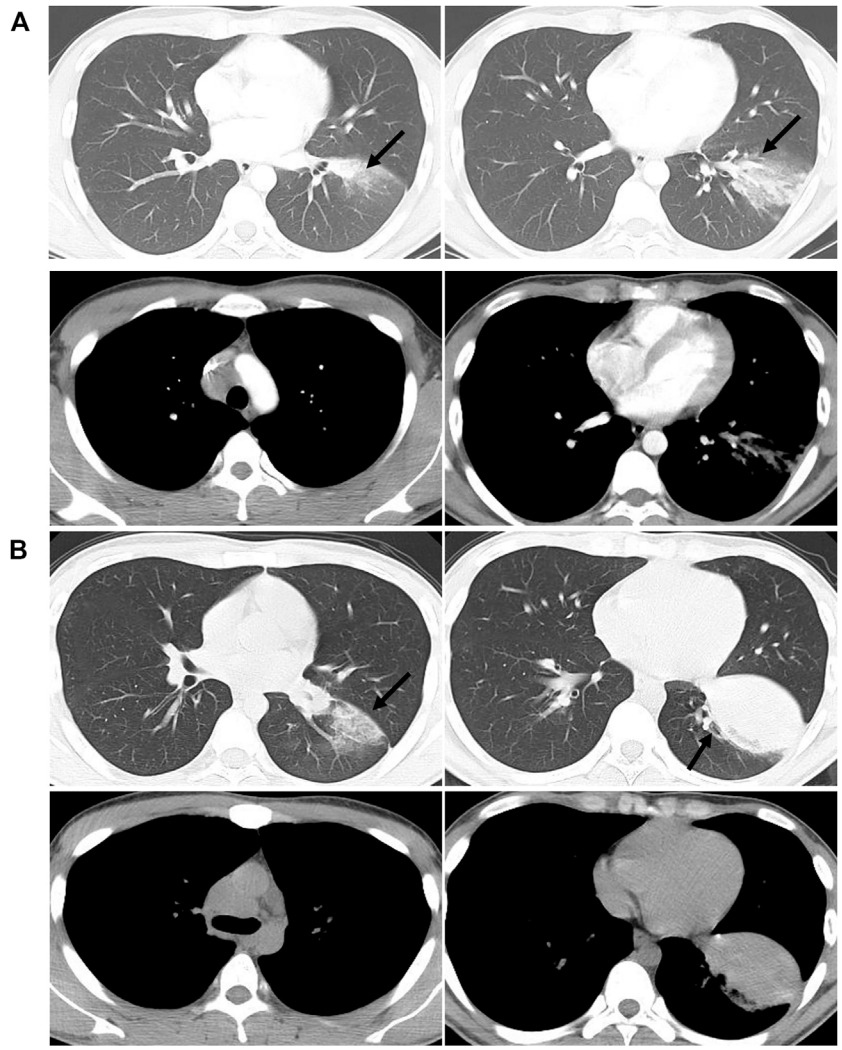

FIGURE 2 | Comparisons of chest CT results before **(A)** and after **(B)** admission. **(A)** shows the patchy shadow in the left lower lobe, with mediastinal lymphadenopathy. **(B)** shows that the left lower lung lesions are enlarged than before, with a solid shadow and lymphadenopathy.

space-occupying lesion (mass effect), pointing to infectious nature and leading to our initial misdiagnosis. However, when both pulmonary and intracranial lesions progressed rapidly under anti-tuberculosis treatment, with chest CT scan showing scattered nodules with ground-glass opacity and some solid masses with uneven density, attention should have been directed to the possibility of the highly invasive lung malignancy.

PPA accounts for 9.3% of total angiosarcomas (Drosos et al., 2019) and tends to grow latently. While local invasion and blood metastasis have often occurred at the time of detection (Maglaras et al., 2004; Grafino et al., 2016), PPA with brain metastasis was extremely rare. Our patient has this feature, with multiple intracranial metastases at the time of presentation. The main lethal factors of common brain metastatic tumors are brain edema and space-occupying effect, while our patient died of uncontrollable epilepsy and cerebral edema (Kim et al., 2015; Sun et al., 2015).

Lung biopsy and immunohistochemistry are the gold standards for the diagnosis of pulmonary angiosarcoma. Percutaneous fine needle aspiration cytology, bronchoscopic lung biopsy and thoracotomy/thoracoscopic biopsy are important means to obtain tissue specimens (Kojima et al., 2003; Campione et al., 2009; Wan Musa et al., 2010). Pathological diagnosis has also been reported through autopsy. Among them, bronchoscopy lung biopsy has a low positive rate for diagnosis of PPA, mainly because the small amount of biopsy tissue may not be sufficient to contain typical pathological features, and involvement of bronchi is not common, as were the case in our patient. Therefore, open lung biopsy is a more effective diagnostic method. Abnormal pleomorphic malignant endothelial cells are characteristic of angiosarcoma. These cells can be round, polygonal or spindle-shaped with or without epithelioid changes. In well-differentiated areas, abnormal endothelial cells form sinuses that connect to normal blood

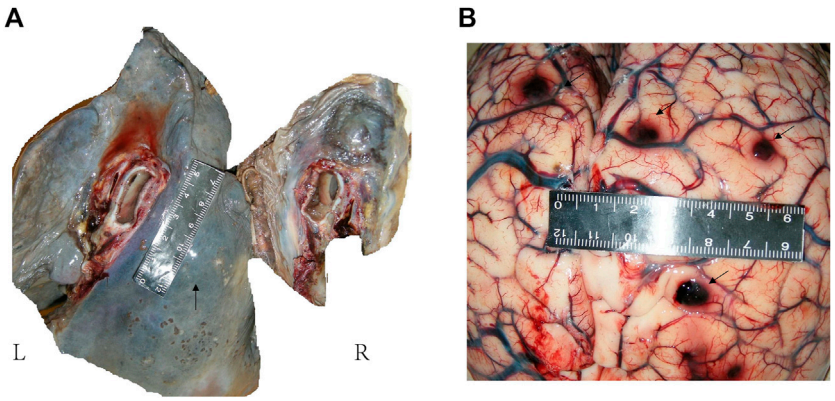

FIGURE 3 | Anatomical examination of lung and brain. **(A)**: Gray-white hard nodules were seen in the hilar and lower lobe. There was a hard mass in the mediastinum, about 5 cm × 2 cm in size. A small amount of gelatinous material was seen in the right main bronchus and pulmonary congestion was seen on section. **(B)**: Multiple hard nodules with bleeding were seen on both sides of the cerebral hemisphere and cerebellum.

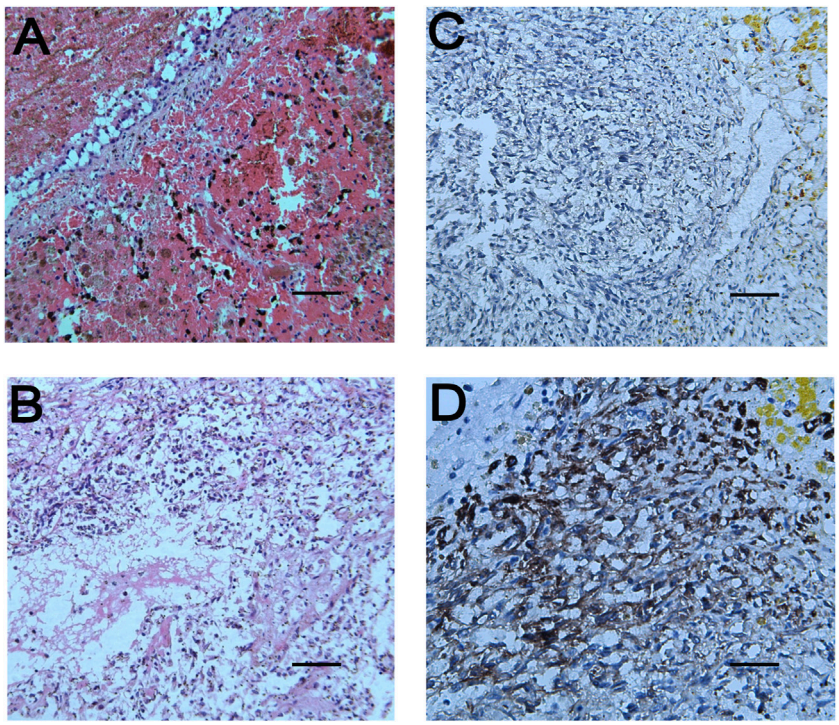

FIGURE 4 | Pathological results of lung and brain tissues. **(A)**: The tumor cells in the pulmonary nodules are arranged in a single thin-walled vascular lumen, filled with red blood cells and accompanied by necrosis, and have a large nuclear-cytoplasmic ratio, dark-colored nuclei and atypia. **(B)**: The lesions of the brain tissue are similar to those of the pulmonary nodules, accompanied by hemorrhage and necrosis. The surrounding brain tissue can be seen in the cuff-like infiltration of lymphocytes-based inflammatory cells around the blood vessels. Necrophages and satellite cells can also be observed. **(C**,**D)** respectively represent immunoreactivity for CD31 and CD34 on immunohistochemical examination (Magnifications: **(A)**, ×100; **(B**,**C)**, ×200; **(D)**, ×400).

vessels. In invasive lesions, this structure becomes chaotic and does not form a well-defined cavity. In poorly differentiated regions, malignant endothelial cells form a continuous monolayer, often accompanied by epithelioid morphology. Although cytological atypia exists, the tumor cells are mainly characterized by relatively single, mitosis, necrosis and hemorrhage (Keel et al., 1999), which is consistent with the autopsy results of our patient. Immunohistochemical markers for diagnosis of pulmonary angiosarcoma include factor VIII-related antigen, CD34 and CD31, with factor VIII-related antigen being the most specific but not as sensitive as CD31, which is expressed in 90% of angiosarcomas (Huo et al., 2006). Our patient

progressed rapidly and die of brain lesions scattered in multiple foci with hemorrhage, necrosis and edema. Positive CD34 and CD31 and histopathology on autopsy tissues confirmed the final diagnosis.

At present there is no unified treatment regimen for PPA. Surgical resection, radiotherapy, chemotherapy, immunotherapy and combined radiotherapy and chemotherapy have been reported in the literature (Kojima et al., 2003; Wilson et al., 2008; Chen et al., 2010; Grafino et al., 2016; Shirey et al., 2018). No treatment has been clinically proven to be effective, but treatment under certain conditions may be effective, such as early removal of focal lesions. However, the disease is often diagnosed at a late stage and beyond the indications for surgery. It has been reported that recombinant IL-2 immunotherapy combined with radiotherapy or gemcitabine combined with docetaxel may also be effective (Kojima et al., 2003). The current literature reports that the prognosis of PPA is extremely poor, with median survival time 7 months in patients with a single lesion, and 2 months in those with multiple lesions (Ren et al., 2016). The disease in this case developed rapidly and was quite aggressive, with advanced lesions beyond surgically resection at presentation, resulting in death in less than 3 months. Therefore, early detection and identification is crucial.

In conclusion, PPA is an extremely rare malignant tumor with a very poor prognosis. Because of the lack of specific clinical manifestations, timely diagnosis is difficult. The PPA patient reported here presented with early and advanced brain metastasis and was diagnosed after autopsy using histopathology and immunohistochemistry biomarkers. This case cautions us that PPA should be considered when a patient's MRI shows multiple mixed signals accompanied by obvious brain edema of unknown origin. Once the disease is suspected, biopsy combined with immunohistochemistry should be used to confirm the diagnosis as soon as possible.

DATA AVAILABILITY STATEMENT

The raw data supporting the conclusions of this article will be made available by the authors, without undue reservation.

ETHICS STATEMENT

Written informed consent was obtained from the individual(s) for the publication of any potentially identifiable images or data included in this article.

AUTHOR CONTRIBUTIONS

XT and JZ wrote the manuscript; FZ, AD, JL, and MY collected the data and images; LD edited language, HT, KH, and LZ led the treatment of patients and directed the writing of the manuscript.

ACKNOWLEDGMENTS

We thank the patient and his family for helping us study this disease. We also thank Daizhong Wang, Jingjing Liu for their efforts in clinical data management.

REFERENCES

Atasoy, Ç., Fitoz, S., Yiğit, H., Atasoy, P., Erden, I., and Akyar, S. (2001). Radiographic, CT, and MRI Findings in Primary Pulmonary Angiosarcoma. *Clin. Imaging* 25 (5), 337–340. doi:10.1016/s0899-7071(01)00302-3

Campione, A., Forte, G., Luzzi, L., Comino, A., Gorla, A., and Terzi, A. (2009). Pulmonary Angiosarcoma Presenting as Spontaneous Recurrent Hemothorax. *Asian Cardiovasc. Thorac. Ann.* 17 (1), 84–85. doi:10.1177/0218492309102544

Chen, Y.-b., Guo, L.-c., Yang, L., Feng, W., Zhang, X.-q., Ling, C.-h., et al. (2010). Angiosarcoma of the Lung: 2 Cases Report and Literature Reviewed. *Lung Cancer* 70 (3), 352–356. doi:10.1016/j.lungcan.2010.09.002

Drosos, E., Kalyvas, A., Komaitis, S., Skandalakis, G. P., Kalamatianos, T., Liouta, E., et al. (2019). Angiosarcoma-related Cerebral Metastases: a Systematic Review of the Literature. *Neurosurg. Rev.* 43, 1019–1038. doi:10.1007/s10143-019-01127-y

Grafino, M., Alves, P., Almeida, M. M. d., Garrido, P., Hasmucrai, D., Teixeira, E., et al. (2016). Angiosarcoma of the Lung. *J. Bras. Pneumol.* 42 (1), 68–70. doi:10.1590/S1806-37562016000000193

Huo, L., Moran, C. A., Fuller, G. N., Gladish, G., and Suster, S. (2006). Pulmonary Artery Sarcoma. *Am. J. Clin. Pathol.* 125 (3), 419–424. doi:10.1309/9h8rhuv1jl1we0qf

Keel, S. B., Bacha, E., Mark, E. J., Nielsen, G. P., and Rosenberg, A. E. (1999). Primary Pulmonary Sarcoma: a Clinicopathologic Study of 26 Cases. *Mod. Pathol.* 12 (12), 1124–1131.

Kim, E. Y., Lee, H. Y., Han, J., and Choi, J. Y. (2015). Primary Pulmonary Low-Grade Angiosarcoma Characterized by Mismatch between18F-FDG PET and Dynamic Contrast-Enhanced CT. *Korean J. Radiol.* 16 (5), 1166–1170. doi:10.3348/kjr.2015.16.5.1166

Kojima, K., Okamoto, I., Ushijima, S., Yoshinaga, T., Kitaoka, M., Suga, M., et al. (2003). Successful Treatment of Primary Pulmonary Angiosarcoma. *Chest* 124 (6), 2397–2400. doi:10.1378/chest.124.6.2397

Maglaras, G. C., Katsenos, S., Kakadelis, J., Katsanos, C., Metafratzi, Z., Stefanou, D. G., et al. (2004). Primary Angiosarcoma of the Lung and Pleura. *Monaldi Arch. Chest Dis.* 61 (4), 234–236. doi:10.4081/monaldi.2004.687

Obeso Carillo, G. A., García Fontán, E. M., Cañizares Carretero, M. Á., and Pérez Pedrosa, A. (2013). Primary Pulmonary Angiosarcoma, an Exceptional Neoplasm with a Poor Prognosis: Reports of Two Cases and Review of the Literature. *Gen. Thorac. Cardiovasc. Surg.* 61 (11), 643–647. doi:10.1007/s11748-012-0200-6

Ozcelik, C., Onat, S., Yaldiz, M., and Ozcelik, Z. (2006). Primary Epithelioid Angiosarcoma of the Lung Presenting as Pulmonary Hemorrhage. *Asian Cardiovasc. Thorac. Ann.* 14 (1), 69–71. doi:10.1177/021849230601400118

Ren, Y., Zhu, M., Liu, Y., Diao, X., and Zhang, Y. (2016). Primary Pulmonary Angiosarcoma: Three Case Reports and Literature Review. *Thorac. Cancer* 7 (5), 607–613. doi:10.1111/1759-7714.12376

Shirey, L., Coombs, D., Talwar, A., and Mickus, T. (2018). Pulmonary Epithelioid Angiosarcoma Responsive to Chemotherapy: A Case Report. *Radiol. Case Rep.* 13 (2), 479–484. doi:10.1016/j.radcr.2018.02.002

Sun, D., Yu, R., Chen, J., Geng, D., and Zhang, L. (2015). A Rare Case of Primary Paranasal Sinus Angiosarcoma with Pulmonary Metastasis Detected by 18F-FDG PET/CT. *Clin. Nucl. Med.* 40 (3), 286–288. doi:10.1097/RLU.0000000000000694

Virarkar, M., Tayyab, S., Thampy, R., Bhosale, P., and Viswanathan, C. (2019). Primary Pulmonary Angiosarcoma: Case Reports and Review of the Literature. *Asian Cardiovasc. Thorac. Ann.* 27 (5), 347–352. doi:10.1177/0218492319836910

Wan Musa, W. R., Abdulwakil Elraied, M. A., Phang, K. S., Kwah, Y. G., Tan, S. P., Harun, R., et al. (2010). Primary Epithelioid Angiosarcoma of the Lung

Presenting as Left-Sided Shoulder Pain. *Ann. Acad. Med. Singap* 39 (8), 658–659.

Weissferdt, A., and Moran, C. A. (2010). Primary Vascular Tumors of the Lungs: a Review. *Ann. Diagn. Pathol.* 14 (4), 296–308. doi:10.1016/j.anndiagpath.2010.03.001

Wilson, R., Glaros, S., Brown, R. K. J., Michael, C., and Reisman, D. (2008). Complete Radiographic Response of Primary Pulmonary Angiosarcomas Following Gemcitabine and Taxotere. *Lung Cancer* 61 (1), 131–136. doi:10.1016/j.lungcan.2007.12.006

Young, R. J., Brown, N. J., Reed, M. W., Hughes, D., and Woll, P. J. (2010). Angiosarcoma. *Lancet Oncol.* 11 (10), 983–991. doi:10.1016/S1470-2045(10)70023-1

Conflict of Interest: The authors declare that the research was conducted in the absence of any commercial or financial relationships that could be construed as a potential conflict of interest.

The reviewer HL declared a shared affiliation, with no collaboration, with one of the authors JZ, to the handling editor at the time of the review.

Publisher's Note: All claims expressed in this article are solely those of the authors and do not necessarily represent those of their affiliated organizations, or those of the publisher, the editors and the reviewers. Any product that may be evaluated in this article, or claim that may be made by its manufacturer, is not guaranteed or endorsed by the publisher.

frontiers in Bioengineering and Biotechnology

ORIGINAL RESEARCH
published: 10 January 2022
doi: 10.3389/fbioe.2021.810897

Electroclinical and Multimodality Neuroimaging Characteristics and Predictors of Post-Surgical Outcome in Focal Cortical Dysplasia Type IIIa

Lingling Zhang[1,2], Hailing Zhou[1], Wei Zhang[3], Xueying Ling[1], Chunyuan Zeng[1], Yongjin Tang[1], Jiefeng Gan[1], Qinghua Tan[3], Xiangshu Hu[3], Hainan Li[4], Baijie Cheng[4], Hao Xu[1] and Qiang Guo[3]**

[1]Department of Nuclear Medicine, PET/CT-MRI Center, Center of Cyclotron and PET Radiopharmaceuticals, The First Affiliated Hospital of Jinan University, Guangzhou, China, [2]Department of Neurology, Affiliated Hangzhou First People's Hospital, Zhejiang University School of Medicine, Zhejiang, China, [3]Epilepsy Center, Guangdong 999 Brain Hospital, Guangzhou, China, [4]Department of Pathology, Guangdong 999 Brain Hospital, Guangzhou, China

OPEN ACCESS

Edited by:
Jian Yang,
Shanghai University, China

Reviewed by:
Erik Dirk Gommer,
Maastricht University Medical Centre, Netherlands
YingZhu Chen,
Yangzhou University, China

***Correspondence:**
Hao Xu
txh@jnu.edu.cn
Qiang Guo
guoqiang999brain@163.com

Specialty section:
This article was submitted to Nanobiotechnology, a section of the journal Frontiers in Bioengineering and Biotechnology

Received: 08 November 2021
Accepted: 26 November 2021
Published: 10 January 2022

Citation:
Zhang L, Zhou H, Zhang W, Ling X, Zeng C, Tang Y, Gan J, Tan Q, Hu X, Li H, Cheng B, Xu H and Guo Q (2022) Electroclinical and Multimodality Neuroimaging Characteristics and Predictors of Post-Surgical Outcome in Focal Cortical Dysplasia Type IIIa. Front. Bioeng. Biotechnol. 9:810897. doi: 10.3389/fbioe.2021.810897

Focal cortical dysplasia (FCD) type IIIa is an easily ignored cause of intractable temporal lobe epilepsy. This study aimed to analyze the clinical, electrophysiological, and imaging characteristics in FCD type IIIa and to search for predictors associated with postoperative outcome in order to identify potential candidates for epilepsy surgery. We performed a retrospective review including sixty-six patients with FCD type IIIa who underwent resection for drug-resistant epilepsy. We evaluated the clinical, electrophysiological, and neuroimaging features for potential association with seizure outcome. Univariate and multivariate analyses were conducted to explore their predictive role on the seizure outcome. We demonstrated that thirty-nine (59.1%) patients had seizure freedom outcomes (Engel class Ia) with a median postsurgical follow-up lasting 29.5 months. By univariate analysis, duration of epilepsy (less than 12 years) (p = 0.044), absence of contralateral insular lobe hypometabolism on PET/MRI ($p_{\text{Log-rank}}$ = 0.025), and complete resection of epileptogenic area ($p_{\text{Log-rank}}$ = 0.004) were associated with seizure outcome. The incomplete resection of the epileptogenic area (hazard ratio = 2.977, 95% CI 1.218–7.277, p = 0.017) was the only independent predictor for seizure recurrence after surgery by multivariate analysis. The results of past history, semiology, electrophysiological, and MRI were not associated with seizure outcomes. Carefully included patients with FCD type IIIa through a comprehensive evaluation of their clinical, electrophysiological, and neuroimaging characteristics can be good candidates for resection. Several preoperative factors appear to be predictive of the postoperative outcome and may help in optimizing the selection of ideal candidates to benefit from epilepsy surgery.

Keywords: characteristics, predictors, postoperative outcome, focal cortical dysplasia type IIIa, drug-resistant epilepsy

INTRODUCTION

Epilepsy is one of the most common severe chronic neurological disorders and is considered a severe public health concern (Blumcke et al., 2017). Drug-resistant epilepsy accounts for at least one-third of people with epilepsy (Montaz-Rosset et al., 2019). The most familiar developmental cortical malformation that leads to intractable epilepsy is focal cortical dysplasia (FCD) (Palmini and Holthausen, 2013). FCD is the most common histopathology diagnosis in children and the third most familiar etiology in adult patients undergoing epilepsy resection (Hauptman and Mathern, 2012). With the development of neuroimaging techniques, especially MRI and ^{18}F-FDG PET (Tassi et al., 2002), more studies have shown that a higher incidence of FCD than previously diagnosed have enhanced the preoperative recognition and classification of these malformations (Widdess-Walsh et al., 2006). These patients have a serious seizure burden: more than 60% suffer from daily seizures, and a large number of FCD patients have onset of epilepsy by the age of 16 years (Chapman et al., 2005).

For these refractory epilepsy patients associated with FCD, the resection of epilepsy has become the most promising alternative therapeutic option to achieve seizure control in recent decades. Among the FCD patients with resection, postoperative seizure control ranged from 52% to 67% (D. W. Kim et al., 2009; Lerner et al., 2009). Incomplete resection of the epileptogenic area could lead to persistent seizures (Najm et al., 2013). These epilepsy individuals are confronted with difficulties because operative seizure outcomes cannot be predicted accurately before operation. Therefore, in patients with intractable epilepsy and FCD, the combination of clinical, electrophysiological data and multimodality neuroimaging features during a detailed preoperative assessment may help to precisely localize the epileptogenic zone (EZ) (Pittau et al., 2014) and predict seizure outcome after surgery (Mintzer and Sperling, 2008).

However, previous researches have focused on investigating the predictors of postoperative outcomes for isolated FCD patients or dual pathology using Palmini's FCD classification (Chang et al., 2011); thus, the predictors of postoperative seizure outcome in FCD associated with other principal lesions according to new classification (Blumcke et al., 2011), especially newly classified FCD type IIIa [FCD type I coexisting with hippocampal sclerosis (HS) in the temporal lobe, which is also a common pathology and different from isolated FCD in temporal lobe epilepsy (TLE) (Marusic et al., 2007)], are less well discussed (Fauser et al., 2015). Although it is very critical to explore the predictors in identifying perfect candidates for epilepsy surgery and evaluating the postoperative outcome of individual patients, there have been only restricted data about the predictive factors involved in the surgical therapy of intractable FCD type IIIa.

In our study, the demographic, clinical, and electrophysiological characteristics, the neuroimaging features, and the postoperative outcome were reviewed in the patients with histologically confirmed FCD type IIIa in our epilepsy center. The goal of the current study was to determine the reliable predictive factors for seizure freedom outcome using the Kaplan–Meier (KM) survival analysis and multivariate Cox proportional hazards model in order to better recognize potential candidates for epilepsy surgery.

MATERIALS AND METHODS

Study Subjects

Our study retrospectively analyzed consecutive individuals diagnosed with medically intractable TLE and FCD type IIIa as determined by histopathology who underwent resective epilepsy surgery at our epilepsy center from January 1, 2014, until April 31, 2019. Drug-resistant epilepsy was diagnosed according to the criteria proposed by International League Against Epilepsy (ILAE), which fulfilled the definition "failure of adequate trials of two tolerated and appropriately chosen anti-epileptic drugs (AEDs) schedules (whether as monotherapies or in combination) to achieve seizure freedom" (Kwan et al., 2010).

The inclusion criteria were as follows: 1) all FCD type IIIa (HS-related FCD type I in the temporal lobe) was diagnosed by histopathology results after surgery according to the 2011 ILAE classification system for FCD (Blumcke et al., 2011); 2) postoperative follow-up was at least 12 months after surgery; and 3) either adult or children patients were included.

Exclusion criteria were as follows: 1) isolated FCD type I and II; 2) FCD in other brain lobes or multiple brain lobes; 3) hemispheric dysplasia, tuberous sclerosis, and periventricular nodular heterotopias; 4) isolated HS; 5) HS associated with tumor, vascular malformation or other early lesions (e.g., trauma, ischemic injury, and encephalitis) in the temporal lobe.

Video Electroencephalogram and Stereoelectroencephalography

All patients underwent long-term scalp video electroencephalogram (VEEG) recording with 21 channels based on the international 10–20 system, with attached anterior temporal electrodes. Interictal and ictal scalp VEEG was recorded in each patient, and at least two habitual seizures during monitoring were reviewed for all patients. Ictal rhythm/interictal spike in the electrodes of an epileptogenic lobe or two adjacent electrodes was considered as a localizing pattern of ictal-onset rhythm/interictal spike.

Stereoelectroencephalography (SEEG) monitoring was recommended if the presurgical noninvasive evaluation was disconcordant, there was no visible causative lesion seen on MRI, or eloquent cortex was included. Some patients were implanted with electrodes in areas that could be associated with the EZ using robotic stereotactic assistance (ROSA) system. Long-term recordings were conducted after implanting electrodes utilizing VEEG monitoring system. And the EZ was defined as the regions covered by the electrodes that presented ictal discharge patterns that occurred either before or simultaneously with clinical behavior (Seo et al., 2011).

Imaging

All epilepsy patients underwent sequential PET/MRI, conducted with CT-based attenuation correction and MRI using a

trimodality PET/CT-MRI system (full ring, time-of-flight discovery PET/CT 690, 3T Discovery MR 750, GE Healthcare, Chicago, IL, USA) in the PET/CT-MRI Center at The First Affiliated Hospital of Jinan University. MRI was conducted first on a 3.0-T MR scanner (GE Discovery 750, Milwaukee, WI, USA). The interictal PET/CT scans for all patients were conducted using a GE Discovery PET-CT 690 system. All patients had clinical seizures no less than 24 h before the PET scan to exclude possible effects on PET sensitivity, and VEEG monitoring was not performed simultaneously with the PET scan. ^{18}F-FDG PET visual analysis was semiquantitative and performed by two experienced nuclear physicians on the GE AW 4.6 workstation during the preoperation evaluation and before invasive SEEG. ^{18}F-FDG PET and MRI data were sent to a dedicated review workstation (GE Advantage workstation, version 4.6; GE Healthcare Life Sciences GE), also evaluated by two experienced nuclear physicians.

Surgery and Pathology

All patients underwent resection after the review of the presurgical evaluation information in a multidisciplinary case discussion. The resection range included the onset zone monitored by intracranial electrodes, the focal dysplastic area adjacent to the zone, and the hypometabolism region around the onset zone. Generally speaking, if the epileptogenic lesion is located in the mesial temporal lobe and temporal neocortex, the involved neocortex and mesial structures needed to be removed. We usually perform standardized anterior temporal lobe resection (ATLR) in our center. The temporal neocortex (4–5 cm on the dominant temporal cortex and 5–6 cm on the nondominant temporal cortex), in combination with the mesial temporal structures (consisting of the hippocampus, parahippocampal gyrus, and amygdala), was removed (Kemerdere et al., 2018). Some patients underwent extended temporal lobectomy and amygdalo-hippocampectomy on the basis of the results of SEEG. All patients underwent MRI to evaluate the completeness of resection after surgery. Complete excision was defined by resection of all of the MRI lesions and seizure onset zones defined by SEEG according to postoperative MRI. Moreover, almost all of these patients had changes in the medial structure, such as HS, which required complete resection. If postoperative MRI showed residual medial structure, it was considered incomplete resection.

The histopathological diagnosis was acquired by disposing of the surgical samples, as previously described (Chang et al., 2011). Histopathology of FCD was classified using ILAE 2011 classification guideline (Blumcke et al., 2011), as follows: FCD type IIIa refers to the temporal cortical dyslamination in combination with HS.

Surgical Outcomes

Seizure outcome for all patients after surgery was determined by a review of clinic visits or telephone contacts. All individuals were followed up until April 31, 2020. Seizure outcome classifications after operation were made using Engel's classification (Engel, 1993): Engel class Ia, completely seizure free after surgery; and Engel class I, seizure free or auras only or convulsions with drug withdrawal only. Patients were considered seizure free only if they never experienced seizures or auras throughout the follow-up period (Engel class Ia outcome), and acute postoperative seizures within the first week were excluded (Cahill et al., 2019).

Statistical Analyses

The study population was divided into two groups including seizure freedom and seizure recurrence based on the prognosis at the last follow-up. For exploratory purposes, the continuous variables were compared between these two groups using the nonparametric Mann–Whitney U test due to non-normal distributions. Categorical variables were compared between two groups using a chi-square test or Fisher's exact test, as appropriate.

KM survival curves were used to characterize the probability of remaining seizure free after surgery over time. First, KM survival analysis was performed to investigate the probability of seizure-free survival in the overall group. All cases lost to follow-up were censored at the date of last clinical contact. Then, the differences between groups in seizure freedom distributions were compared using the log-rank test for the univariate analysis. Variables with $p < 0.1$ in univariate analysis were then included in the multivariate Cox proportional regression model to analyze independent prognostic effect for seizure recurrence, Mantel–Haenszel hazard ratio (HR), and 95% CI were calculated.

All data analyses were conducted using the IBM SPSS 19.0 software package (SPSS Inc., Chicago, IL, USA) and GraphPad Prism, version 8.0 (GraphPad Software, La Jolla, CA, USA). A two-tailed $p < 0.05$ was considered statistically significant for all statistical tests.

RESULTS

Patient Demographic and Clinical Characteristics

We first selected three hundred and forty-eight drug-resistant epilepsy patients who underwent resection in our epilepsy center. Then we excluded patients with other types of potentially epileptogenic lesions (n = 128), FCD in other brain lobes or multiple brain lobes (n = 120), other types of FCD in temporal lobe (n = 22), insufficient postoperative follow-up (n = 8), undetermined death (n = 2), and lost to follow-up (n = 2). Finally, sixty-six patients met the inclusion criteria (**Figure 1**). The patients' basic demographics and clinical characteristics are summarized in **Table 1**.

The most common preoperative seizure type based on the new classification method of seizure types (Fisher et al., 2017) was focal impaired awareness seizure (FIAS) (62.1%), followed by focal to bilateral tonic–clonic seizure (FBTCS) (36.4%). The frequency of seizures before surgery was divided into three categories: daily seizures (≥1 seizure each day), weekly seizures (≥1 seizure each week), and monthly seizures (≥1 seizure each month) (Chang et al., 2011). Among these, eighteen (27.3%) patients had daily seizures. Finally, twenty-four patients (36.4%) underwent ATLR, and fifty-seven (86.4%) patients underwent complete resection of epileptogenic area.

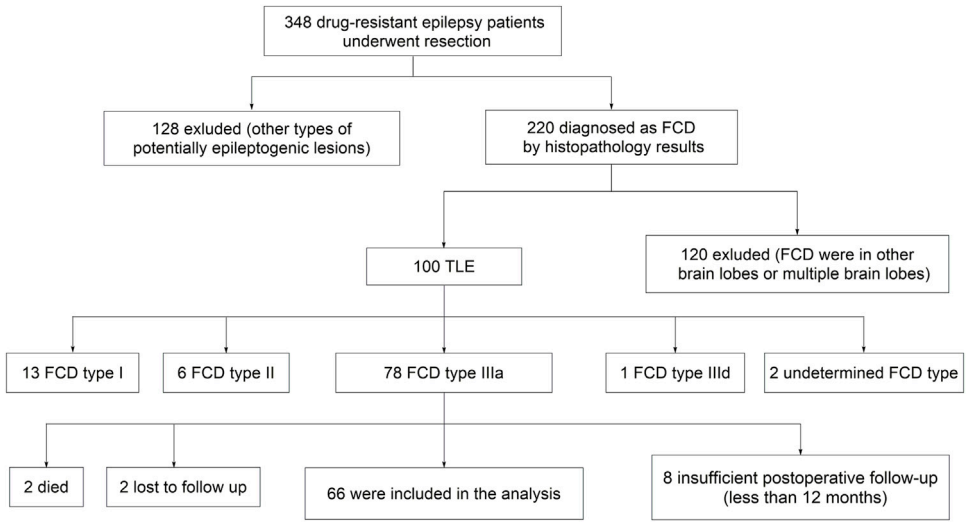

FIGURE 1 | Flowchart of patient selection. FCD, focal cortical dysplasia; TLE, temporal lobe epilepsy.

Preoperative Electrophysiological and Neuroimaging Characteristics

The electrophysiological characteristics of these patients are demonstrated in **Table 2**. Focal interictal epileptiform discharges (IEDs) on scalp VEEG were localized in thirty-two (48.5%) patients. Moreover, localized ictal onset zone on scalp EEG was clearly localized in twenty-seven (40.9%) patients. SEEG was conducted in sixty (90.9%) cases using the ROSA system (Medtech, Montpellier, France), confirming that ictal discharge patterns occurred confined to either the mesial temporal lobe or neocortical areas.

We also assessed the preoperative neuroimaging features in overall cases (**Table 2**). Structural MRI could only detect thirteen (19.7%) patients with FCD type IIIa. Approximately 63.6% of patients had typical HS lesions on structural MRI, whereas only six (9.1%) patients presented gray–white matter transition blurring. Moreover, cortical thickening and subcortical T2/fluid-attenuated inversion recovery (FLAIR) abnormality were significantly less frequent in only three (4.5%) and two (3%) patients, respectively. MRI findings were closely concordant with ictal scalp VEEG onset pattern in twenty-three (34.8%) patients.

Moreover, we further analyzed the metabolism pattern in these sixty-six patients using ^{18}F-FDG PET/MRI coregistration. Contralateral temporal lobe hypometabolism (TLH) was observed in only five (7.6%) patients. Contralateral frontal lobe hypometabolism and bilateral frontal lobe hypometabolism were also found in about eight (12.1%) and six (9.1%) patients, respectively. We also demonstrated that contralateral insular lobe hypometabolism was relatively infrequent in three (4.5%) patients.

Postoperative Seizure Outcomes

The continuous Engel class Ia seizure freedom outcome after the operation is illustrated using KM curves (**Figure 2**). The cumulative probability of seizure freedom survival was 69.7% (95% CI, 58.6–80.8%), 62.3% (95% CI, 50.3–74.4%), 56.5% (95% CI, 43.0–70.0%), and 48.4% (95% CI, 29.8–67.1%) at 12, 24, 36, and 60 months or more after surgery, respectively.

To evaluate in detail the seizure outcomes after surgery, we further investigated each Engel classification outcome distribution at different follow-up times (≥12 months) in sixty-six patients (**Figure 3**). At the last follow-up time (median, 29.5 months), thirty-nine patients (59.1%) were free of seizures and auras (Engel class Ia) after surgery, and one patient (1.5%) had Engel class Ib–d outcome. Seventeen patients (25.8%) had Engel class II outcome, three patients (4.5%) had Engel class III outcome, and six patients (9.1%) had an Engel class IV outcome.

Predictors of Seizure Freedom Outcome

We firstly performed a univariate analysis of the predictive factors influencing the seizure outcome (**Table 1**, **2**), and the postoperative seizure outcome was classified as two groups including seizure freedom and seizure recurrence at last follow-up. The preoperative clinical, electrophysiological, and neuroimaging characteristics were explored. More patients with complete resection of the epileptogenic area were likely to obtain seizure freedom outcomes (94.9 *versus* 74.1%, p = 0.040). The patients with a duration of epilepsy less than 12 years had increased likelihood of seizure freedom after surgery (69.2 *versus* 44.4%, p = 0.044). The patients with ATLR were more likely to obtain seizure freedom (41.0 *versus* 29.6%) but did not reach significance (p = 0.344). Moreover, the presence of gray–white blurring or HS on MRI was also more likely to obtain seizure freedom but failed to reach significance (p = 0.406 and p = 0.539, respectively).

We further explored some univariate predictors utilizing the KM survival curves of seizure freedom outcome (**Figures 4**, **5**). In our included patients, the influence of the two preoperative factors on seizure outcome was statistically significant, as follows (**Figure 4D**, **Figure 5D**): 1) the patients with complete

TABLE 1 | | Demographic and clinical characteristics.

Variable	Outcome		*p*-Value
—	Seizure freedom	Seizure recurrence	—
No. of patients	39 (59.1%)	27 (40.9%)	—
Gender	—	—	0.756[a]
Male	26 (66.7%)	17 (63.0%)	—
Female	13 (33.3%)	10 (37.0%)	—
Duration of follow-up (months), median (IQR)	29.0 (22.0–40.5)	33.0 (22.0–42.0)	0.953[b]
Age at operation (years), median (IQR)	24.0 (16.0–29.0)	23.0 (19.0–28.0)	0.629[b]
Age at seizure onset (years), median (IQR)	12.0 (4.0–18.0)	9.0 (5.0–14.0)	0.368[b]
Duration of epilepsy (years), median (IQR)	10.0 (6.0–15.0)	12.0 (9.0–20.0)	0.098[b]
Duration of epilepsy (< 12 years)	27 (69.2%)	12 (44.4%)	0.044[a]*
Presence of FC	6 (15.4%)	7 (25.9%)	0.290[a]
Early brain injury	0 (0%)	0 (0%)	—
Family history	2 (5.1%)	0 (0%)	0.509[c]
Cerebral anoxia	0 (0%)	0 (0%)	—
CNS infection	4 (10.3%)	3 (11.1%)	1.000[a]
Head trauma	11 (28.2%)	8 (29.6%)	0.900[a]
Seizure type			
FIAS	26 (66.7%)	15 (55.6%)	0.360[a]
FAS	1 (2.6%)	0 (0%)	1.000[c]
FBTCS	12 (30.8%)	12 (44.4%)	0.256[a]
Auras	23 (59.0%)	17 (63.0%)	0.744[a]
Fear	6 (15.4%)	1 (3.7%)	0.268[a]
Epigastric	4 (10.3%)	4 (14.8%)	0.862[a]
Semiology			
Hypermotor	9 (23.1%)	8 (29.6%)	0.549[a]
Autonomic	23 (59.0%)	19 (70.4%)	0.344[a]
BATS	3 (7.7%)	0 (0%)	0.382[a]
Unilateral deviation	8 (20.5%)	6 (22.2%)	0.867[a]
Automatisms	28 (71.8%)	16 (59.3%)	0.288[a]
Seizure frequency			
Daily	12 (30.8%)	6 (22.2%)	0.443[a]
Weekly	8 (20.5%)	5 (18.5%)	0.841[a]
Monthly	19 (48.7%)	16 (59.3%)	0.399[a]
Type of epilepsy surgery (ATLR)	16 (41.0%)	8 (29.6%)	0.344[a]
Left side of surgery	26 (66.7%)	15 (55.6%)	0.360[a]
Complete resection of epileptogenic area	37 (94.9%)	20 (74.1%)	0.040[a]*

Note. Categorical variables are n (%) unless stated otherwise.
IQR, interquartile range; FC, febrile convulsion; CNS, central nervous system; FIAS, focal impaired awareness seizure; FAS, focal aware seizure; FBTCS, focal to bilateral tonic–clonic seizure; BATS, bilateral asymmetric rigidity; ATLR, anterior temporal lobe resection.
**Statistically significant.*
[a]*Chi-square test.*
[b]*Mann–Whitney U test.*
[c]*Fisher's exact test.*

resection of the epileptogenic area were significantly more likely to achieve seizure freedom (Engel class Ia) compared with patients with incomplete resection of epileptogenic area ($p_{\text{Log-rank}}$ = 0.004). 2) Patients without contralateral insular lobe hypometabolism were significantly more likely to achieve seizure freedom as compared with patients with contralateral insular lobe hypometabolism ($p_{\text{Log-rank}}$ = 0.025). We found that duration of epilepsy (more or less than 12 years), absence or presence of FC or FBTCS, and ATLR did not influence the Engel class Ia outcome ($p_{\text{Log-rank}}$ = 0.110, $p_{\text{Log-rank}}$ = 0.428, $p_{\text{Log-rank}}$ = 0.237, $p_{\text{Log-rank}}$ = 0.275, respectively) (**Figures 4A–C,E**). The KM survival curves demonstrated no significant effect of absence or presence of gray–white blurring on MRI on seizure freedom outcome ($p_{\text{Log-rank}}$ = 0.246) (**Figure 5A**). There was no significance on Engel class Ia outcome of concordance or discordance of preoperative MRI with preoperative ictal scalp VEEG ($p_{\text{Log-rank}}$ = 0.566) (**Figure 5B**). Moreover, the absence or presence of contralateral frontal lobe hypometabolism on PET/MRI did not impact seizure outcome ($p_{\text{Log-rank}}$ = 0.278) (**Figure 5C**).

To further confirm the above univariable predictor identified as potentially significant in the KM survival curves analysis, we conducted a multivariable analysis utilizing a Cox proportional hazards regression model (**Table 3**). In the overall patients, the presence of incomplete resection of the epileptogenic area was the independent significant predictor of seizure recurrence and was correlated with an approximately three-fold increase in the risk of postoperative seizure recurrence (HR = 2.977, 95% CI 1.218–7.277, p = 0.017) as compared with patients who underwent complete resection. The predictive value of the presence of contralateral insular lobe hypometabolism on PET/MRI was also investigated, but the predictor failed to

TABLE 2 | | Electrophysiological and multimodality neuroimaging characteristics.

Variable	Outcome		*p*-Value
—	Seizure freedom	Seizure recurrence	—
Interictal scalp VEEG, focal IED	18 (46.2%)	14 (51.9%)	0.649[a]
Bilateral temporal lobe IED	6 (15.4%)	6 (22.2%)	0.701[a]
Ictal scalp VEEG, localized ictal onset zone	14 (35.9%)	13 (48.1%)	0.320[a]
Invasive SEEG (number)	37 (94.9%)	23 (85.2%)	0.363[a]
MRI			
Gray–white blurring	5 (12.8%)	1 (3.7%)	0.406[a]
Cortical thickening	1 (2.6%)	2 (7.4%)	0.743[a]
Hippocampal sclerosis	26 (66.7%)	16 (59.3%)	0.539[a]
Subcortical T2/FLAIR abnormality	2 (5.1%)	0 (0%)	0.509[b]
MRI-Ictal VEEG concordance	15 (38.5%)	8 (29.6%)	0.459[a]
PET/MRI coregistration			
Presence of contralateral TLH	3 (7.7%)	2 (7.4%)	1.000[a]
Contralateral frontal lobe hypometabolism	3 (7.7%)	5 (18.5%)	0.346[a]
Bilateral frontal lobe hypometabolism	2 (5.1%)	4 (14.8%)	0.363[a]
Contralateral insular lobe hypometabolism	0 (0%)	3 (11.1%)	0.126[a]

Note. Categorical variables are n (%) unless stated otherwise.
VEEG, video electroencephalogram; IED, interictal epileptiform discharges; FLAIR, fluid-attenuated inversion recovery; TLH, temporal lobe hypometabolism.
[a]*Chi-square test.*
[b]*Fisher's exact test.*

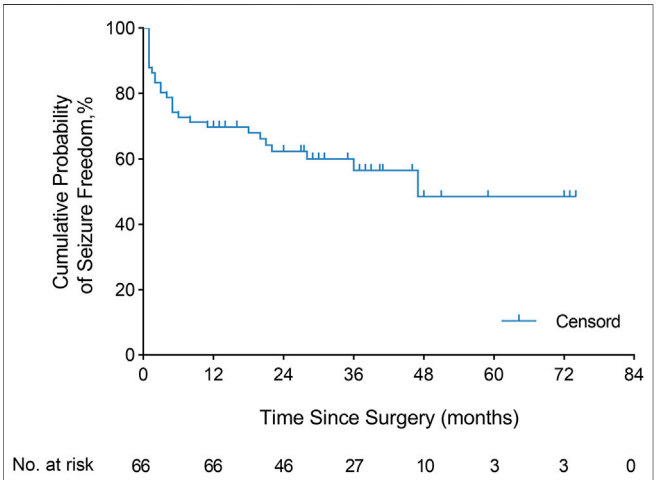

FIGURE 2 | Engel class Ia seizure freedom. Kaplan–Meier curve demonstrated the seizure freedom outcome after resection in the overall population (66 patients). The cumulative probability of continuous seizure freedom was 69.7% (95% CI, 58.6–80.8%), 62.3% (95% CI, 50.3–74.4%), 56.5% (95% CI, 43.0–70.0%), and 48.4% (95% CI, 29.8–67.1%) at 12, 24, 36, and 60 months or more after surgery, respectively.

reach statistical significance (HR = 2.885, 95% CI 0.819–10.857, $p = 0.099$).

DISCUSSION

Although some studies have investigated the electroclinical, imaging characteristics and predictive factors of postoperative outcomes in the patients with FCD, the features and predictive role for FCD type IIIa patients have yet to be evaluated. This is the first cohort including children and adults followed up 22.0–40.6 months after operative treatment of drug-resistant epilepsy caused by FCD type IIIa according to the new ILAE classification method. In this retrospective study, we demonstrated that duration of epilepsy (less than 12 years), absence of contralateral insular lobe hypometabolism on PET/MRI, and complete resection of the epileptogenic area were associated with seizure outcome by univariate analysis. Multivariate Cox regression analysis indicated that the incomplete resection of the epileptogenic area was the only independent predictor for seizure recurrence after surgery.

In the present study, we showed that FIAS was the most common seizure type in FCD type IIIa patients, followed by FBTCS. The most common symptoms were automatisms and autonomic behavior. A large number of patients (60.6%) with FCD type IIIa had auras. This result was less than 90% reported by Fauser et al. (2013). Moreover, we demonstrated that the patients with ATLR were more likely to obtain seizure freedom but did not reach significance, which was in accordance with the previous finding, which reported that patients with FCD type IIIa were more likely to achieve better seizure outcomes after ATLR compared with HS alone (Duhrsen et al., 2018). We also found that only a fraction of patients with FCD type IIIa had the manifestation of FCD on MRI including gray–white blurring, cortical thickening, and subcortical T2/FLAIR abnormality, which was concordant with the previous findings (D. W. Kim et al., 2012). Paradoxically, Fauser et al. reported that 88% of patients with FCD type IIIa presented with the gray–white blurring or subcortical signal intensity abnormality on MRI. This result also demonstrated that the presurgical identification of FCD type IIIa by MRI remained difficult and doubtful to a certain degree. These comprehensively clinical, electrophysiological and neuroimaging features could sufficiently help the clinician to diagnose and evaluate the patients with FCD type IIIa.

We reported that 59.1% of patients had the postoperative seizure freedom outcome at the last follow-up. This result aligned

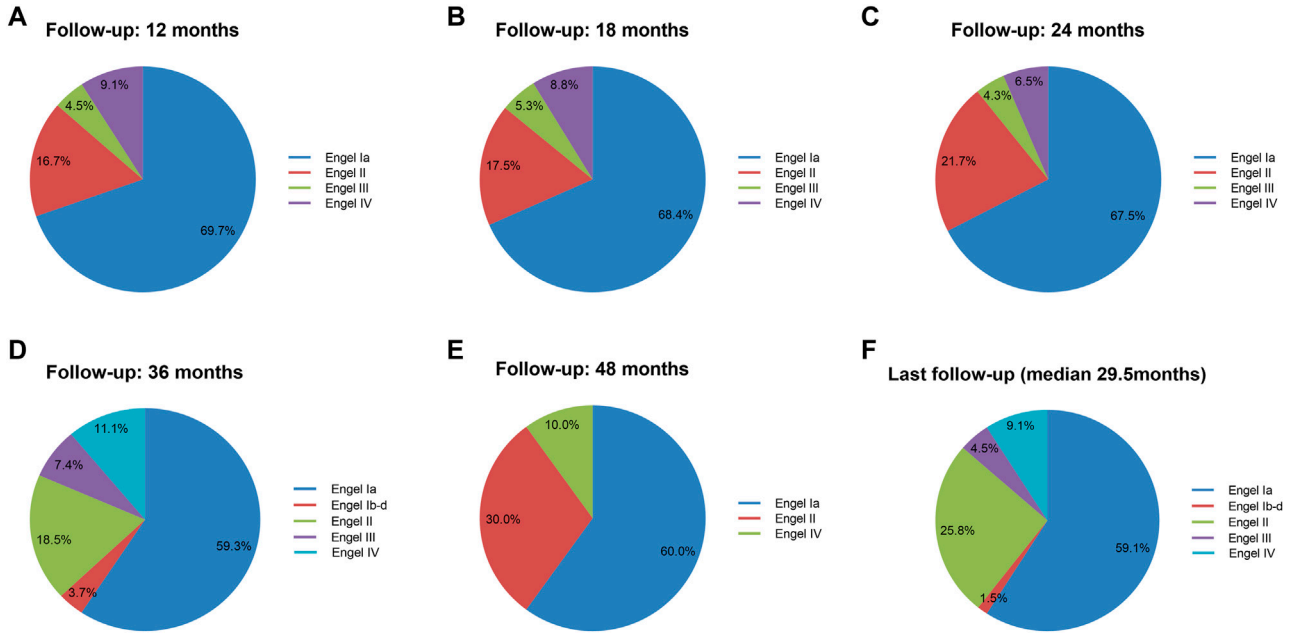

FIGURE 3 | Engel classification outcome during postoperative follow-up. Engel classification outcomes at postoperative 12, 18, 24, 36, and 48 months and last follow-up. Total numbers of investigated cohorts and the rates of cohorts were illustrated for each Engel class outcome. The Engel class Ia outcome worsened with time.

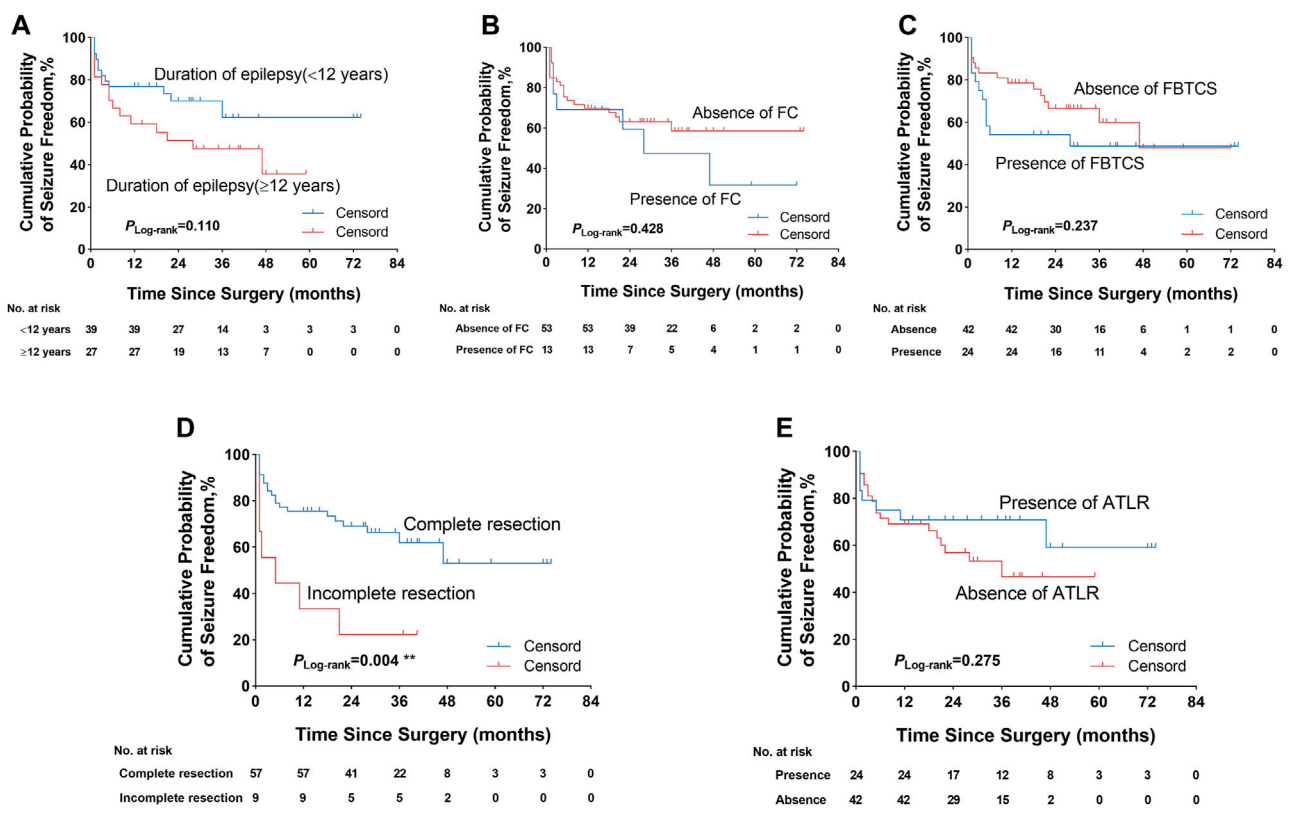

FIGURE 4 | Kaplan–Meier survival curves of Engel class Ia seizure freedom depending on different outcome predictors. **(A)** Duration of epilepsy was not significantly associated with seizure freedom. **(B)** Absence or presence of FC did not significantly influence seizure outcome. **(C)** Absence or presence of FBTCS did not impact seizure outcome. **(D)** Complete resection of the epileptogenic area was significantly more likely to obtain seizure freedom. **(E)** ATLR was also not significantly associated with seizure outcome. $^{**}p < 0.01$. FC, febrile convulsion; FBTCS, focal to bilateral tonic–clonic seizure; ATLR, anterior temporal lobe resection.

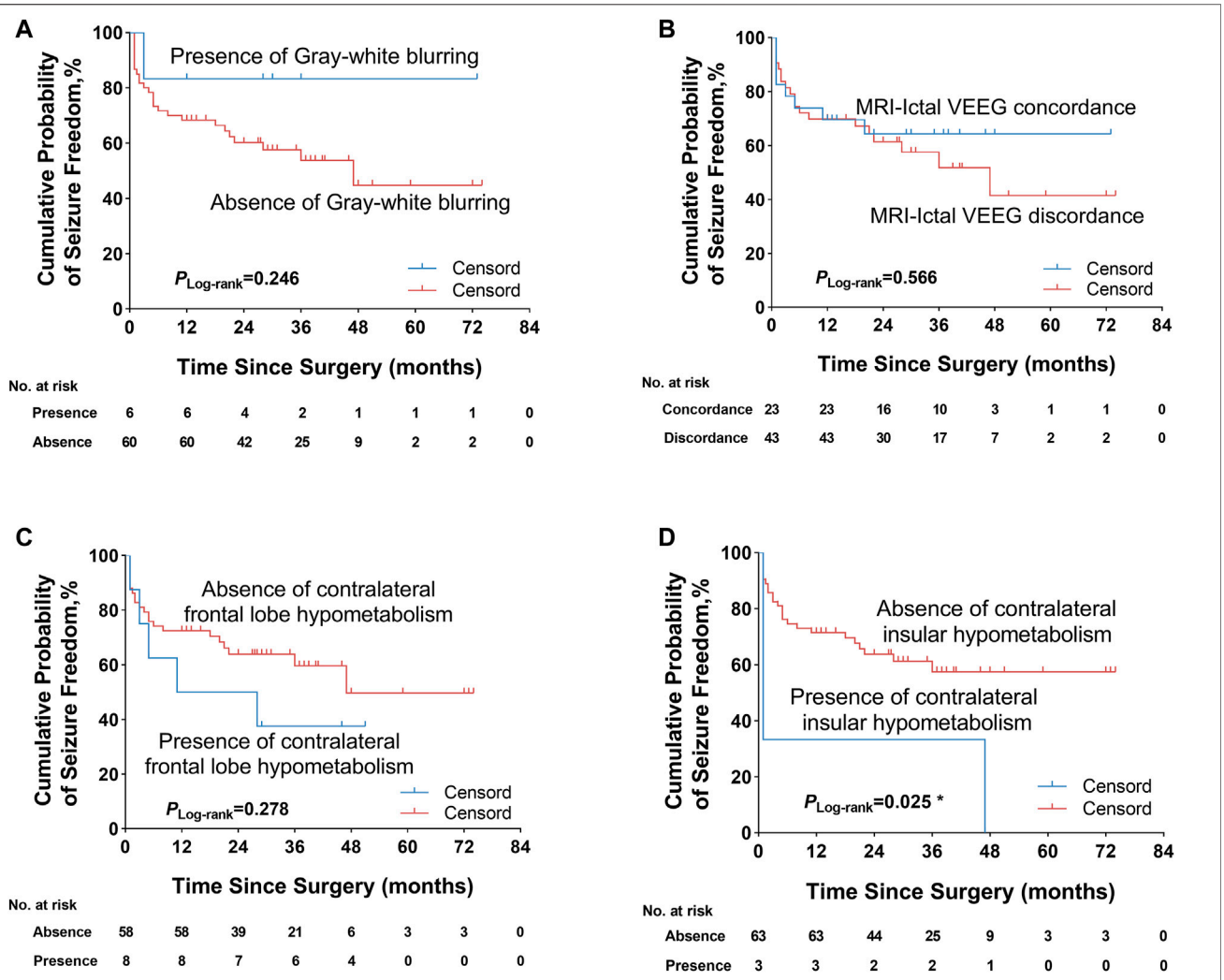

FIGURE 5 | Kaplan–Meier survival curves of Engel class Ia seizure freedom since surgery. **(A)** Absence or presence of gray–white blurring on MRI was not significantly associated with seizure outcome. **(B)** Concordance or discordance of preoperative MRI with ictal scalp VEEG did not significantly influence seizure outcome. **(C)** Absence or presence of contralateral frontal lobe hypometabolism on PET/MRI was also not significantly correlated with seizure outcome. **(D)** Patients without contralateral insular lobe hypometabolism on PET/MRI were significantly more likely to obtain seizure freedom. *$p < 0.05$. VEEG, video electroencephalogram.

with the seizure freedom outcome reported by the previous findings (Fauser et al., 2013; Deleo et al., 2016) and worse than the favorable outcome reported by Fauser et al. (2015) and Jayalakshmi et al. (2019). We further investigated that the predictive factors of postoperative seizure freedom were complete resection of the EZ, absence of contralateral insular lobe hypometabolism on PET/MRI, and duration of epilepsy less than 12 years. However, we could not replicate previously reported predictors such as younger age at the surgery, absence of acute postoperative seizure, and intracranial electrode implantation (Kim et al., 2011; Jin et al., 2016; Andrews et al., 2019; Chen et al., 2019).

Our study first indicated that contralateral insular lobe hypometabolism on PET/MRI coregistration was correlated with seizure recurrence in patients with FCD type IIIa but was not an independent predictive factor for seizure outcome by multivariate Cox regression analysis. This was similar to the previous finding reported by Hur et al. (2013), who observed the trend towards a worse postoperative outcome in patients with insular hypometabolism, but the results did not reach significance. It was a sign that the insular cortex present dense interconnection neural network and allowed for the fast spread of ictal epileptic discharges. Such extensive involvement of the ictal discharges led to wider regions of hypometabolism in interictal PET/MRI imaging. Further studies are needed to explore the relationship between the hypometabolism pattern and postoperative outcome.

In accordance with the previous studies (D. W. Kim et al., 2009; Fauser et al., 2015; Oluigbo et al., 2015; Jin et al., 2016), our current study also demonstrated that complete resection of the EZ was the independent predictor of postoperative seizure outcome for FCD type IIIa. This study found that the patients

TABLE 3 | | Predictors of postoperative seizure recurrence in FCD type IIIa patients.

Variable	Hazard ratio (HR)	95% CI	*p*
Incomplete resection of epileptogenic area	2.977	1.218–7.277	0.017*
Presence of contralateral insular lobe hypometabolism	2.885	0.819–10.857	0.099

Note. HR, hazard ratio.
**Statistically significant.*

with incomplete resection of the epileptogenic area had an approximately three-fold increase in the risk of seizure recurrence after surgery as compared with those with complete resection. However, our results also indicated that among the patients undergoing complete resection, 35.0% with complete resection of the epileptogenic area had seizure recurrence, which was higher than the previous finding (Jin et al., 2016). This phenomenon possibly resulted from the preoperative inaccurate recognition of the epileptogenic area and the development or maturation of a new EZ (Najm et al., 2013). Moreover, we indicated that the shorter duration of epilepsy (less than 12 years) was also a predictive factor of seizure freedom outcome after surgery, which was in accordance with some studies that duration of epilepsy was significantly associated with surgical outcome (Kral et al., 2003; Fauser et al., 2008; Fauser et al., 2015). This result highlighted that we should consider early epilepsy surgery in patients in whom drug-resistant epilepsy becomes obvious. However, in another study, Jin et al. (2016) did not observe the significant association of duration of epilepsy with surgical outcome.

In the current study, we showed that age at operation and seizure onset was not associated with the seizure outcome, which was in concordance with the previous studies that there was no significant influence of age at operation and seizure onset on postoperative seizure outcome (D. W. Kim et al., 2009; Krsek et al., 2009; Rowland et al., 2012; Jin et al., 2016). However, a large study about FCD including FCD type IIIa demonstrated that a younger age at operation could aid in obtaining seizure freedom (Fauser et al., 2015). In addition, Kim et al. (2011) also reported that younger age at the time of surgery was more likely to achieve good postoperative outcomes. This discordance may have resulted from the various criteria of patient selection and the different FCD subtypes. The relationship between the operation time and postoperative outcome for FCD, especially FCD type IIIa, was needed for further investigation.

Several limitations should be considered in the explanation of these results. Firstly, this is a retrospective study, so the selection bias is inherent to the study. We try to minimize bias as much as possible by performing blinded electrophysiological, imaging, and histopathology review utilizing novel classification methods. Secondly, this single-center and retrospective study limits its general relevance. Moreover, another limitation of our study is that we do not record EEG during the ^{18}F-FDG PET scan and cannot exclude ictal scans.

In summary, postoperative seizure outcome in the surgical treatment of FCD type IIIa was in more than half of the patients. This underlines that surgery can be a critically effective therapy option for FCD type IIIa patients. More specifically, we comprehensively concluded the clinical, electrophysiological, and neuroimaging characteristics of FCD type IIIa, and we further investigated the prognostic factors of FCD type IIIa by surgical treatment. The surgical outcome of FCD type IIIa is affected by critical determinants, including duration of epilepsy, complete resection of the epileptogenic area, and contralateral insular lobe hypometabolism on PET/MRI. The complete resection of the epileptogenic area is the only independent predictor for seizure freedom outcome after surgery. With the advancement of both noninvasive multimodality imaging and comprehensive invasive assessment with SEEG, we will further improve preoperative evaluation and the postoperative outcome for patients with intractable epilepsy associated with FCD type IIIa.

DATA AVAILABILITY STATEMENT

The raw data supporting the conclusion of this article will be made available by the authors, without undue reservation.

ETHICS STATEMENT

The studies involving human participants were reviewed and approved by the Ethics Committee from Guangdong 999 Brain Hospital and conducted in accordance with the Declaration of Helsinki guidelines. Written informed consent was obtained from patients prior to surgery. We confirm that we have read the Journal's position on issues involved in ethical publication and affirm that this report is consistent with those guidelines. Written informed consent to participate in this study was provided by the participants' legal guardian/next of kin. Written informed consent was obtained from the minors' legal guardian/next of kin for the publication of any potentially identifiable images or data included in this article.

AUTHOR CONTRIBUTIONS

LZ, HZ, and WZ contributed to the writing of the manuscript. LZ, HZ, WZ, JG, and YT collected the original data. LZ and CZ contributed to the statistical analysis of the data and constructed the figures and tables. QT and XH contributed to the analysis of electrophysiological data. HL and BC contributed to the analysis of histopathological information. XL and YT contributed to the

analysis of imaging information. QG and HX conceived the paper layout and modified the paper. All authors had read and approved the final version of the manuscript.

FUNDING

This work was financially supported by the Project of Innovative Team for the Guangdong Universities (No. 2018KCXTD001), the National Natural Science Foundation of China (No. 81701751, 81871383), and Guangdong Basic and Applied Basic Research Foundation (No. 2020A1515011192).

ACKNOWLEDGMENTS

We thank Boston Professional Group (BPG) Editing for editing the paper.

REFERENCES

Andrews, J. P., Gummadavelli, A., Farooque, P., Bonito, J., Arencibia, C., Blumenfeld, H., et al. (2019). Association of Seizure Spread with Surgical Failure in Epilepsy. *JAMA Neurol.* 76, 462–469. doi:10.1001/jamaneurol.2018.4316

Blumcke, I., Spreafico, R., Haaker, G., Coras, R., Kobow, K., Bien, C. G., et al. (2017). Histopathological Findings in Brain Tissue Obtained during Epilepsy Surgery. *N. Engl. J. Med.* 377, 1648–1656. doi:10.1056/NEJMoa1703784

Blümcke, I., Thom, M., Aronica, E., Armstrong, D. D., Vinters, H. V., Palmini, A., et al. (2011). The Clinicopathologic Spectrum of Focal Cortical Dysplasias: A Consensus Classification Proposed by an Ad Hoc Task Force of the ILAE Diagnostic Methods Commission1. *Epilepsia* 52, 158–174. doi:10.1111/j.1528-1167.2010.02777.x

Cahill, V., Sinclair, B., Malpas, C. B., McIntosh, A. M., Chen, Z., Vivash, L. E., et al. (2019). Metabolic Patterns and Seizure Outcomes Following Anterior Temporal Lobectomy. *Ann. Neurol.* 85, 241–250. doi:10.1002/ana.25405

Chang, E. F., Wang, D. D., Barkovich, A. J., Tihan, T., Auguste, K. I., Sullivan, J. E., et al. (2011). Predictors of Seizure freedom after Surgery for Malformations of Cortical Development. *Ann. Neurol.* 70, 151–162. doi:10.1002/ana.22399

Chapman, K., Wyllie, E., Najm, I., Ruggieri, P., Bingaman, W., Lüders, J., et al. (2005). Seizure Outcome after Epilepsy Surgery in Patients with normal Preoperative MRI. *J. Neurol. Neurosurg. Psychiatry* 76, 710–713. doi:10.1136/jnnp.2003.026757

Chen, J., Huang, Z., Li, L., Ren, L., and Wang, Y. (2019). Histological Type of Focal Cortical Dysplasia Is Associated with the Risk of Postsurgical Seizure in Children and Adolescents. *Tcrm* 15, 877–884. doi:10.2147/TCRM.S203039

Deleo, F., Garbelli, R., Milesi, G., Gozzo, F., Bramerio, M., Villani, F., et al. (2016). Short- and Long-Term Surgical Outcomes of Temporal Lobe Epilepsy Associated with Hippocampal Sclerosis: Relationships with Neuropathology. *Epilepsia* 57, 306–315. doi:10.1111/epi.13277

Dührsen, L., Sauvigny, T., House, P. M., Stodieck, S., Holst, B., Matschke, J., et al. (2018). Impact of Focal Cortical Dysplasia Type IIIa on Seizure Outcome Following Anterior Mesial Temporal Lobe Resection for the Treatment of Epilepsy. *J. Neurosurg.* 128, 1668–1673. doi:10.3171/2017.2.JNS161295

Engel, J. V. N. P., Jr, Rasmussen, T. B., and Ojemann, L. M. (1993). "Outcome with Respect to Epileptic Seizures," in *Surgical Treatment of the Epilepsies*. Editor J Engel. 2nd ed. (New York: Raven Press), 609–621.

Fauser, S., Bast, T., Altenmüller, D.-M., Schulte-Mönting, J., Strobl, K., Steinhoff, B. J., et al. (2008). Factors Influencing Surgical Outcome in Patients with Focal Cortical Dysplasia. *J. Neurol. Neurosurg. Psychiatry* 79, 103–105. doi:10.1136/jnnp.2007.116038

Fauser, S., Essang, C., Altenmüller, D.-M., Staack, A. M., Steinhoff, B. J., Strobl, K., et al. (2015). Long-term Seizure Outcome in 211 Patients with Focal Cortical Dysplasia. *Epilepsia* 56, 66–76. doi:10.1111/epi.12876

Fauser, S., Essang, C., Altenmüller, D. M., Staack, A., Steinhoff, B. J., Strobl, K., et al. (2013). Is There Evidence for Clinical Differences Related to the New Classification of Temporal Lobe Cortical Dysplasia? *Epilepsia* 54, 909–917. doi:10.1111/epi.12147

Fisher, R. S., Cross, J. H., D'Souza, C., French, J. A., Haut, S. R., Higurashi, N., et al. (2017). Instruction Manual for the ILAE 2017 Operational Classification of Seizure Types. *Epilepsia* 58, 531–542. doi:10.1111/epi.13671

Hauptman, J. S., and Mathern, G. W. (2012). Surgical Treatment of Epilepsy Associated with Cortical Dysplasia: 2012 Update. *Epilepsia* 53 (Suppl. 4), 98–104. doi:10.1111/j.1528-1167.2012.03619.x

Hur, J. A., Kang, J. W., Kang, H.-C., Kim, H. D., Kim, J. T., and Lee, J. S. (2013). The Significance of Insular Hypometabolism in Temporal Lobe Epilepsy in Children. *J. Epilepsy Res.* 3, 54–62. doi:10.14581/jer.13011

Jayalakshmi, S., Nanda, S. K., Vooturi, S., Vadapalli, R., Sudhakar, P., Madigubba, S., et al. (2019). Focal Cortical Dysplasia and Refractory Epilepsy: Role of Multimodality Imaging and Outcome of Surgery. *AJNR Am. J. Neuroradiol* 40, 892–898. doi:10.3174/ajnr.A6041

Jin, B., Wang, J., Zhou, J., Wang, S., Guan, Y., and Chen, S. (2016). A Longitudinal Study of Surgical Outcome of Pharmacoresistant Epilepsy Caused by Focal Cortical Dysplasia. *J. Neurol.* 263, 2403–2410. doi:10.1007/s00415-016-8274-1

Kemerdere, R., Ahmedov, M. L., Alizada, O., Yeni, S. N., Oz, B., and Tanriverdi, T. (2018). Effect of Temporal Neocortical Pathology on Seizure Freeness in Adult Patients with Temporal Lobe Epilepsy. *World Neurosurg.* 116, e801–e805. doi:10.1016/j.wneu.2018.05.095

Kim, D. W., Kim, S., Park, S.-H., Chung, C.-K., and Lee, S. K. (2012). Comparison of MRI Features and Surgical Outcome Among the Subtypes of Focal Cortical Dysplasia. *Seizure* 21, 789–794. doi:10.1016/j.seizure.2012.09.006

Kim, D. W., Lee, S. K., Chu, K., Park, K. I., Lee, S. Y., Lee, C. H., et al. (2009). Predictors of Surgical Outcome and Pathologic Considerations in Focal Cortical Dysplasia. *Neurology* 72, 211–216. doi:10.1212/01.wnl.0000327825.48731.c3

Kim, Y. H., Kang, H.-C., Kim, D.-S., Kim, S. H., Shim, K.-W., Kim, H. D., et al. (2011). Neuroimaging in Identifying Focal Cortical Dysplasia and Prognostic Factors in Pediatric and Adolescent Epilepsy Surgery. *Epilepsia* 52, 722–727. doi:10.1111/j.1528-1167.2010.02950.x

Kral, T., Clusmann, H., Blümcke, I., Fimmers, R., Ostertun, B., Kurthen, M., et al. (2003). Outcome of Epilepsy Surgery in Focal Cortical Dysplasia. *J. Neurol. Neurosurg. Psychiatry* 74, 183–188. doi:10.1136/jnnp.74.2.183

Krsek, P., Maton, B., Jayakar, P., Dean, P., Korman, B., Rey, G., et al. (2009). Incomplete Resection of Focal Cortical Dysplasia Is the Main Predictor of Poor Postsurgical Outcome. *Neurology* 72, 217–223. doi:10.1212/01.wnl.0000334365.22854.d3

Kwan, P., Arzimanoglou, A., Berg, A. T., Brodie, M. J., Allen Hauser, W., Mathern, G., et al. (2010). Definition of Drug Resistant Epilepsy: Consensus Proposal by the Ad Hoc Task Force of the ILAE Commission on Therapeutic Strategies. *Epilepsia* 51, 1069–1077. doi:10.1111/j.1528-1167.2009.02397.x

Lerner, J. T., Salamon, N., Hauptman, J. S., Velasco, T. R., Hemb, M., Wu, J. Y., et al. (2009). Assessment and Surgical Outcomes for Mild Type I and Severe Type II Cortical Dysplasia: a Critical Review and the UCLA Experience. *Epilepsia* 50, 1310–1335. doi:10.1111/j.1528-1167.2008.01998.x

Marusic, P., Tomásek, M., Krsek, P., Krijtová, H., Zárubová, J., Zámecník, J., et al. (2007). Clinical Characteristics in Patients with Hippocampal Sclerosis with or without Cortical Dysplasia. *Epileptic Disord.* 9 (Suppl. 1), S75–S82. doi:10.1684/epd.2007.0152

Mintzer, S., and Sperling, M. R. (2008). When Should a Resection Sparing Mesial Structures Be Considered for Temporal Lobe Epilepsy? *Epilepsy Behav.* 13, 7–11. doi:10.1016/j.yebeh.2008.02.015

Montaz-Rosset, M.-S., Scholly, J., Voulleminot, P., Severac, F., Hirsch, E., Valenti-Hirsch, M. P., et al. (2019). Comparison of Functional Deficit Zone Defined by FDG PET to the Epileptogenic Zones Described in Stereo-Electroencephalograph in Drug-Resistant Epileptic Patients Treated by Surgery. *Clin. Nucl. Med.* 44, 526–531. doi:10.1097/RLU.0000000000002615

Najm, I., Jehi, L., Palmini, A., Gonzalez-Martinez, J., Paglioli, E., and Bingaman, W. (2013). Temporal Patterns and Mechanisms of Epilepsy Surgery Failure. *Epilepsia* 54, 772–782. doi:10.1111/epi.12152

Oluigbo, C. O., Wang, J., Whitehead, M. T., Magge, S., Myseros, J. S., Yaun, A., et al. (2015). The Influence of Lesion Volume, Perilesion Resection Volume, and Completeness of Resection on Seizure Outcome after Resective Epilepsy Surgery for Cortical Dysplasia in Children. *J Neurosurg Pediatr* 15, 644–650. doi:10.3171/2014.10.Peds14282

Palmini, A., and Holthausen, H. (2013). Focal Malformations of Cortical Development: a Most Relevant Etiology of Epilepsy in Children. *Handb Clin. Neurol.* 111, 549–565. doi:10.1016/b978-0-444-52891-9.00058-0

Pittau, F., Mã©gevand, P., Sheybani, L., Abela, E., Grouiller, F. d. r., Spinelli, L., et al. (2014). Mapping Epileptic Activity: Sources or Networks for the Clinicians? *Front. Neurol.* 5, 218. doi:10.3389/fneur.2014.00218

Rowland, N. C., Englot, D. J., Cage, T. A., Sughrue, M. E., Barbaro, N. M., and Chang, E. F. (2012). A Meta-Analysis of Predictors of Seizure freedom in the Surgical Management of Focal Cortical Dysplasia. *Jns* 116, 1035–1041. doi:10.3171/2012.1.Jns111105

Seo, J. H., Holland, K., Rose, D., Rozhkov, L., Fujiwara, H., Byars, A., et al. (2011). Multimodality Imaging in the Surgical Treatment of Children with Nonlesional Epilepsy. *Neurology* 76, 41–48. doi:10.1212/WNL.0b013e318204a380

Tassi, L., Colombo, N., Garbelli, R., Francione, S., Lo Russo, G., Mai, R., et al. (2002). Focal Cortical Dysplasia: Neuropathological Subtypes, EEG, Neuroimaging and Surgical Outcome. *Brain* 125, 1719–1732. doi:10.1093/brain/awf175

Widdess-Walsh, P., Diehl, B., and Najm, I. (2006). Neuroimaging of Focal Cortical Dysplasia. *J. Neuroimaging* 16, 185–196. doi:10.1111/j.1552-6569.2006.00025.x

Conflict of Interest: The authors declare that the research was conducted in the absence of any commercial or financial relationships that could be construed as a potential conflict of interest.

Publisher's Note: All claims expressed in this article are solely those of the authors and do not necessarily represent those of their affiliated organizations, or those of the publisher, the editors, and the reviewers. Any product that may be evaluated in this article, or claim that may be made by its manufacturer, is not guaranteed or endorsed by the publisher.

frontiers in Bioengineering and Biotechnology

METHODS
published: 12 January 2022
doi: 10.3389/fbioe.2021.814638

Dual in Utero Electroporation in Mice to Manipulate Two Specific Neuronal Populations in the Developing Cortex

Longbo Zhang[1,2*†], *Stephanie A. Getz*[2†] *and Angelique Bordey*[2]

[1]*Departments of Neurosurgery, And National Clinical Research Center of Geriatric Disorders, Xiangya Hospital, Central South University, Changsha, China,* [2]*Departments of Neurosurgery, And Cellular and Molecular Physiology, School of Medicine, Yale University, New Haven, CT, United States*

Precise regulation of gene expression during development in cortical neurons is essential for the establishment and maintenance of neuronal connectivity and higher-order cognition. Dual in utero electroporation provides a precise and effective tool to label and manipulate gene expression in multiple neuronal populations within a circuit in a spatially and temporally regulated manner. In addition, this technique allows for morphophysiological investigations into neuronal development and connectivity following cell-specific gene manipulations. Here, we detail the dual *in utero* electroporation protocol.

Keywords: *in utero* electroporation, neuron, development, cortex, neuroonal connectivity

OPEN ACCESS

Edited by:
Zikai He,
Harbin Institute of Technology, China

Reviewed by:
Xingchun Gao,
Xi'an Medical University, China
Qiang Cai,
Renmin Hospital of Wuhan University, China

****Correspondence:***
Longbo Zhang
longbo.zhang@yale.edu

†These authors have contributed equally to this work

Specialty section:
This article was submitted to Nanobiotechnology, a section of the journal Frontiers in Bioengineering and Biotechnology

Received: *14 November 2021*
Accepted: *10 December 2021*
Published: *12 January 2022*

Citation:
Zhang L, Getz SA and Bordey A (2022) Dual in Utero Electroporation in Mice to Manipulate Two Specific Neuronal Populations in the Developing Cortex. Front. Bioeng. Biotechnol. 9:814638. doi: 10.3389/fbioe.2021.814638

INTRODUCTION

In utero electroporation (IUE) is a powerful tool to target specific neuronal populations in the developing cortex with temporal and spatial resolution (Saito and Nakatsuji, 2001; Fukuchi-Shimogori and Grove, 2001). The protocol below describes a detailed protocol to perform dual IUE to target layers (L) 2/3 and 4/5 pyramidal neurons in the somatosensory cortex (SSC) with different fluorescent markers to study neuronal development, including dendrite growth and synaptic connectivity (Zhang et al., 2021) (**Figure 1**). To do this, DNA in a plasmid form is introduced into the lateral ventricle of embryos, and an electric pulse is applied to drive the DNA into the desired neural progenitor cell populations. IUE at embryonic day (E) 13.5 and 15.5 is targeted to neural progenitor cells that generate pyramidal neurons destined to reach L4/5 and L2/3, respectively (Molyneaux et al., 2007). Mechanistically, the current from the tweezertrode anode drives the negatively charged DNA toward the desired cortical region, while the electrical pulses generate pores to facilitate DNA delivery into the selected progenitor cell population. The DNA is then passed on to the daughter cells, i.e., neurons, from the progenitor cells upon cell division. These newborn neurons migrate to their target cortical layers and then differentiate into mature pyramidal neurons. Thus, a single IUE allows to manipulate a specific neuronal population within a discrete cortical location.

This protocol can be utilized to target different cortical regions, such as the medial prefrontal cortex (mPFC), as well as the hippocampus. In the DNA-encoding vector, different promoters can be used to restrict gene expression in neurons while bypassing expression in neural progenitor cells (e.g., doublecortin promoter; (Lin et al., 2016). This allows to selectively examine the impact of gene manipulations in neurons vs neural progenitor cells. Overexpression and short hairpin RNA-encoding vectors as well as CRISPR/Cas9 system can be used to examine the impact of gene overexpression, knockdown, or mutations on neuron development. Finally, the IUE procedure can be adapted to target unilateral or bilateral cortices. Taken together, dual IUE provides an excellent tool to target and manipulate one or multiple cell populations in a temporally- and spatially regulated manner to study neuronal development and ultimately connectivity, network activity, and animal behavior. Cortices can also be collected and plated for primary neuronal culture studies.

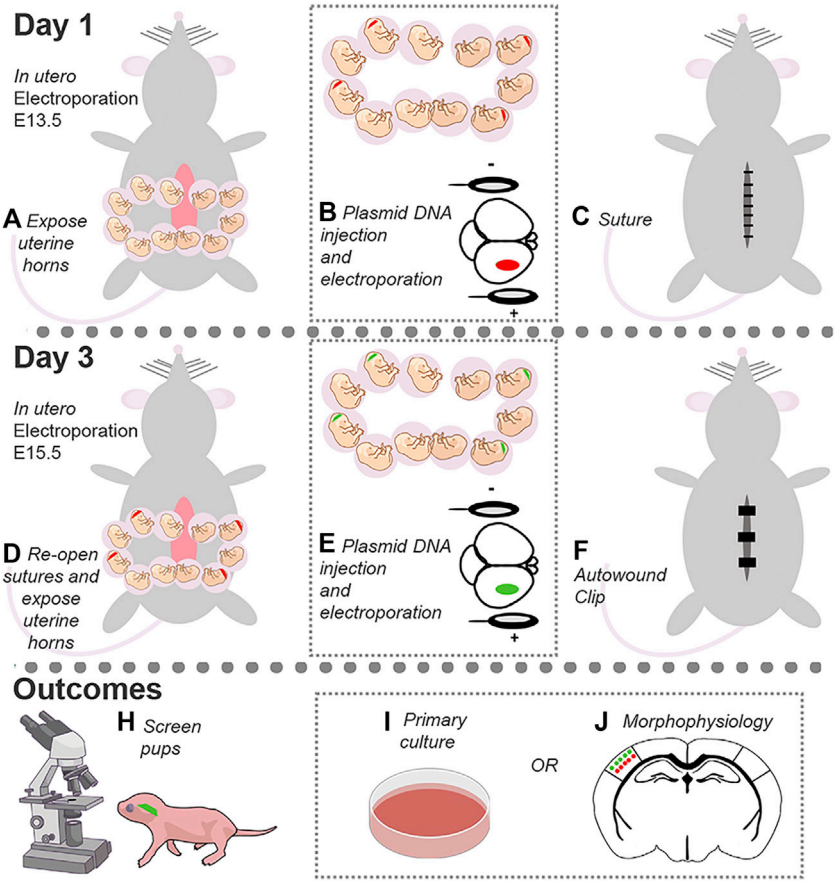

GRAPHICAL ABSTRACT |

MATERIALS AND EQUIPMENT

Key Resources Table |

Reagent or Resource	Source	Identifier
Chemicals, peptides, and recombinant proteins		
Fast Green FCF	Sigma	Ref F7252
PBS, 1x, pH 7.4	Quality Biological	Ref 114-058-101
Paraformaldehyde 32% Solution	Electron Microscopy Sciences	Ref 15714-S
Experimental models: Organisms/strains		
CD-1 IGS Mice	Charles River Laboratories	Ref 022
Recombinant DNA		
pCAG-GFP	Addgene	Addgene # 11150; Matsuda et al. (2004) PNAS
pCAG-tdTomato	Addgene	Addgene # 83029; Pathania et al. (2012) PLos One
pCALNL-DsRed	Addgene	Addgene # 13769; Matsuda et al. (2007) PNAS
pCAG-Cre	Addgene	Plasmid # 13775; Matsuda et al. (2007) PNAS
Surgical tools		
Small Round-Tipped Forceps; 3 mm O.D., 2.2 mm I.D.	Hammacher Instrumente	Ref HSC_703–93
Large Round-Tipped Forceps; 6 mm O.D., 4.8 mm I.D.	Hammacher Instrumente	Ref HSC_703–96
Microdissecting Scissors; Straight; 23 mm Blade Length	ROBOZ; SouthPointe Surgical Supply	Ref RS-5910SC

(Continued on following page)

Key Resources Table | (*Continued*)

Reagent or Resource	Source	Identifier
Webster Needle Holder; Serrated, Extra Delicate	WPI	Ref 14109
5–0 UNIFY PGA Absorbable Braided, Coated Suture, Undyed; 18″	AD Surgical	Ref S-G518R13-U
Autoclip 9 mm	Clay Adams Brand	Ref 300216
MikRon 9 mm AutoClip Applier	Clay Adams Brand	Ref NC9021392
Anesthesia system		
Vaporizor; EZ-7000 Classic System	Vaporizor; EZ-7000 Classic System	Vaporizor; EZ-7000 Classic System
Isoflurane; 100 ml	Isoflurane; 100 ml	Isoflurane; 100 ml
IUE tools		
Electrode Puller	Narishige Japan	Model PP-830
Borosilicate Glass with Filament; Fire Polished; O.D.: 1.5mm, I.D. 1.10 mm, 10 cm	Sutter Instrument	Ref BF150-110-10
Electro Square Porator; ECM 830	BTX Harvard Apparatus	Ref W3 45-0052
Tweezertrodes Platinum Plated 3 mm	BTX Harvard Apparatus	Ref 45-0487
Tweezertrodes Platinum Plated 5 mm	BTX Harvard Apparatus	Ref 45-0489
Tweezertrodes Cable Adaptors	BTX Harvard Apparatus	Ref 45-0204
15″ Aspirator Tube Assembly	Drummond Scientific	Ref 2-000-000
Pre- and post-surgery treatment drugs		
Rimadyl (carprofen); Injectable 50 mg/ml; 20 ml	Zoetis; Covetrus	Ref 024 751
Buprenorphine HCl Injection: 0.3 mg/ml; C3	Covetrus	Ref 059 122
lidocaine 2.5% and prilocaine 2.5% Cream	Akorn; McKesson	Cat. No. 1331487
Puralube Vet Ointment	Dechra; Medvet	Cat. No. PH-PURALUBE-VET
Screening and images collection		
Fluorescence Microscope	Olympus	Ref SZX16
FV1000	Olympus	
Vibratome	Leica	Ref VT1000S
Perfusion and fixation		
Forceps for Perfusion	ROBOZ	RS-5136
Large scissors for Perfusion	WPI	Ref 19,520
Medium scissors for Perfusion	WPI	Ref 191 210
Spring scissors for Perfusion	WPI	Ref 501 235
Micro spatula for Perfusion	Sigma	Ref Z513377
Other		
0.9% Sodium Chloride Injection; 10 ml	Hospira	Ref NDC 0409-4888-02
Sterile Empty Vial; 10 ml	Hospira	Ref 5816–11
30G x ½ (0.3 mm × 13 mm) PrecisionGlide Needle	Betcon, Dickinson and Company	Ref 305106
1 ml syringe; Tuberculin Slip Tip	Betcon, Dickinson and Company	Ref 309569
Polylined Sterile Field; Non-Fenestrated	Busse Hospital Disposables	Ref 696
Wahl Lithium-Ion Vacuum Trimmer Kit with Adjustable Vacuum Intake	Walmart	Cat. No. 9870
Non-Woven Sponges; Non-Sterile	McKesson	Ref 94442000
Prevantics	McKesson	Ref B108000
Alcohol Prep Pad	McKesson	Ref 58–204
30 CC syringe; Luer Lock Tip; Sterile	McKesson	Ref 16-S40C
Millex-GV Duapore PVDF Membrane; 0.22 um Filter unit	Millipore Sigma	Ref SLGVR33RS
Acrodisc Syringe Filter; 0.2 um Supor Membrane Low Protein Binding	Pall Life Sciences	Ref 4602
Parafilm; 4 in x 125 ft	Millipore Sigma	Ref P7793
Halogen Light Source	AmScope	Ref HL250 AY
Snuggle Safe Heat Pad	Walmart	Cat. No. 596688379

METHODS

DNA Dilution Preparation

Timing: 15 min.

1. Obtain DNA plasmids, filtered sterile PBS, and Fast Green (0.25%) for electroporation.
   a. Use a plasmid encoding a fluorescent protein under the CAG promoter (i.e., pCAG-tdTomato or pCAG-GFP; CAG is a cytomegalovirus [CMV] early enhancer fused to modified chicken actin promoter) pCAG-tdTomato or pCAG-GFP, to label neurons and detect efficient electroporation at birth in live mice.

Optional: use an inducible CAG promoter encoding DsRed following a floxed stop cassette (pCAG-*LoxP*-stop-*LoxP*-DsRed, called pCALNL-DsRed, addgene: #13769) together with pCAG-GFP and low concentration of pCAG-Cre to label a subset of GFP-expressing neurons within the electroporated region (Zhang et al., 2021).

Key Resources Table |

DNA Dilution

Reagent	Final concentration	Amount
Plasmid DNA (pCAG-tdTomato)	1.5 μg/μL	Depends on concentration
Plasmid DNA (pCAG-GFP)	1.5 μg/μL	Depends on concentration
Fast green 0.25%	0.025%	2.5 μL
PBS 1x	n/a	Up to 10 μL
Total	n/a	10 μL

Note: *Make the day of surgeries and store at room temperature once made. One or more plasmids can be used per condition. Fast green concentration can be as low as 0.01%.* ***Optional:*** *to label a subset of single neurons within the electroporated region, use a combination of plasmids pCALNL-DsRed and pCAG-Cre at 1000:1 ratio.*

Key Resources Table |

Electroporator Setup

Electroporator parameters	Value
Pulse Voltage	36 mV (E13.5); 39 mV (E15.5)
Programmable Pulses	5
Pulse Width	50 ms
Space Between Pulses	950 ms

Key Resources Table |

Anesthesia System Setup

Anesthesia parameters	Isoflurane	LPM
Induction	4%	NA
Maintenance	2%	NA
Primary Flowmeter	NA	2.5
Secondary Flowmeter	NA	1.5

2. Combine reagents so that there is a total of 10 μL plasmid DNA per mouse. DNA dilution can range from 1 to 4 μg/ μL. The table below uses 1.5 μg/ μL as an example. Dilute fast green to a final concentration of 0.025%. PBS will be used to bring the final volume to 10 μL.
3. Store stock DNA plasmids at −20°C and working aliquots at 4°C.

CRITICAL: Do not vortex DNA and avoid freeze-thawing. Flick the tube and spin down before use.

CRITICAL: Plasmid DNA concentration must be high enough, ideally, no lower than 5 μg/ μL, to allow for adequate expression in cells. Further, avoid thick plasmid DNA; if the DNA plasmid consistency is too viscous, then it will be challenging to use for electroporation.

Electrode Preparation

Timing: 15 min.

4. Pull electrodes using a glass micropipette puller.
   a. Have at least two electrodes per condition per animal when beginning surgeries.
   b. If using a dual-stage glass micropipette puller (Narashige Model PP-830), then heat electrodes to 70.5 °C for these experiments. Use only the bottom electrode.
5. Place the micropipette tip inside the 6 mm O.D. large round-tipped forceps and gently break off the tip to create an angle of about 45° (**Figure 2**). Break multiple sizes to test which tip diameter works best for each embryonic age.

CRITICAL: If the micropipette tip is too dull, then it will not penetrate the embryonic sac. If the tip is too thin, then it will be challenging to deposit plasmid into the brain. If there is clear damage to the cortex after electroporation, then the tip is likely too thick (**Figure 2**).

Surgical Tool Preparation

Timing: 1.5 h.

6. Autoclave large and small round-tipped forceps, needle driver, and scissors. This can be completed the day of or the night before.
7. Place sterile 1x PBS into 30- or 50-ml syringes fitted with a 0.22 mm filter for surgeries.
8. Sterilize fenestrated drapes and gauze.

Primary IUE

Timing: 0.5–1.0 h.

1. Prewarm the heating pad in a microwave and PBS to 37°C in a water bath. Wipe down the surgical area with 70% ethanol.
2. Just before beginning surgery, administer 0.1 mg/ kg body weight subcutaneous (s.c.) buprenorphine to timed-pregnant mice.
3. Anesthetize a E13.5 timed-pregnant mouse by placing it in the isoflurane induction chamber.
   a. Turn on oxygen, and open primary and secondary flowmeters. Set the secondary flowmeter to ~1.5 LPM.
   b. Turn on isoflurane to 4% and wait until the mouse is immobile, then decrease the level to 2%.
4. After ~3 min, take the mouse out of the chamber and shave the mouse's belly with clippers while it is anesthetized.

Note: Suitable embryonic age can be differ depending on the regions.

CRITICAL: If the mouse starts waking up after completion of the shaving procedure, place it back in the induction chamber and repeat Step 3.

5. Move the mouse onto the heating pad with its abdomen exposed and place its nose into the nose cone.
   a. Put ophthalmic ointment on the eyes.
   b. Place 2.5% lidocaine prilocaine cream on its abdomen and tape the limbs down.
6. Wipe down the abdomen using alternative swabs of prevantics and alcohol. Do this three times, starting with prevantics and ending with alcohol.
7. Cover the abdomen with a piece of fenestrated sterile drape and gauze.
   a. Align the hole to be around the area of the incision.
   b. Drench the gauze with the warm, sterile PBS.
8. Pinch the skin using the small ringed forceps and lift skin, make a skin incision of ~2 cm long though the midline with scissors.

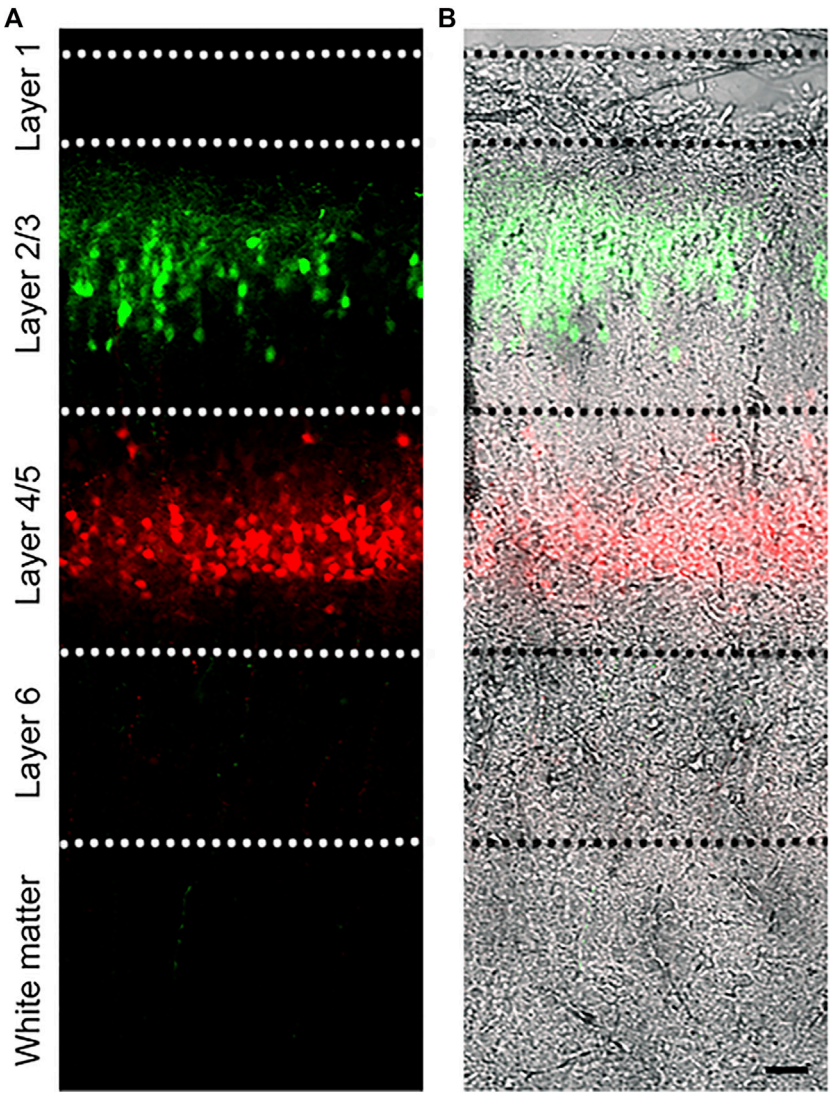

FIGURE 1 | Dual IUE image in the SSC. **(A)**: Image of a postnatal day (P) 14 mouse coronal section containing GFP-expressing L2/3 cortical neurons and tdTomato-expressing L4/5 neurons following IUE at E15.5 and E13.5, respectively. **(B)**: Fluorescent image overlaid with bright field. Bar: 50 μm.

9. Using the small ringed forceps, lift the muscle of abdominal wall and make an incision with scissors through the linea alba (white line) to avoid cutting of major blood vessels.

CRITICAL: Lifting the muscle before the incision of abdominal wall is important to avoid injuries of organs and embryos underneath. Begin with a small cut to allow the air in to push apart the abdominal wall and tissue underneath.

10. Gently move the uterine horns out through the incision using the large ring forceps and lay the uterine horns on the top of the gauze with the number of embryos counted and write the sequence of embryos in a notebook (**Figure 3A**). Regularly wet uterine horns with warm PBS.

CRITICAL: Carefully pull the uterine horns out of the abdominal cavity with the large ring forceps. Gently pull at the areas where embryos meet, rather than pulling directly on the embryos, to avoid damaging them. Alternatively, one can use fingers to gently move the embryos out while holding the peritoneum up and to the side with large ringed forceps.

11. Inject 1–2 μL plasmid DNA solution into the lateral ventricle using a mouth-controlled micropipette, which consists of a 1 ml syringe sans plunger, 15″ aspirator tube assembly, 0.22 mm filter, and micropipette (**Figure 3B**).

Note: The lateral ventricle should be filled with fast green if the injection is successful (**Figure 3B**).

CRITICAL: To increase survival rate after the second IUE, inject embryos in an alternating pattern.

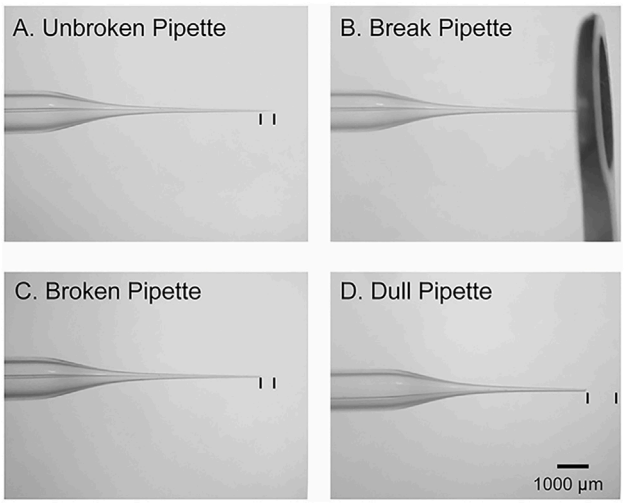

FIGURE 2 | Micropipette preparation. **(A)**: Image of an intact glass micropipette that was generated by a vertical puller. The black lines denote the amount of tip that should be removed prior to insertion into the embryo. **(B)**: Image of the large round forceps used to break the tip of micropipette. **(C)**: Image of an adequately broken micropipette with an ~45-degree-tip. The black lines denote the amount of tip that was removed. **(D)**: An example of a dull pipette. The black lines denote the amount of tip that was removed.

CRITICAL: Avoid placing too much of the micropipette tip inside the embryonic sac. Doing so leads to holes, which can cause amniotic fluid to leak and increase the risk of abortion.

CRITICAL: Micropipette tips should not be reused for more than 10 embryos since the tip becomes blunt, which increases potential damage to embryos. Do not reuse electrodes across litters and conditions.

12. Place forceps-type electrodes (tweezertrode diameter: 2 mm) parallel to DNA-injected embryos (position and direction of electrodes depend on the desired target areas) and deliver 36 mV for 50 ms-long electric pulses with a 950 ms pulse interval.

Note: The electrodes should be placed in PBS-containing conical tube to keep them wet.

CRITICAL: The tweezertrode anode should be placed to direct the DNA toward the progenitor cell population of interest. For the SSC, the tweezertrodes will be orthogonally oriented with the anode on the barrel cortex. The embryo should move slightly when electrical pulses are being applied.

CRITICAL: Gently push the embryo towards the embryonic sac to ensure more efficient electroporation delivery. The limbs of embryo should move after each electric pulse.

13. Repeat steps 11–12 for the desired embryos. Keep track of which embryos and hemispheres are electroporated.

CRITICAL: Regularly drop warm PBS onto the uterine horns before moving to the next electroporation.

14. Reposition the horns carefully using the large ring forceps back into the abdominal cavity. Fill cavity with warm PBS.
15. Suture the abdominal wall and skin with absorbable PDS suture line.
16. Cover the skin incision with triple antibiotic.
17. Administer 5 mg/ kg/s.c. Rimadyl (carprofen).
18. Place the mouse in an empty cage on top of a heating pad until awake.
19. Upon waking, move the mouse back to its home cage. Put moistened food in the cage.

Secondary IUE

Timing: 0.5–1.0 h.

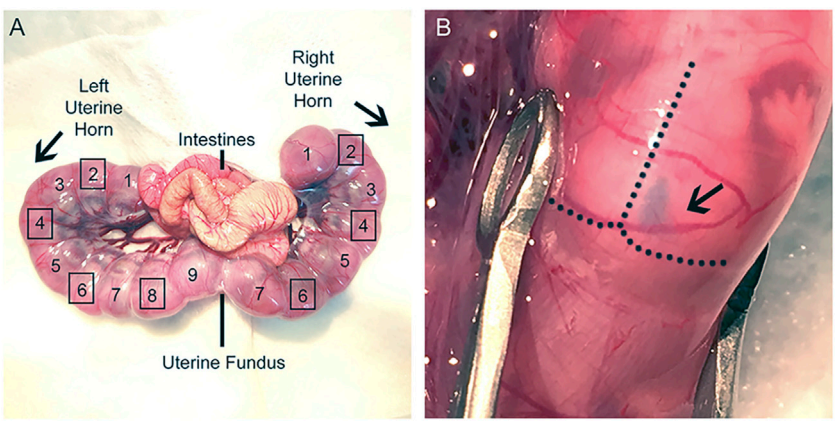

FIGURE 3 | Uterine horns exposure during IUE surgery. **(A)**: Image of dissected uterine horns and labeling of desired IUE embryos. Uterine fundus is a useful marker to distinguish the two uterine horns and can be used as a reference to identify the electroporated embryos prior to the second IUE. Label embryos beginning at the uterine knots and continue sequentially to the uterine fundus for each uterine horn. Do not electroporate the embryos at the uterine knot or at the fundus (Left horn: 1, 9; Right horn: 1, 7). Squares surrounding the numbered embryos denote which embryos should receive IUE (Left horn: 2, 4, 6, 8; Right horn: 2, 4, 6). Electroporate embryos in an alternating fashion in the same hemisphere for both IUEs. **(B)**: Image of lateral ventricle injection. Plasmid DNA was injected into E15 embryo, and the right lateral ventricle was filled with fast green.

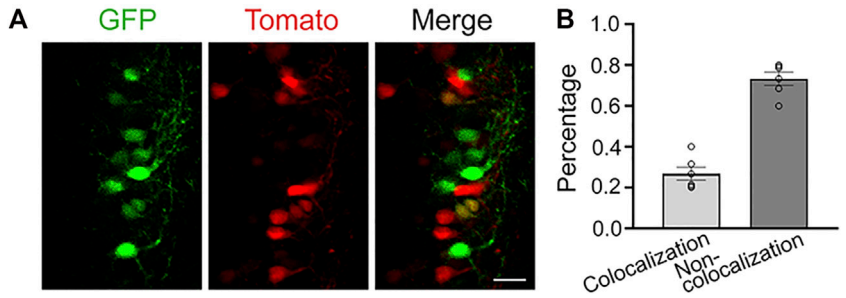

FIGURE 4 | Dual IUE 12-h apart leads to colocalization between the two electroporated cell populations. **(A)**: Images of electroporated neurons in the SSC following a dual IUE 12-h apart (green: pCAG-GFP; red: pCAG-tdTomato). **(B)**: Quantification of the GFP and RFP colocalization and non-colocalization. Bar: 25 μm, 2 slices per mouse, N = 3 mice.

20. Monitor mouse at 24 h post-surgery and administer 5 mg/kg/s.c. Rimadyl (carprofen).
21. 48 h after the first IUE (E15.5), and 10 min prior to surgery, administer 0.1 mg/kg/s.c. Buprenorphine.

CRITICAL: Performing the second IUE too soon (e.g., 12 h instead of 48 h) following the first IUE results in a larger degree of co-localization between electroporated cell populations (**Figure 4**).

22. Anesthetize the mouse and repeat steps 1–7.
23. Using the small ringed forceps to pinch and lift skin, cut the suture line from the first surgery and gently open the original skin and abdominal wall incision.

Optional: Trim the skin and abdominal wall if needed.

24. Guide uterine horns out and lay them on the top of the gauze. Regularly wet uterine horns with warm PBS.
25. Find the electroporated embryos from last surgery and inject 1–2 μL plasmid DNA solution into the lateral ventricle using a micropipette. Make sure the lateral ventricle is filled with fast green.
26. Electroporate using forceps-type electrodes (Tweezertrodes diameter: 5 mm; parameter setting: 39 mV for 50 ms-long electric pulses, 950 ms pulse interval). Make sure the embryos move with the electrical pulses.
27. After finishing the second IUE of the embryos, reposition the horns carefully using the large ring forceps into the abdominal cavity. Fill cavity with warm PBS.
28. Suture the abdominal wall with absorbable PDS suture line. Next, place one suture in the middle of the incision on the skin and staple the skin closed using autowound clips.
29. Repeat steps 16–19.
30. Post-surgical care: monitor mouse every day for 72-h post-surgery and administer 5 mg/kg/s.c. Rimadyl (carprofen) daily.

EXPECTED OUTCOMES

Mice are typically born between E19 and E20. They can then be screened for fluorescence expression. IUE in CD1 mice are typically well-tolerated with 70–90% of electroporated pups being born. There could be some variability in the targeted region between mice and across litters. Practice can limit variability. In addition, including controls in the same litter is critical depending on the parameters (e.g., behavior) that are analyzed. Electroporated mice can be used for many purposes, including preparing fixed brain sections for imaging and morphological characterizations, preparing acute slices for electrophysiology, behavior analysis, and dissecting cells for *in vitro* experiments.

DISCUSSION

Dual IUE can target cortical neurons within the same cortical region but in different layers or target neurons in different cortical regions and layers. However, dual IUE may have a reduced efficacy compared to single IUE. One must be gentle with the embryos to maximize survival. When researchers are beginning this procedure, begin with a single IUE in the desired cortical location. Once it is established, then transition to dual IUE.

Troubleshooting

Problem 1

Cannot penetrate the embryonic sac with the micropipette.

Potential Solution

The micropipette tip is too dull or wide. Change to a sharper tip and repeat. Proceeding with a micropipette tip that is too dull or wide could damage the embryo (**Figure 2**).

Problem 2

Cannot deposit the plasmid into the lateral ventricle.

Potential Solution

There could be multiple causes for this (Saito and Nakatsuji, 2001): The tip has bypassed or passed through the lateral ventricle and is somewhere else in the brain. Pull back on the tip while continuing to gently blow out the plasmid (Fukuchi-Shimogori and Grove, 2001). The micropipette tip is too thin to inject DNA solution into lateral ventricle. Change

micropipette to a slightly larger tip diameter (Zhang et al., 2021). There is too much pressure on the pup. Loosen the grip on the pup and try again.

Problem 3
The embryonic sac is leaking amniotic fluid.

Potential Solution
The micropipette tip may be too dull or wide. Adjust micropipette sharpness or thickness accordingly (Fukuchi-Shimogori and Grove, 2001). The micropipette was placed too deep into the embryonic sac during plasmid injection. Ensure the micropipette is properly inserted in the lateral ventricle.

Problem 4
Popping of the embryonic sac during handling.

Potential Solution
If this happened, the embryos will not likely survive. Handle the embryos more gently.

Problem 5
The dam is bleeding.

Potential Solution
Although this procedure should not result in excessive bleeding, there could be blood between the skin and peritoneum. As long as it is only a small amount of blood, this will resolve as the surgery is completed. If an organ was ruptured, then there would be more blood within the peritoneal cavity. If so, euthanize the animal.

Problem 6
Few or no electroporated pups are born.

Potential Solution
The experimenter was likely not gentle enough with the embryos during surgery. The experimenter should put less pressure on the embryos, deposit the DNA plasmids with less force, and consider altering micropipette sizes. In addition, pups at the top of the uterine horn (near the knots) and at the junction between the two uterine horns should not be electroporated otherwise this increases the chances of spontaneous abortions.

Problem 7
Electroporated pups are born, but the fluorescent protein is expressed in subcortical or incorrect cortical locations.

Potential Solution
If the fluorescent reporter is in subcortical locations, then the micropipette was too deep. Ensure the plasmid DNA is properly injected into the lateral ventricle. If it is expressed in incorrect cortical locations, then adjust tweezertrode orientation to obtain the correct location.

Problem 8
Electroporated pups are born, but there is noticeable damage to the cortex or hydrocephalus.

Potential Solution
If there is damage to the cortex, then the micropipette was too dull. Hydrocephalus can happen with IUE, but it is uncommon. This could occur for several reasons: 1) too much pressure when depositing the plasmid into the lateral ventricle, 2) from the micropipette injection causing bleeding inside the lateral ventricle, or 3) inflammation. Ensure sterilizing the surgical and IUE tools before start, and deposit plasmid DNA gently.

Problem 9
Only some of the pups have dual IUE, while others have a single IUE.

Potential Solution
This is likely because one of the IUEs was unsuccessful, or the second IUE was performed out of sequence and did not target the electroporated embryos. Some embryos could die between the first and second IUE. A dying embryo has an opaque white-yellowish color prior to being fully resorbed. Be mindful to count all the embryos carefully during the first and second IUEs, and note which embryos are no longer healthy. Skip unhealthy or dying embryos, even if they were part of the first IUE. When skipping those dying embryos, make sure to remain in sequence with the previous IUE pattern so that all healthy embryos that received the first IUE (E13.3) also receive the second IUE (E15.5).

DATA AVAILABILITY STATEMENT

The original contributions presented in the study are included in the article/Supplementary Material, further inquiries can be directed to the corresponding author.

ETHICS STATEMENT

The animal study was reviewed and approved by Yale University Institutional Animal Care and Use Committee.

AUTHOR CONTRIBUTIONS

All authors listed have made a substantial, direct, and intellectual contribution to the work and approved it for publication

FUNDING

The work was funded by a National Natural Science Foundation of China 82171171 (LZ), Tuberous sclerosis complex Alliance research grant (AB).

REFERENCES

Fukuchi-Shimogori, T., and Grove, E. A. (2001). Neocortex Patterning by the Secreted Signaling Molecule FGF8. *Science* 294 (5544), 1071–1074. doi:10.1126/science.1064252

Lin, T. V., Hsieh, L., Kimura, T., Malone, T. J., and Bordey, A. (2016). Normalizing Translation through 4E-BP Prevents mTOR-Driven Cortical Mislamination and Ameliorates Aberrant Neuron Integration. *Proc. Natl. Acad. Sci. USA* 113 (40), 11330–11335. doi:10.1073/pnas.1605740113

Molyneaux, B. J., Arlotta, P., Menezes, J. R. L., and Macklis, J. D. (2007). Neuronal Subtype Specification in the Cerebral Cortex. *Nat. Rev. Neurosci.* 8 (6), 427–437. doi:10.1038/nrn2151

Saito, T., and Nakatsuji, N. (2001). Efficient Gene Transfer into the Embryonic Mouse Brain Using *In Vivo* Electroporation. *Developmental Biol.* 240 (1), 237–246. doi:10.1006/dbio.2001.0439

Zhang, L., Zhang, X., Hsieh, L. S., Lin, T. V., and Bordey, A. (2021). Rab27a-Dependent Paracrine Communication Controls Dendritic Spine Formation and Sensory Responses in the Barrel Cortex. *Cells* 10 (3), 622. doi:10.3390/cells10030622

Conflict of Interest: The authors declare that the research was conducted in the absence of any commercial or financial relationships that could be construed as a potential conflict of interest.

frontiers in Bioengineering and Biotechnology

ORIGINAL RESEARCH
published: 28 January 2022
doi: 10.3389/fbioe.2021.811972

^{68}Ga-DOTA-DiPSMA PET/CT Imaging: Biodistribution, Dosimetry, and Preliminary Application in Prostate Cancer

*Jiaying Zhang[1†], Zefang Lin[1†], Xiaojun Zhang[2], Rong Lin[1], Mengchao Cui[2], Weibing Miao[1,3] and Shaobo Yao[1,3]**

[1]Department of Nuclear Medicine, The First Affiliated Hospital of Fujian Medical University, Fuzhou, China, [2]Key Laboratory of Radiopharmaceuticals, Ministry of Education, Beijing Normal University, Beijing, China, [3]Fujian Provincial Key Laboratory of Precision Medicine for Cancer, The First Affiliated Hospital of Fujian Medical University, Fuzhou, China

OPEN ACCESS

Edited by:
Lu Wang,
First Affiliated Hospital of Jinan University, China

Reviewed by:
Shaoyu Liu,
First Affiliated Hospital of Guangzhou Medical University, China
Ganghua Tang,
Southern Medical University, China
Hongguang Liu,
Northeastern University, China

***Correspondence:**
Shaobo Yao
yaoshaobo008@163.com

†These authors have contributed equally to this work

Specialty section:
This article was submitted to Nanobiotechnology, a section of the journal Frontiers in Bioengineering and Biotechnology

Received: 09 November 2021
Accepted: 17 December 2021
Published: 28 January 2022

Citation:
Zhang J, Lin Z, Zhang X, Lin R, Cui M, Miao W and Yao S (2022) ^{68}Ga-DOTA-DiPSMA PET/CT Imaging: Biodistribution, Dosimetry, and Preliminary Application in Prostate Cancer. Front. Bioeng. Biotechnol. 9:811972. doi: 10.3389/fbioe.2021.811972

Purpose: This prospective trial aimed to evaluate the safety, dosimetry, and biodistribution of a novel theranostic probe ^{68}Ga-DOTA-DiPSMA. Also, we have performed the first preliminary application with ^{68}Ga-DOTA-DiPSMA in prostate cancer (PCa) patients.

Methods: Five healthy volunteers and ten PCa patients were injected with an intravenous bolus of ^{68}Ga-DOTA-DiPSMA. They received serial whole-body PET scans from the time of injection up to 60 min post-injection, with a second PET/CT scanning at 120 min post-injection. In PCa patients, low-dose CT scan and whole-body PET were performed with 2 min per bed position in 40 min post-injection. Absorbed organ doses and effective doses were calculated using OLINDA/EXM. Normal organ uptake and tumor lesion uptake were measured. A lesion-by-lesion analysis was performed.

Results: ^{68}Ga-DOTA-DiPSMA administration was safe and well-tolerated. The kidneys received the highest absorbed dose (114.46 ± 29.28 μSv/MBq), followed by the urinary bladder wall (100.82 ± 46.22 μSv/MBq) in accordance with the expected Prostate-Specific Membrane Antigen (PSMA) renal excretion of the tracer. The mean effective dose was 19.46 ± 1.73 μSv/MBq. The SUV_{max} of ^{68}Ga-DOTA-DiPSMA PET/CT for PCa lesions, bone metastases, and lymph node metastases was 4.41 ± 2.72, 2.95 ± 1.11, and 3.26 ± 1.20, respectively.

Conclusion: Injection of ^{68}Ga-DOTA-DiPSMA is safe and associated with low absorbed and effective doses. ^{68}Ga-DOTA-DiPSMA shows favorable kinetics and imaging characteristics in patients who warrant further head-to-head comparison to validate ^{68}Ga-DOTA-DiPSMA as an alternative for gallium-68-labeled PSMA clinical PET. Low nonspecific uptake in normal organs of ^{68}Ga-DOTA-DiPSMA indicates potential radioligand therapy (RLT) application when labeled with ^{177}Lu, ^{90}Y, or ^{225}Ac.

Keywords: prostate cancer, ^{68}Ga-DOTA-DiPSMA, biodistribution, dosimetry, PET/CT

INTRODUCTION

Prostate cancer (PCa) is one of the most frequently diagnosed cancers in men and the lethal malignant diseases leading to male cancer-related death worldwide (Attard et al., 2016). The accurate presence and location of primary or recurrent tumors are critical for planning effective patient management (Mottet et al., 2021).

The diagnostic capability of conventional anatomic imaging such as MRI and CT to determine PCa is limited in metastases and specificity (Vos et al., 2013). Only prostate biopsy is the definitive way to confirm PCa (Attard et al., 2016). Multiple needle biopsies will increase the positive rate of lesion determination significantly. However, it is difficult to determine distant metastases and increase the risk of complications resulting from biopsy operation (Attard et al., 2016). There has been an unmet need for more advanced imaging modalities to determine primary and metastatic lesions that can be helpful to PCa patient management (observation, salvage local therapy, and systemic therapy). PET with ^{18}F-FDG is effective for most malignant tumors, but it lacks sensitivity for PCa. Therefore, it is urgent to discover new nuclear medicine imaging agents with more specificity for PCa.

Prostate-Specific Membrane Antigen (PSMA) is a transmembrane glycoprotein enzyme selectively overexpressed in PCa cells, with its expression increasing in higher-grade malignancy (Bouchelouche et al., 2010). PET imaging with PSMA probes targeting various PCa-specific markers will provide additional molecular information to facilitate lesion detection and staging (Perera et al., 2020).

Recently, a relatively new nuclear imaging modality ^{68}Ga-PSMA PET/CT imaging with good PCa diagnosis and staging performance has become increasingly utilized to evaluate PCa aggressiveness, especially in patients with biochemical recurrence after surgery (Sachpekidis et al., 2016; Koerber et al., 2017; Wang et al., 2020). PSMA can be coupled with different chelators and labeled with corresponding radionuclides for different purposes. The most widely used PSMA ligands in the clinical examination are PSMA-11 and PSMA-617 containing different linkers and chelators. According to the previously published papers, ^{68}Ga-PSMA-11 and ^{177}Lu-PSMA-617 are a molecular pair in metastatic castration-resistant PCa (mCRPC) diagnosis and radioligand therapy (RLT) (Rahbar et al., 2017; Sun et al., 2020; Violet et al., 2020). However, considering the high nonspecific uptake in the salivary, kidneys, and bone marrow of ^{68}Ga-PSMA-11 and ^{177}Lu-PSMA-617, novel PSMA tracers with lower accumulation in normal organs are urgently needed.

We have discovered a new PSMA dimer (DOTA-DiPSMA, **Figure 1**). The Prof. Cui group from Beijing Normal University will discuss the discovery and preclinical experiments, which will be published elsewhere. Preclinical experiments proved its good imaging ability and low unspecific uptake in normal organs including the liver, kidneys, spleen, and salivary glands. In addition, the affinity of DiPSMA-DOTA-COOH to the PSMA receptor can reach 1.56 nM. This was the first study in humans, following the abovementioned preclinical studies. In this study, we aimed to evaluate the safety, biodistribution, and dosimetry of ^{68}Ga-DOTA-DiPSMA in healthy volunteers and its diagnostic efficacy in PCa patients.

METHODS

Healthy Volunteers and Patients

This study was approved by the Independent Ethics Committee of First Affiliated Hospital of Fujian Medical University [No. MRCTA, ECFAH of FMU (2019)293]. All subjects gave written informed consent and were registered at ClinicalTrials.gov (NCT04525612). Five healthy volunteers and ten patients were enrolled in this study. Five healthy volunteers [5 men, age range 42–76 years (mean age ± SD, 59.83 ± 11.65 years); weight range, 55.0–78.0 kg (mean weight ± SD, 70.27 ± 13.05 kg)] were enrolled to validate the safety, biodistribution, and radiation dosimetry of ^{68}Ga-DOTA-DiPSMA in this study. Exclusion criteria consisted of mental illness conditions, severe liver or kidney disease with

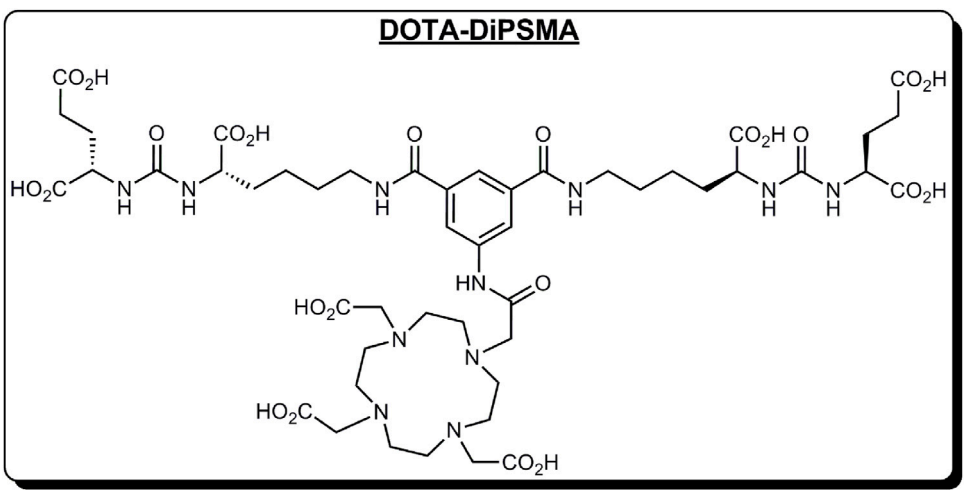

FIGURE 1 | Structure of DOTA-DiPSMA.

TABLE 1 | Summary of the healthy volunteer and patient characteristics and PET findings in ten newly diagnosed prostate cancer patients with ^{68}Ga-DOTA-DiPSMA.

No.	Age (year)	Sex	Weight (kg)	Inject dose	Serum PSA (ng/ml)	SUV_{max} for detected lesions	Lesion location
HV1	55	M	73.8	3.3	—	—	—
HV2	42	M	92.3	5.5	—	—	—
HV3	67	M	60.2	3.8	—	—	—
HV4	56	M	74.3	5.44	—	—	—
HV5	50	M	65.9	5.5	—	—	—
1	68	M	51.8	3.6	26.95	3.3	Prostate
						1.9	T8 vertebrae
						4.1	Sacrum
						3.7	Iliac
						2.1	Iliac
2	76	M	67.2	3.0	10.5	2.9	Prostate
						2.6	Prostate
3	67	M	61	4.1	10.3	1.9	Prostate
						1.7	Prostate
						3.7	Prostate
4	71	M	92.4	3.05	9.56	6.4	Prostate
						3.8	Prostate
5	73	M	67	3.06	8.62	4.0	Prostate
6	77	M	65.1	3.85	6.27	2.1	Prostate
						2.3	Prostate
7	77	M	57.9	2.70	17.22	9.76	Prostate
8	69	M	65.6	2.98	37.9	10.6	Prostate
						3.0	Prostate
						5.8	Seminal vesicle
						2.1	Seminal vesicle
9	78	M	56	2.8	35.72	6.6	Prostate
10	80	M	68	2.8	60.1	5.9	Prostate
						2.6	Iliac lymph node
						3.1	Iliac lymph node
						4.6	Iliac lymph node
						4.3	Iliac lymph node
						1.7	Iliac lymph node

Note. PSA, prostate-specific antigen.

serum creatinine greater than 3.0 mg/dl, or any hepatic enzyme level 5 times or more than the standard upper limit. Participants were also excluded if they were known to have severe allergy or hypersensitivity to intravenous radiographic contrast or claustrophobia during PET/CT scanning.

A total of 10 patients who were newly diagnosed as having PCa by sextant core-needle biopsy and had not received any prior therapy were enrolled with written informed consent. The inclusion criteria were those aged between 40 and 80 years, who have a prostate neoplasm identified by ultrasound or MRI, and were diagnosed by needle biopsy as having PCa. The exclusion criteria included claustrophobia, kidney or liver failure, and inability to fulfill the study. The demographics of healthy volunteers and patients are listed in **Table 1**.

Subject age averaged 73.6 ± 4.6 years (median 74.5 years; range 67–80 years), and body mass averaged 65.2 ± 11.0 kg (median 65.4 kg; range 51.8–92.4 kg). Serum prostate-specific antigen (PSA) values averaged 22.3 ± 17.6 ng/ml (median 13.9 ng/ml; range 6.27–60.1 ng/ml). The reported serum PSA levels were the most recent clinical values at the time of PET/CT imaging. Subjects were numbered chronologically in the order of imaging with ^{68}Ga-DOTA-DiPSMA.

Safety Assessment

Patient safety was assessed and graded according to Common Terminology Criteria for Adverse Events (version 5.0), electrocardiograms, physical examination, and vital signs (blood pressure, respiratory rate, heart rate, and body temperature). Within the first 72 h after ^{68}Ga-DOTA-DiPSMA injection, the research team kept phone contact with each subject, monitoring their adverse event (AE) responses.

Radiopharmaceutical Preparation

Precursors were supplied by Prof. Cui from Key Laboratory of Radiopharmaceuticals, Ministry of Education, Beijing Normal University. Radiolabeling of DiPSMA-DOTA-COOH was performed in a sterile hot cell manually. $^{68}Ga^{3+}$ was eluted from a ^{68}Ge/^{68}Ga generator (JSC Isotope, Moscow, Russia) using 0.1 M of HCl. The clinical doses of DOTA-DiPSMA (30 μg) were compounded in 1.25 M of NaOAc buffer to adjust pH to around 4.0 and labeled with an average of 585.34 ± 177.97 MBq (15.82 ± 4.81 mCi) of $^{68}Ga^{3+}$ using a reaction temperature of 95°C for 10 min. Our protocol permits the radiochemical purity of the product ^{68}Ga-DOTA-DiPSMA to exceed 99% so that we omit the purification step. The final product will pass through a sterile filter membrane (Millipore,

TABLE 2 | Quality control test items.

Test item	Acceptance criteria	Test method
Appearance	Colorless and particle-free	Visual inspection
pH	3.5–6.0	pH strip
Radiochemical purity	—	Radio TLC
^{68}Ga-DOTA-DiPSMA	≥90%	—
Maximum injection volume	≤5 ml	Injector
Sterility	No growth after 14 days of incubation at 37°C	Petri dish inoculation method
Bacterial endotoxins	≤15 EU per ml	LAL test

Note. TLC, thin-layer chromatography; LAL, limulus amebocyte lysate.

Billerica, MA, United States) and then be diluted to 5 ml in a sterile syringe for injection. The total time required for completion of radiolabeling and quality control averaged approximately 30 min. Quality control items are shown in **Table 2**.

Examination Procedures

For healthy volunteers, the blood pressure, pulse, respiratory frequency, and temperature were measured; and routine blood and urine tests, liver function, and renal function were examined immediately before and 24 h after the scan. In addition, any possible side effects during ^{68}Ga-DOTA-DiPSMA PET/CT scanning and within 1 week after the examination were collected and analyzed. No specific subject preparation was requested on the day of ^{68}Ga-DOTA-DiPSMA PET/CT. For the volunteers, after the whole-body low-dose CT scan, 111–222 MBq (3–6 mCi) of ^{68}Ga-DOTA-DiPSMA were injected intravenously, followed by serial whole-body PET acquisitions. The whole body (from the top of the skull to the middle of the femur) of each volunteer was covered by 6 bed positions. The acquisition duration was 2 min/bed position at 5, 15, 30, 45, 60, and 120 min after injection.

For the patients, ^{68}Ga-DOTA-DiPSMA PET/CT scanning was performed at 40 min after tracer administration. For each patient, 103.6–151.7 MBq (2.8–4.1 mCi) of ^{68}Ga-DOTA-DiPSMA was injected intravenously. After a low-dose CT scan, whole-body PET was performed with 2 min per bed position (5–6 bed positions depending on the patient's height). The emission data were corrected for randomness, dead time, scattering, and attenuation. The conventional reconstruction algorithm was used, and the images were zoomed with a factor of 1.2. The images were transferred to an MMWP workstation (Siemens, Erlangen, Germany) for analysis.

Biodistribution Assessment and Dosimetry

Image analysis was performed using MIM v6.9.4 (MIM Software Inc., Cleveland, OH, United Ststes). The volume of interests (VOIs) were drawn over healthy organs on all ^{68}Ga-DOTA-DiPSMA PET images, and SUV_{mean} in these VOIs was determined to obtain the biodistribution of this tracer. Tumor lesions were evaluated in consensus by two nuclear medicine physicians.

All source organs with relevant detectable activity were delineated on the PET images with CT guidance for the healthy volunteers, using MIM software v6.9.4. Time-integrated activity coefficients (normalized cumulated activity (NCA)) were calculated for each source organ by integrating their time–activity curves through curve fitting and normalizing the cumulated activity to the injected activity. Based on the time-integrated activity coefficients, individual absorbed organ doses and the effective dose were determined using OLINDA/EXM v1.1 (Vanderbilt University, Nashville, TN, United States).

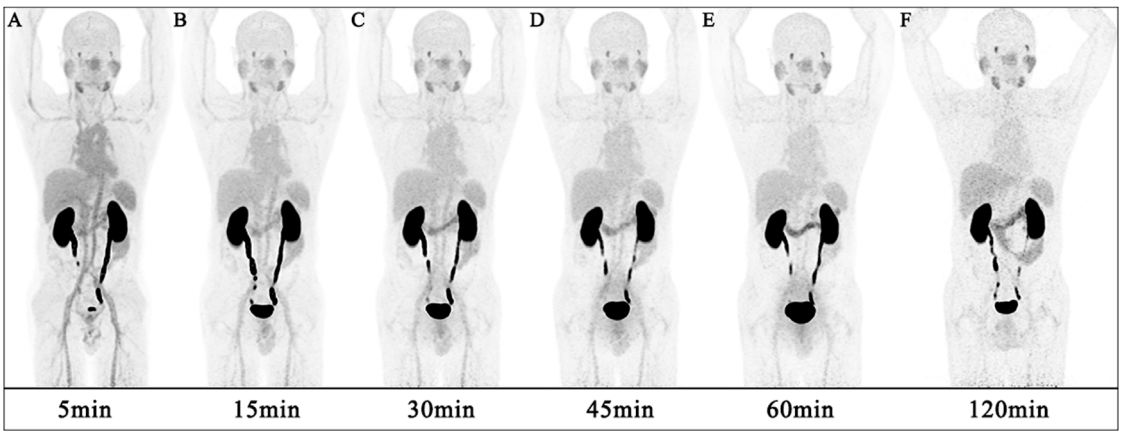

FIGURE 2 | A maximum intensity projection PET images at several time points post-injection of a 56-year-old male healthy volunteer.

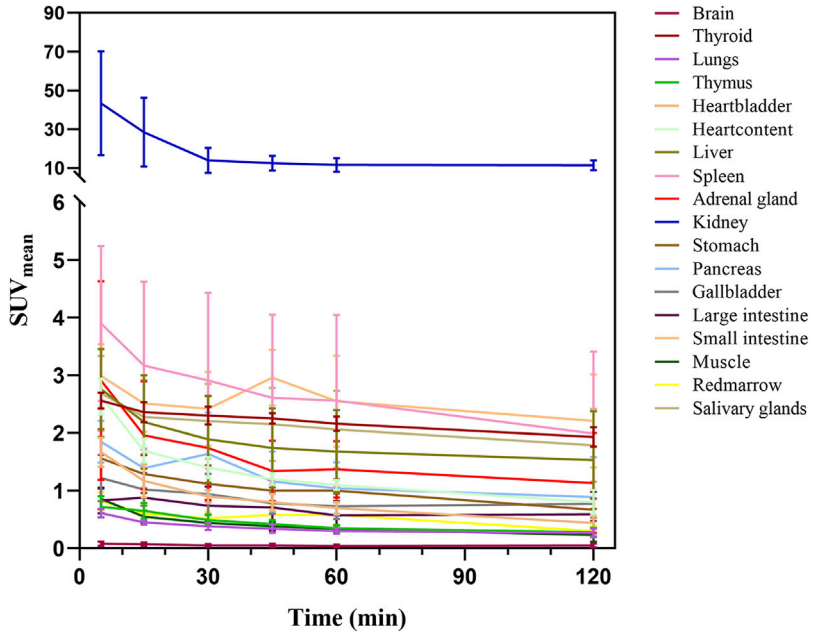

FIGURE 3 | Biodistribution of ^{68}Ga-DOTA-DiPSMA in healthy volunteers.

Calculations were performed with modeling of urinary bladder voiding. Parameters representing the fraction leaving the body *via* urine and biologic half-time were obtained from the fit and used to model urinary bladder voiding. Urinary bladder voiding models with voiding intervals of 1 h were applied. The 70-kg adult male models were used. Organ-absorbed doses, effective doses, and effective dose equivalents were calculated as mean ± SD across subjects. SPSS 23.0 Software (IBM SPSS, Chicago, IL, United States) was used for statistical analyses.

RESULT

Patient Safety

^{68}Ga-DOTA-DiPSMA was found to be safe and well-tolerated in all subjects. No AEs or serious AEs occurred after ^{68}Ga-DOTA-DiPSMA injection for all the healthy volunteers and patients. No apparent changes in vital signs or clinical laboratory tests were found before and after the injection of ^{68}Ga-DOTA-DiPSMA.

Biodistribution

Figures 2, **3** illustrate the biodistribution of ^{68}Ga-DOTA-DiPSMA as a function of time in healthy volunteers. The whole-body background of ^{68}Ga-DOTA-DiPSMA was low. The highest uptake was observed in the kidney with a SUV_{mean} of 43.4 ± 26.8 at 5 min p.i. and further decreased to 11.4 ± 6.5 at 120 min p.i. The spleen, liver, salivary gland, and small intestine showed moderate uptake, with SUV_{mean} of 2.90 ± 1.5, 1.89 ± 0.75, 2.30 ± 0.87, and 2.42 ± 0.64 at 30 min after injection, respectively. Low background uptakes were observed in the brain, lungs, muscle, red marrow, heart, thyroid, gall bladder, pancreas, stomach, bone, and large intestine. The rapid presence in the kidneys, followed by a passage toward the urinary bladder, illustrated the tracer's fast and mainly renal excretion.

TABLE 3 | Estimated absorbed organ doses and effective dose for ^{68}Ga-DOTA-DiPSMA in healthy volunteers.

Absorbed dose	Mean (μSv/MBq)	SD (μSv/MBq)
Adrenals	14.44	0.34
Brain	11.16	0.43
Breasts	10.94	0.42
Gallbladder wall	13.12	3.33
LLI wall	12.47	3.71
Small intestine	12.36	3.61
Stomach wall	11.74	3.51
ULI wall	12.18	3.57
Heart wall	11.38	3.48
Kidneys	114.46	29.28
Liver	24.76	5.38
Lungs	12.12	0.41
Muscle	12.24	0.30
Ovaries	14.26	0.13
Pancreas	14.56	0.31
Red marrow	11.38	3.74
Osteogenic cells	14.53	5.46
Skin	10.68	0.33
Spleen	30.98	7.76
Testes	12.38	0.13
Thymus	12.14	0.48
Thyroid	12.04	0.48
Urinary bladder wall	100.82	46.22
Uterus	15.54	0.61
Salivary glands	24.32	7.11
Total body	9.71	4.93
Effective dose equivalent	26.42	3.68
Effective dose	19.46	1.73

Note. LLI, lower large intestine; ULI, upper large intestine.

TABLE 4 | Different organs' SUV_{max} for ^{68}Ga-DOTA-DiPSMA in PCa patients.

	SUV_{max}	SD
Thyriod	1.12	0.21
Brain	0.07	0.04
Lung	0.40	0.09
Thymus	0.53	0.19
Heart bladder	1.18	0.21
Heart content	1.94	0.50
Liver	2.92	1.05
Kidney	23.40	11.27
Stomach	0.99	0.57
Adrenal gland	1.76	0.64
Pancreas	1.48	0.43
Spleen	3.16	0.64
Gallbladder	0.97	0.41
Large intestine	0.92	0.33
Small intestine	2.26	1.70
Red marrow	0.44	0.20
Muscle	0.65	0.24
Salivary gland	4.88	2.04
Prostate lesions	4.41	2.72
Lymph node metastasis	3.26	1.20
Bone metastasis	2.95	1.11
Seminal vesicle metastasis	3.95	2.62

Note. PCa, prostate cancer.

Dosimetry

The average estimated absorbed organ in healthy volunteers is summarized in **Table 3**. The highest absorbed dose was received by the kidneys (114.46 ± 29.28 μSv/MBq), followed by the urinary bladder wall (100.82 ± 46.22 μSv/MBq). The mean effective dose was 19.46 ± 1.73 μSv/MBq.

Detection of Primary Prostate Cancer

For the 10 patients with primary PCa, ^{68}Ga-DOTA-DiPSMA PET/CT showed 27 positive findings, including 16 prostate lesions, 4 bone metastases, 5 lymph node metastases, and 2 seminal vesicle metastases. The primary lesions were confirmed by needle biopsy. SUV_{max} for prostate lesions, bone metastases, and lymph node metastases were 4.41 ± 2.72, 2.95 ± 1.11, and 3.26 ± 1.20, respectively (**Table 1**; **Figure 4**). Low background uptake was observed in ^{68}Ga-DOTA-DiPSMA (the salivary glands SUV_{max} 4.88 ± 2.04, liver SUV_{max} 2.92 ± 1.05, kidneys SUV_{max} 23.40 ± 11.27, and spleen SUV_{max} 3.16 ± 0.64) (**Table 4**; **Figure 5**).

DISCUSSION

To our knowledge, this was the first human study to evaluate the novel tracer ^{68}Ga-DOTA-DiPSMA in healthy volunteers and patients with PCa. This tracer is a new type of ^{68}Ga-labeled dimer PSMA imaging agent with a simple structure, easy synthesis, and low synthesis cost. ^{68}Ga-DOTA-DiPSMA can be prepared by a one-step labeling reaction in a high yield greater than 95% between $^{68}Ga^{3+}$ ions eluted from a germanium–gallium generator and the precursor DiPSMA-DOTA-COOH.

Here, we presented the results of an independently performed first clinical evaluation of ^{68}Ga-DOTA-DiPSMA in five healthy volunteers, including biodistribution, dosimetry, and safety. Also, we have performed the first initial application with ^{68}Ga-DOTA-DiPSMA in PCa patients. The results showed that this tracer displayed favorable biodistribution and dosimetry features and was well-tolerated in all patients. ^{68}Ga-DOTA-DiPSMA showed

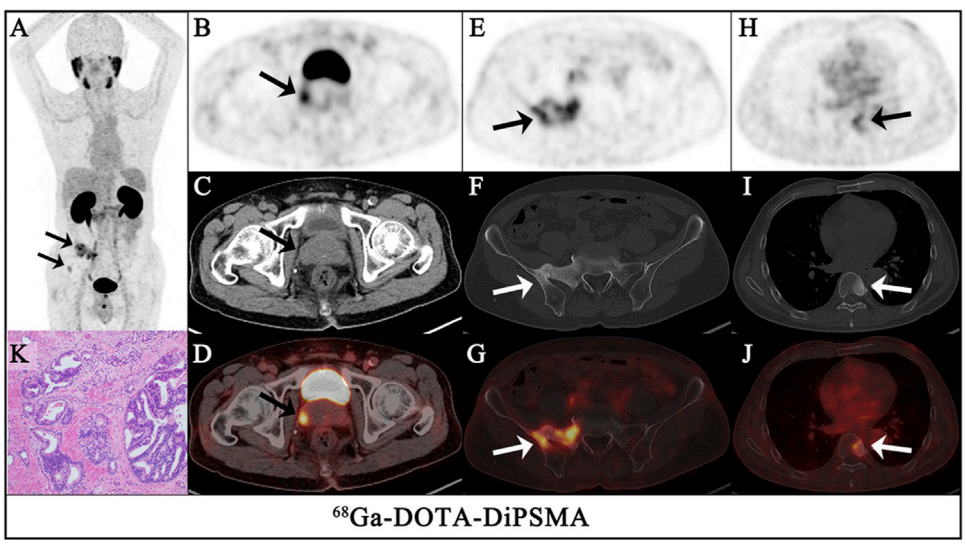

FIGURE 4 | A 68-year-old-man had confirmed prostate cancer after a needle biopsy of the prostate for 1 week. The maximum intensity projection (MIP) of ^{68}Ga-DOTA-DiPSMA PET/CT [**(A)**, arrows] showed significantly abnormal uptake in the image. Axial views of the prostate (top, PET; middle, CT; bottom, fusion image) show intense uptake (SUV_{max} 3.3) in the isodense nodule of the prostate [**(B–D)**, arrows]. In the other level axial views, increased ^{68}Ga-DOTA-DiPSMA uptake was observed in the sacrum and iliac [**(E–G)**, arrows] and the 8th thoracic vertebrae lesions [**(H–J)**, arrows], which were concomitant with bone density increased. Postoperative pathology confirmed it as adenocarcinoma of the prostate (K).

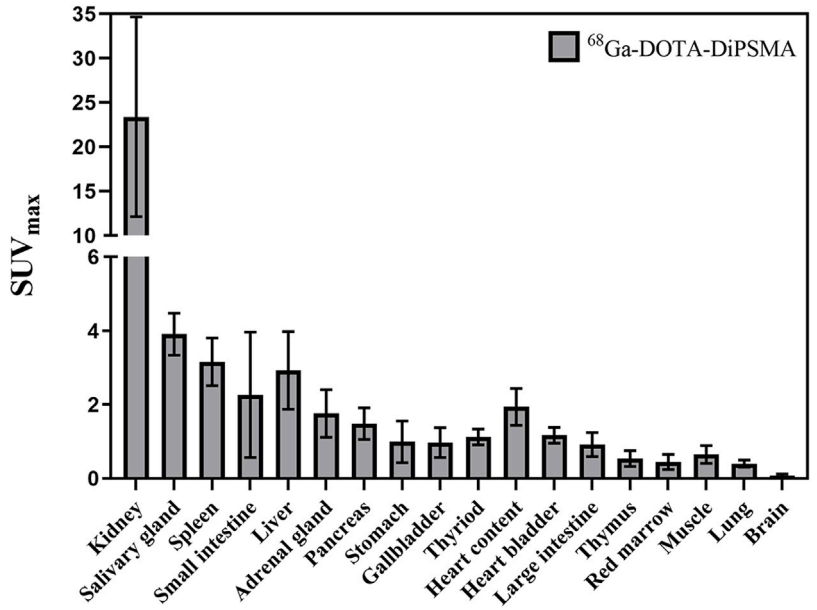

FIGURE 5 | Normal organs' SUV_{max} (average in 10 patients) of ^{68}Ga-DOTA-DiPSMA.

high PSMA affinity. The biodistribution of ^{68}Ga-DOTA-DiPSMA was similar to that of ^{68}Ga-PSMA-11 (Pfob et al., 2016). The rapid presence in the kidneys, followed by a passage toward the urinary bladder, illustrates the tracer's fast and mainly renal excretion. The highest uptake was observed in the kidneys and rapidly cleared through the urinary system in both tracers, consistent with the published ^{68}Ga-PSMA-11 results (Afshar-Oromieh et al., 2016; Zamboglou et al., 2016; Chen et al., 2019; Sandgren et al., 2019). However, ^{68}Ga-DOTA-DiPSMA observed SUV_{mean} values at 60 min for the kidneys, liver, spleen, and parotids (11.93 ± 3.54, 1.68 ± 0.72, 2.56 ± 1.49, and 2.16 ± 0.89, respectively) were in general lower than ^{68}Ga-PSMA-11 (30.1 ± 6.6, 3.3 ± 0.6, 5.2 ± 2.5, and 9.4 ± 2.0, respectively) (Green et al., 2017).

The dosimetry data of ^{68}Ga-DOTA-DiPSMA showed a little lower yet comparable effective dose than ^{68}Ga-PSMA-11 (0.019 vs. 0.022/0.023 mSv/MBq) (Afshar-Oromieh et al., 2016; Sandgren et al., 2019), salivary glands (0.024 vs. 0.089 mSv/MBq), kidney (0.114 vs. 0.240 mSv/MBq), liver (0.0240 vs. 0.053 mSv/MBq), and spleen (0.031 vs. 0.046 mSv/MBq) (Sandgren et al., 2019). We thought that the lower liver and spleen dose of ^{68}Ga-DOTA-DiPSMA might be attributed to the dosimetry methodology.

It is crucial to reduce the radiation dose of nonspecific organs and tissues in the field of radionuclide therapy (RLT) (ICRP, 2002). ^{177}Lu-PSMA-617 RLT is a promising option for patients with mCRPC (Delker et al., 2016; Kratochwil et al., 2016; Paganelli et al., 2020; Rasul et al., 2020). Based on the lower nonspecific uptake and effective dose of ^{68}Ga-DOTA-DiPSMA, the radiation dosimetry in normal organs seemed to be reduced when DOTA-DiPSMA was labeled with ^{177}Lu for RLT. Low background uptakes were observed in the brain, lungs, muscle, red marrow, heart, thyroid, gall bladder, pancreas, stomach, bone, and large intestine. The low uptake of the dimer DOTA-DiPSMA in the parotid glands and the clearance in the kidneys were impressive, which could be an advantage for RLT.

A critical finding of our study is the high tumor accumulation of ^{68}Ga-DOTA-DiPSMA, which showed high tumor uptakes with the highest SUV_{max} up to 10.6 on ^{68}Ga-DOTA-DiPSMA. The primary lesions showed the highest uptake (SUV_{max} 4.41 ± 2.72). For metastasis lesions, the highest uptake was shown in a seminal vesicle (SUV_{max} 3.95 ± 2.61), followed by the iliac lymph node (SUV_{max} 3.26 ± 1.20), and the lowest uptake was observed in the bone (SUV_{max} 2.95 ± 1.11). However, the lower uptake of ^{68}Ga-DOTA-DiPSMA in normal organs may be its advantage (Afshar-Oromieh et al., 2015; Fendler et al., 2017). The study on ^{68}Ga-DOTA-DiPSMA provided a new radiotracer targeting PSMA to diagnose PCa. It was conducive to the accuracy of PCa staging. The small lesion near the urinary bladder would be more apparent with this relatively low background. The mechanism of DOTA-DiPSMA in reducing the uptake in the salivary gland and kidney was still unknown, which needs further studies to confirm.

The primary limitation of our study is the sample size, which did not enable accurate multivariate regression analysis in comparing the diagnosis efficacy of ^{68}Ga-DOTA-DiPSMA with ^{68}Ga-PSMA-11, which is the next work in our research group. Besides, neither blood nor urine samples were collected in our study, which will allow for the stability test *in vivo*. Further detailed and head-to-head comparison studies are required.

CONCLUSION

^{68}Ga-DOTA-DiPSMA is safe and well-tolerated and shows favorable dosimetry and biodistribution in healthy volunteers

and detection performances in PCa patients. The low uptake of the dimer DOTA-DiPSMA in the parotid glands and the clearance in the kidneys were impressive. The lower background of ^{68}Ga-DOTA-DiPSMA showed its potential application for RLT when labeled with ^{177}Lu. DOTA-DiPSMA is a promising novel theranostic tracer for both PCa patient diagnosis and RLT. Further validation by head-to-head comparison is warranted.

DATA AVAILABILITY STATEMENT

The original contributions presented in the study are included in the article/supplementary material, further inquiries can be directed to the corresponding author.

ETHICS STATEMENT

The studies involving human participants were reviewed and approved by the Independent Ethics Committee of First Affiliated Hospital of Fujian Medical University. The patients/participants provided their written informed consent to participate in this study.

AUTHOR CONTRIBUTIONS

MC, WM, and SY: research design. JZ, ZL, XZ, and RL: acquisition of data. All were involved in the analysis and/or interpretation of data and drafting the article or revising it critically. All approved the submitted and final version.

FUNDING

This study was funded in part by the Joint Funds for the Innovation of Science and Technology, Fujian Province (2020Y9101), National Natural Science Foundation of China (82171982), Natural Science Foundation of Fujian (2020J05249), and Fujian Provincial Health Technology Project (2020GGA045).

REFERENCES

Afshar-Oromieh, A., Avtzi, E., Giesel, F. L., Holland-Letz, T., Linhart, H. G., Eder, M., et al. (2015). The Diagnostic Value of PET/CT Imaging with the 68Ga-labelled PSMA Ligand HBED-CC in the Diagnosis of Recurrent Prostate Cancer. *Eur. J. Nucl. Med. Mol. Imaging.* 42, 197–209. doi:10.1007/s00259-014-2949-6

Afshar-Oromieh, A., Hetzheim, H., Kübler, W., Kratochwil, C., Giesel, F. L., Hope, T. A., et al. (2016). Radiation Dosimetry of 68Ga-PSMA-11 (HBED-CC) and Preliminary Evaluation of Optimal Imaging Timing. *Eur. J. Nucl. Med. Mol. Imaging.* 43, 1611–1620. doi:10.1007/s00259-016-3419-0

Attard, G., Parker, C., Eeles, R. A., Schröder, F., Tomlins, S. A., Tannock, I., et al. (2016). Prostate Cancer. *The Lancet.* 387, 70–82. doi:10.1016/S0140-6736(14)61947-4

Bouchelouche, K., Choyke, P. L., and Capala, J. (2010). Prostate Specific Membrane Antigen- a Target for Imaging and Therapy with Radionuclides. *Discov. Med.* 9, 55–61. PMID: 20102687.

Chen, M., Zhang, Q., Zhang, C., Zhao, X., Marra, G., Gao, J., et al. (2019). Combination of 68Ga-PSMA PET/CT and Multiparametric MRI Improves the Detection of Clinically Significant Prostate Cancer: A Lesion-By-Lesion Analysis. *J. Nucl. Med.* 60, 944–949. doi:10.2967/jnumed.118.221010

Delker, A., Fendler, W. P., Kratochwil, C., Brunegraf, A., Gosewisch, A., Gildehaus, F. J., et al. (2016). Dosimetry for 177Lu-DKFZ-PSMA-617: a New Radiopharmaceutical for the Treatment of Metastatic Prostate Cancer. *Eur. J. Nucl. Med. Mol. Imaging.* 43, 42–51. doi:10.1007/s00259-015-3174-7

Fendler, W. P., Eiber, M., Beheshti, M., Bomanji, J., Ceci, F., Cho, S., et al. (2017). 68Ga-PSMA PET/CT: Joint EANM and SNMMI Procedure Guideline for Prostate Cancer Imaging: Version 1.0. *Eur. J. Nucl. Med. Mol. Imaging.* 44, 1014–1024. doi:10.1007/s00259-017-3670-z

Green, M. A., Eitel, J. A., Fletcher, J. W., Mathias, C. J., Tann, M. A., Gardner, T., et al. (2017). Estimation of Radiation Dosimetry for 68Ga-HBED-CC (PSMA-11) in Patients with Suspected Recurrence of Prostate Cancer. *Nucl. Med. Biol.* 46, 32–35. doi:10.1016/j.nucmedbio.2016.11.002

ICRP (2002). Basic Anatomical and Physiological Data for Use in Radiological protection: Reference Values. A Report of Age- and Gender-Related Differences in the Anatomical and Physiological Characteristics of Reference Individuals. ICRP Publication 89. *Ann. ICRP.* 8932, 5–265. PMID: 14506981. doi:10.3109/14653249.2010.487901

Koerber, S. A., Utzinger, M. T., Kratochwil, C., Kesch, C., Haefner, M. F., Katayama, S., et al. (2017). 68Ga-PSMA-11 PET/CT in Newly Diagnosed Carcinoma of the Prostate: Correlation of Intraprostatic PSMA Uptake with Several Clinical Parameters. *J. Nucl. Med.* 58, 1943–1948. doi:10.2967/jnumed.117.190314

Kratochwil, C., Giesel, F. L., Stefanova, M., Benešová, M., Bronzel, M., Afshar-Oromieh, A., et al. (2016). PSMA-Targeted Radionuclide Therapy of Metastatic Castration-Resistant Prostate Cancer with 177Lu-Labeled PSMA-617. *J. Nucl. Med.* 57, 1170–1176. doi:10.2967/jnumed.115.171397

Mottet, N., van den Bergh, R. C. N., Briers, E., Van den Broeck, T., Cumberbatch, M. G., De Santis, M., et al. (2021). EAU-EANM-ESTRO-ESUR-SIOG Guidelines on Prostate Cancer-2020 Update. Part 1: Screening, Diagnosis, and Local Treatment with Curative Intent. *Eur. Urol.* 79, 243–262. doi:10.1016/j.eururo.2020.09.042

Paganelli, G., Sarnelli, A., Severi, S., Sansovini, M., Belli, M. L., Monti, M., et al. (2020). Dosimetry and Safety of 177Lu PSMA-617 Along with Polyglutamate Parotid Gland Protector: Preliminary Results in Metastatic Castration-Resistant Prostate Cancer Patients. *Eur. J. Nucl. Med. Mol. Imaging.* 47, 3008–3017. doi:10.1007/s00259-020-04856-1

Perera, M., Papa, N., Roberts, M., Williams, M., Udovicich, C., Vela, I., et al. (2020). Gallium-68 Prostate-specific Membrane Antigen Positron Emission Tomography in Advanced Prostate Cancer-Updated Diagnostic Utility, Sensitivity, Specificity, and Distribution of Prostate-Specific Membrane Antigen-Avid Lesions: A Systematic Review and Meta-Analysis. *Eur. Urol.* 77, 403–417. doi:10.1016/j.eururo.2019.01.049

Pfob, C. H., Ziegler, S., Graner, F. P., Köhner, M., Schachoff, S., Blechert, B., et al. (2016). Biodistribution and Radiation Dosimetry of 68Ga-PSMA HBED CC—a PSMA Specific Probe for PET Imaging of Prostate Cancer. *Eur. J. Nucl. Med. Mol. Imaging.* 43, 1962–1970. doi:10.1007/s00259-016-3424-3

Rahbar, K., Ahmadzadehfar, H., Kratochwil, C., Haberkorn, U., Schäfers, M., Essler, M., et al. (2017). German Multicenter Study Investigating 177Lu-PSMA-617 Radioligand Therapy in Advanced Prostate Cancer Patients. *J. Nucl. Med.* 58, 85–90. doi:10.2967/jnumed.116.183194

Rasul, S., Hacker, M., Kretschmer-Chott, E., Leisser, A., Grubmüller, B., Kramer, G., et al. (2020). Clinical Outcome of Standardized 177Lu-PSMA-617 Therapy in Metastatic Prostate Cancer Patients Receiving 7400 MBq Every 4 Weeks. *Eur. J. Nucl. Med. Mol. Imaging.* 47, 713–720. doi:10.1007/s00259-019-04584-1

Sachpekidis, C., Kopka, K., Eder, M., Hadaschik, B. A., Freitag, M. T., Pan, L., et al. (2016). 68Ga-PSMA-11 Dynamic PET/CT Imaging in Primary Prostate Cancer. *Clin. Nucl. Med.* 41, e473–e479. doi:10.1097/RLU.0000000000001349

Sandgren, K., Johansson, L., Axelsson, J., Jonsson, J., Ögren, M., Ögren, M., et al. (2019). Radiation Dosimetry of [68Ga]PSMA-11 in Low-Risk Prostate Cancer Patients. *EJNMMI Phys.* 6, 2. doi:10.1186/s40658-018-0239-2

Sun, M., Niaz, M. O., Nelson, A., Skafida, M., and Niaz, M. J. (2020). Review of 177Lu-PSMA-617 in Patients With Metastatic Castration-Resistant Prostate Cancer. *Cureus.* 12, e8921. doi:10.7759/cureus.8921

Violet, J., Sandhu, S., Iravani, A., Ferdinandus, J., Thang, S.-P., Kong, G., et al. (2020). Long-Term Follow-Up and Outcomes of Retreatment in an Expanded 50-Patient Single-Center Phase II Prospective Trial of 177Lu-PSMA-617 Theranostics in Metastatic Castration-Resistant Prostate Cancer. *J. Nucl. Med.* 61, 857–865. doi:10.2967/jnumed.119.236414

Vos, E. K., Litjens, G. J. S., Kobus, T., Hambrock, T., Kaa, C. A. H.-v. d., Barentsz, J. O., et al. (2013). Assessment of Prostate Cancer Aggressiveness Using Dynamic Contrast-Enhanced Magnetic Resonance Imaging at 3 T. *Eur. Urol.* 64, 448–455. doi:10.1016/j.eururo.2013.05.045

Wang, B., Gao, J., Zhang, Q., Fu, Y., Liu, G., Shi, J., et al. (2020). Diagnostic Value of 68Ga-PSMA PET/CT for Detection of Phosphatase and Tensin Homolog Expression in Prostate Cancer: A Pilot Study. *J. Nucl. Med.* 61, 873–880. doi:10.2967/jnumed.119.236059

Zamboglou, C., Wieser, G., Hennies, S., Rempel, I., Kirste, S., Soschynski, M., et al. (2016). MRI Versus 68Ga-PSMA PET/CT for Gross Tumour Volume Delineation in Radiation Treatment Planning of Primary Prostate Cancer. *Eur. J. Nucl. Med. Mol. Imaging.* 43, 889–897. doi:10.1007/s00259-015-3257-5

Conflict of Interest: The authors declare that the research was conducted in the absence of any commercial or financial relationships that could be construed as a potential conflict of interest.

Publisher's Note: All claims expressed in this article are solely those of the authors and do not necessarily represent those of their affiliated organizations, or those of the publisher, the editors and the reviewers. Any product that may be evaluated in this article, or claim that may be made by its manufacturer, is not guaranteed or endorsed by the publisher.

frontiers in Bioengineering and Biotechnology

ORIGINAL RESEARCH
published: 10 February 2022
doi: 10.3389/fbioe.2021.812818

Biodistribution and Dosimetry Evaluation for a Novel Tau Tracer [^{18}F]-S16 in Healthy Volunteers and Its Application in Assessment of Tau Pathology in Alzheimer's Disease

Ying Wang[1], *Li Cai*[1], *Kaixiang Zhou*[2], *Mengchao Cui*[2] *and Shaobo Yao*[1,3]*

[1]Department of PET/CT Diagnostic, Tianjin Medical University General Hospital, Tianjin, China, [2]Key Laboratory of Radiopharmaceuticals, Ministry of Education, Beijing Normal University, Beijing, China, [3]Department of Nuclear Medicine, Fujian Provincial Key Laboratory of Precision Medicine for Cancer, The First Affiliated Hospital of Fujian Medical University, Fuzhou, China

OPEN ACCESS

Edited by:
Chao Zheng,
Yale University, United States

Reviewed by:
Zihua Wang,
Fujian Medical University, China
Jian Yang,
Shanghai University, China
Zhihui Liu,
Stanford University, United States

***Correspondence:**
Shaobo Yao
yaoshaobo008@163.com

Specialty section:
This article was submitted to Nanobiotechnology, a section of the journal Frontiers in Bioengineering and Biotechnology

Received: *10 November 2021*
Accepted: *30 December 2021*
Published: *10 February 2022*

Citation:
Wang Y, Cai L, Zhou K, Cui M and Yao S (2022) Biodistribution and Dosimetry Evaluation for a Novel Tau Tracer [^{18}F]-S16 in Healthy Volunteers and Its Application in Assessment of Tau Pathology in Alzheimer's Disease. Front. Bioeng. Biotechnol. 9:812818. doi: 10.3389/fbioe.2021.812818

Background: The goal of this study was to report a fully automated radiosynthetic procedure of a novel tau tracer [^{18}F]-S16 and its safety, biodistribution, and dosimetry in healthy volunteers as well as the potential utility of [^{18}F]-S16 positron emission tomography (PET) in Alzheimer's disease (AD).

Methods: The automated radiosynthesis of [^{18}F]-S16 was performed on a GE Tracerlab FX2 N module. For the biodistribution and dosimetry study, healthy volunteers underwent a series of PET scans acquired at 10, 60, 120, and 240 min post-injection. The biodistribution and safety were assessed. For the AD study, both AD and healthy controls (HCs) underwent dynamic [^{18}F]-S16 and static [^{18}F]-FDG PET imaging. [^{18}F]-S16 binding was assessed quantitatively using standardized uptake value ratios (SUVRs) measured at different regions of interest (ROIs). [^{18}F]-S16 SUVRs were compared between the AD patients and HCs using the Mann–Whitney *U*-test. In AD patients with all cortical ROIs, Spearman rank-correlation analysis was used to calculate the voxel-wise correlations between [^{18}F]-S16 and [^{18}F]-FDG.

Results: The automated radiosynthesis of [^{18}F]-S16 was finished within 45 min, with a radiochemical yield of 30 ± 5% (n = 8, non-decay-corrected). The radiochemical purity was greater than 98%, and the specific activity was calculated to be 1,047 ± 450 GBq/μmol (n = 5), and [^{18}F]-S16 was stable *in vitro*. In the healthy volunteer study, no adverse effect was observed within 24 h post-injection, and no defluorination was observed *in vivo*. The radiotracer could pass through the blood–brain barrier easily and was rapidly cleared from the circulation and excreted through the hepatic system. The whole-body mean effective dose was 15.3 ± 0.3 μSv/MBq. In AD patients, [^{18}F]-S16 accumulation was identified as involving the parietal, temporal, precuneus, posterior cingulate, and frontal lobes. No specific [^{18}F]-S16 cerebral uptake was identified in HCs. The SUVR of AD patients was significantly higher than that of HCs. No specific binding uptake was found in the choroid plexus, venous sinus, and white matter. A significant correlation was found between [^{18}F]-S16 binding and hypometabolism across neocortical regions.

Conclusion: [18F]-S16 could be synthesized automatically, and it showed favorable biodistribution and safety in humans. [18F]-S16 PET indicated a high image quality for imaging tau deposition in AD and distinguishing AD from HCs.

Keywords: radiation dosimetry, Alzheimer's disease, tau, [18F]-S16, PET/CT

INTRODUCTION

Alzheimer's disease (AD) is a progressive, neurodegenerative condition that results in both cognitive and functional decline. The enormous human and socioeconomic burden associated with AD has motivated an intense international research effort directed toward earlier and more accurate diagnosis and the development of disease-modifying treatments. Amyloid-β (Aβ) plaques, together with tau neurofibrillary tangles (NFTs), are the neuropathological hallmarks of AD (Dani et al., 2018). It has been proposed to classify AD according to the biomarkers for amyloid, tau, and neuronal injury by the A/T/N scheme (Jack et al., 2016).The correlations among amyloid accumulation, neurodegeneration, and clinical decline are not straightforward. Conversely, the distribution and burden of NFTs show a closer association with neurodegeneration and clinical status (Spires-Jones and Hyman, 2014).

Tau is a complex protein with multiple isoforms and post-translational modifications. Tracers may bind to specific or multiple isoforms. As tau is an intracellular protein, radioligands must cross the cell membrane of neurons. In addition, Aβ and tau both manifest a β-sheet structure which binds planar polyaromatic ligands. A selective ligand needs to have at least 10-fold higher binding affinity for tau compared with Aβ (Dani et al., 2016). In the recent 10 years, a number of tau ligands for *in vivo* positron emission tomography (PET) imaging have been developed and evaluated in both preclinical and clinical studies. Tau-PET imaging has opened a unique window to expand our insight into the pathology of AD and other tau-related neurodegenerative diseases. Representative tau-PET ligands, including the first-generation tracers—THK tracers, T807/T808, and [11C]-PBB3—and the second-generation tracers—[18F]-MK-6240, [18F]APN-1607, and [18F]PI-2620—can reflect the timing and distribution of tau in the early phases of neurodegenerative diseases (Fodero-Tavoletti et al., 2011; Chien et al., 2014; Marquié et al., 2015; Walji et al., 2016; Marquié et al., 2017).

However, almost all of the first-generation tau tracers mentioned above presented the same drawback, various degrees of what has been called "off-target" binding. This means the retention of radiotracers in brain areas without tau deposition, such as the basal ganglia, the choroid plexus, or the thalamus (Marquié et al., 2015; Marquié et al., 2017). In addition, the THK tracers—including [18F]-THK523, [18F]-THK5317, and [18F]-THK5351—displayed some white matter retention which hindered an accurate visual interpretation of signals (Betthauser et al., 2017; Hsiao et al., 2017). [18F]-T808 showed high binding affinity and good selectivity for tau over Aβ, with rapid uptake and washout in transgenic mice. However, high defluorination *in vivo* hindered its further development and application in clinical studies (Chien et al., 2014). The drawbacks of [11C]-PBB3 include its short half-life requiring on-site synthesis and the formation of *cis*-trans isomers under the light during radiosynthesis (Hashimoto et al., 2014; Kimura et al., 2015; Ni et al., 2018). Initial human studies of some second-generation tracers such as [18F]-MK6240 have shown no "off-target" binding so far. However, further detailed clinical trials were still needed (Betthauser et al., 2018).

We had developed a novel tau PET radiotracer [18F]-S16 ([18F]-(S)-1-(4-(6-(dimethylamino)quinoxalin-2-yl)phenoxy)-3-fluoropropan-2-ol) with a 2-phenylquinoxaline scaffold. [18F]-S16 displayed high affinity and selectivity for tangles over Aβ as well as sufficient blood–brain barrier penetration and rapid brain washout in normal mice (Zhou et al., 2021). The goal of this study was to report a fully automated radiosynthetic procedure of [18F]-S16 and to evaluate its safety, biodistribution, and dosimetry in healthy volunteers. Moreover, we aimed to identify the [18F]-S16 binding patterns in AD patients relative to sex- and age-matched healthy controls (HCs) and the relationship between cerebral tau pathology and hypometabolism patterns with dual [18F]-S16 (T) and [18F]-FDG (N). The flow chart of the study design is shown in **Supplementary Figure S1**.

MATERIALS AND METHODS

General

All chemicals obtained commercially were of analytical grade (Sigma-Aldrich, United States) and used without further purification unless otherwise stated. The tosylate precursor and [19F]-labeled reference ligand were supplied by Prof. Cui. Sep-Pak light QMA and Sep-Pak plus (light) C18 cartridges were obtained from Waters (Milford, United States). The Sep-Pak light QMA cartridges were pre-conditioned with 8.4% $NaHCO_3$ (8 ml) and water (10 ml) before use. The Sep-Pak C18 plus cartridges were preconditioned with ethanol (10 ml) and water (10 ml) in advance. Fetal bovine serum was purchased from HyClone (Thermo Scientific, United States) and stored under −20°C before use.

Automated Radiosynthesis of [18F]-S16

[18F]-S16 was prepared by a one-pot two-step reaction described in **Supplementary Figure S2**. The automated radiosynthesis of [18F]-S16 was performed on the GE Tracerlab FX2 N synthesis unit (GE Healthcare, United States). No-carrier-added [18F]-fluoride was produced through the nuclear reaction ^{18}O (p, n) ^{18}F by irradiation of more than 95% [18O] enriched water target with 10 MeV proton beam on the GE MINItrace cyclotron. Millexs-GV 0.22-μm-filter units were purchased from Merck Milipore Ltd. The analysis radio-HPLC system was equipped

with a gamma ray radiodetector and a UV detector [Varian system: Waters Symmetry C18 column (5 μm, 4.6 × 250 mm); mobile phase: 1 ml/min with an eluent of CH_3CN/H_2O 50/50]. Radioactivity was measured by CRC-15PET Radioisotope Dose Calibrator (Capintec. Inc., United States).

Before production, vial 1 was filled with a mixture of Kryptofix 222 (K_{222}, 13 mg), potassium carbonate (K_2CO_3, 1.1 mg), CH_3CN (0.3 ml), and H_2O (0.3 ml); vial 2 was filled with anhydrous CH_3CN (1 ml); vial 3 was filled with compound **1** (3 mg) dissolved in anhydrous CH_3CN (1.5 ml); vial 4 was filled with 0.5 M HCl (0.5 ml); vial 5 was filled with 0.5 M NaOH (0.5 ml); vial 6 was filled with 2.5 ml CH_3CN/H_2O (60/40) mixture; vial 12 was filled with saline (10 ml); vial 13 was filled with ethanol (1 ml); vial 14 was filled with H_2O (10 ml); and the round bubble vessel at the bottom-right was filled with 50 ml H_2O.

After [18F]-fluoride (800–1,000 mCi) was delivered from the cyclotron and trapped on QMA, the excess $^{18}H_2O$ was removed. The trapped [18F] activity was eluted to the reactor 1 with K_{222} elution (0.6 ml, vial 1). The reaction mixture was evaporated under a stream of nitrogen (80 ml/min) at 95°C under reduced pressure. The residue was azeotropically dried with CH_3CN (1 ml, vial 2) at 95°C again. Then, a solution of compound 1 (3 mg) in anhydrous CH_3CN (1.5 ml, vial 3) was added, and fluorination was carried out at 100°C for 5 min. The reaction mixture was bubbled with N_2 to dryness. HCl solution (0.5 ml, vial 4) was added to the reaction vessel, and this was heated at 100°C for 3 min. After adding NaOH solution (0.5 ml, vial 5) and a mixture of CH_3CN and H_2O (2.5 ml, vial 6), the mixture was loaded to the semi-prep HPLC system (Syknm S1122 Solvent Delivery System) equipped with a gamma ray radiodetector and a UV detector [Machery-Nagel Nucleosil 100-7 C18 column (16 × 250 mm); mobile phase: 16 ml/min with an eluent of CH_3CN/H_2O, 60/40]. After the collection of product gradient, the elution was diluted with H_2O (50 ml) in the bubble vessel and transferred to the C18 cartridge. The C18 cartridge was washed with H_2O (10 ml, vial 14) to remove high-polarity impurities and dried with helium. The radioactivity was eluted by ethanol (1 ml, vial 13) and diluted by saline (10 ml, vial 12). [18F]-S16 saline was filtered through a sterile Millipore GV filter (0.22 μm, 25 mm) directly into a sterile product vial (20-ml size).

Chemical identification of the purified product was carried out by HPLC co-injection with the non-radioactive reference [19F]-S16, using UV detector at 254 nm UV and a gamma ray radiodetector. The analysis radio-HPLC condition was the same as mentioned above.

For *in vitro* assays, 0.1-ml samples of [18F]-S16 (1.85 MBq, 50 μCi) were dissolved in sterile saline and incubated with 0.2 ml of fetal bovine serum (FBS) at 37°C with gentle shaking. An aliquot of the injection saline and the serum sample was analyzed by radio-HPLC to determine the percentage of intact [18F]-S16 at 120 min.

Participants and Methods

This clinical study was approved by the Institute Review Board of Tianjin Medical University General Hospital (IRB2018-072-01). Participant recruitment and the clinical trial were conducted from August 10, 2018 to August 10, 2020. The trial was registered on Clinicaltrial.gov with the identification number NCT03620552.

In the pilot study, four healthy volunteers with the age of 49.25 ± 11.52 years [three men and one woman, Mini-Mental State Examination (MMSE) 30] were enrolled after giving their written informed consent. These subjects were deemed to be in good health based on their clinical history, physical examination, standard blood and urine tests, and electrocardiogram. The subjects were contacted by telephone approximately 24 h after [18F]-S16 administration to monitor adverse events.

In the AD diagnosis study, 15 probable AD patients and six age- and sex-matched HCs were recruited from research cohorts of the Department of Neurology. They all received a standard clinical evaluation, including a comprehensive neurological history and physical and neurological examinations (brain MRI and neuropsychological assessment with a battery of tests). All the subjects were Han Chinese. The clinical diagnosis was determined by consensus of a multidisciplinary team. The diagnosis of probable AD was based on the NINCDS/ADRDA and DSM-IV criteria. At screening, the Clinical Dementia Rating (CDR) score was at least 0.5, and the MMSE score was no more than 28. They all had positive [11C]-Pittsburgh compound B ([11C]-PiB) PET scan (assessing *in vivo* amyloid pathology) under the published procedures (Wang et al., 2019). The inclusion criteria for HCs were no history of major psychiatric or neurological illnesses, no head injury, and no family history of AD. The MMSE score was more than 28, and the CDR score was 0. The HCs had negative [11C]-PiB PET scans. All participants (or their legal representatives) provided written informed consent to participate in the study. The demographics and clinical data are summarized in **Supplementary Table S1**.

[18F]-S16 and [18F]-FDG PET/CT

In the pilot study, four healthy volunteers underwent a total of four sequential whole-body [18F]-S16 PET/CT scans from the base of the skull to the proximal thigh using Discovery PET/CT 710 scanner (GE Healthcare, Milwaukee, WI, United States). The [18F]-S16 radiotracer was injected through a venous line into the arm of healthy volunteers, with a mean administered activity of 444 ± 37 MBq. The radiotracers were administered to the subjects by a rapid bolus injection (5 ml over 15 s). The low-dose CT scan of each subject for location and attenuation correction was obtained from the base of the skull to the proximate thigh (CT settings: 120 keV; ^{30m}As; pitch, 0.984; slice thickness, 3.75 mm; rotation time, 0.8 s). The scanning protocol included 2-min emission scans for four cycles at 10, 60, 120, and 240 min post-injection. Each cycle consisted of eight bed positions. Thus, the whole-body scanning time was 16 min per cycle. A 10-min static brain scan was also performed, following the second whole-body scan, at approximately 76 min after injection. All data were decay-corrected to the starting time of each individual scan. All PET images were corrected for photon attenuation, dead time, random events, and scatter. Images were reconstructed in the three-dimensional mode using an OSEM + PSF + TOF reconstruction technique (ordered-subset expectation maximization with 24 subsets and two iterations). The image

matrix was 256 × 256 (pixel size, 2.73 mm), and the slice thickness was 3.75 mm.

In the AD diagnosis study, each subject completed the [18F]-S16 and [18F]-FDG PET scans within 1 week. The participants, who were given an intravenous injection of [18F]-S16 (383.6 ± 30.6 MBq), participated in an acquisition scheme: 70–100 min (5 frames: 6 × 300 s). A few days later, after having fasted for at least 6 h, the participants were injected with about 259 MBq [18F]-FDG, and 10-min static PET scans were acquired at 40 min post-injection. Each frame produced 47 slices of 3.75-mm thickness, which covered the whole brain. The images were reconstructed to 256 × 256 matrix.

Safety, Biodistribution, and Radiation Dosimetry

Safety and tolerability were assessed, including blood and urine samples for laboratory tests, electrocardiograms, and physical and clinical examinations. Adverse events were assessed by telephone approximately 24 h after the examination. Whole-organ volumes of interest were drawn manually over the source organs, including spleen, liver, kidneys, pituitary glands, vertebral bodies L1–L5, and urinary bladder, at each time point. The non-decay-corrected activities at different time points were documented as the percentage of injected dosage and fitted with mono-exponential curves. The area under the time–activity curve between time 0 and the first time point was calculated assuming a linear increase from 0 to the first measured activity. The area under the time–activity curve after the first time point was calculated by trapezoidal integration from the first time point to the last time point and extrapolation from the last data point using the fitted mono-exponential function. For bone marrow, the residence time was derived by an image-based integration of L1–L5 vertebra, assuming L1–L5 to be with 12.3% of the whole-body bone marrow. The urinary bladder residence time was determined by using the voiding bladder model implemented in OLINDA/EXM software, with 2 h set as the bladder voiding interval. The residence time of the rest of the body was calculated as the maximum possible residence time (based on physical decay only) minus the sum of the residence time of all source organs. The absorbed dose of target organs and the whole-body effective dose were measured with OLINDA/EXM software by adult male models.

Region of Interest Analyses for [18F]-S16

In the pilot study, three experienced nuclear medicine physicians read all of the images through consensus reading. The same nuclear medicine physicians examined and measured the semiquantitative values for the final analysis. GE MMWP workstation was used for postprocessing. The physiologic uptake of the following organs was evaluated at all time points: brain, salivary gland, heart, liver, spleen, bone marrow, kidneys, urinary bladder, and small intestine. Regions of interest were drawn over these organs to exclude focal lesions, and the maximum standardized uptake value (SUV_{max}) and mean standardized uptake value (SUV_{mean}) normalized to the body weight of the patients were recorded.

In the AD diagnosis study, images were analyzed in the software package PMOD (version 3.7, PMOD Technologies Ltd., Zurich, Switzerland). Dynamic [18F]-S16 images were co-registered to the standard Montreal Neurologic Institute (MNI) space by applying the 70–100-min transformation (brain normalization settings: nonlinear warping, 8-mm input smoothing, 16 iterations, frequency cutoff: 3, regularization: 1.0, no thresholding). All images were analyzed in MNI space. A total number of nine predefined regions of interest (ROIs), deriving from the Hammers atlas (Ossenkoppele et al., 2018), were delineated in the MNI space, including frontal (superior and middle gyri and orbitofrontal cortex), lateral temporal (superior, middle, and inferior gyri), parietal (inferior, superior, and supmarginal gyri), occipital (calcarine, cuneus, and lateral occipital cortex), posterior cingulate and precuneus, medial temporal [entorhinal cortex, hippocampus, and parahippocampus, medial temporal lobe (MTL)], lentiform (putamen and pallidum), and thalamus and white matter. The mean standardized uptake value ratios (SUVRs) of [18F]-S16 were calculated by using mean activity in the cerebellar gray matter as the reference region. These regions were selected as we aimed to assess the full spectrum of the Braak stages.

For [18F]-S16, non-displaceable binding potential (BP_{ND}), a measure of specific binding, was determined for each Hammers atlas region of interest using a basis function implementation of the simplified reference tissue model operating upon the Hammers atlas and reference tissue ROI data. Dynamic 70–100 min [18F]-S16 data were analyzed using the non-invasive Logan graphical analysis ($k_2' = 0.05\ min^{-1}$, $t^* = 80$ min), which were used to determine directly BP_{ND} using the cerebellar gray matter as the reference region.

Region of Interest Analyses for [18F]-FDG PET

The mean SUVRs of [18F]-FDG were calculated for 10-min static data by using mean activity in the pons as the reference region. SUVs were calculated by normalizing the uptake values by the injected dose divided by the subject weight. Target-to-pons SUVRs were calculated for 10-min static data and compared with [18F]-S16 SUVRs.

Statistical Analysis

The comparison of demographics between AD and HC groups was performed by one-way analysis of variance across groups and Fisher's exact test. The [18F]-S16 SUVR data were compared between the AD and HC groups in different ROIs using the Mann–Whitney *U*-test. In AD patients with all cortical ROI regions, Spearman rank-correlation analysis was used to calculate the voxel-wise correlations between [18F]-S16 and [18F]-FDG PET. A significance level of $p < 0.05$ was applied in all analyses. All statistical analyses were performed using SPSS (version 25.0, IBM, Armonk, New York, United States).

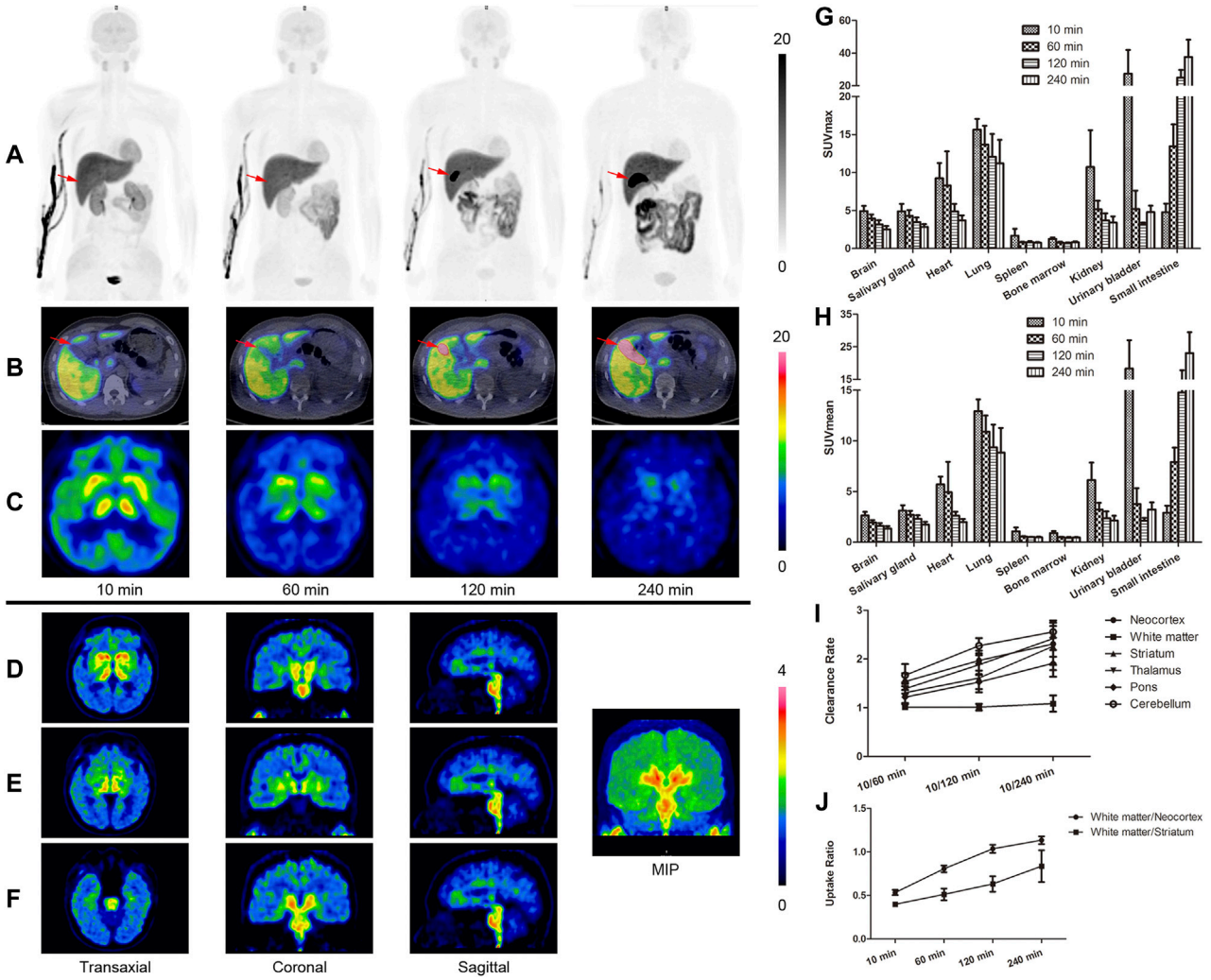

FIGURE 1 | Whole-body positron emission tomography (PET) images of [^{18}F]-S16 obtained in a healthy volunteer acquired over 8-bed positions of varying duration. The maximum intensity projection images of [^{18}F]-S16 at 4 different time points after intravenous injection **(A)**. The time distribution pattern of [^{18}F]-S16 in the gall bladder (**B**, red arrow) and in the brain **(C)**. The brain PET images obtained after the second whole-body scan, approximately 76 min post-injection, presented a transverse, coronal, and sagittal plane **(D–F)**. SUV_{max} **(G)** and SUV_{mean} **(H)** value of [^{18}F]-S16 in the main organs of healthy volunteers (n = 4) at 10, 60, 120, and 240 min post-injection. Brain clearance rate (10/60, 10/120, and 10/240 min) **(I)** and white matter/necortex and white matter/striatum uptake ratio (10, 60, 120, and 240 min) **(H)** were summarized.

RESULTS

Automated Radiosynthesis of [^{18}F]-S16

[^{18}F]-S16 was synthesized for 45 min with a high radiochemical yield of 30 ± 5% (n = 8, non-decay-corrected). The identity of [^{18}F]-S16 was confirmed by a co-injection of [^{19}F]-S16 as a standard (**Supplementary Figures S3A,B**). The radiochemical purity of [^{18}F]-S16 injection was greater than 98%, and the specific activity was 1,047 ± 450 GBq/μmol (n = 5) (**Supplementary Figure S4**). [^{18}F]-S16 showed high *in vitro* stability in FBS and saline, and more than 93 and 96% of [^{18}F]-S16 remained intact within 120 min (longer times were tested) (**Supplementary Figures S3C,D**).

Safety and Biodistribution

[^{18}F]-S16 was found to be safe and well tolerated in all subjects. No adverse effects due to [^{18}F]-S16 administration were observed in healthy volunteers up to 24 h after injection. The radiotracer was cleared mainly from the circulation and excreted into the gut through the hepatic–biliary system. The whole-body maximum intensity projection images of [^{18}F]-S16 at four different time points (10–26, 60–76, 120–136, and 240–256 min) post-injection in a healthy volunteer are presented in **Figure 1A**. The probe was initially detected in the vascular compartment, then rapidly distributed through the extracellular space, and finally excreted through the liver, gall bladder (marked with red arrows), colon, and small intestine (**Figures 1A,B**). Consistent with the

TABLE 1 | Absorbed doses to target organs and effective dose.

Target organs	Organ doses (μGy/MBq)
Adrenals	17.0 ± 0.6
Brain	15.2 ± 1.0
Breasts	7.9 ± 0.3
Gallbladder wall	133.7 ± 60.9
Lower large intestine wall	11.8 ± 0.6
Small intestine	44.5 ± 5.4
Stomach wall	12.7 ± 0.2
Upper large intestine wall	18.9 ± 1.1
Heart wall	16.6 ± 0.7
Kidneys	31.6 ± 2.2
Liver	88.5 ± 11.2
Lungs	11.1 ± 0.2
Muscle	9.5 ± 0.3
Ovaries	13.7 ± 0.6
Pancreas	17.1 ± 0.6
Red marrow	11.3 ± 0.6
Osteogenic cells	11.7 ± 0.6
Skin	7.0 ± 0.3
Spleen	10.7 ± 0.3
Testes	7.7 ± 0.5
Thymus	9.2 ± 0.4
Thyroid	8.3 ± 0.5
Urinary bladder wall	10.6 ± 0.5
Uterus	13.2 ± 0.6
Parotid	14.3 ± 3.8
Total body	12.3 ± 0.1
Effective dose (mSv/MBq)	15.3 ± 0.3

hydrophobic characteristic of [^{18}F]-S16 (log *p*-value of 2.61 ± 0.05, reported in a previous paper), it was observed that [^{18}F]-S16 accumulated significantly in the liver (hepatic system), not in the kidney (renal system). Moderate uptake was observed in the spleen, heart, brain, parotid gland, and salivary gland. Low radioactive uptake was observed in the lungs, pancreas, muscles, and bone marrow, which indicates high anti-defluorination stability *in vivo*. The quantitative biodistribution (SUV_{max} and SUV_{mean}) in the main organs of healthy volunteers is summarized in **Figures 1G,H**. Static brain PET images are presented in **Figures 1D-F**, presented as transverse, coronal, and sagittal planes which were obtained following the second whole-body scanning at 76 min post-injection. No obvious radioactive uptake was found in the cerebral cortex, choroid, and sagittal sinus. Moderate radioactive uptake was observed mainly in the bilateral striatum, thalamus, and brainstem at 10 min post-injection, then decreased rapidly from 60 to 120 min, and was cleared from the blood pool at 240 min. The brain clearance rate, including neocortex, white matter, striatum, thalamus, pons, and cerebellum, was higher in 60, 120, and 240 min (**Figure 1I**). The uptake ratio of white matter/neocortex and white matter/striatum further increased during 10, 60, 120, and 240 min (**Figure 1H**).

Radiation Dosimetry

The absorbed radiation doses of target organs are summarized in **Table 1**. The gallbladder wall received the highest radiation dose at 133.7 ± 60.9 μSv/MBq. The effective dose was 15.3 ± 0.3 μSv/MBq. The radioactive uptake of the hematopoietic system and genital system was low, which also proved its safety.

[^{18}F]-S16 Visual Assessment

The demographic and clinical characteristics of 15 AD subjects and 6 HCs are summarized in **Supplementary Table S1**. In HCs, no areas of specific [^{18}F]-S16 cerebral uptake were identified visually (**Figure 2**), and a consistent pattern of initial uptake and washout was observed. In AD subjects, tracer accumulation was identified in cortical regions mainly involving the parietal and temporal lobes, precuneus, occipital lobes, and frontal lobes. One AD patient (subject #8) revealed some posterior cerebral artery (PCA) syndromes, showing a significantly higher [^{18}F]-S16 retention in the occipital lobe. Two AD patients revealed notably higher S16 retention in the bilateral frontal lobe (subject #10) and lower glucose metabolism compared to other AD cases. In addition, subject #12 (male, age 64) displayed a higher S16 retention in the left posterior temporal and inferior parietal lobes as well as hypometabolism in the same regions. Radiotracer retention was observed in the substantia nigra and brainstem of both HCs and AD subjects. No binding higher than the uptake in the reference region was found in the choroid plexus, venous sinus, and white matter.

^{18}F-S16 Binding Related to Clinical Diagnosis and Quantitative Analyses

A comparison of a representative AD and HC subject in the mean [^{18}F]-S16 BP_{ND} PET map is shown in **Figures 3A,B**. [^{18}F]-S16 accumulation in AD subject #6 was identified in the cortical regions mainly involving the parietal, temporal, precuneus, and frontal lobes. No areas of specific [^{18}F]-S16 cerebral uptake were identified visually in HC subject #16. [^{18}F]-S16 retention was observed in the substantia nigra and brainstem of both AD and HC subjects.

The ROI analysis of SUVRs is summarized in **Table 2**. The SUVRs of AD patients ranged from 1.12 to 1.87 (white matter and lentiform, respectively). The lentiform, thalamus, and medial temporal lobe showed the greatest SUVRs in AD. Without the substantia nigra ROIs, the highest SUVR in AD was the medial temporal lobe (1.59), followed by posterior cingulate and precuneus (1.35), and parietal (1.35) and temporal lobe (1.33). The SUVRs for HC ranged from 1.01 (white matter) to 1.96 (thalamus). The lentiform, thalamus, and medial temporal lobe also presented with the highest SUVRs in HC. The region with the lowest SUVR in both AD and HC groups was the white matter. All ROIs had SUVRs that were greater than 1.0, indicating that the uptake of [^{18}F]-S16 was greater than that of the cerebellar reference region.

[^{18}F]-S16 uptake in different ROIs of AD and HC subjects is shown as SUVR box plots in **Figure 3C**. The AD subjects showed generally higher SUVRs than HCs in the cortical regions, especially in the parietal lobe ($p < 0.0001$), posterior cingulate and precuneus ($p < 0.001$), lateral temporal and occipital lobes ($p < 0.01$), and frontal lobe ($p < 0.05$). However, there was no statistically significant difference in the medial temporal lobe. The SUVR analyses of the subcortical regions did not show

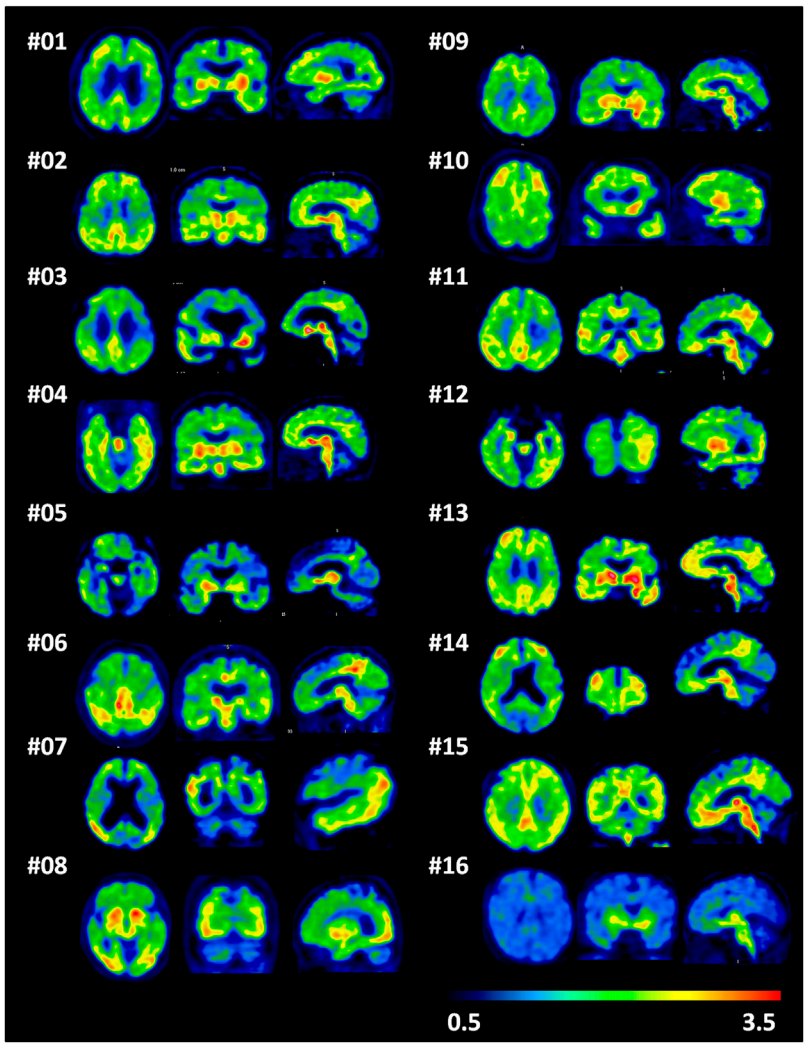

FIGURE 2 | A single frame of [18F]-S16 positron emission tomography images (85–90 min) in a transverse, coronal, and sagittal plane for all Alzheimer's disease patients (subjects 1–15) and one representative healthy control (subject 16).

statistically significant differences between AD and HC subjects in the thalamus and white matter. However, lentiform revealed a significant difference between AD and HCs ($p < 0.05$).

[18F]-S16 Quantitative Analyses and Correlation With Glucose Metabolism

The SUVR values of the summed [18F]-S16 PET and [18F]-FDG PET image were related to all six cortical regions to investigate the regional relationship between tau deposition and glucose metabolism. Spearman rank-correlation coefficient (r) was compared between [18F]-S16 PET and [18F]-FDG PET for all cortical ROI regions in AD patients. The correlation coefficients were determined by comparing [18F]-S16 SUVR and [18F]-FDG SUVR (global mean and normalization). The correlation plots of [18F]-S16 PET and [18F]-FDG PET are shown in **Figure 4**. There was a significant difference in the correlation coefficients between [18F]-S16 and [18F]-FDG PET ($r = -0.44$, $p < 0.0001$) for global mean normalization.

DISCUSSION

In this study, we have reported the fully automated radiosynthesis and the first human PET study of [18F]-S16. No radioactive uptake in the bone of healthy volunteers guaranteed its stability *in vivo*. In addition, the suitable lipophilicity and molecular weight of [18F]-S16 resulted in their excellent characteristics of crossing the blood–brain barrier. The biodistribution of [18F]-S16 in humans was consistent with that of animal studies as previously reported. The line of activity seen in **Figure 1A** is tracer accumulation in the vein, which is obvious soon after injection but gradually disappears. The bladder did not show intensive uptake

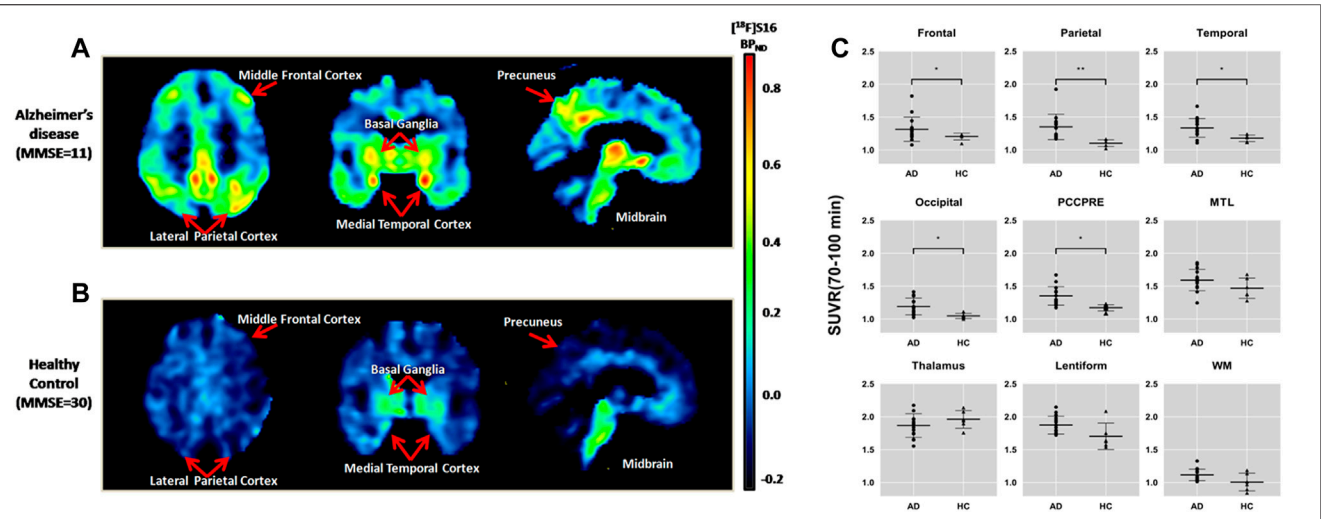

FIGURE 3 | Comparison of an Alzheimer's disease patient [subject 6, Mini-Mental State Examination (MMSE) = 11] **(A)** and a healthy control (subject 16, MMSE = 30) **(B)** in the mean [^{18}F]-S16 BP_{ND} positron emission tomography maps. The images were normalized to the Montreal Neurologic Institute space and presented as a transverse, coronal, and sagittal plane. Box plot of standardized uptake value ratio (SUVR; 70–100 min) of each diagnosis group for different brain regions **(C)**. Box plot of SUVR (70–100 min) of each diagnosis group for different brain regions.*$p < 0.05$, **$p < 0.01$.

TABLE 2 | Standardized uptake value ratios.

ROI	AD	HCs
Frontal	1.32 (0.183)	1.21 (0.053)
Parietal	1.35 (0.192)	1.10 (0.050)
Temporal	1.33 (0.141)	1.18 (0.049)
Occipital	1.19 (0.127)	1.05 (0.039)
Posterior cingulate and precuneus	1.35 (0.141)	1.17 (0.048)
Medial temporal	1.59 (0.163)	1.47 (0.155)
Thalamus	1.87 (0.180)	1.96 (0.135)
Lentiform	1.88 (0.135)	1.70 (0.201)
White matter	1.12 (0.087)	1.01 (0.134)

Standardized uptake value ratios mean values (standard deviation) from 70 to 100 min using the cerebellar cortex as the reference region.
AD, Alzheimer's disease; HCs, healthy controls; ROI, region of interest.

throughout the study. As a result, we deduced that [^{18}F]-S16 was mainly excreted through the hepatic–biliary system, resulting in a high accumulation in the liver and gall bladder. The radioactive uptake in the gall bladder, colon, and small intestine increased rapidly, while that in the kidneys and bladder decreased sharply. The time–distribution pattern of [^{18}F]-S16 in the gall bladder is shown in **Figure 1B** (marked with red arrows). The uptake in the gall bladder was low at 10 min post-injection, and it increased to a high level at 60 and 120 min when the probe was gradually secreted into the gall bladder cavity. At 240 min post-injection, the probe was almost fully secreted into the gall bladder.

The effective dose of [^{18}F]-S16 was 15.3 ± 0.3 μSv/MBq, which is in the typical range for F-18 radioligand (Zanotti-Fregonara et al., 2013). The dosimetry data of [^{18}F]-S16 showed a slightly lower effective dose compared to that of other tau tracers (22.5 ± 3.6 μSv/MBq for [^{18}F]-AV1451, 22.7 ± 1.3 μSv/MBq for [^{18}F]-THK5351, and 29.4 ± 0.6 μSv/MBq for [^{18}F]-MK6240) (Choi et al., 2016; Hsiao et al., 2017; Koole et al., 2020).

The present study showed the accumulation of [^{18}F]-S16 in regions known to have tau deposition in Aβ-positive clinically probable AD subjects. The HC subjects showed a very low [^{18}F]-S16 accumulation in all cortical brain regions, and the AD subjects could be clearly distinguished. In the AD group, all cortical ROIs revealed average SUVR values over 1.19, especially in significant brain areas of the medial temporal lobe, posterior cingulate and precuneus, parietal lobe, lateral temporal, frontal lobe, and occipital lobes associated with tau deposition (Braak and Braak, 1997). The highest uptake of [^{18}F]-S16 was observed in the medial temporal lobe (including entorhinal cortex, hippocampus, and parahippocampus). A higher uptake of [^{18}F]-S16 was observed in the posterior cingulate and precuneus, lateral temporal, and parietal lobe. The spatial distribution observed here parallels neuropathologic data reporting tau spread from the entorhinal cortex through the inferior-lateral temporal and medial parietal areas to the neocortex (Braak et al., 2006). The distribution and density of tracer uptake in AD subjects observed in this study are also consistent with previous tau PET imaging studies (Jack et al., 2018; Ossenkoppele et al., 2018). Besides this, the present study revealed that tracer binding predominantly occurred in the gray matter of the AD group. The white matter showed the lowest uptake of [^{18}F]-S16 both in the AD and HC groups. High gray-to-white-matter ratios in the AD cases reflect radiotracer binding to the cortical neurons that are most affected and are in good agreement with the excellent contrast observed in human PET scans.

The uptake of [^{18}F]-S16 was significant in the MTL of HCs, which was consistent with previously reported tau tracers. Tau imaging in cognitively normal elderly individuals using [^{18}F]-THK series and [^{18}F]-AV1451 showed radioactivity retention in

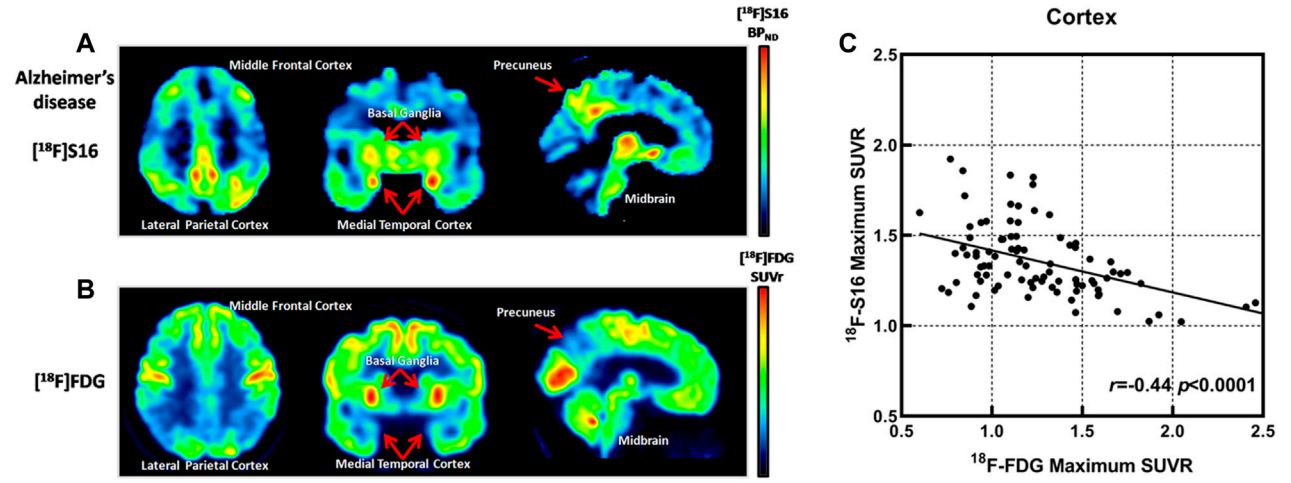

FIGURE 4 | Comparison of [^{18}F]-S16 BP_{ND} positron emission tomography (PET) map and [^{18}F]-FDG SUVR PET map obtained in the same Alzheimer's disease patient (subject 6). The images were normalized to the Montreal Neurologic Institute space and presented as a transverse, coronal, and sagittal plane **(A,B)**. Correlation plots for [^{18}F]-S16 and [^{18}F]-FDG PET. $r = -0.44$, $p < 0.0001$ **(C)**.

the MTL (Chiotis et al., 2016; Cho et al., 2016). This pattern of MTL binding is consistent with the neuropathological literature (Braak et al., 2011) and may reflect an age-related process of tau accumulation in this region (Tomlinson et al., 1970), the so-called primary age-related tauopathy (Jellinger et al., 2015), which has been shown to result in hippocampal atrophy and mild amnestic deficits that are independent of amyloid-β (Josephs et al., 2017). The age-related accumulation of tau, followed by the spreading of tau potentiated by Aβ, disrupts functional memory circuits by disconnecting key MTL structures. Tau pathology plays a role in disconnecting the hippocampus from specific MTL memory systems, leading to increased local coherence and memory decline (Harrison et al., 2019).

In this study, we found that one AD patient showed a significantly higher tracer retention in the occipital lobe (subject #8). This patient revealed PCA syndromes. PCA is a focal neurodegenerative disorder of higher visual processing and spatial praxis with relative sparing of memory and insight, which is considered one subtype of variant AD. In PCA, a high consistency between the phospho-tau-specific antibody AT8 immunohistochemical staining and tau tracer binding was observed (Yap et al., 2021). Tau-PET imaging showed significantly higher binding compared to patients with similar clinical features arising from dementia with Lewy bodies (Nedelska et al., 2019). Patients with PCA presented with a higher uptake in the occipital and parietal brain regions, while patients with amnestic-predominant presentation showed the highest binding in the medial temporal and lateral temporoparietal regions (Ossenkoppele et al., 2016). Our data was consistent with previous immunohistochemical and tau-PET studies. We found that two AD patients revealed notably higher S16 retention in the bilateral frontal lobe (subject #10) and lower glucose metabolism compared to other AD cases. The clinical presentations of these two patients showed dysexecutive deficits and impulsive and repetitive movements. They may belong to the behavioral variant of Alzheimer's disease, which represents another rare variant of AD. It was characterized by early and predominant behavioral deficits and personality changes caused by the AD pathology. In addition, subject #12 (male, age 64) presented with language impairment in fluency and sentence repetition. He displayed higher S16 retention in the left posterior temporal and inferior parietal lobe as well as hypometabolism in the same regions. This patient may belong to the language variant of Alzheimer's disease.

We observed the strongest binding for the lentiform and thalamus both in the AD and HC groups, which might be largely associated with off-target binding. Off-target binding is a major limitation associated with the first-generation tau radioligands. In particular, the basal ganglia and thalamus were found to be affected by extensive binding to monoamine oxidase B (MAO-B) (Yap et al., 2021). MAO-B is a flavoenzyme in the mitochondrial outer membrane and plays a major role in the metabolism of neuroactive and vasoactive amines. In previous studies, MAO-B binding was also considered as an important off-target binding of THK probes. A previous study from Prof. Cui indicated that the [^{18}F]-S16 shared the same THK binding site of NFTs (Zhou et al., 2021). We followed the successful optimization strategy of THK derivatives in order to achieve an appropriate tau-targeting probe with high binding affinity and selectivity over Aβ plaques and with low off-target binding and suitable *in vivo* pharmacokinetics. When a unique fluoropropanol side chain was introduced to the THK scaffold, to give [^{18}F]THK-5117 and [^{18}F]THK-5351, they showed higher selectivity for tau and more favorable *in vivo* kinetics. We introduced the chiral fluoropropanol side chain at the phenolate position and N,N-dimethylamino/N-monomethylamino group at position 6 or 7 of the 2-phenylquinoxaline scaffold to find compounds with increased binding affinity and selectivity toward NFTs. Thus, [^{18}F]-S16, which was a [^{18}F]-labeled chiral 2-phenylquinoxaline derivative, was designed, synthesized, and evaluated as a PET

imaging probe for tangles. We found that this quinoxaline derivative was capable of binding with NFTs on the brain sections of AD patients *in vitro*. The parallel comparison between [18F]-S16 and [18F]-THK5351 revealed that S16 had many advantages, such as high binding affinity, selectivity, initial brain uptake, and low off-target binding (Zhou et al., 2021). As such, there was lower [18F]-S16 binding in the MAO-B-rich lentiform in HCs than in the AD group in this study.

In this study, we directly compared [18F]-S16 SUVR and [18F]-FDG SUVR for all cortical ROIs in AD patients. Studies have shown a significant correlation between [18F]-S16 binding and hypometabolism across neocortical regions. This finding was consistent with other tau radioligand PET studies (Ossenkoppele et al., 2015; Bischof et al., 2016; Ossenkoppele et al., 2016; Dronse et al., 2017; Whitwell et al., 2018). The A/T/N classification scheme suggests that the tau pathology follows in the time course of disease development after amyloid-β pathology. Early Aβ deposition occurs across much of the cortex even in clinically normal aging (*e.g.*, preclinical AD), while tau pathology begins in the transentorhinal cortex in the MTL and may spread in an activity-dependent manner along vulnerable functional networks (Harrison et al., 2019). Animal studies have indeed shown the spread of tau pathology *via* synaptic connections, with this process accompanied by neurodegenerative changes (de Calignon et al., 2012; Ahmed et al., 2014). The tau protein plays a key role in the formation of intraneuronal NFTs and might represent an important therapeutic target in AD because tau deposition is highly associated with neurodegeneration and cognitive decline. Our findings clearly demonstrate that [18F]-S16 PET can provide information on "T". [18F]-S16 tau PET imaging has the potential to facilitate an accurate diagnosis of tauopathy, a precise assessment of disease severity and disease progression, and a specific appraisal of efficacy of potential disease-modifying anti-tau treatments.

CONCLUSION

[18F]-S16 could be automatically synthesized on a large scale, and it shows favorable biodistribution and safety to the human body. The dosimetry data are comparable to that of other tau tracers. The AD subjects show a generally higher [18F]-S16 uptake than HCs in the cortical regions, and a significant correlation between [18F]-S16 binding and hypometabolism across neocortical regions could be observed. We find prominent [18F]-S16 uptake in regions where abnormal tau aggregates are expected to accumulate. Our results suggest that the new tau PET tracer is a suitable tool to distinguish AD and HCs. It is necessary to conduct more studies on more subjects and involve other tauopathy reactions.

DATA AVAILABILITY STATEMENT

The original contributions presented in the study are included in the article/**Supplementary Material**. Further inquiries can be directed to the corresponding author.

ETHICS STATEMENT

The studies involving human participants were reviewed and approved by the Institute Review Board of Tianjin Medical University General Hospital. The patients/participants provided their written informed consent to participate in this study.

AUTHOR CONTRIBUTIONS

MC and SY contributed to research design. YW, LC, and KX contributed to acquisition of data. All authors were involved in the analysis and/or interpretation of data and drafting of the article or revising it critically. All authors approved the submitted and final version.

FUNDING

This study was funded in part by the National Natural Science Foundation of China (82171982), Tianjin Education Commission Scientific Research Project (2018KJ060), Joint Funds for the Innovation of Science and Technology, Fujian Province (2020Y9101), Natural Science Foundation of Fujian (2020J05249), and Fujian Provincial Health Technology Project (2020GGA045).

ACKNOWLEDGMENTS

The authors gratefully acknowledge Dr. Shuo Gao (Department of PET/CT Diagnostic, Tianjin Medical University General Hospital, Tianjin, China) for experimental design. In addition, we thank Yansheng Li, Hailei Yang, and Biyao Hu for the technical assistance to this study.

SUPPLEMENTARY MATERIAL

The supplementary material for this article can be found online at: https://www.frontiersin.org/articles/10.3389/fbioe.2021.812818/full#supplementary-material

REFERENCES

Ahmed, Z., Cooper, J., Murray, T. K., Garn, K., McNaughton, E., Clarke, H., et al. (2014). A Novel *In Vivo* Model of Tau Propagation with Rapid and Progressive Neurofibrillary Tangle Pathology: the Pattern of Spread Is Determined by Connectivity, Not Proximity. *Acta Neuropathol.* 127, 667–683. doi:10.1007/s00401-014-1254-6

Betthauser, T. J., Cody, K. A., Zammit, M. D., Murali, D., Converse, A. K., Barnhart, T. E., et al. (2018). *In Vivo* Characterization and Quantification of

Neurofibrillary Tau PET Radioligand 18F-MK-6240 in Humans from Alzheimer Disease Dementia to Young Controls. *J. Nucl. Med.* 60 (1), 93–99. doi:10.2967/jnumed.118.209650

Betthauser, T. J., Lao, P. J., Murali, D., Barnhart, T. E., Furumoto, S., Okamura, N., et al. (2017). *In Vivo* Comparison of Tau Radioligands 18F-THK-5351 and 18F-THK-5317. *J. Nucl. Med.* 58, 996–1002. doi:10.2967/jnumed.116.182980

Bischof, G. N., Jessen, F., Fliessbach, K., Dronse, J., Hammes, J., Neumaier, B., et al. (2016). Impact of Tau and Amyloid burden on Glucose Metabolism in Alzheimer's Disease. *Ann. Clin. Transl Neurol.* 3, 934–939. doi:10.1002/acn3.339

Braak, H., Alafuzoff, I., Arzberger, T., Kretzschmar, H., and Del Tredici, K. (2006). Staging of Alzheimer Disease-Associated Neurofibrillary Pathology Using Paraffin Sections and Immunocytochemistry. *Acta Neuropathol.* 112, 389–404. doi:10.1007/s00401-006-0127-z

Braak, H., and Braak, E. (1997). Frequency of Stages of Alzheimer-Related Lesions in Different Age Categories. *Neurobiol. Aging* 18, 351–357. doi:10.1016/s0197-4580(97)00056-0

Braak, H., Thal, D. R., Ghebremedhin, E., and Del Tredici, K. (2011). Stages of the Pathologic Process in Alzheimer Disease: Age Categories from 1 to 100 Years. *J. Neuropathol. Exp. Neurol.* 70, 960–969. doi:10.1097/nen.0b013e318232a379

Chien, D. T., Szardenings, A. K., Bahri, S., Walsh, J. C., Mu, F., Xia, C., et al. (2014). Early Clinical PET Imaging Results with the Novel PHF-Tau Radioligand [F18]-T808. *J. Alzheimers Dis.* 38, 171–184. doi:10.3233/JAD-130098

Chiotis, K., Saint-Aubert, L., Savitcheva, I., Jelic, V., Andersen, P., Jonasson, M., et al. (2016). Imaging *In-Vivo* Tau Pathology in Alzheimer's Disease with THK5317 PET in a Multimodal Paradigm. *Eur. J. Nucl. Med. Mol. Imaging* 43, 1686–1699. doi:10.1007/s00259-016-3363-z

Cho, H., Choi, J. Y., Hwang, M. S., Kim, Y. J., Lee, H. M., Lee, H. S., et al. (2016). *In Vivo* cortical Spreading Pattern of Tau and Amyloid in the Alzheimer Disease Spectrum. *Ann. Neurol.* 80, 247–258. doi:10.1002/ana.24711

Choi, J. Y., Lyoo, C. H., Lee, J. H., Cho, H., Kim, K. M., Kim, J. S., et al. (2016). Human Radiation Dosimetry of [18F]AV-1451(T807) to Detect Tau Pathology. *Mol. Imaging Biol.* 18, 479–482. doi:10.1007/s11307-015-0924-7

Dani, M., Edison, P., and Brooks, D. J. (2016). Imaging Biomarkers in Tauopathies. *Parkinsonism Relat. Disord.* 22, S26–S28. doi:10.1016/j.parkreldis.2015.08.011

Dani, M., Wood, M., Mizoguchi, R., Fan, Z., Walker, Z., Morgan, R., et al. (2018). Microglial Activation Correlates *In Vivo* with Both Tau and Amyloid in Alzheimer's Disease. *Brain* 141 (9), 2740–2754. doi:10.1093/brain/awy188

de Calignon, A., Polydoro, M., Suárez-Calvet, M., William, C., Adamowicz, D. H., Kopeikina, K. J., et al. (2012). Propagation of Tau Pathology in a Model of Early Alzheimer's Disease. *Neuron* 73, 685–697. doi:10.1016/j.neuron.2011.11.033

Dronse, J., Fliessbach, K., Bischof, G. N., von Reutern, B., Faber, J., Hammes, J., et al. (2017). *In Vivo* Patterns of Tau Pathology, Amyloid-β Burden, and Neuronal Dysfunction in Clinical Variants of Alzheimer's Disease. *J. Alzheimers Dis.* 55, 465–471. doi:10.3233/JAD-160316

Fodero-Tavoletti, M. T., Okamura, N., Furumoto, S., Mulligan, R. S., Connor, A. R., McLean, C. A., et al. (2011). 18F-THK523: a Novel *In Vivo* Tau Imaging Ligand for Alzheimer's Disease. *Brain* 134, 1089–1100. doi:10.1093/brain/awr038

Harrison, T. M., Maass, A., Adams, J. N., Du, R., Baker, S. L., and Jagust, W. J. (2019). Tau Deposition Is Associated with Functional Isolation of the hippocampus in Aging. *Nat. Commun.* 10 (1), 4900. doi:10.1038/s41467-019-12921-z

Hashimoto, H., Kawamura, K., Igarashi, N., Takei, M., Fujishiro, T., Aihara, Y., et al. (2014). Radiosynthesis, Photoisomerization, Biodistribution, and Metabolite Analysis of 11C-PBB3 as a Clinically Useful PET Probe for Imaging of Tau Pathology. *J. Nucl. Med.* 55, 1532–1538. doi:10.2967/jnumed.114.139550

Hsiao, I.-T., Lin, K.-J., Huang, K.-L., Huang, C.-C., Chen, H.-S., Wey, S.-P., et al. (2017). Biodistribution and Radiation Dosimetry for the Tau Tracer 18F-THK-5351 in Healthy Human Subjects. *J. Nucl. Med.* 58, 1498–1503. doi:10.2967/jnumed.116.189126

Jack, C. R., Jr, Bennett, D. A., Blennow, K., Carrillo, M. C., Feldman, H. H., Frisoni, G. B., et al. (2016). A/T/N: An Unbiased Descriptive Classification Scheme for Alzheimer Disease Biomarkers. *Neurology* 87, 539–547. doi:10.1212/wnl.0000000000002923

Jack, C. R., Jr, Wiste, H. J., Schwarz, C. G., Lowe, V. J., Senjem, M. L., Vemuri, P., et al. (2018). Longitudinal Tau PET in Ageing and Alzheimer's Disease. *Brain* 141, 1517–1528. doi:10.1093/brain/awy059

Jellinger, K. A., Alafuzoff, I., Attems, J., Beach, T. G., Cairns, N. J., Crary, J. F., et al. (2015). PART, a Distinct Tauopathy, Different from Classical Sporadic Alzheimer Disease. *Acta Neuropathol.* 129, 757–762. doi:10.1007/s00401-015-1407-2

Josephs, K. A., Murray, M. E., Tosakulwong, N., Whitwell, J. L., Knopman, D. S., Machulda, M. M., et al. (2017). Tau Aggregation Influences Cognition and Hippocampal Atrophy in the Absence of Beta-Amyloid: a Clinico-Imaging-Pathological Study of Primary Age-Related Tauopathy (PART). *Acta Neuropathol.* 133, 705–715. doi:10.1007/s00401-017-1681-2

Kimura, Y., Ichise, M., Ito, H., Shimada, H., Ikoma, Y., Seki, C., et al. (2015). PET Quantification of Tau Pathology in Human Brain with 11C-PBB3. *J. Nucl. Med.* 56, 1359–1365. doi:10.2967/jnumed.115.160127

Koole, M., Lohith, T. G., Valentine, J. L., Bennacef, I., Declercq, R., Reynders, T., et al. (2020). Preclinical Safety Evaluation and Human Dosimetry of [18F]MK-6240, a Novel PET Tracer for Imaging Neurofibrillary Tangles. *Mol. Imaging Biol.* 22, 173–180. doi:10.1007/s11307-019-01367-w

Marquié, M., Normandin, M. D., Meltzer, A. C., Siao Tick Chong, M., Andrea, N. V., Antón-Fernández, A., et al. (2017). Pathological Correlations of [F-18]-AV-1451 Imaging in Non-alzheimer Tauopathies. *Ann. Neurol.* 81, 117–128. doi:10.1002/ana.24844

Marquié, M., Normandin, M. D., Vanderburg, C. R., Costantino, I. M., Bien, E. A., Rycyna, L. G., et al. (2015). Validating Novel Tau Positron Emission Tomography Tracer [F-18]-AV-1451 (T807) on Postmortem Brain Tissue. *Ann. Neurol.* 78, 787–800. doi:10.1002/ana.24517

Nedelska, Z., Josephs, K. A., Graff-Radford, J., Przybelski, S. A., Lesnick, T. G., Boeve, B. F., et al. (2019). 18 F-AV-1451 Uptake Differs between Dementia with Lewy Bodies and Posterior Cortical Atrophy. *Mov Disord.* 34, 344–352. doi:10.1002/mds.27603

Ni, R., Ji, B., Ono, M., Sahara, N., Zhang, M.-R., Aoki, I., et al. (2018). Comparative *In Vitro* and *In Vivo* Quantifications of Pathologic Tau Deposits and Their Association with Neurodegeneration in Tauopathy Mouse Models. *J. Nucl. Med.* 59 (6), 960–966. doi:10.2967/jnumed.117.201632

Ossenkoppele, R., Rabinovici, G. D., Smith, R., Cho, H., Schöll, M., Strandberg, O., et al. (2018). Discriminative Accuracy of [18F]flortaucipir Positron Emission Tomography for Alzheimer Disease vs Other Neurodegenerative Disorders. *JAMA* 320, 1151–1162. doi:10.1001/jama.2018.12917

Ossenkoppele, R., Schonhaut, D. R., Baker, S. L., O'Neil, J. P., Janabi, M., Ghosh, P. M., et al. (2015). Tau, Amyloid, and Hypometabolism in a Patient with Posterior Cortical Atrophy. *Ann. Neurol.* 77, 338–342. doi:10.1002/ana.24321

Ossenkoppele, R., Schonhaut, D. R., Schöll, M., Lockhart, S. N., Ayakta, N., Baker, S. L., et al. (2016). Tau PET Patterns Mirror Clinical and Neuroanatomical Variability in Alzheimer's Disease. *Brain* 139 (Pt 5), 1551–1567. doi:10.1093/brain/aww027

Spires-Jones, T. L., and Hyman, B. T. (2014). The Intersection of Amyloid Beta and Tau at Synapses in Alzheimer's Disease. *Neuron* 82, 756–771. doi:10.1016/j.neuron.2014.05.004

Tomlinson, B. E., Blessed, G., and Roth, M. (1970). Observations on the Brains of Demented Old People. *J. Neurol. Sci.* 11, 205–242. doi:10.1016/0022-510x(70)90063-8

Walji, A. M., Hostetler, E. D., Selnick, H., Zeng, Z., Miller, P., Bennacef, I., et al. (2016). Discovery of 6-(Fluoro-18f)-3-(1h-Pyrrolo[2,3-C]pyridin-1-Yl) isoquinolin-5-Amine ([18F]-MK-6240): A Positron Emission Tomography (PET) Imaging Agent for Quantification of Neurofibrillary Tangles (NFTs). *J. Med. Chem.* 59, 4778–4789. doi:10.1021/acs.jmedchem.6b00166

Wang, Y., Shi, Z., Zhang, N., Cai, L., Li, Y., Yang, H., et al. (2019). Spatial Patterns of Hypometabolism and Amyloid Deposition in Variants of Alzheimer's Disease Corresponding to Brain Networks: a Prospective Cohort Study. *Mol. Imaging Biol.* 21 (1), 140–148. doi:10.1007/s11307-018-1219-6

Whitwell, J. L., Graff-Radford, J., Tosakulwong, N., Weigand, S. D., Machulda, M. M., Senjem, M. L., et al. (2018). Imaging Correlations of Tau, Amyloid, Metabolism, and Atrophy in Typical and Atypical Alzheimer's Disease. *Alzheimer's Demen.* 14 (8), 1005–1014. doi:10.1016/j.jalz.2018.02.020

Yap, S. Y., Frias, B., Wren, M. C., Schöll, M., Fox, N. C., Årstad, E., et al. (2021). Discriminatory Ability of Next-Generation Tau PET Tracers for Alzheimer's Disease. *Brain* 144 (8), 2284–2290. doi:10.1093/brain/awab120

Zanotti-Fregonara, P., Lammertsma, A. A., and Innis, R. B. (2013). Suggested Pathway to Assess Radiation Safety of 18F-Labeled PET Tracers for First-In-

Human Studies. *Eur. J. Nucl. Med. Mol. Imaging* 40, 1781–1783. doi:10.1007/s00259-013-2512-x

Zhou, K., Yang, F., Li, Y., Chen, Y., Zhang, X., Zhang, J., et al. (2021). Synthesis and Evaluation of Fluorine-18 Labeled 2-Phenylquinoxaline Derivatives as Potential Tau Imaging Agents. *Mol. Pharmaceutics* 18, 1176–1195. doi:10.1021/acs.molpharmaceut.0c01078

Conflict of Interest: The authors declare that the research was conducted in the absence of any commercial or financial relationships that could be construed as a potential conflict of interest.

The reviewer ZW declared a shared parent affiliation with the author SY to the handling editor at the time of the review.

Publisher's Note: All claims expressed in this article are solely those of the authors and do not necessarily represent those of their affiliated organizations or those of the publisher, the editors, and the reviewers. Any product that may be evaluated in this article or claim that may be made by its manufacturer is not guaranteed or endorsed by the publisher.

frontiers in Bioengineering and Biotechnology

ORIGINAL RESEARCH
published: 14 February 2022
doi: 10.3389/fbioe.2022.839756

Nivolumab-DTPA-Based PD-1 Imaging Reveals Structural and Pathological Changes in Colorectal Carcinoma

Danni Li[1†], Xiao Li[1†], Jian Yang[1†], Zhang Shi[2], Lu Zhang[1], Rou Li[1], Ye Peng[1], Jiajun Liu[1] and Changjing Zuo[1]**

[1]Department of Nuclear Medicine, Shanghai Changhai Hospital, Shanghai, China, [2]Department of Radiology, Shanghai Changhai Hospital, Shanghai, China

OPEN ACCESS

Edited by:
Lu Wang,
First Affiliated Hospital of Jinan University, China

Reviewed by:
Yiran Zheng,
Soochow University, China
Honglin Jin,
Huazhong University of Science and Technology, China

***Correspondence:**
Changjing Zuo
changjing.zuo@qq.com
Jiajun Liu
ljj12286@rjh.com.cn

†These authors have contributed equally to this work and share first authorship

Specialty section:
This article was submitted to Nanobiotechnology, a section of the journal Frontiers in Bioengineering and Biotechnology

Received: 20 December 2021
Accepted: 21 January 2022
Published: 14 February 2022

Citation:
Li D, Li X, Yang J, Shi Z, Zhang L, Li R, Peng Y, Liu J and Zuo C (2022) Nivolumab-DTPA-Based PD-1 Imaging Reveals Structural and Pathological Changes in Colorectal Carcinoma. Front. Bioeng. Biotechnol. 10:839756. doi: 10.3389/fbioe.2022.839756

Programmed cell death protein 1 (PD-1) expression is considered a prognostic marker of tumor response to the immuno-blocking therapy. In this study, nivolumab was conjugated with diethylenetriamine pentaacetate (DTPA) via condensation reaction between amidogen and *p*-SCN-Bn-DTPA, which provided labeling sites for $^{99m}Tc^{4+}$ or Gd^{3+} ions. SPECT and magnetic resonance T1 weighted imaging (T_1WI) analyses were performed on mouse models of colorectal carcinoma expressing humanized PD-1 antigen. Furthermore, PD-1 expression in intestinal tracks was assessed by immunohistochemistry, and then compared with the imageological findings. Nivolumab-DTPA was synthesized with varying molar ratios and was labeled with Gd or ^{99m}Tc with a chemical purity of 96.28 ± 1.16% and good stability. In SPECT images, lesions with high ^{99m}Tc-DTPA-nivolumab uptake and relatively clear background were shown at 6 h. Thereafter, the suspected intestinal thickening in Gd-free T_1WI was observed at 2 h after the addition of Gd-DTPA-nivolumab. Notably, the results of both SPECT and T_1WI analyses were consistent with the postmortem examination and immunohistochemistry results (for linear correlation with target to non-target ratios, $R^2 = 0.8038$, $p < 0.05$). In conclusion, nivolumab-DTPA could act as a probe precursor for identifying PD-1-positive lesions, not only through integrating the advantages of immunohistochemistry and molecular imaging but also by providing a noninvasive method for monitoring systemic changes.

Keywords: programmed cell death protein 1, nivolumab, SPECT, T1-weighted imaging, colorectal carcinoma, imaging probe precursor

INTRODUCTION

Until recently, Food and Drug Administration (FDA)-approved therapeutic agents targeting the programmed cell death protein 1 (PD-1)/programmed cell death ligand 1 (PD-L1) axis have achieved impressive results in clinical immune checkpoint inhibitor (ICI) treatments, and serve as a crucial treatment for increasing cancer types, such as advanced melanoma (MM), non-small cell lung cancer (NSCLC), and colorectal carcinoma (CRC) (Constantinidou et al., 2019). Despite the encouraging advances, some adverse events have been shown to occur during ICI treatments as well. For instance, some patients respond well to the ICI treatment, while others do not respond at all. Clinical failure in

many patients is not solely due to the inability to induce immune reactivation, but rather to an imbalance between T-cell reactivation and tumor burden (Huang et al., 2017). In addition to the expanding research on immunoblocking therapy (IBT), the search for prognostic biomarkers and relevant detection methods is urgently required to effectively categorize patients who are eligible for IBT or not.

Several studies have previously demonstrated that antigen expression is a prognostic marker for the therapeutic response of PD-1/PD-L1-based IBT (Gandini et al., 2016; Herbst et al., 2016). Therefore, immunohistochemistry (IHC) assay based on needle biopsy or surgical resection is currently used as the primary method of PD-1/PD-L1 evaluation. However, due to the diversity of tumor microenvironment and the dynamic changes in PD-1/PD-L1 expression resulting from concomitant treatments (Lim et al., 2016; Thomas et al., 2019), the spatial and temporal limitations of IHC analysis lead to uncertainty in decision-making for carrying out IBT. As an alternative, molecular imaging of PD-1/PD-L1 expression could timely assist in analyzing tumor lesions and metastasis as a whole, providing reproducible and non-invasive systemic monitoring of PD-1/PD-L1 expression.

Recently, nuclear medical imaging techniques, including positron emission tomography (PET), single photon emission computed tomography (SPECT), and multimodal imaging, have been considered for assessing PD-1/PD-L1 expression of diverse tumor types (Bensch et al., 2018; Gao et al., 2020; Lv et al., 2020). In this regard, imaging probes have been found to play a key role in molecular imaging, where the specific polypeptides or antibodies are often utilized as the target molecule of probe precursor (Wei et al., 2020). It is notable that findings of quantitative analysis of PD-1/PD-L1 imaging closely correlate with IHC analysis, which further provide a more comprehensive understanding of systemic immunity, for example, ^{89}Zr-C4 PET in evaluating PD-L1 expression of NSCLC and prostate cancer (Truillet et al., 2018), ^{111}In-PDL1.3.1 SPECT in evaluating PD-L1 expression of breast cancer (Heskamp et al., 2015), and ^{89}Zr-nivolumab PET in evaluating PD-1 expression of advanced NSCLC (Niemeijer et al., 2018). Furthermore, the clinical significance of immune-related molecular imaging was demonstrated in establishing the treatment and predicting the downstream response as well. For example, Xing et al. conducted a phase I trial in patients with NSCLC, suggesting that anti-PD-L1-sdAb SPECT/CT using ^{99m}Tc-NM-01 could be used to closely monitor changes in PD-L1 expression during PD-L1 immunotherapy (Xing et al., 2019). By imaging NSCLC, advanced bladder cancer, and triple-negative breast cancer with ^{89}Zr-Atezolizumab PET, heterogeneity varying within and among lesions, patients, and tumor types was demonstrated, and thus it formed the basis for establishing the clinical treatment scheme, and as a result, the predictive value of molecular imaging was higher than that of IHC or RNA-sequencing-based predictive biomarkers (Bensch et al., 2018).

Considering the clinical needs for combined therapy, especially when PD-1/PD-L1 IBT is combined with surgery or stereotactic radiotherapy (SRT), the need of structural imaging was raised. Therefore, in such cases, functional magnetic resonance imaging (MRI) is considered to provide more accurate anatomical information. For T1 weighted imaging (T_1WI), the accurate outlining of antigen-positive lesions can be achieved by analyzing before-and-after images upon Gadolinium (Gd)-based probe injection. Accordingly, the multiparametric imaging and its superior soft tissue contrast resolution, MRI is best suited for evaluation of the abdomen, and higher resolution with more details can be achieved considering the multiple parameters of MRI scans. Above all, functional imaging and anatomical imaging developed on the basis of specific antibodies have promising application prospects in PD-1 evaluation and potentially can provide further benefits for IBT.

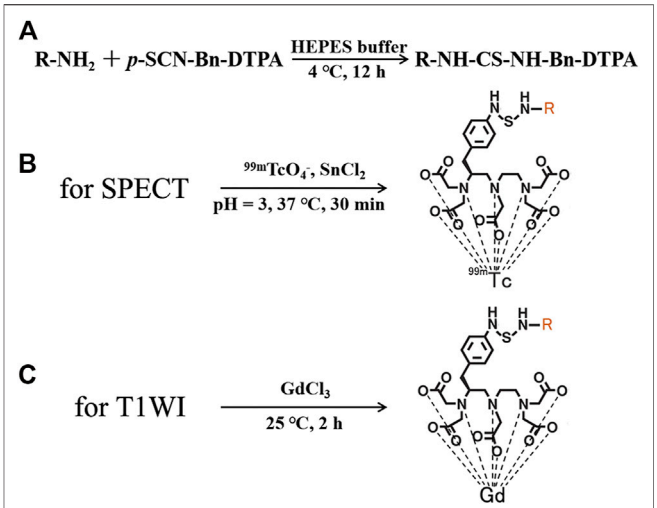

FIGURE 1 | (A) Synthesis of nivolumab-DTPA, Structures of **(B)** ^{99m}Tc-DTPA-nivolumab, and **(C)** Gd-DTPA-nivolumab.

As a clinically approved PD-1 antibody, nivolumab exhibits high affinity (K_d = 2.6 nM) and specificity for PD-1 antigen (Wang et al., 2014). In order to further expand the application of functional PD-1 imaging in the clinical research, nivolumab-DTPA was developed as an imaging probe precursor suitable for qualitative PD-1 assessment using Gd-based T_1WI, and quantitative PD-1 assessment using Tc-99 m-based SPECT (**Figure 1**). Diagnostic values of the integrated functional imaging techniques were evaluated using the mouse models expressing humanized PD-1 antigen and bearing *in situ* colorectal carcinoma, which are necessary for clinical research and for a more comprehensive diagnosis based on combined therapy of PD-1 IBT and SRT.

MATERIALS AND METHODS

Material and Reagents

Nivolumab was purchased from SelleckChem, and *p*-SCN-Bn-DTPA was purchased from Macrocyclics, Inc., Plano, Texas. ^{18}F-FDG and $^{99m}TcO_4^-$ were purchased from Xinke Pharmaceutical Ltd., Shanghai, China. Gadolinium (III) chloride hexahydrate [$GdCl_3.6(H_2O)$] and stannous chloride

[$SnCl_2.2(H_2O)$] were purchased from Adamas, Inc., CA, United States. Dialysis bags were purchased from Membrane Solutions, LLC, Shanghai, China. Other chemicals were purchased from Sigma-Aldrich China, Inc., Shanghai, China unless otherwise stated.

Animals

Humanized PD-1 over-expressing (line name: C57BL/6J-Pdcd1$^{em1(hPDCD1)/Smoc}$) female mice (6-weeks-old, 18–22 g) were purchased from Shanghai Model Organisms Center, Inc., Shanghai, China. Mice were raised under specific pathogen-free conditions. All the animal experiments were approved by the Ethics Committee of Shanghai Changhai Hospital and were conducted using the guidelines of ethical principles governing the animal welfare, rearing, and experimentation.

Synthesis of Tracers

Nivolumab-DTPA was synthesized by conjugating nivolumab with the bifunctional chelator (BFC) *p*-SCN-Bn-DTPA. As shown in **Figure 1**, the isothiocyano group of *p*-SCN-Bn-DTPA was reacted with the amino group of nivolumab to form nivolumab-DTPA. In detail, *p*-SCN-Bn-DTPA was dissolved in DMSO at a concentration of 10 mg/ml. Around 500 μg of nivolumab (145 kDa) was dissolved in HEPES buffer and the pH was adjusted to 8. Thereafter, BFC was added in the solution at 4, 20, or 100 times more than nivolumab. Reaction was carried out at 4°C for 12 h. The excess *p*-SCN-Bn-DTPA was removed by using a 50 kDa millipore ultrafiltration tube.

For MRI probe preparation, 500 μg nivolumab-DTPA (nivolumab content) in PBS was reacted with $GdCl_3$ at 100 M times more than nivolumab at 25°C for 2 h. Free Gd^{3+} ions were removed using a dialysis bag. In detail, a dialysis bag with a molecular weight cut-off of 20 kDa was used to seal the reaction system, and then placed in a beaker with distilled water. Magnetic stirring was used to promote ion exchange. Distilled water was changed every 4 h, and this operation was repeated 3 times to obtain the purified Gd-DTPA-nivolumab. For the measurement of nivolumab-DTPA with different DTPA ratios, 200 μg Gd-DTPA-nivolumab (nivolumab content) was ionized and dissolved in 100 μl, and then diluted to $1/10^4$ with distilled water. Around 100 μl solution was used to test the concentration of Gd^{3+} using inductively coupled plasma-mass spectrometry (ICP-MS; Perkin Elmer NexION 300D).

For SPECT probe preparation, newly prepared 111 MBq $^{99m}TcO_4^-$ was reduced by 20 μl $SnCl_2$ (1 mg/ml, in HCl with pH = 3), and then was used to label 100 μg of nivolumab-DTPA at 37°C for 30 min. Radiochemical purity (RCP) was determined using a silica gel plate (solid phase) and acetone (mobile phase) system. Purified ^{99m}Tc-DTPA-nivolumab was dissolved in 0.01 M PBS or 1% fetal bovine serum for the *in vitro* stability tests. The labeling rate and stability after 6 h at 37°C were measured by thin-layer chromatography (TLC) with a radioactive detector.

In vitro Assay

Splenocytes were isolated from the spleens obtained from humanized PD-1 over-expressing mice following standard protocol. Referring to our previous labeling protocol (Li et al., 2018), ^{125}I labeled Nivolumab and Nivolumab-DTPA, respectively. To perform co-culture, ^{125}I-Nivolumab and ^{125}I-Nivolumab-DTPA (0.37 MBq/μg) were added to the freshly isolated splenocytes (1×10^6 cells) grown in 6-well plates, respectively. After incubation for 12 h at 4°C, cells were collected after rinsing three times with PBS. ^{125}I radioactivity was determined in a gamma counter to evaluate their binding efficiency to PD-1.

Single Photon Emission Computed Tomography/CT and MR Imaging

Four *in situ* CRC mouse models (highly expressed human PD-1 antigen) prepared using azoxymethane (AOM)/dextran sulfate sodium (DSS) chemical induction were used in this study. According to a previous study (Tanaka et al., 2003), AOM (10 mg/kg) was injected intraperitoneally. Seven days later, three cycles of feeding with water (2% DSS included) for 7 days, followed by pure water feeding for 17 days was followed. Thereafter, normal diet was followed, which lasted for another 50 days. Four mice without significant weight difference were randomly selected, and fluorine-18 fluorodeoxyglucose (^{18}F-FDG) micro-PET/CT was performed to verify the successful preparation of the *in situ* CRC model. One of the above mice was sacrificed to evaluate the PD-1 expression of the observed foci by IHC analysis, and the other three were used for the subsequent imaging assays.

The imaging evaluation was as follows: 1) ^{99m}Tc-DTPA-nivolumab (11.1 MBq/10 μg) was injected through the tail vein, and SPECT scan was performed 2 and 6 h after the injection. After an interval of 48 h, 2) T_1WI was observed 2 h after the injection of 100 μg Gd-DTPA-nivolumab through the tail vein and was compared with the intestinal morphology and signals of the pre-injection image.

For SPECT/CT imaging, 50 μl lidocaine (3 wt%) was intraperitoneally injected before each scan. SPECT/CT (Symbia T16, Siemens, Erlangen, Germany) scans were performed to evaluate the distribution and metabolism of tracer. Scan parameters used were as follows: low-energy university collimator, matrix, 128 × 128; zoom, 2.67; energy peak, 140 keV; window width, 20%; and frames, 60 s/frame. CT scan: tube voltage, 130 kV; tube current, 35 mA; and slice thickness, 1 mm. For ^{99m}Tc-nivolumab SPECT/CT images, suspicious tumor lesions with high tracer uptake were outlined, and radioactivity of both lesions and whole body were recorded.

For MRI scans, a Siemens scanner (Magnetom Trio 3.0T, Siemens Medical Solutions, Erlangen, Germany) with a hand coil was used. The scan parameters were as follows: for T_1WI, TE, 13.8 ms; TR, 4,000 ms; slice space, 1 mm; slice thickness, 2 mm; FOV, 120 mm × 120 mm; matrix, 128 × 128; number of excitations, 1. For image reading of Gd-nivolumab T_1WI, the anatomy structure of intestinal tracts was observed, and the images were compared with that of Gd-free T_1WI to determine the signal enhancement resulting from tracer uptake.

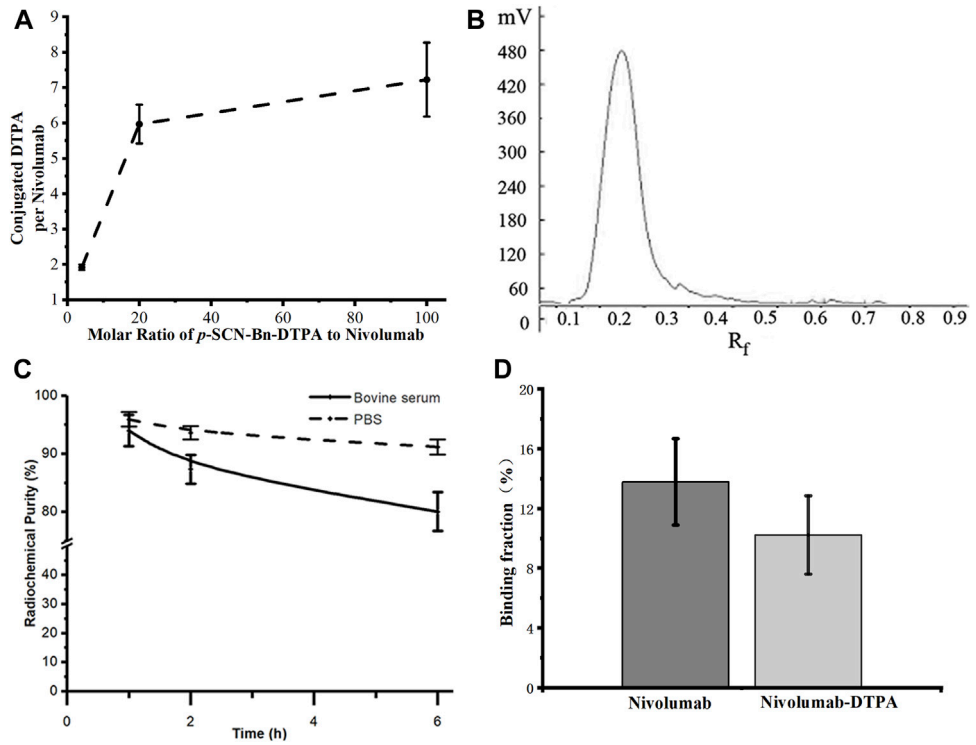

FIGURE 2 | (A) Quantification of conjugated DTPA to nivolumab, **(B)** radioactive TLC spectrum of purified ^{99m}Tc-labeled nivolumab, **(C)** the *in vitro* stability of ^{99m}Tc-DTPA-nivolumab in 0.01 M PBS and fetal bovine serum concentration of 1% (w/w). **(D)** Validation of *in vitro* binding efficiency of Nivolumab and Nivolumab-DTPA to PD-1.

After the acquisition of MRI, the mice were sacrificed to record the focal anatomy and evaluate PD-1 expression using IHC analysis. ImageJ software (NIH) was used to quantify positively stained areas of immunostaining images. SPECT and T_1WI results were compared with that of IHC and visual observation to evaluate the diagnostic performance.

Quantification and Statistical Analysis

Data, including the RCPs and biodistribution, were presented as the mean ± SD of at least N = 3. The related-coefficient test was used for data comparisons. Differences with *p*-values less than 0.05 were considered as statistically significant. Data were analyzed using SPSS v.23.0 for Windows (SPSS Inc., Chicago, IL, United States).

RESULTS

Conjugation Efficiency of Nivolumab and *p*-SCN-Bn-DTPA

Due to the 1:1 correspondence between Gd and DTPA in Gd-DTPA-nivolumab, the molar ratio of DTPA to nivolumab was indirectly quantified through the quantification of labeled Gd on nivolumab-DTPA. For this, Gd-DTPA-nivolumab was dissociated and the free Gd was quantified using ICP-MS. The ratios of conjugated DTPA to nivolumab were 1.92 ± 0.08, 5.97 ± 0.55, and 7.23 ± 1.05, when the molar ratios of *p*-SCN-Bn-DTPA to nivolumab were 4, 20, and 100, respectively (**Figure 2A**). Considering that the conjugated DTPA reached the upper limit when the ratio of *p*-SCN-Bn-DTPA to nivolumab was 100, the ratio of 20 was used in the following steps as 5.97 ± 0.55 DTPA conjugated to per nivolumab. Additionally, a free Gd concentration below the ppm level provided *in vitro* stability to Gd-DTPA-nivolumab after 6 h at 37°C in 0.01 M PBS or in 1% fetal bovine serum.

Radiochemical Purity and Stability of ^{99m}Tc-DTPA-Nivolumab and Specific Binding Characteristics

The radiochemical purity of ^{99m}Tc-DTPA-nivolumab was estimated as 96.28 ± 1.16% after purification (**Figure 2B**). *In vitro* stability studies at 37°C showed that 91.15 ± 1.26% stability was maintained after 6 h of incubation in 0.01 M PBS and 80.05 ± 3.35% stability was maintained after 6 h of incubation in 1% fetal bovine serum (**Figure 2C**). As shown in **Figure 2D**, the cell binding ratio of ^{125}I-Nivolumab and ^{125}I-Nivolumab-DTPA to PD-1 was 13.78 ± 2.90% and 10.22 ± 2.62%, respectively ($p > 0.05$). The similar PD-1-binding efficiency of Nivolumab and Nivolumab-DTPA indicated that conjugating of DTPA does not affect targeting of Nivolumab to PD-1 *in vitro*.

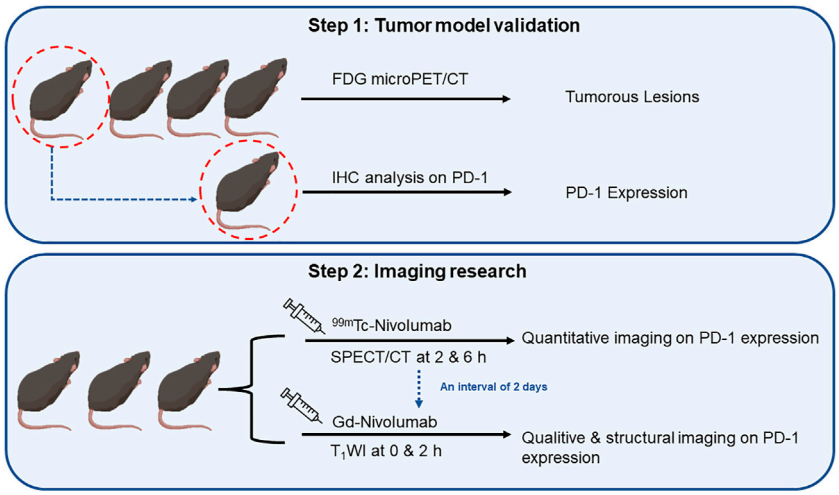

FIGURE 3 | The flowchart of research on quantitative and qualitative PD-1 imaging, including the validation of tumor model mice and sequence of SPECT/CT and T_1WI.

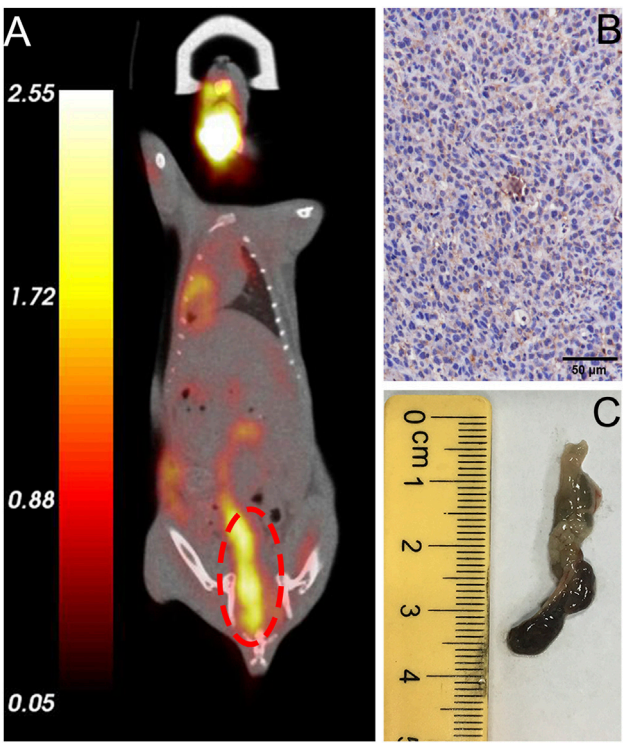

FIGURE 4 | Validation of typical *in situ* colon tumor mice. **(A)** FDG micro-PET/CT image of a tumor mouse model showing a lesion at the end of the colon (marked in red circle), **(B)** IHC analysis revealed high expression of humanized PD-1, **(C)** Specimen of colorectal carcinoma that exhibited high FDG uptake.

Validation of the Tumor Model Mice With PD-1-Positive CRC

All mice were validated using FDG microPET/CT scan, and one of them were sacrificed for evaluation of PD-1 expression by IHC analysis (step1 in **Figure 3**). For lesions detected on FDG PET/CT scan, hyperemia, edema, and nodules with high PD-1 expression were found in the corresponding intestinal tracts. The locally high uptake of ^{18}F-FDG and PD-1-expressed tumor tissues indicated the successful establishment of animal models. Before subjecting to further imaging analysis (step2 in **Figure 3**), all mice were tested through FDG PET/CT scan, and the ones who fulfilled the criteria of locally high uptake of FDG were chosen. Approximately 70% (7/10) of mice developed with one or more primary lesions of colorectal carcinomas, and the distribution of lesions was random. A typical FDG PET/CT scan image of the mouse model and corresponding PD-1 IHC and postmortem examinations are shown in **Figure 4**.

Qualitative PD-1 Imaging of the Tumor Model Mice

Nivolumab-DTPA shared the same *in vivo* distribution. A series of typical imageological findings were presented in **Figure 5**. In SPECT/CT images, a focus with high ^{99m}Tc-DTPA-nivolumab uptake was shown in the right colon at 6 h post injection, while a relatively clear background appeared without indicating any unusual high uptake. Conversely, SPECT images at 2 h post injection presented a high background in untargeted organs, such as the liver, heart, and abdomen, which shielding the colorectal lesions. In MR T_1W images, suspected thickening of the intestinal wall in the right intestine was displayed. Furthermore, an enhanced scan image was acquired at 2 h after the injection of Gd-DTPA-nivolumab, which revealed a marked signal enhancement of the suspected thickening of the intestinal wall. Based on these imageological findings, a clear description of intestinal lesions with high PD-1 expression was obtained.

The findings based on Gd-DTPA-nivolumab T_1WI and ^{99m}Tc-DTPA-nivolumab SPECT/CT were found to be consistent with the postmortem examinations, in which

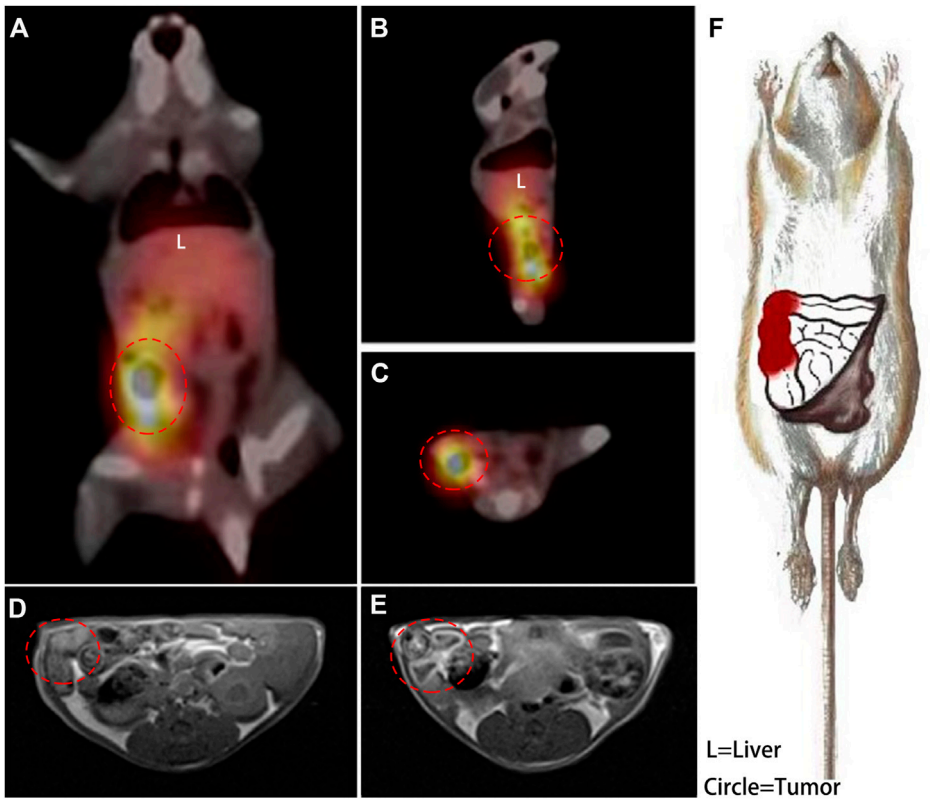

FIGURE 5 | A coronal plane **(A)**, sagittal plane **(B)** and cross-section **(C)** SPECT images acquired at 6 h post injection of ^{99m}Tc-DTPA-nivolumab, and the right colon with high tracer uptake is circled. In transverse T_1WI **(D)**, the suspected thickened intestine is circled, and the enhanced intestinal wall is circled in an enhanced scan acquired at 2 h post injection of Gd-DTPA-nivolumab **(E)**. A detailed description of lesions with high PD-1 (in red) was drawn based on these functional imaging findings **(F)**.

congestion and necrosis of the intestinal lesion were detected. Hematoxylin-eosin (HE) staining of the intestinal tumor tissues in mice demonstrated that the heteromorphism of the cancer cells was evident, and the nucleoli were clearly observed. Further, it also indicated that the cancer cells grew densely. Quantitative analysis of the images and IHC are summarized next.

Quantitative PD-1 Imaging of the Tumor Model Mice

Quantitative PD-1 imaging mainly relied on the ^{99m}Tc-DTPA-nivolumab SPECT/CT, where the tumor to liver ratios of tracer uptake varied from 1.55 to 3.11. IHC results indicated that the intestinal tumor exhibited high PD-1 expression, with 17.05–42.62% positively stained areas, and that the PD-1 area of IHC staining linearly correlated with target to non-target (T/NT) ratios with R^2 = 0.8038 ($p < 0.05$). This linear dependence exists in both lesions and normal tissues with T/NT values less than 1 (**Figure 6**).

DISCUSSION

In our previous work, we evaluated the pharmacokinetic properties of I-125 labeled nivolumab using the nude mouse xenograft model of colorectal carcinoma. Since only the B and NK cells were used, we could prove PD-1 targeting partially (Li et al., 2018). In this study, the tumor growth and angiogenesis of *in situ* tumor models were almost achieved in the humanized mouse cancer model, and therefore, the results obtained for systemic uptake of antibodies-based tracers were more convincing.

Being different from the nuclear medicine imaging, the probe precursor of nivolumab-DTPA could be successfully and stably labeled with Tc-99m and Gd, thereby proving to be suitable for functional SPECT and structural T_1WI MRI analyses to further evaluate PD-1 expression and to outline the fine anatomies with high PD-1 expression. Utilizing the additive information of T_1WI, tumorous lesions could easily be distinguished from others with high PD-1 expression, facilitating the establishment of therapies, such as the combined therapy involving stereotactic radiotherapy and PD-1 blockade therapy. Nivolumab-DTPA was developed on the basis of a commercial IgG antibody with a stable structure and bio-specificity to PD-1. This method has been efficiently utilized in the development of PD-L1 imaging probe ^{89}Zr-atezolizumab, which has shown significant clinical value (Bensch et al., 2018).

As **Figure 5** shown, a hypointensity region was depicted on the right colorectal area on T_1WI (**Figure 5D**), and an obvious hyperintensity signal region was shown in the same colorectal area on contrast T1W image (**Figure 5E**). It indicted that the

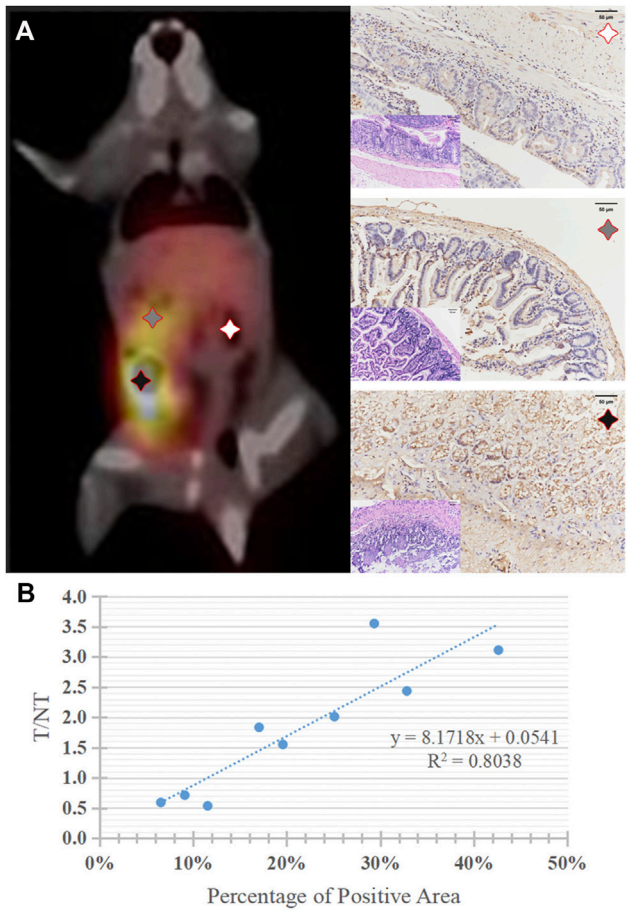

FIGURE 6 | (A) A typical ^{99m}Tc-DTPA-nivolumab SPECT/CT image of tumor mouse model, and corresponding histopathology (HE staining, × 200) and PD-1positive expression of lesions with high, medium, and very low ^{99m}Tc-DTPA-nivolumab uptake, brownish yellow staining was observed on the surface of tumor cells (IHC, × 200). **(B)** The correlation of quantitative imaging (reflected by T/NT values) and IHC (reflected by the percentage of PD-1 positive areas).

enhancement region could be the high PD-1 expression in early imaging at 2 h. Meanwhile, although 6 h assessment was needed for a clear background, SPECT was used for the quantification and whole-body assessment. When compared with FDG PET/CT, ^{99m}Tc-DTPA-nivolumab SPECT/CT integrated with Gd-DTPA-nivolumab T_1WI focused on pathological changes, potentially decreasing the false-positive diagnosis resulting from inflammation. In clinical practice, imaging modalities can be selected on the basis of clinical needs. The limitation of this study is that the T_1W sequence that has been used does not appear to be fat suppressed, which makes it difficult to assess the enhancement effect. The use of a 3D T_1W sequence may be preferable in future studies.

CONCLUSION

In this study, it was demonstrated that nivolumab-DTPA, as an imaging probe platform, could be used in qualitative imaging by Gd-based T_1WI, and quantitative imaging by Tc-99 m-based SPECT. Also, we believe that integrated functional imaging may be helpful in accurately evaluating the systemic expression of PD-1 in colorectal carcinoma and other cancer types. Moreover, translational values of the antibody-coupled imaging precursor were indicated in diagnosing microscopic cancers and tracking metastasis through PD-1 expression in this study.

DATA AVAILABILITY STATEMENT

The original contributions presented in the study are included in the article/supplementary files, further inquiries can be directed to the corresponding author.

ETHICS STATEMENT

The animal study was reviewed and approved by Ethics Committee of Shanghai Changhai Hospital.

AUTHOR CONTRIBUTIONS

DL, XL and JY were responsible for conceptualization of the study and chemical synthesis; DL, ZS, LZ, RL and YP carried out the animal studies, imaging, and *ex vivo* analysis; JL and CZ provided the guidance and supervision for the execution of experiments; DL, XL, and CZ prepared the draft of the manuscript. All the authors have read and agreed to the final version of the manuscript.

FUNDING

This work was funded by the National Natural Science Foundation of China (81471714, 81871390, 81701761) and Youth research plan supported by Shanghai Changhai hospital (2018QNA006).

REFERENCES

Bensch, F., van der Veen, E. L., Lub-de Hooge, M. N., Jorritsma-Smit, A., Boellaard, R., Kok, I. C., et al. (2018). 89Zr-Atezolizumab Imaging as a Non-invasive Approach to Assess Clinical Response to PD-L1 Blockade in Cancer. *Nat. Med.* 24, 1852–1858. doi:10.1038/s41591-018-0255-8

Constantinidou, A., Alifieris, C., and Trafalis, D. T. (2019). Targeting Programmed Cell Death -1 (PD-1) and Ligand (PD-L1): A New Era in Cancer Active Immunotherapy. *Pharmacol. Ther.* 194, 84–106. doi:10.1016/j.pharmthera.2018.09.008

Gandini, S., Massi, D., and Mandalà, M. (2016). PD-L1 Expression in Cancer Patients Receiving Anti PD-1/PD-L1 Antibodies: A Systematic Review and Meta-Analysis. *Crit. Rev. Oncology/Hematology* 100, 88–98. doi:10.1016/j.critrevonc.2016.02.001

Gao, H., Wu, Y., Shi, J., Zhang, X., Liu, T., Hu, B., et al. (2020). Nuclear Imaging-Guided PD-L1 Blockade Therapy Increases Effectiveness of Cancer Immunotherapy. *J. Immunother. Cancer* 8, e001156. doi:10.1136/jitc-2020-001156

Herbst, R. S., Baas, P., Kim, D.-W., Felip, E., Pérez-Gracia, J. L., Han, J.-Y., et al. (2016). Pembrolizumab versus Docetaxel for Previously Treated, PD-L1-Positive, Advanced Non-small-cell Lung Cancer (KEYNOTE-010): A Randomised Controlled Trial. *The Lancet* 387, 1540–1550. doi:10.1016/S0140-6736(15)01281-7

Heskamp, S., Hobo, W., Molkenboer-Kuenen, J. D. M., Olive, D., Oyen, W. J. G., Dolstra, H., et al. (2015). Noninvasive Imaging of Tumor PD-L1 Expression Using Radiolabeled Anti-PD-L1 Antibodies. *Cancer Res.* 75, 2928–2936. doi:10.1158/0008-5472.CAN-14-3477

Huang, A. C., Postow, M. A., Orlowski, R. J., Mick, R., Bengsch, B., Manne, S., et al. (2017). T-cell Invigoration to Tumour Burden Ratio Associated with Anti-PD-1 Response. *Nature* 545, 60–65. doi:10.1038/nature22079

Li, D., Wang, C., Zhang, D., Peng, Y., Ren, S., Li, X., et al. (2018). Preliminary Application of 125I-Nivolumab to Detect PD-1 Expression in colon Cancer via SPECT. *J. Radioanal. Nucl. Chem.* 318, 1237–1242. doi:10.1007/s10967-018-6124-6

Lim, S. H., Hong, M., Ahn, S., Choi, Y.-L., Kim, K.-M., Oh, D., et al. (2016). Changes in Tumour Expression of Programmed Death-Ligand 1 after Neoadjuvant Concurrent Chemoradiotherapy in Patients with Squamous Oesophageal Cancer. *Eur. J. Cancer* 52, 1–9. doi:10.1016/j.ejca.2015.09.019

Lv, G., Sun, X., Qiu, L., Sun, Y., Li, K., Liu, Q., et al. (2020). PET Imaging of Tumor PD-L1 Expression with a Highly Specific Nonblocking Single-Domain Antibody. *J. Nucl. Med.* 61, 117–122. doi:10.2967/jnumed.119.226712

Niemeijer, A. N., Leung, D., Huisman, M. C., Bahce, I., Hoekstra, O. S., van Dongen, G. a. M. S., et al. (2018). Whole Body PD-1 and PD-L1 Positron Emission Tomography in Patients with Non-small-cell Lung Cancer. *Nat. Commun.* 9, 4664. doi:10.1038/s41467-018-07131-y

Tanaka, T., Kohno, H., Suzuki, R., Yamada, Y., Sugie, S., and Mori, H. (2003). A Novel Inflammation-Related Mouse Colon Carcinogenesis Model Induced by Azoxymethane and Dextran Sodium Sulfate. *Cancer Sci.* 94, 965–973. doi:10.1111/j.1349-7006.2003.tb01386.x

Thomas, A., Vilimas, R., Trindade, C., Erwin-Cohen, R., Roper, N., Xi, L., et al. (2019). Durvalumab in Combination with Olaparib in Patients with Relapsed SCLC: Results from a Phase II Study. *J. Thorac. Oncol.* 14, 1447–1457. doi:10.1016/j.jtho.2019.04.026

Truillet, C., Oh, H. L. J., Yeo, S. P., Lee, C.-Y., Huynh, L. T., Wei, J., et al. (2018). Imaging PD-L1 Expression with ImmunoPET. *Bioconjug. Chem.* 29, 96–103. doi:10.1021/acs.bioconjchem.7b00631

Wang, C., Thudium, K. B., Han, M., Wang, X.-T., Huang, H., Feingersh, D., et al. (2014). *In Vitro* Characterization of the Anti-PD-1 Antibody Nivolumab, Bms-936558, and *In Vivo* Toxicology in Non-human Primates. *Cancer Immunol. Res.* 2, 846–856. doi:10.1158/2326-6066.CIR-14-0040

Wei, W., Rosenkrans, Z. T., Liu, J., Huang, G., Luo, Q.-Y., and Cai, W. (2020). ImmunoPET: Concept, Design, and Applications. *Chem. Rev.* 120, 3787–3851. doi:10.1021/acs.chemrev.9b00738

Xing, Y., Chand, G., Liu, C., Cook, G. J. R., O'Doherty, J., Zhao, L., et al. (2019). Early Phase I Study of a 99mTc-Labeled Anti-programmed Death Ligand-1 (PD-L1) Single-Domain Antibody in SPECT/CT Assessment of PD-L1 Expression in Non-small Cell Lung Cancer. *J. Nucl. Med.* 60, 1213–1220. doi:10.2967/jnumed.118.224170

Conflict of Interest: The authors declare that the research was conducted in the absence of any commercial or financial relationships that could be construed as a potential conflict of interest.

Publisher's Note: All claims expressed in this article are solely those of the authors and do not necessarily represent those of their affiliated organizations, or those of the publisher, the editors, and the reviewers. Any product that may be evaluated in this article, or claim that may be made by its manufacturer, is not guaranteed or endorsed by the publisher.

frontiers in Bioengineering and Biotechnology

ORIGINAL RESEARCH
published: 23 February 2022
doi: 10.3389/fbioe.2022.812277

Integrin α6-Targeted Molecular Imaging of Central Nervous System Leukemia in Mice

Wenbiao Zhang[1,2†], Yongjiang Li[2,3†], Guanjun Chen[2,4†], Xiaochun Yang[3], Junfeng Hu[3], Xiaofei Zhang[2,3], Guokai Feng[2]* and Hua Wang[4]**

[1]Department of Medical Imaging, Sun Yat-sen University Cancer Center, Guangzhou, China, [2]State Key Laboratory of Oncology in South China, Collaborative Innovation Center for Cancer Medicine, Sun Yat-sen University Cancer Center, Guangzhou, China, [3]Department of Nuclear Medicine, Sun Yat-sen University Cancer Center, Guangzhou, China, [4]Department of Hematological Oncology, Sun Yat-sen University Cancer Center, Guangzhou, China

OPEN ACCESS

Edited by:
Gianni Ciofani,
Italian Institute of Technology, Italy

Reviewed by:
Wen Shi,
University of Nebraska Medical Center, United States
Jianguo Lin,
Jiangsu Institute of Nuclear Medicine, China
Yu Chunjing,
Affiliated Hospital of Jiangnan University, China

***Correspondence:**
Xiaofei Zhang
zhangxf1@sysucc.org.cn
Guokai Feng
fengguok@sysucc.org.cn
Hua Wang
wanghua@sysucc.org.cn

†These authors have contributed equally to this work

Specialty section:
This article was submitted to Nanobiotechnology, a section of the journal Frontiers in Bioengineering and Biotechnology

Received: 10 November 2021
Accepted: 17 January 2022
Published: 23 February 2022

Citation:
Zhang W, Li Y, Chen G, Yang X, Hu J, Zhang X, Feng G and Wang H (2022) Integrin α6-Targeted Molecular Imaging of Central Nervous System Leukemia in Mice. Front. Bioeng. Biotechnol. 10:812277. doi: 10.3389/fbioe.2022.812277

Central nervous system leukemia (CNS-L) is caused by leukemic cells infiltrating into the meninges or brain parenchyma and remains the main reason for disease relapse. Currently, it is hard to detect CNS-L accurately by clinically available imaging models due to the relatively low amount of tumor cells, confined blood supply, and the inferior glucose metabolism intensity. Recently, integrin α6-laminin interactions have been identified to mediate CNS-L, which suggests that integrin α6 may be a promising molecular imaging target for the detection of CNS-L. The acute lymphoblastic leukemia (ALL) cell line NALM6 stabled and transfected with luciferase was used to establish the CNS-L mouse model. CNS-L-bearing mice were monitored and confirmed by bioluminescence imaging. Three of our previously developed integrin α6-targeted peptide-based molecular imaging agents, Cy5-S5 for near-infrared fluorescence (NIRF), Gd-S5 for magnetic resonance (MR), and ^{18}F-S5 for positron emission tomography (PET) imaging, were employed for the molecular imaging of these CNS-L-bearing mice. Bioluminescence imaging showed a local intensive signal in the heads among CNS-L-bearing mice; meanwhile, Cy5-S5/NIRF imaging produced intensive fluorescence intensity in the same head regions. Moreover, Gd-S5/MR imaging generated superior MR signal enhancement at the site of meninges, which were located between the skull bone and brain parenchyma. Comparatively, MR imaging with the clinically available MR enhancer Gd-DTPA did not produce the distinguishable MR signal in the same head regions. Additionally, ^{18}F-S5/PET imaging also generated focal radio-concentration at the same head regions, which generated nearly 5-times tumor-to-background ratio compared to the clinically available PET radiotracer ^{18}F-FDG. Finally, pathological examination identified layer-displayed leukemic cells in the superficial part of the brain parenchyma tissue, and immunohistochemical staining confirmed the overexpression of the integrin α6 within the lesion. These findings suggest the potential application of these integrin α6-targeted molecular imaging agents for the accurate detection of CNS-L.

Keywords: leukemia, molecular imaging, integrin α6, positron emission tomography, central nervous system leukemia

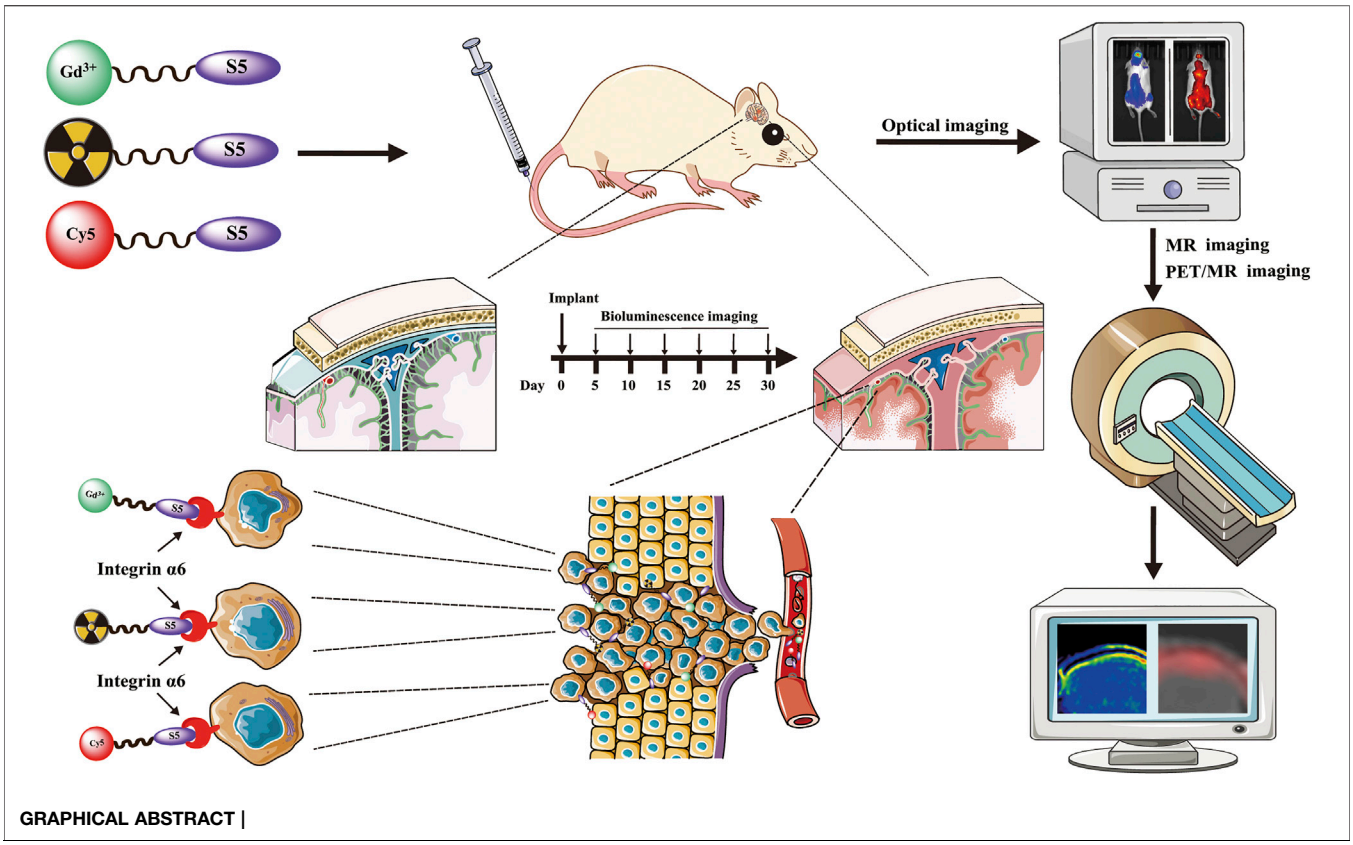

GRAPHICAL ABSTRACT |

INTRODUCTION

Acute lymphoblastic leukemia (ALL) is a malignant proliferation of lymphocytes that could invade the bone marrow, blood, and extramedullary tissues or organs, with an estimated incidence of about 157/100,000 and a distinctive prevalence in children, especially in those at 1–4 years old (Siegel et al., 2019; Malard and Mohty, 2020). About 80–90% patients could achieve a complete response after multiagent chemotherapy. However, central nervous system involvement of ALL, caused by leukemic cells infiltrating into the meninges or brain parenchyma, which is also called central nervous system leukemia (CNS-L), remains the main reason for disease relapse during the remission period. Because most chemotherapeutic drugs could not penetrate the blood–brain barrier, leukemic cells hidden in the central nervous system could not be effectively eliminated and become the origin of extramedullary leukemia recurrence (Pinnix et al., 2018; Zhang C et al., 2020). Nevertheless, accurate diagnosis of the central nervous system (CNS) involvement is a major clinical challenge that commonly leads to delayed or excessive treatment (Frishman-Levy and Izraeli, 2017; Jin et al., 2018). Due to the diagnosis insufficiency, prophylactic intrathecal chemotherapy (methotrexate in most regimens) is routinely administered for all patients in the clinical setting regardless of their CNS status, and chemotherapy-induced CNS toxicity always accompanied numerous adverse clinical manifestations including impaired consciousness, focal deficits, seizures, and headaches (Vagace et al., 2012). In addition, patients evaluated at a high risk of CNS infiltration routinely received additional cranial irradiation, which could further exacerbate neurocognitive impairment and the risk of secondary malignancies (Zhou et al., 2020).

The current gold standard for assessing CNS-L is pathological detection of leukemic cells in the cerebrospinal fluid through lumbar puncture (Bürger et al., 2003). However, the examination method has a relatively high false-negative rate, and the positivity is hysteretic than the primary CNS involvement, which highlights the urgent need for novel diagnostic methods. New strategies aimed at improving the diagnostic sensitivity of cerebrospinal fluid examination by qPCR or flow cytometry encountered methodological challenges (Yousafzai et al., 2019; Thastrup et al., 2020). Imaging diagnosis by detecting CNS lesions could be more district and intuitive; however, conventional imaging examinations including enhanced computerized tomography (CT), magnetic resonance imaging (MRI), or ^{18}F-FDG positron emission tomography (PET) showed limited ability in detecting CNS-L lesions because of a relatively low amount of tumor cells, confined blood supply, and inferior glucose metabolism intensity compared with other solid tumor lesions (Ranta et al., 2017a; Ranta et al., 2017b). Based on the premises, the development of a specific molecular probe for imaging could provide a novel way for the targeted imaging of CNS-L.

Integrins are heterodimeric transmembrane receptors consisting of α and β subunits, each with a single-pass transmembrane domain and a typically short cytoplasmic domain (Erdreich-Epstein et al., 2005; Zhu et al., 2007). Integrin α6 is encoded by the ITGA6 gene and dimerizes with integrin β1 or β4 to form integrin α6β1 and α6β4 (Takada et al., 2007). Integrin α6 normally expresses on the cell surface and acts as the mediator of intracellular and extracellular matrix adhesion (Krebsbach and Villa-Diaz, 2017). Numerous studies have revealed that integrin α6 was highly expressed in tumor cells of ALL patients and the corresponding cell lines (Blase et al., 1996). According to the GEPIA database, ITGA6 was significantly overexpressed in leukemia cells than the paired normal blood cells and the brain tissues (http://gepia.cancer-pku.cn/). Recent studies have found that ALL chemoresistance was dependent on ALL cells adhering to the stroma through the adhesion of integrin α6, and its expression mediated the invasion to the CNS tissues *via* neuromigration pathways (Yao et al., 2018; Gang et al., 2020; Lenk et al., 2020). Thus, integrin α6 could serve as a potential molecular target for the imaging of CNS-L lesions.

In our previous study, we have identified a peptide CRWYDENAC (dubbed RWY) that could bind specifically to integrin α6 by phage display technology (Feng G et al., 2019). We further translated the RWY peptide into an integrin α6-targeted PET probe and MRI probe that have been successfully applied for tumor imaging of the integrin α6 expression (Feng GK et al., 2019; Xiao et al., 2019; Zhang Y et al., 2020; Gao et al., 2020). Recently, our group improved the characteristics of the peptide by alanine scanning and obtained a novel integrin α6-targeting peptide CRWYDANAC (dubbed S5) which exhibited a higher specificity and affinity to integrin α6 (Mei et al., 2020; Lin et al., 2021). On these bases, we further developed the targeted molecular imaging probes for near-infrared fluorescence (NIRF) imaging, MRI, and PET based on the S5 peptide, which is called Cy5-S5, Gd-S5, and ^{18}F-S5 in short. In this study, the affinity of the synthesized S5 peptide to ALL cell lines was verified, and the imaging of CNS-L mouse models using NIRF, MRI, and PET scanners was conducted to test the imaging efficacy of the targeted imaging probes for CNS-L.

MATERIALS AND METHODS

Cells and Animals

The human ALL cell lines including NALM6, Reh, Jurkat, and CCRF-CEM were purchased from the American Type Culture Collection (ATCC) and cultured in RPMI 1640 medium supplemented with 10% fetal bovine serum and 0.5% penicillin–streptomycin and incubated at 37 °C/5%CO_2. To facilitate tumor monitoring, luminescent cells NALM6-luciferase were generated by stable transfection with luciferase. Female NOD/SCID mice (6 weeks old) were purchased from Vita River, Charles River Laboratories, China (Beijing, China). NOD/SCID mice were injected *via* the tail vein with 1×10^6 luciferased cells suspended in 150 μl of sterile phosphate-buffered saline (PBS). Bioluminescence imaging was applied to monitor the leukemic burden. All animal experiments were approved by the Institutional Animal Care and Use Committee (IACUC) at the Sun Yat-sen University Cancer Center (IACUC approval number L102012020070M), and the welfare and treatment of the laboratory animals were in accordance with the corresponding animal management regulations.

Preparation of S5 Peptide-Based Imaging Probes for NIRF, MR, and PET

The integrin α6-targeted peptide S5 was synthesized by the standard Fmoc-based solid-phase synthesis and provided by Chinese Peptide Company (Hangzhou, China). In order to make a better combination of S5 and Gd and to reduce the complexity of the process, we used the S5 peptide sequence as a straight peptide in the synthesis of the peptide Gd-S5, while the other two synthetic peptides were cyclic peptides. Briefly, DOTA-S5 or NOTA-S5 was synthesized through a condensation reaction between carboxyl groups in DOTA or NOTA and amine groups in reverse S5. The crude product was eluted with a gradient of acetonitrile, and the end product was purified by high-performance liquid chromatography (HPLC), followed by characterization using matrix-assisted laser desorption/ionization time-of-flight (MALDI-TOF) mass spectrometry (Bruker Daltonics, Germany). Then, Cy5-S5 was compounded by conjugating the Cy5 to the S5 peptide through an amidation reaction, and Gd-S5 was synthesized by complexation of Gd with the DOTA-S5.

As ^{18}F has a relatively fast rate of decay, ^{18}F-S5 would be synthesized each time before use by radiolabeling the NOTA-S5 with ^{18}F. In brief, the S5 peptide solution was freeze-dried with the lyophilized kits, with an 8 nmol S5 peptide and 6 nmol $AlCI_3$.6H2O in each vial unit. The reaction procedure was performed as follows: 1 vial unit was added with 65 μl of ^{18}F (approximately 10 mCi) in DI water, 5 μl of acetic acid, and 330 μl ethanol and heated for 10 min at 100°C. The reaction mixture was diluted with 10 ml of water and trapped in a Varian Bond Elut C18 column (100 mg). The column was washed with 10 ml of water and then eluted with 400 μl of ethanol twice. Then, the eluate was air-dried by nitrogen. Finally, the end product was dissolved with PBS before injection.

Flow Cytometry

NALM6, Ref, Jurkat, and CCRF-CEM cells were seeded into six-well plates, respectively, and then incubated with 10 μl/10^6 cell concentration of the anti-integrin α6 antibody (R&D, FAB13501P) and IgG2A (R&D, IC006P) at 4°C for 30 min, protected from light. After incubating for 30 min, the cells were washed with PBS three times and resuspended in 500 μl of PBS. The fluorescence intensity was measured by flow cytometry (Beckman Coulter, CytoFLEX S, United States).

Immunofluorescence

Approximately 1×10^6 NALM6 cells were seeded on cover slips in 24-well plates and incubated for 24 h. Subsequently, the 80 μM S5 peptide was added into the culture medium and incubated with cells for 4 h, while the blank control group was

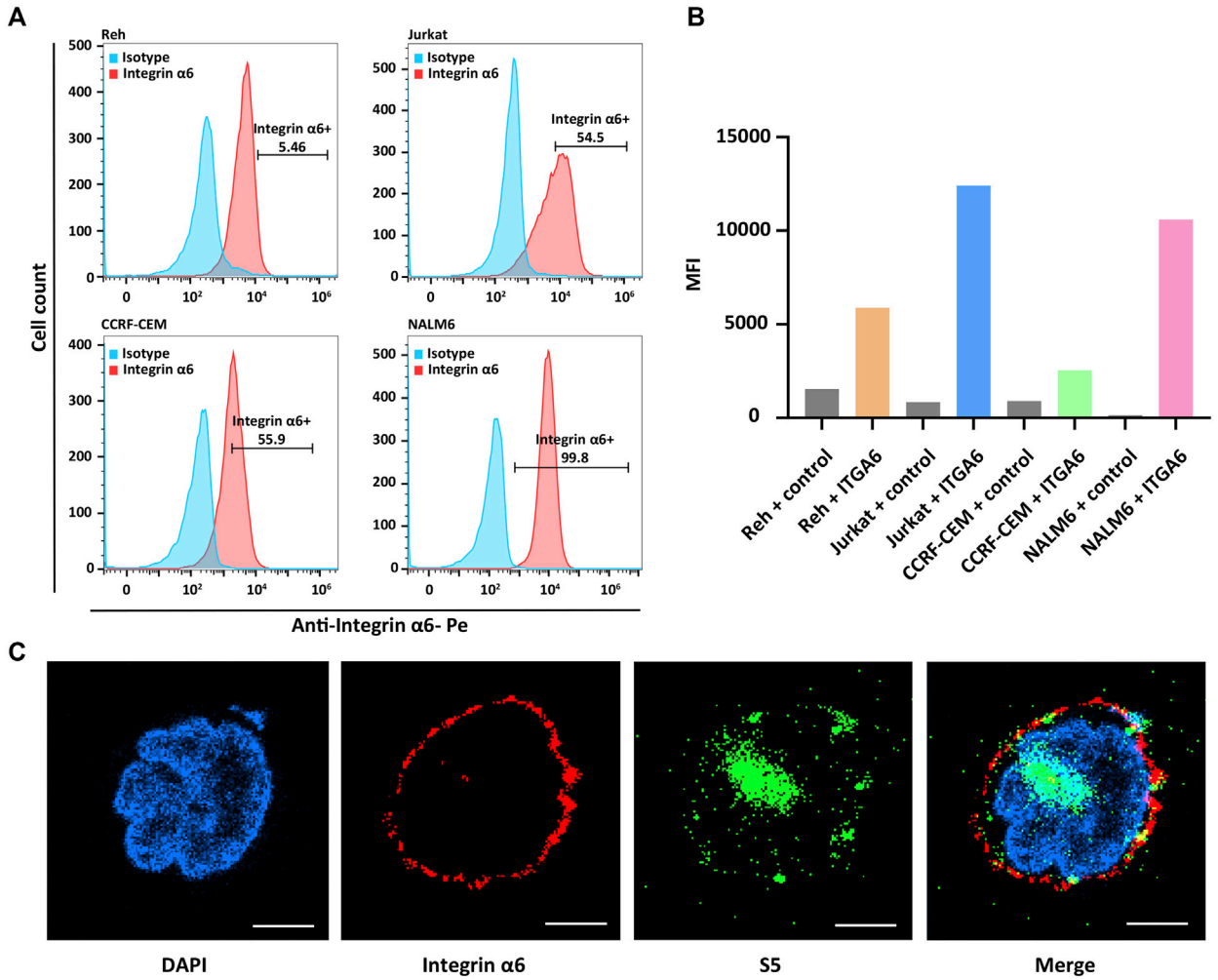

FIGURE 1 | Surface expression of integrin α6 in human ALL cell lines and binding of the S5 peptide to NALM6 cells. **(A)** Flow cytometry identified the surface expression of integrin α6 in human ALL cell lines including NALM6, Ref, Jurkat, and CCRF-CEM, and **(B)** the highest expression of integrin α6 was observed in NALM6 cells. **(C)** Confocal microscopy confirmed the cellular localization of integrin α6 and the S5 peptide in NALM6 cells (Scale bar, 4 μm).

added to the same volume of RPMI 1640 medium. After that, cells of each group were washed with PBS five times, fixed with 4% paraformaldehyde for 15 min, permeabilized with 0.1% Triton X-100 (Sigma-Aldrich, Germany), and blocked with 1% BSA for 30 min. The cover slips were incubated with the anti-integrin α6 antibody (Abcam, ab181551) at 4°C overnight, followed by incubation with streptavidin-Cy3 (Thermo Fisher 434315, United States) and the goat anti-mouse Alexa Fluor 488 secondary antibody (Abcam, ab150113) for 1 h at room temperature in a dark chamber. Finally, cover slips were incubated with 1 μg/ml DAPI and mounted with slides with ProLong gold antifade (Invitrogen P26930, United States). Fluorescence images were visualized and captured under a confocal microscopy confocal laser-scanning system (Zeiss, LSM980, Germany) at 40× and 100× magnification. Co-localization was analyzed by ImageJ (http://rsbweb.nih.gov/ij/) and the co-localization finder plug-in.

NIRF Imaging

Both bioluminescence and NIRF imaging are performed using IVIS Spectrum equipment manufactured by PerkinElmer, United States. We performed bioluminescence imaging on days 5, 10, 15, 20, 25, and 30 after the tail vein injection of leukemic cells until the imaging results confirmed the presence of focal luminescence intensity around the head of the mice. Bioluminescence imaging was performed starting 5 min after the intraperitoneal injection of luciferin. NIRF was acquired with an excitation at 640 nm and emission at 680 nm (exposure time: 3 s). Mice with CNS-L confirmed by bioluminescence were used for NIRF imaging studies on the following day. Mice were anesthetized with 3% isoflurane and maintained under anesthesia with 1–2% isoflurane and oxygen. An injection of Cy5-S5 and Cy5-CG7C solutions was freshly prepared in saline, and the solution was stabilized for 20 min before injection. Each mouse was injected intravenously with an equivalent of 10 nmol (0.5 mg/Kg) of Cy5-S5 and Cy5-CG7C.

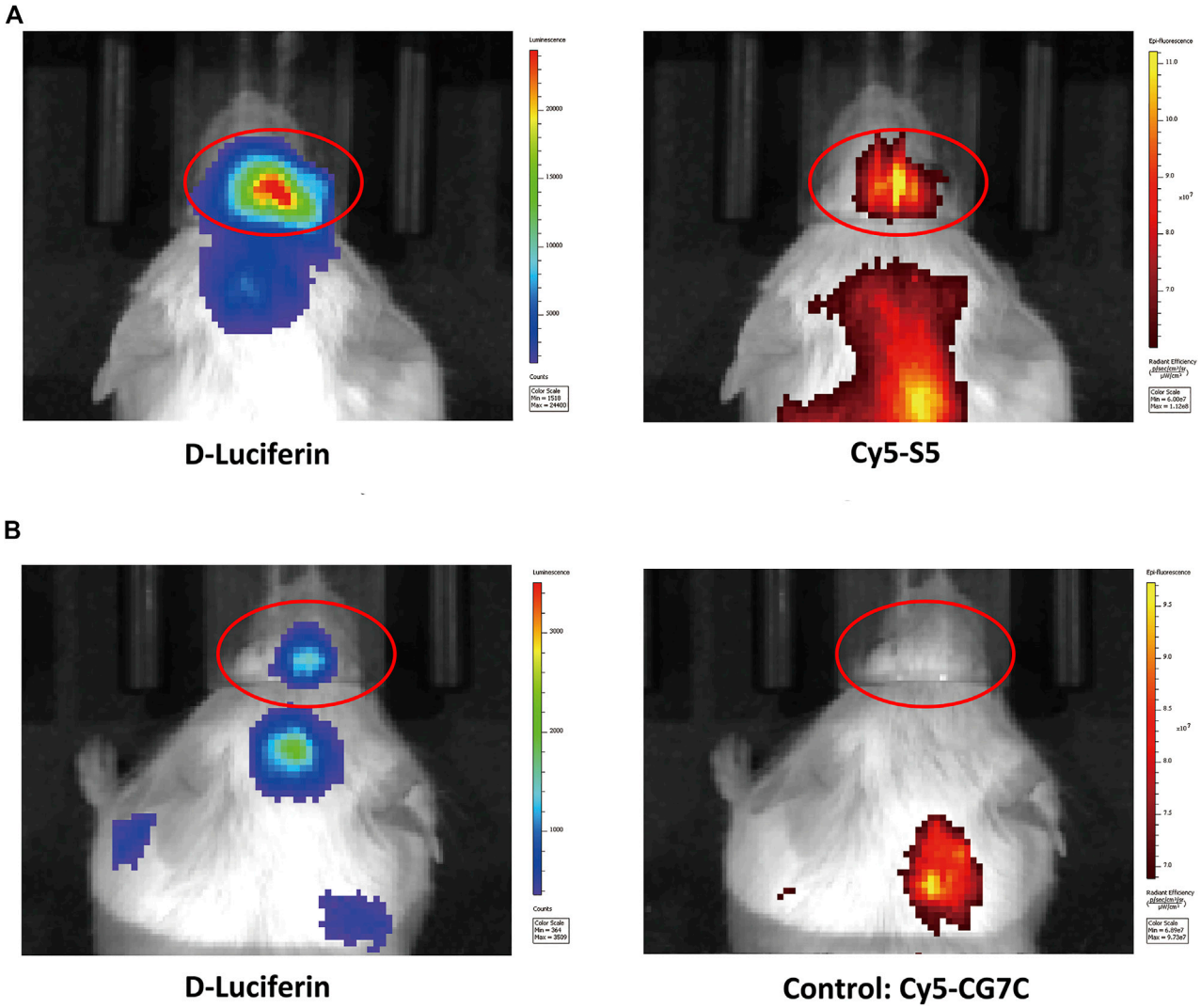

FIGURE 2 | NIFR imaging with Cy5-S5 in ALL mouse models verified by bioluminescence imaging. **(A)** Cy5-S5 exhibited intensive fluorescence intensity in the similar tumor location of bioluminescence imaging, while **(B)** Cy5-CG7C did not show significant fluorescence intensity.

Fluorescence signals from the tumor were recorded before and 48 h after intravenous injection of the probes.

MR Imaging

Bioluminescence confirmed CNS-L mice were used for MR and PET imaging studies in the next few days after the NIRF imaging. MR imaging was performed using a Philips Achieva 3.0 T system. Mice were anesthetized with 2,2,2-Tribromoethanol (100 μl/g), fixed on the holder, and placed into the mouse-imaging coil. Gd-S5 or a control agent was delivered by the tail vein at a dose of 0.03 mmol of Gd/kg for the T1 mapping sequence in NALM6-luciferase tumor-bearing mice. The clinical commonly used MR contrast medium gadolinium-diethylenetriamine pentaacetic acid (Gd-DTPA), which is a nonspecific agent, was used as control. On two separate days, mice received either a control enhance-agent (0.03 mmol of Gd/kg) or Gd-S5 (0.03 mmol of Gd/kg) injection and subsequent MR imaging, with at least 3 days between the scans to ensure most of the gadolinium were cleared. Axial T1-weighted images were acquired by using a gradient-echo sequence with the following parameters: TR/TE = 8.771/2.878 ms, FOV = 4.0 cm, slice thickness = −1 mm, slice spacing = 0.5, pixel spacing = 0.234 mm × 0.234 mm, and matrix = 128 × 128.

PET Imaging

PET imaging was performed using a hybrid 3.0T PET/MR scanner (uPMR 790, United Imaging Healthcare). As described above, mice were anesthetized with 2,2,2-Tribromoethanol (100 μl/g), fixed on the holder, and placed into the mouse-imaging coil. Approximately, 3.7×10^6 Bq (100 μCi) of ^{18}F-S5 or the clinical commonly used PET tracer ^{18}F-fluorodeoxyglucose (FDG) as control was injected *via* the tail vein before PET imaging. PET scans of the tumor-bearing mice were performed 60 min after

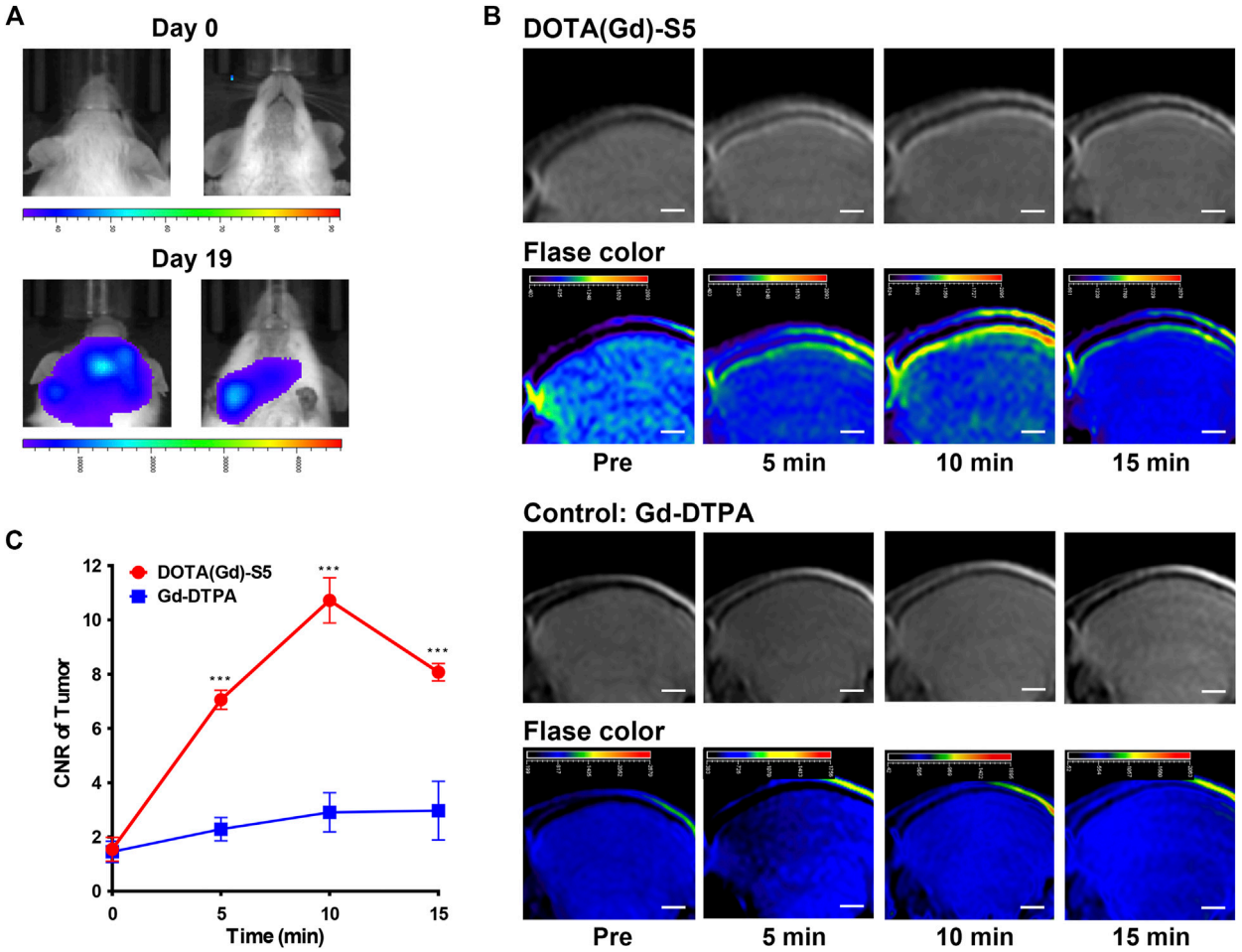

FIGURE 3 | MR imaging with Gd-S5 in ALL mouse models. **(A)** Bioluminescence imaging exhibited focal luminescence intensity around the head 19 days after injection of NALM6-luciferased cells. **(B)** T1-weighted MR images at the baseline and 5, 10, and 15 min post-injection of Gd-S5 and the control probe Gd-DTPA (Scale bar, 1 mm). **(C)** Gd-S5 generated a significantly higher signal enhancement at the site of meninges which were located between the skull bone and brain parenchyma at 5, 10, and 15 min post-injection, with the greatest gap at about 10 min post-injection (n = 3).

injection, with the following parameters: TR/TE = 8.771/2.878 ms, FOV = 4.0 cm, slice thickness = 1 mm, slice spacing = 0.5, pixel spacing = 0.234 mm × 0.234 mm, and matrix = 128 × 128.

HE Staining and Immunohistochemistry

At the end of imaging experiments, the mice were sacrificed by cervical dislocation and immediately dissected. The head part was collected, and haired skin and soft tissue were removed from the cranial surface. Paraffin sections (3 μm) were stained with hematoxylin and eosin (H&E) for routine histologic practice. Immunohistochemical (IHC) staining was performed following the conventional procedure, as we reported previously (Feng GK et al., 2019). Briefly, paraffin sections were dewaxed into xylene, rehydrated through graded alcohol, and microwaved for antigen retrieval. Blocking to inhibit the endogenous peroxidase activity and nonspecific binding, the sections were incubated with an anti-integrin α6 antibody (Abcam, ab181551, and 1:150) overnight at 4°C, followed by an HRP-conjugated polyclonal secondary antibody (1:200) at room temperature for 1 h. Finally, the positive immunoreactivity was visualized by staining with DAB (Zhongshan Jinqiao, ZLI-9017, China) and observed under a microscope (Nikon Eclipse, Japan).

Statistical Analysis

Statistical analysis was performed with SPSS 19.0 software (SPSS Inc., Chicago, United States). The significance was tested by the two-tailed Student's t-test, and a p value less than 0.05 was considered to be statistically significant.

RESULTS

Surface Expression of Integrin α6 in Human ALL Cell Lines

The surface expression of integrin α6 was assayed by flow cytometry in human ALL cell lines including NALM6, Ref, Jurkat, and CCRF-CEM. As expected, flow cytometry

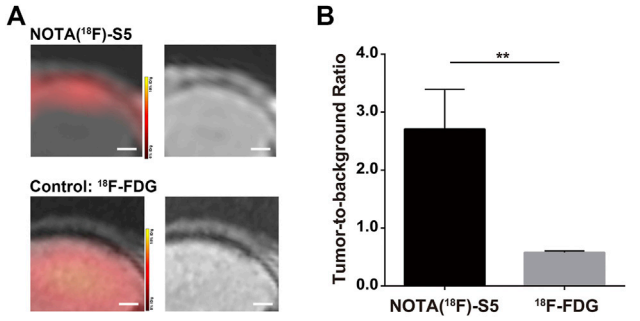

FIGURE 4 | ^{18}F-S5 PET/MR imaging in ALL mouse models. **(A)** ^{18}F-S5 generated focal radioactivity at the same location of the enhanced signals in MR imaging. **(B)** ^{18}F-S5 probe generated a significantly higher tumor-to-background ratio than the ^{18}F-FDG probe (2.71 vs. 0.58, p = 0.006).

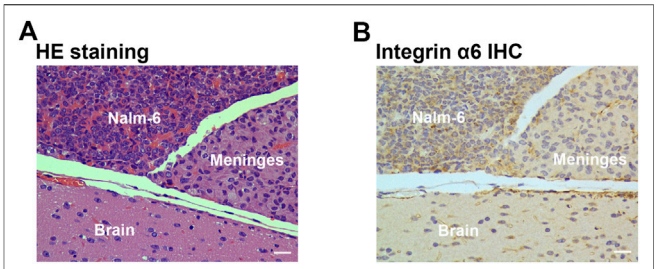

FIGURE 5 | Pathological examination of tumor tissue. HE staining **(A)** identified layer-displayed leukemic cells in the superficial part of the brain parenchyma tissue, and immunohistochemical staining **(B)** confirmed the integrin α6 overexpression of the lesion (Scale bar, 40 μm).

confirmed the surface expression of integrin α6 in all the cell lines (**Figure 1A**). In **Figure 1B**, we describe the mean fluorescence intensity (MFI) of different cell flow assays. MFI means total fluorescence intensity divided by the number of positive cells. The highest expression of integrin α6 was observed in NALM6 cells with a positive rate of 99.8% (**Figure 1B**), which was used to establish ALL models for subsequent imaging experiments.

Synthesis and Characterization

The S5 peptide was synthesized using Fmoc-based solid-phase synthesis. Then, the S5 peptide was condensed with a PEG4 spacer and the Cy5, NOTA, or DOTA structure to furnish the Cy5-S5, NOTA-S5, and DOTA-S5. The purity of Cy5-S5, NOTA-S5, and DOTA-S5 was over 95% by high-performance liquid chromatography (HPLC). The molecular weight was measured to be 1985, 1,632, and 1,435 by MALDI-TOF mass spectrometry, which was in agreement with the theoretical molecular weight calculated from the predicted amino acid sequence. Then, the DOTA-S5 was complexed with Gd, and the NOTA-S5 peptide was radiolabeled with the radionuclide ^{18}F to form the MR enhancer Gd-S5 and the PET radiotracer ^{18}F-S5 (**Supplementary Figure S1**). The structural formula used for the Gd-S5 peptide used for MR imaging is a straight peptide, based on the convenience and requirements of the synthesis process and the fact that our preliminary experiments have confirmed that the binding of cyclic and straight peptides is equivalent. The corresponding results are supplemented in **Supplementary Figures S2A, S2B**. In addition, the binding experiments with S5 carrying NOTA groups found that the attachment of NOTA did not affect the binding affinity of the peptide (**Supplementary Figures S2C, S2D**).

Biding of the S5 Peptide to NALM6 Cells and NIRF Imaging

The cellular localization of the S5 peptide in NALM6 cells was visualized by confocal microscopy. Green fluorescence represented the S5 polypeptide, which entered the cytoplasm through cytocytosis after binding to the cell membrane. Red fluorescence represented the integrin α6 antibody, which was bound to the cell membrane and was then immobilized on the cell membrane. According to the fluorescence microscopy data, the S5 peptide was enriched and localized at the nuclei of NALM6 cells after 4 h of co-culturing (**Figure 1C**), indicating the targeted ability of the S5 peptide to integrin α6 that was dominantly distributed on the nuclei. To further investigate the *in vivo* tumor-binding ability of the S5 peptide, NIRF imaging with Cy5-S5 and Cy5-CG7C (negative control) was conducted. The NALM6-luciferase tumor-bearing mice were verified by bioluminescence imaging with a focal luminescence intensity around the head, and in NIRF imaging, Cy5-S5 exhibited intensive fluorescence intensity in the similar tumor location (**Figure 2A**), while the control imaging group with Cy5-CG7C did not show significant fluorescence intensity (**Figure 2B**).

MR Imaging in NALM6-Luciferase Tumor-Bearing Mice

Similarly, a leukemia CNS-L mouse model using NALM6 cells with the luciferase expression by tail vein injection was established. Approximately 3 weeks after tumor cell injection, the presence of focal luminescence intensity around the head was confirmed by bioluminescence imaging (**Figure 3A**). T1-weighted MR imaging was conducted before and at different time points after Gd-S5 or Gd-DTPA injection. To improve visibility, MR signals were also displayed in rainbow pseudo color. As shown in **Figure 3B**, Gd-S5 gradually produced contrast enhancement signals at the site of meninges located between the skull bone and brain parenchyma at 5 min post-injection, which conformed to the primary intracranial infiltrating location of CNS-L (Yao et al., 2018), reaching the peak at 10 min, and gradually decreased thereafter. The control group with Gd-DTPA injection did not show obvious enhancement signals. The signal intensity comparison according to the post-injection duration is presented in **Figure 3C**, indicating that Gd-S5 generated significantly higher signals than Gd-DTPA.

PET Imaging in NALM6-Luciferase Tumor-Bearing Mice

The PET imaging for ^{18}F-S5 was conducted 60 min after injection of the radiotracer through the tail vein. ^{18}F-S5 generated focal radioactivity at the site of meninges which is at the same location of enhanced signals generated by Gd-S5 in the previous MR imaging, whereas the brain parenchyma did not show significant radioactivity (**Figure 4A**). For the clinical commonly used PET radiotracer ^{18}F-FDG, it generated diffuse enhanced radioactivity in the brain tissue due to the hypermetabolism of glucose (**Figure 4A**). The tumor-to-background ratio of the ^{18}F-S5 probe was significantly higher than that of the ^{18}F-FDG probe (2.71 vs. 0.58, $p = 0.006$; **Figure 4B**).

HE Staining and Immunohistochemistry

At the end of the imaging experiments, mice were euthanized, and tumor tissues were removed for pathological examination. Pathological examination identified layer-displayed leukemic cells in the superficial part of the brain parenchyma tissue, and immunohistochemical staining confirmed the overexpression of integrin α6 within the lesion (**Figure 5**).

DISCUSSION

To date, the detection of CNS-L still remains a great challenge due to the lack of accurate diagnostic tools. CNS-L could occur at any time during the full course of leukemia, when the disease is apparently well-controlled even during relapse. Current diagnostic approaches including CNS symptoms and pathological detection of leukemic cells in the cerebrospinal fluid are generally hysteretic than the primary CNS involvement. Imaging detection of CNS-L lesions could be more distinct. MRI provides excellent soft tissue contrast and spatial resolution without ionizing radiation, which has been widely used due to its relatively low cost and easy accessibility (Mirzaei and Adeli, 2018). Meanwhile, PET imaging has been widely utilized in the diagnosis and management of cancer patients with relatively high sensitivity and quantitative-imaging ability (Shankar et al., 2020; Overcast et al., 2021). However, these imaging examinations have showed a limited ability in the imaging of CNS-L mainly due to the special histopathological characteristics of the disease.

Meningeal infiltration through the penetration of sinuses and small blood vessels is the earliest pathological process at the occurrence of CNS-L, followed by parenchymal infiltration, leukostasis, meningitis, intracranial edema, hemorrhage, and herniation (Yao et al., 2018; Halsey and Escherich, 2021). Distinctive from the other intracranial tumors, solid lesions hardly formed during the course of CNS-L, which caused a great challenge for conventional imaging methods (Pfeifer et al., 2003; Izraeli and Eckert, 2017). In addition, because of the physiological glucose hypermetabolism of a normal brain tissue, the most commonly used PET tracer ^{18}F-FDG was less applicable to the intracranial lesions. Based on the premises, the development of novel molecular imaging probes with targeted ability could offer novel opportunities for the imaging of CNS-L.

Here, we focused on the potential tumor biomarker integrin α6, which was found to be overexpressed in a series of cancers (Huang et al., 2012; Brooks et al., 2016; Beaulieu, 2018). Physiologically, integrin α6 was mainly involved in cell proliferation, migration, survival, and differentiation by mediating cell-to-cell and cell-to-stroma adhesion. The expression and function of integrin α6 were abnormally altered in tumor cells, which promoted tumorigenesis, invasion, angiogenesis, metastasis, immune escape, and tolerance to radiotherapy and chemotherapy (Lathia et al., 2010; Beaulieu, 2019). In ALL, integrin α6 has been implicated to be crucial in the migration into CNS tissues and promote the survival of minimal residual disease after chemotherapy (Yao et al., 2018). Besides, silencing of integrin α6 could induce apoptosis and sensitize ALL cells to nilotinib or chemotherapy regimens, suggesting its important role in mediating chemoresistance (Yamakawa et al., 2012; Gang et al., 2020). As a membrane protein, integrin α6 also had a relatively long N-terminal extracellular domain that could be approached and bounded by targeted agents and which rendered it a potentially suitable target for molecular imaging and antitumor therapy.

In this study, the overexpression of integrin α6 was identified in numerous ALL cell lines including NALM6, REH, and CCRF-CEM cells, and the dominating membrane location of integrin α6 and the S5 peptide was confirmed by confocal microscopy. Then, the S5 peptide-based NIRF-, MRI-, and PET-targeted imaging probes were successfully constructed in four major domains: the S5 peptide domain for tumor targeting; Cy5, Gd, or ^{18}F for the NIRF tracer, MRI contrast enhancement, or PET radiotracer; DOTA or NOTA as a chemical complexation ligand for linking Gd or ^{18}F; and a PEG4 spacer to avoid the steric hindrance of the Cy5, Gd-DOTA, or ^{18}F-NOTA monoamide to the S5 peptide. The synthesized agents Cy5-S5, Gd-S5, and ^{18}F-S5 were hydrophilic and had good water solubility, suggesting its potential for further imaging development.

Our results illustrated that the gradually enhanced MRI signals were acquired at the site of meninges that were located between the skull bone and brain parenchyma of the mouse models, which was in accordance with the primary intracranial infiltrating location of CNS-L (Yao et al., 2018), reaching the peak at around 10 min, which was significantly highlighted compared to the surrounded brain tissues and easy to be recognized in visual, whereas the MRI images of the control group did not show significant enhancement signals. The quantitative signal analysis revealed that the S5 peptide-based probe generated, in approximately, signal enhancement 3 folds more than the control agent within the first 5 min post-injection, and the gap widened to nearly 4 folds at 10 min after injection. The signal enhancement gradually decreased thereafter and was still distinctive at 15 min post-injection. The PET imaging also showed regional radiation concentration at the same site of the MRI signal enhancement. Although the absolute SUV

value was not high, its relative ratio to the brain parenchymal tissue reached near 3 folds, indicating considerable imaging ability of the S5-based PET probe.

Tumor-specific antibodies have been developed for targeted imaging; however, typically several days were needed to achieve the optimal imaging condition due to the long blood circulation duration of the antibodies. Targeted peptides have several advantages compared to the antibodies including the small size, sufficient capillary permeability, low immunogenicity, short biological half-time, rapid clearance from non-target tissues, ease of manufacture, and readily labeled with specific nuclides (Lee et al., 2010; Yao et al., 2016; Araste et al., 2018). In our study, Gd-S5 and ^{18}F-S5 could be quickly excreted through the kidney due to its small molecular structure and good permeability, which enables the basis for imaging safety.

On the other hand, our study also has several limitations. First, the diagnostic efficacy of the molecular probes, compared to conventional cerebrospinal fluid examinations that are routinely conducted in clinics, was not investigated and could be further identified in larger animal models in which the cerebrospinal fluid is more accessible. Besides, the binding affinity of the S5 peptide to integrin α6 could be further enhanced through optimizing the peptide structure.

In conclusion, the study demonstrated that integrin α6 could serve as a feasible target for the molecular targeted imaging of CNS-L. The S5 peptide-based MRI and PET enhancement probes showed considerable ability in the imaging of CNS-L lesions in mouse models, indicating their potential for further development and clinical translation.

DATA AVAILABILITY STATEMENT

The original contributions presented in the study are included in the article/**Supplementary Material**, further inquiries can be directed to the corresponding authors. The authenticity of this article has been validated by uploading the key raw data onto the Research Data Deposit public platform (www.researchdata.org.cn), with the approval RDD number as RDDB2022504768.

ETHICS STATEMENT

The animal study was reviewed and approved by the Ethics Committee of the Sun Yat-sen University Cancer Center.

AUTHOR CONTRIBUTIONS

HW, GF, and XZ conceived the presented idea. GF developed the linkage mode of the tracer. XZ developed the chemical structure of tracers and the radiosynthesis method. HW designed the imaging verifying methods. WZ, YL, and GC conducted the experiments. WZ carried out the cell line constructions and *in vitro* studies. YL performed the imaging scans. GC carried out the tracer labeling and administration. XC and JH provided the study materials and technique support. Rodents used in the experiments were provided by XC. Confocal images and PET images were obtained with the help of JH.

FUNDING

This work was carried out with the support of the National Natural Science Foundation of China (NSFC) (Grant: 81700148) and the Natural Science Foundation of Guangdong Province Funding (Grant: 2021A1515010093).

SUPPLEMENTARY MATERIAL

The Supplementary Material for this article can be found online at: https://www.frontiersin.org/articles/10.3389/fbioe.2022.812277/full#supplementary-material

REFERENCES

Araste, F., Abnous, K., Hashemi, M., Taghdisi, S. M., Ramezani, M., and Alibolandi, M. (2018). Peptide-based Targeted Therapeutics: Focus on Cancer Treatment. *J. Control. Release* 292, 141–162. doi:10.1016/j.jconrel.2018.11.004

Beaulieu, J.-F. (2018). Integrin Î±6 Variants and Colorectal Cancer. *Gut* 67, 1747–1748. doi:10.1136/gutjnl-2017-315415

Beaulieu, J.-F. (2019). Integrin α6β4 in Colorectal Cancer: Expression, Regulation, Functional Alterations and Use as a Biomarker. *Cancers* 12, 41. doi:10.3390/cancers12010041

Blase, L., Merling, A., Engelmann, S., Möller, P., and Schwartz-Albiez, R. (1996). Characterization of Cell Surface-Expressed Proteochondroitin Sulfate of Pre-B Nalm-6 Cells and its Possible Role in Laminin Adhesion. *Leukemia* 10, 1000–1011.

Brooks, D. L. P., Schwab, L. P., Krutilina, R., Parke, D. N., Sethuraman, A., Hoogewijs, D., et al. (2016). ITGA6 Is Directly Regulated by Hypoxia-Inducible Factors and Enriches for Cancer Stem Cell Activity and Invasion in Metastatic Breast Cancer Models. *Mol. Cancer* 15, 26. doi:10.1186/s12943-016-0510-x

Bürger, B., Zimmermann, M., Mann, G., Kühl, J., Löning, L., Riehm, H., et al. (2003). Diagnostic Cerebrospinal Fluid Examination in Children with Acute Lymphoblastic Leukemia: Significance of Low Leukocyte Counts with Blasts or Traumatic Lumbar Puncture. *J. Clin. Oncol.* 21, 184–188. doi:10.1200/jco.2003.04.096

Erdreich-Epstein, A., Tran, L. B., Cox, O. T., Huang, E. Y., Laug, W. E., Shimada, H., et al. (2005). Endothelial Apoptosis Induced by Inhibition of Integrins αvβ3 and αvβ5 Involves Ceramide Metabolic Pathways. *Blood* 105, 4353–4361. doi:10.1182/blood-2004-08-3098

Feng G, G., Zhang, M., Wang, H., Cai, J., Chen, S., Wang, Q., et al. (2019). Identification of an Integrin α6-Targeted Peptide for Nasopharyngeal Carcinoma-specific Nanotherapeutics. *Adv. Ther.* 2, 1900018. doi:10.1002/adtp.201900018

Feng GK, G.-K., Ye, J.-C., Zhang, W.-G., Mei, Y., Zhou, C., Xiao, Y.-T., et al. (2019). Integrin α6 Targeted Positron Emission Tomography Imaging of Hepatocellular Carcinoma in Mouse Models. *J. Control. Release* 310, 11–21. doi:10.1016/j.jconrel.2019.08.003

Frishman-Levy, L., and Izraeli, S. (2017). Advances in Understanding the Pathogenesis of CNS Acute Lymphoblastic Leukaemia and Potential for Therapy. *Br. J. Haematol.* 176, 157–167. doi:10.1111/bjh.14411

Gang, E. J., Kim, H. N., Hsieh, Y.-T., Ruan, Y., Ogana, H. A., Lee, S., et al. (2020). Integrin α6 Mediates the Drug Resistance of Acute Lymphoblastic B-Cell Leukemia. *Blood* 136, 210–223. doi:10.1182/blood.2019001417

Gao, S., Jia, B., Feng, G., Dong, C., Du, H., Bai, L., et al. (2020). First-in-human Pilot Study of an Integrin α6-targeted Radiotracer for SPECT Imaging of Breast Cancer. *Sig. Transduct. Target. Ther.* 5, 147. doi:10.1038/s41392-020-00266-9

Halsey, C., and Escherich, G. (2021). A "Goldilocks" Approach to CNS Leukemia Is Needed. *Blood* 138, 288–289. doi:10.1182/blood.2021011461

Huang, P., Rani, M. R. S., Ahluwalia, M. S., Bae, E., Prayson, R. A., Weil, R. J., et al. (2012). Endothelial Expression of TNF Receptor-1 Generates a Proapoptotic Signal Inhibited by Integrin α6β1 in Glioblastoma. *Cancer Res.* 72, 1428–1437. doi:10.1158/0008-5472.can-11-2621

Izraeli, S., and Eckert, C. (2017). Targeted Therapy of CNS Leukemia? *Blood* 130, 562–563. doi:10.1182/blood-2017-06-788430

Jin, M. W., Xu, S. M., and An, Q. (2018). Central Nervous Disease in Pediatric Patients during Acute Lymphoblastic Leukemia (ALL): a Review. *Eur. Rev. Med. Pharmacol. Sci.* 22, 6015–6019. doi:10.26355/eurrev_201809_15937

Krebsbach, P. H., and Villa-Diaz, L. G. (2017). The Role of Integrin α6 (CD49f) in Stem Cells: More Than a Conserved Biomarker. *Stem Cell Dev.* 26, 1090–1099. doi:10.1089/scd.2016.0319

Lathia, J. D., Gallagher, J., Heddleston, J. M., Wang, J., Eyler, C. E., Macswords, J., et al. (2010). Integrin Alpha 6 Regulates Glioblastoma Stem Cells. *Cell Stem Cell* 6, 421–432. doi:10.1016/j.stem.2010.02.018

Lee, S., Xie, J., and Chen, X. (2010). Peptides and Peptide Hormones for Molecular Imaging and Disease Diagnosis. *Chem. Rev.* 110, 3087–3111. doi:10.1021/cr900361p

Lenk, L., Alsadeq, A., and Schewe, D. M. (2020). Involvement of the central Nervous System in Acute Lymphoblastic Leukemia: Opinions on Molecular Mechanisms and Clinical Implications Based on Recent Data. *Cancer Metastas. Rev.* 39, 173–187. doi:10.1007/s10555-020-09848-z

Lin, B.-Q., Zhang, W.-B., Zhao, J., Zhou, X.-H., Li, Y.-J., Deng, J., et al. (2021). An Optimized Integrin α6-Targeted Magnetic Resonance Probe for Molecular Imaging of Hepatocellular Carcinoma in Mice. *J. Hepatocell. Carcinoma* 8, 645–656. doi:10.2147/jhc.s312921

Malard, F., and Mohty, M. (2020). Acute Lymphoblastic Leukaemia. *Lancet* 395, 1146–1162. doi:10.1016/s0140-6736(19)33018-1

Mei, Y., Li, Y. H., Yang, X. C., Zhou, C., Li, Z. J., Zheng, X. B., et al. (2020). An Optimized Integrin α6-targeted Peptide for Positron Emission Tomography/magnetic Resonance Imaging of Pancreatic Cancer and its Precancerous Lesion. *Clin. Transl. Med.* 10, e157. doi:10.1002/ctm2.157

Mirzaei, G., and Adeli, H. (2018). Segmentation and Clustering in Brain MRI Imaging. *Rev. Neurosci.* 30, 31–44. doi:10.1515/revneuro-2018-0050

Overcast, W. B., Davis, K. M., Ho, C. Y., Hutchins, G. D., Green, M. A., Graner, B. D., et al. (2021). Advanced Imaging Techniques for Neuro-Oncologic Tumor Diagnosis, with an Emphasis on PET-MRI Imaging of Malignant Brain Tumors. *Curr. Oncol. Rep.* 23, 34. doi:10.1007/s11912-021-01020-2

Pfeifer, H., Wassmann, B., Hofmann, W. K., Komor, M., Scheuring, U., Brück, P., et al. (2003). Risk and Prognosis of central Nervous System Leukemia in Patients with Philadelphia Chromosome-Positive Acute Leukemias Treated with Imatinib Mesylate. *Clin. Cancer Res.* 9, 4674–4681.

Pinnix, C. C., Yahalom, J., Specht, L., and Dabaja, B. S. (2018). Radiation in Central Nervous System Leukemia: Guidelines from the International Lymphoma Radiation Oncology Group. *Int. J. Radiat. Oncol. Biol. Phys.* 102, 53–58. doi:10.1016/j.ijrobp.2018.05.067

Ranta, S., Palomäki, M., Levinsen, M., Taskinen, M., Abrahamsson, J., Mellgren, K., et al. (2017). Role of Neuroimaging in Children with Acute Lymphoblastic Leukemia and central Nervous System Involvement at Diagnosis. *Pediatr. Blood Cancer* 64, 64–70. doi:10.1002/pbc.26182

Ranta, S., Palomäki, M., Levinsen, M., Taskinen, M., Abrahamsson, J., Hasle, H., et al. (2017). Presenting Features and Imaging in Childhood Acute Myeloid Leukemia with central Nervous System Involvement. *Pediatr. Blood Cancer* 64, e26459. doi:10.1002/pbc.26459

Shankar, A., Bomanji, J., and Hyare, H. (2020). Hybrid PET-MRI Imaging in Paediatric and TYA Brain Tumours: Clinical Applications and Challenges. *J. Pers. Med.* 10, 218. doi:10.3390/jpm10040218

Siegel, R. L., Miller, K. D., and Jemal, A. (2019). Cancer Statistics, 2019. *CA Cancer J. Clin.* 69, 7–34. doi:10.3322/caac.21551

Takada, Y., Ye, X., and Simon, S. (2007). The Integrins. *Genome Biol.* 8, 215. doi:10.1186/gb-2007-8-5-215

Thastrup, M., Marquart, H. V., Levinsen, M., Grell, K., Abrahamsson, J., Albertsen, B. K., et al. (2020). Flow Cytometric Detection of Leukemic Blasts in Cerebrospinal Fluid Predicts Risk of Relapse in Childhood Acute Lymphoblastic Leukemia: a Nordic Society of Pediatric Hematology and Oncology Study. *Leukemia* 34, 336–346. doi:10.1038/s41375-019-0570-1

Vagace, J. M., de la Maya, M. D., Caceres-Marzal, C., Gonzalez de Murillo, S., and Gervasini, G. (2012). Central Nervous System Chemotoxicity during Treatment of Pediatric Acute Lymphoblastic Leukemia/lymphoma. *Crit. Rev. Oncol. Hematol.* 84, 274–286. doi:10.1016/j.critrevonc.2012.04.003

Xiao, Y.-T., Zhou, C., Ye, J.-C., Yang, X.-C., Li, Z.-J., Zheng, X.-B., et al. (2019). Integrin α6-Targeted Positron Emission Tomography Imaging of Colorectal Cancer. *ACS Omega* 4, 15560–15566. doi:10.1021/acsomega.9b01920

Yamakawa, N., Kaneda, K., Saito, Y., Ichihara, E., and Morishita, K. (2012). The Increased Expression of Integrin α6 (ITGA6) Enhances Drug Resistance in EVI1high Leukemia. *PloS one* 7, e30706. doi:10.1371/journal.pone.0030706

Yao, V. J., D'Angelo, S., Butler, K. S., Theron, C., Smith, T. L., Marchiò, S., et al. (2016). Ligand-targeted Theranostic Nanomedicines against Cancer. *J. Control. Release* 240, 267–286. doi:10.1016/j.jconrel.2016.01.002

Yao, H., Price, T. T., Cantelli, G., Ngo, B., Warner, M. J., Olivere, L., et al. (2018). Leukaemia Hijacks a Neural Mechanism to Invade the central Nervous System. *Nature* 560, 55–60. doi:10.1038/s41586-018-0342-5

Yousafzai, Y. M., Smith, L., Smith, A., Bhatti, S., Gardiner, M., Cousins, A., et al. (2019). Use of Quantitative Polymerase Chain Reaction (qPCR) for the Diagnosis and Monitoring of CNS Leukaemia. *Leuk. Res.* 87, 106232. doi:10.1016/j.leukres.2019.106232

Zhang C, C., Zhong, J. F., and Zhang, X. (2020). Revealing the Molecular Mechanism of central Nervous System Leukemia with Single-Cell Technology. *Crit. Rev. Oncol. Hematol.* 153, 103046. doi:10.1016/j.critrevonc.2020.103046

Zhang Y, Y., Zhao, J., Cai, J., Ye, J.-C., Xiao, Y.-T., Mei, Y., et al. (2020). Integrin α6-Targeted Magnetic Resonance Imaging of Hepatocellular Carcinoma in Mice. *Mol. Imaging Biol.* 22, 864–872. doi:10.1007/s11307-019-01437-z

Zhou, C., Zhuang, Y., Lin, X., Michelson, A. D., and Zhang, A. (2020). Changes in Neurocognitive Function and central Nervous System Structure in Childhood Acute Lymphoblastic Leukaemia Survivors after Treatment: a Meta-analysis. *Br. J. Haematol.* 188, 945–961. doi:10.1111/bjh.16279

Zhu, J., Carman, C. V., Kim, M., Shimaoka, M., Springer, T. A., and Luo, B.-H. (2007). Requirement of α and β Subunit Transmembrane helix Separation for Integrin Outside-In Signaling. *Blood* 110, 2475–2483. doi:10.1182/blood-2007-03-080077

Conflict of Interest: The authors declare that the research was conducted in the absence of any commercial or financial relationships that could be construed as a potential conflict of interest.

Publisher's Note: All claims expressed in this article are solely those of the authors and do not necessarily represent those of their affiliated organizations, or those of the publisher, the editors, and the reviewers. Any product that may be evaluated in this article, or claim that may be made by its manufacturer, is not guaranteed or endorsed by the publisher.

frontiers | Frontiers in Bioengineering and Biotechnology

ORIGINAL RESEARCH
published: 04 July 2022
doi: 10.3389/fbioe.2022.901452

Identification of a Novel Heterozygous Mutation in the *EIF2B4* Gene Associated With Vanishing White Matter Disease

Yun Tian[1,2†], *Qiong Liu*[3,4†], *Yafang Zhou*[1,2†], *Xiao-Yu Chen*[5], *Yongcheng Pan*[3,4], *Hongwei Xu*[1,2] *and Zhuanyi Yang*[5*]

[1]Department of Geriatrics, Xiangya Hospital, Central South University, Changsha, China, [2]National Clinical Research Center for Geriatric Disorders, Xiangya Hospital, Central South University, Changsha, China, [3]Department of Neurology, Xiangya Hospital, Central South University, Changsha, China, [4]Key Laboratory of Hunan Province in Neurodegenerative Disorders, Central South University, Changsha, China, [5]Department of Neurosurgery, Xiangya Hospital, Central South University, Changsha, China

Vanishing white matter disease (VWM) is one of the most common childhood inherited leukoencephalopathies with autosomal recessive inheritance. Mutations in five genes, *EIF2B1-5*, have been identified as the major cause of VWM. In this study, a targeted gene capture sequencing panel comprising 160 known pathogenic genes associated with leukoencephalopathies was performed in a large Han Chinese family affected by adult-onset VWM, and a novel heterozygous missense mutation (c.1337G > A [p. R446H]) in *EIF2B4* (NM_001034116.2) was detected. Further functional studies in HEK 293 cells showed dramatically reduced EIF2Bδ protein levels in the mutated group compared with the wild-type group. This study revealed that a heterozygous missense mutation (c.1337G > A [p. R446H]) in *EIF2B4* was potentially associated with the adult-onset mild phenotype of VWM. In contrast to previous reports, autosomal dominant inheritance was also observed in adult-onset VWM.

Keywords: vanishing white matter disease, EIF2B4, heterozygous missense mutation, loss of function, targeted gene capture sequencing panel

OPEN ACCESS

Edited by:
Youmei Bao,
Yale University, United States

Reviewed by:
Rachita Yadav,
Massachusetts General Hospital and Harvard Medical School, United States
Nguyen Quoc Khanh Le,
Taipei Medical University, Taiwan

***Correspondence:**
Zhuanyi Yang
neuroyzy@csu.edu.cn

[†]*These authors have contributed equally to this work*

Specialty section:
This article was submitted to Nanobiotechnology, a section of the journal Frontiers in Bioengineering and Biotechnology

Received: *22 March 2022*
Accepted: *23 May 2022*
Published: *04 July 2022*

Citation:
Tian Y, Liu Q, Zhou Y, Chen X-Y, Pan Y, Xu H and Yang Z (2022) Identification of a Novel Heterozygous Mutation in the EIF2B4 Gene Associated With Vanishing White Matter Disease. Front. Bioeng. Biotechnol. 10:901452. doi: 10.3389/fbioe.2022.901452

INTRODUCTION

Vanishing white matter disease (VWM), also known as childhood ataxia with central nervous system hypomyelination (CACH), is one of the most common childhood inherited leukoencephalopathies. It is an autosomal recessive disease characterized by progressive ataxia, spasticity, and leukoencephalopathy. The age of the VWM onset varies from before birth to adulthood, with most patients presenting with an onset between the ages of 2 and 6 years (Wu et al., 2009). Mental function is better preserved than motor function. For instance, intellectual problems are relatively rare in VWM, and psychiatric symptoms may occur as an initial manifestation in adult-onset patients. Episodic neurological regression and coma provoked by fever and head trauma usually appear during the progressive course of the disease (Van Der Knaap et al., 1997; Bugiani et al., 2010). Some female patients also experience ovarian failure (Fogli et al., 2003). The clinical phenotypes of VWM vary between studies; notably, the earlier the age of onset, the more severe the disease (Hamilton et al., 2018). Most individuals with VWM display a severe progressive phenotype in early childhood that may end in early death (Van Der Knaap et al., 2003), while a few instances have developed in adulthood and presented much milder progression (Pronk et al., 2006). Compared to

early childhood-onset VWM, adult-onset VWM has rarely been reported. The clinical course of adult-onset VWM may be milder and slower, but it is still progressive, and many patients ultimately lose the ability to perform daily living activities (Labauge et al., 2009). Typical brain magnetic resonance imaging (MRI) shows extensive leukoencephalopathy with diffuse fluid-like signals as a strong indicator of VWM (Van Der Knaap et al., 1999).

The eIF2B complex, which consists of five subunits (eIF2Bα, β, γ, δ, and ε) encoded by *EIF2B1-5* genes, is critical for the initiation of protein translation (Pavitt, 2005; Lorsch and Dever, 2010; Hinnebusch, 2011). Defects in any of these five subunits impair protein synthesis by reducing eIF2B activity (Pavitt et al., 1997; Kimball et al., 1998; Sonenberg and Hinnebusch, 2009; Elsby et al., 2011). Mutations in the *EIF2B1-5* genes have been identified as the major cause of VWM and follow an autosomal recessive inheritance mode (Leegwater et al., 2001; Van Der Knaap et al., 2002). Patients diagnosed with VWM have been reported to have either homozygous or compound heterozygous variants in one of the aforementioned five genes, while very few harbor heterozygous mutations (Wu et al., 2009; Zhang et al., 2015). To date, more than 150 mutations in EIF2B have been reported (Zhang et al., 2015). Most of the reported patients with VWM are Caucasian, while Han Chinese patients with *EIF2B* gene mutations have rarely been reported. Moreover, none of the Chinese affected individuals had adult-onset (Wu et al., 2009; Zhang et al., 2015).

In this study, we performed targeted gene capture sequencing followed by Sanger sequencing validation in a Chinese family affected by adult-onset VWM and identified a novel heterozygous missense mutation (c.1337G > A [p. R446H]) in *EIF2B4*, which led to dramatically reduced EIF2B4 protein levels when overexpressed in HEK 293T cells.

MATERIALS AND METHODS

Subjects

A Han Chinese VWM-affected family and healthy controls were recruited for this study. All study participants were carefully evaluated by at least two trained neurologists. VWM was diagnosed according to the clinical manifestation of motor and/or cognitive dysfunction accompanied by typical leukoencephalopathy with diffuse fluid-like signals on brain MRI. Clinical data and blood samples were collected from all participants.

This study was approved by the Ethics Committee of Xiangya Hospital of Central South University in China. Written informed consent was obtained from all the participants.

Mutation Screening

A QIAGEN kit was used to extract genomic DNA from peripheral blood leukocytes. To screen for mutations in the probands, we used a targeted gene capture sequencing panel composed of 160 genes reported to be associated with leukoencephalopathies, including *AARS2*, *ABAT*, *ABCD1*, *ACOX1*, *ACTA2*, *ADH1C*, *AIMP1*, *ALDH3A2*, *APBB2*, *ARSA*, *ASPA*, *BCKDHA*, *BCKDHB*, *BCS1L*, *CHM*, *CLCN2*, *COA5*, *COX15*, *COX6B1*, *CSF1R*, *CTC1*, *CYP27A1*, *DARS2*, *DBT*, *DDC*, *DLD*, *DNAJC13*, *DNAJC6*, *ECM1*, *EIF2B1*, *EIF2B2*, *EIF2B3*, *EIF2B4*, and *EIF2B5* (**Supplementary Table S1**). Biotinylated RNA probes were used to capture the known DNA sequences from the GRCh37/hg19 human reference sequence. After QC was used for quality control of sequencing data, low-quality reads were filtered out. The sequence reads were then aligned to the GRCh37/hg19 human reference genome using the Burrows–Wheeler Aligner (BWA, v.0.7.15). Raw variant calling was performed using the Genome Analysis Toolkit (GATK, v.3.2). The variants, including single nucleotide variants (SNVs) and indels (insertions and deletions), were annotated using ANNOVAR. Public databases, including 1,000 human genome datasets (1,000 Genomes) and the Genome Aggregation Database dataset (gnomAD, v2.11), were used to screen mutations among previously obtained SNVs and indels. The variants were filtered in accordance with allele frequencies, with minor allele frequencies (MAFs) < 0.001. Damaging missense and splicing mutations were predicted using the database for nonsynonymous SNPs' functional prediction descriptions (dpNSFP, v.4.0), Sorting Intolerant from Tolerant (SIFT) (Alanazi et al., 2011) and Polymorphism Phenotyping v2 (PolyPhen-2) (Adzhubei et al., 2010). Amino acid conservation around mutated positions was evaluated using T-Coffee (v.11.00) (Di Tommaso et al., 2011), to blast multiple sequences of eIF2Bδ proteins from different species. A 3D structural protein model was predicted using Phyre2 (Kelley et al., 2015). In addition, reported mutations were screened using the Human Gene Mutation Database (HGMD) and the ClinVar database. All variants were classified based on the sequence variant standards and guidelines of the American College of Medical Genetics and Genomics (ACMG) (Li et al., 2017). Further Sanger sequencing validation of family members was also performed.

Expression Plasmids

The wild-type *EIF2B4* plasmid was generated by cloning the complementary DNA (cDNA) of *EIF2B4* (NM_001034116.2) into mammalian expression vectors (pcDNA3.1) with a FLAG tag at the C-terminus. *EIF2B4* variants (p. R374C and p. R446H) were generated using a QuickChange II site-directed mutagenesis kit (Stratagene, 200523). The authenticity of all constructs was confirmed using Sanger sequencing.

Antibodies

The primary antibodies used in this study included FLAG (Sigma, F1804), vinculin (Cell Signaling Technology, 13901), and β-actin (Cell Signaling Technology, 4967L). The secondary antibodies were donkey anti-rabbit and donkey anti-mouse antibodies (Jackson ImmunoResearch).

Cell Culture and Transfection

Human embryonic kidney (HEK) 293 cells were grown at 37°C under 5% CO2 in Dulbecco's modified Eagle's medium supplemented with 10% fetal bovine serum and 100 U/mL of penicillin/streptomycin. Expression plasmids were transfected into cells using Lipofectamine 2000 reagent

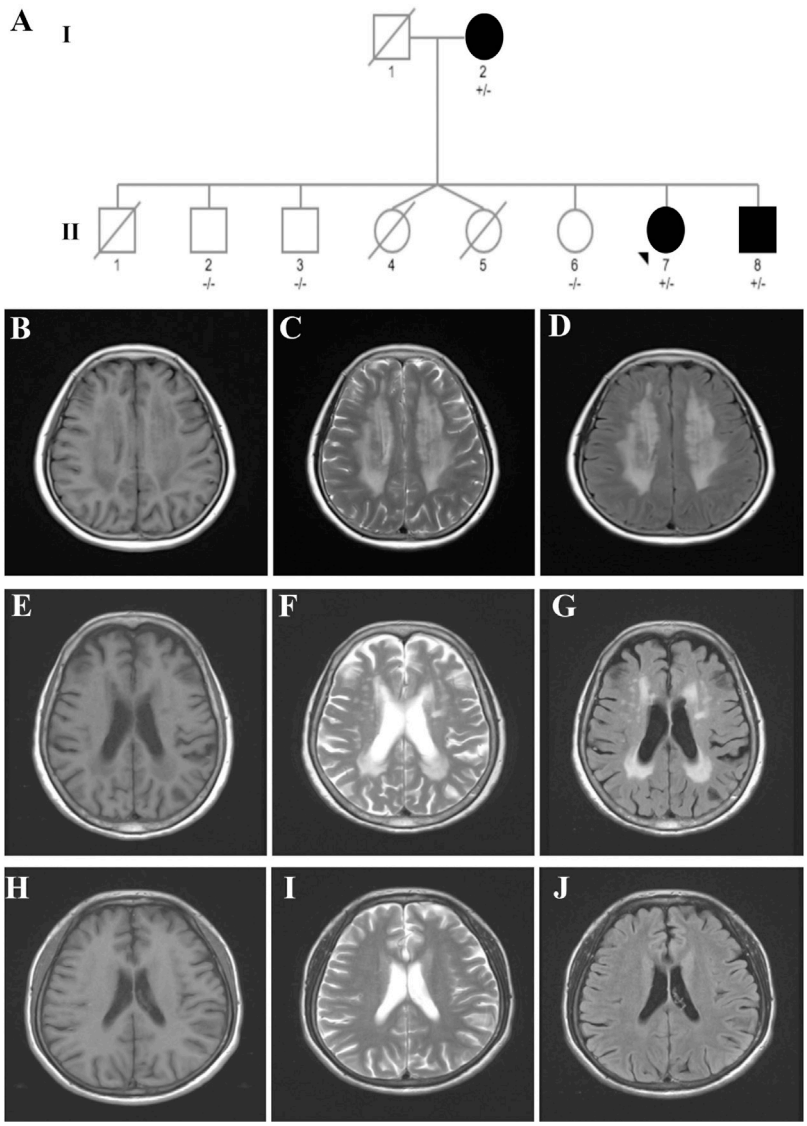

FIGURE 1 | Pedigree of a family affected by VWM. **(A)** Pedigree of the VWM-affected family. **(B–D)** Brain MRI of the proband (case II-7) indicating typical symmetric and diffuse periventricular leukoencephalopathy and a cerebrospinal fluid-like signal within the area on T1-weighted **(B)**, T2-weighted **(C)**, and flair images **(D)**. **(E–G)** Brain MRI of the mother (case I-2) showing moderate leukoencephalopathy. **(H–J)** Brain MRI of the brother (case II-8) revealed no leukoencephalopathy.

(Invitrogen), according to the manufacturer's protocol. The cells were collected for Western blotting 48 hours after transfection.

Western Blot

Transfected cells were lysed in ice-cold RIPA buffer containing a protease inhibitor cocktail and PMSF. The protein samples were separated using 10% SDS-PAGE and transferred onto a PVDF membrane (Millipore). After blocking, the blots were probed overnight with the appropriate antibodies. Blots were developed using an ECL prime chemiluminescence kit (GE Healthcare). Images were obtained using ChemiDoc XRS+ with Image Lab software (Bio-Rad).

RESULTS

Clinical Assessment of the VWM-Affected Family

The pedigree with VWM included three affected individuals (**Figure 1A**).

The proband case (case II-7) was a 53-year-old woman who presented with progressive cognitive decline for 3 years. At the age of 50, she experienced memory loss and became easily lost in new places. Four days before admission, her symptoms worsened after staying up late. Patients with ovarian failure or other medical history were excluded. The neurological examination revealed memory loss, a decline in calculation ability, language

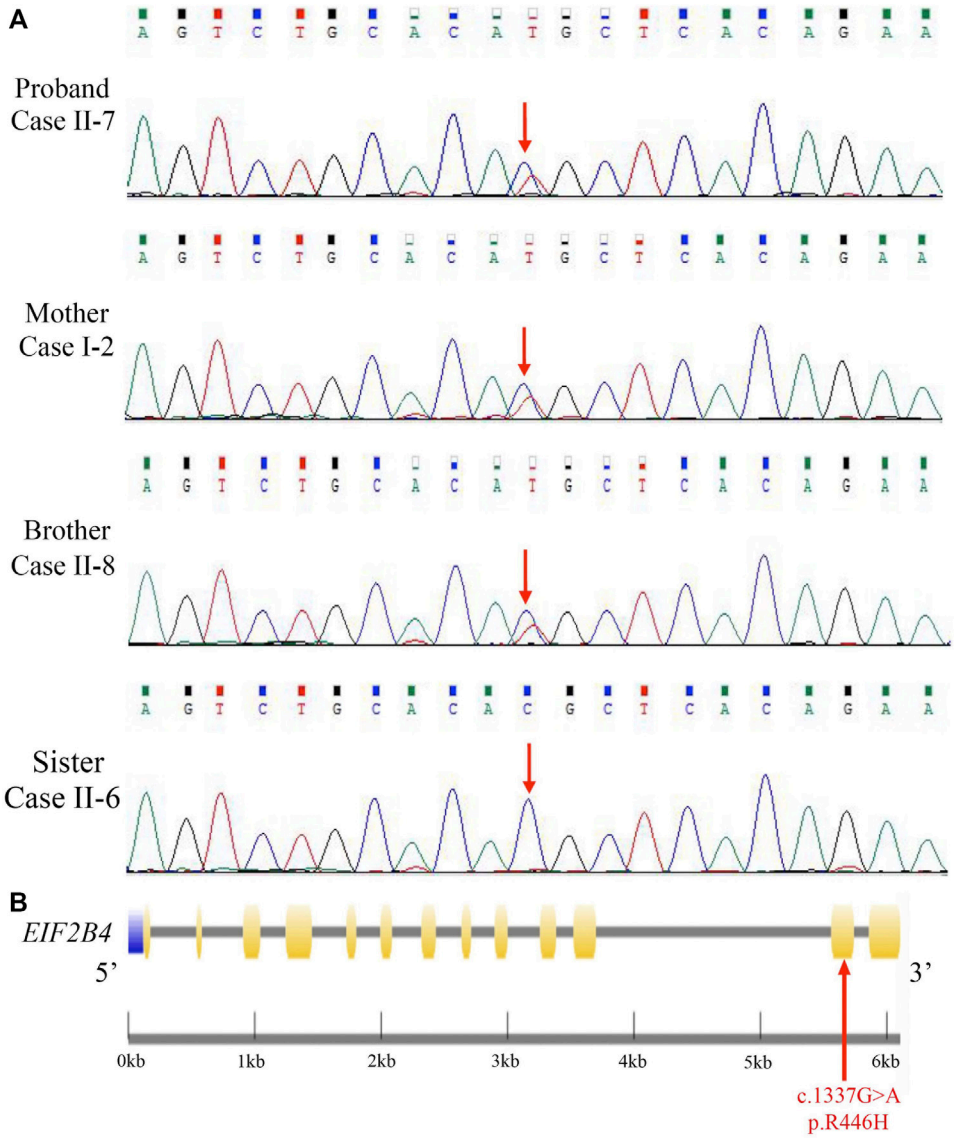

FIGURE 2 | Identification of a novel heterozygous *EIF2B4* mutation. **(A)** Sanger sequencing validated a missense mutation (c.1337G > A [p. R446H]) in the *EIF2B4* gene in family members. **(B)** Schematic presentation of the *EIF2B4* gene with an R446H substitution located in exon 12. Purple: upstream; yellow: exons; black line: introns.

dysfunction, and visuospatial disorders. Her Mini-Mental State Examination (MMSE) score was 14, and the Montreal Cognitive Assessment (MoCA) Scale score was 12. Magnetic resonance imaging (MRI) revealed symmetric and diffuse leukoencephalopathy in the periventricular and cerebrospinal fluid-like signal within the area on T1-weighted, T2-weighted, and flair images (**Figures 1B–D**).

The mother of the proband (case I-2), an 85-year-old woman, was referred to our hospital with a 20-year history of cognitive dysfunction. Neurological examination revealed mild cognitive impairment. Her MMSE score was 18, with 0-year education. Moderate leukoencephalopathy was observed on her brain MRI, while no fluid-like signal was observed (**Figures 1E–G**).

The younger brother of the proband (case II-8) was a 50-year-old man who presented with abnormal behavior at the age of 44. He had been diagnosed with schizophrenia 5 years before and had received risperidone for treatment. He had been experiencing memory loss since childhood and was unable to walk until 7 years of age. However, no leukoencephalopathy was observed on his brain MRI (**Figures 1H–J**).

It is noteworthy that case II:1 died at the age of 3 years for unknown reasons. Coincidently, cases II-4 and 5, a pair of twin sisters, died a few days after birth. It is possible that these three patients may have been affected by VWM and died young. However, further confirmation was difficult because we were unable to obtain their exact medical history and DNA samples.

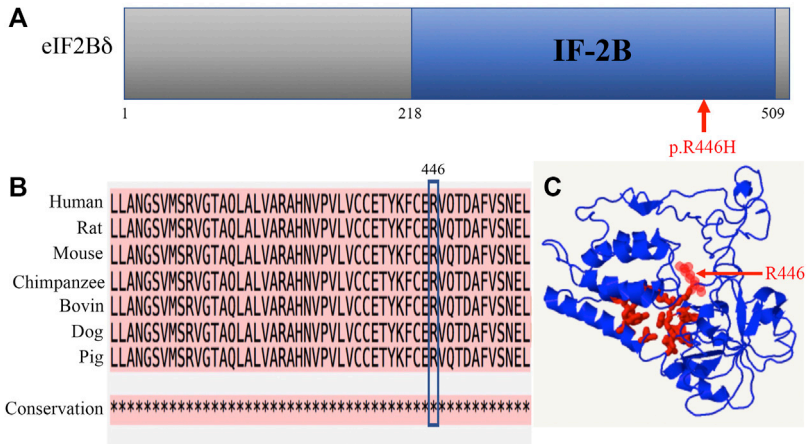

FIGURE 3 | Amino acid R446 is highly conserved among mammals. **(A)** Location of the R446H mutation in the eIF2Bδ protein. **(B)** Amino acid sequence alignments across species indicate high conservation around residue R446. * fully conserved. **(C)** 3D structural prediction of the eIF2Bδ protein. Red: pocket; red arrow: residue R446.

Identification of Novel Heterozygous Mutations in *EIF2B4*

Mutation screening was performed in the proband by using a targeted gene capture sequencing panel composed of 160 genes associated with leukoencephalopathies. A novel heterozygous missense mutation (c.1337G > A [p. R446H]) in *EIF2B4* (NM_001034116.2) was identified, but no other potential variants in reported genes associated with leukoencephalopathies were detected. Sanger sequencing validation showed that none of the cases had other pathogenic or likely pathogenic mutations in this gene (**Figure 2A**).

The *EIF2B4* gene is located on chromosome 2p23.2, encoding a 67-kD protein. This mutation lies in exon 11 (**Figure 2B**), resulting in an amino acid substitution of arginine to histidine (R446H) at the C-terminus of the eIF2Bδ protein. The majority of mutations reported to contribute to VWM or ovarioleukodystrophy (OLD) are missense mutations in the *EIF2B4* gene (Fogli et al., 2004; Scali et al., 2006), but this mutation has not been reported in the HGMD and ClinVar databases. We reanalyzed the sequencing data from 12 previously unrelated patients with non-vascular leukoencephalopathies, and no other patients were found to carry the R446H mutation. We further checked whole-exome sequencing data from 1,017 patients with neurological disorders, and none of them carried this mutation. The p. R446H substitution is absent from the human population database 1,000 Genomes, and the frequency of the p.R446H variant is 0.00006 in the gnomAD.

The p.R446H substitution was predicted to affect protein function by SIFT and was expected to be probably damaged by PolyPhen-2. The mutation lies in the IF-2B domain of the eIF2Bδ protein (**Figure 3A**). IF-2B resembles a domain that belongs to the initiation factor 2 subunit family, which includes IF-2Bα, β, and δ subunits from eukaryotes and some other proteins of unknown function from archaebacteria and prokaryotes (Kyrpides and Woese, 1998). The amino acid sequence alignments remained highly conserved across vertebrates within this region (**Figure 3B**), indicating that these residues play a critical role in eI2Bδ function. The 3D structural protein model revealed that residue R446 is located close to the predicted pocket region (**Figure 3C**), which might be functionally important.

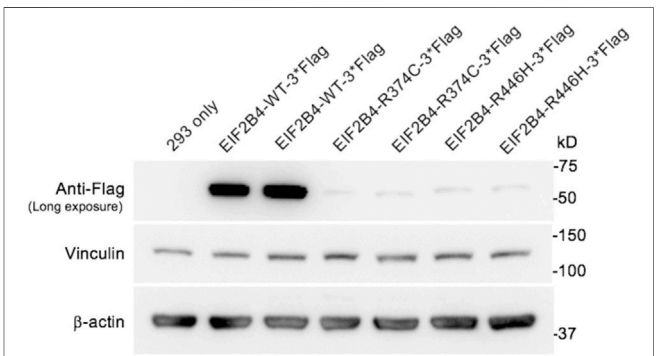

FIGURE 4 | Expression of wild-type and mutant eIF2Bδ in transfected HEK 293 cells. The levels of eIF2Bδ–R374C and R446H were significantly reduced compared with the wild-type protein.

Furthermore, the *EIF2B4* (c.1337G > A [p. R446H]) mutation was found in all affected individuals but not in unaffected family members of the pedigree (**Figure 2A** and **Supplementary Figure S1**). According to the ACMG guidelines, the novel R446H substitution is classified as a variant of uncertain significance (VUS), indicating that a heterozygous (c.1337G > A [p. R446H]) mutation in the *EIF2B4* gene may be associated with VWM.

The p. R446H Substitution Significantly Reduces eIF2Bδ Protein Levels

To evaluate the pathogenicity of the R446H substitution, vectors containing wild-type and mutant *EIF2B4* (R374C and R446H, respectively) with a C-terminal flag tag were transfected into HEK 293 cells for functional *in vitro* studies. The R374C variant is also a missense mutation that has been previously reported to be related to VWM before (Van Der Knaap et al., 2002). The expression levels of

R374C and R446H were measured using an anti-flag antibody and were found to significantly decrease compared to wild type (**Figure 4**). These results suggest that both p.R446H and p.R374C substitutions lead to haploinsufficiency of eIF2B, δ, which may contribute to VWM.

DISCUSSION

To date, at least 250 patients with VWM and 150 mutations in *EIF2B* genes have been reported (Zhang et al., 2015). Most *EIF2B* gene mutations have been reported in Caucasian populations, and the only study that was conducted in a Chinese population reported 34 patients with VWM and 37 *EIF2B* gene mutations (Zhang et al., 2015). Among all reported *EIF2B* mutations, *EIF2B4* gene mutations were observed in both Caucasian and Chinese patients with frequencies of 17% and 22%, respectively (Scali et al., 2006; Zhang et al., 2015). Rare mutations in the *EIF2B4* gene have been reported to account for 10–15% of Caucasian patients with VWM (Fogli et al., 2004; Pronk et al., 2006) and 18% of Han Chinese patients with VWM (Zhang et al., 2015). Most of the reported pathogenic mutations are missense mutations, which are mainly distributed in the highly conserved C-terminal region of eIF2B (Pavitt, 2005).

Patients with VWM with *EIF2B4* gene mutations are either homozygous or compound heterozygous, and the majority develop symptoms before adulthood. Consistent with patients with VWM with other *EIF2B* gene mutations, *EIF2B4* gene mutations are usually associated with motor dysfunction, rather than cognitive decline, as cognitive function is preserved relatively well. Some patients present motor development delays, speech delays, or school difficulties before the disease onset (Fogli et al., 2004; Ohlenbusch et al., 2005; Zhang et al., 2015). Only two adult-onset patients with *EIF2B4* gene mutations have been previously reported, both of which were compound heterozygous variants. Furthermore, both patients experienced cognitive impairment and motor symptoms, with mild progression (Kanbayashi et al., 2015).

In our study, we identified a novel heterozygous missense mutation (c.1337G > A [p. R446H]) in the *EIF2B4* gene in a family with a milder form of adult-onset VWM with cognitive decline or abnormal behavior as their chief complaint. The younger brother of the proband (case II-8) had motor developmental delays in early childhood. Unlike previously reported adult-onset cases of *EIF2B4* mutations, no motor symptoms were observed in this study.

The R446H variant identified here is located in a highly conserved region within the C-terminus of eIF2Bδ. The eIF2Bδ protein is ubiquitously expressed in human organs and is one of the five subunits of the eIF2B complex. The eIF2B complex is involved in translation initiation, where its guanine nucleotide exchange (GEF activity) turns inactive GDP-eIF2 to an active GTP-bound form (Leng et al., 2011). Furthermore, the eIF2B complex is composed of two α, β, and δ subunits in the central region, with one γε heterodimer on each side (Kashiwagi et al., 2019). The catalytic center of the γε subcomplex interacts with eIF2 and exhibits GEF activity (Pavitt, 2005), while the $\alpha_2\beta_2\delta_2$ subcomplex recognizes phosphorylated eIF2α and inhibits GEF activity (Kashiwagi et al., 2019). The C-terminus of the δ subunit shares a similar sequence with the α and β subunits, annotated as the initiation factor 2 subunit family, which suggests that these three subunits may interact with each other to regulate the eIF2B complex (Kyrpides and Woese, 1998; Pavitt, 2005).

Our functional study revealed that overexpression of the R446H variant resulted in a significant reduction in eIF2Bδ levels, which may reduce the activity of the eIF2B complex and impair its physiological function (Bugiani et al., 2010). It is reasonable to postulate that the R446H variant may cause VWM, even in a heterozygous status, by reducing the activity of eIF2B in patients.

In conclusion, our work indicated that a heterozygous missense mutation (c.1337G > A [p. R446H]) in the *EIF2B4* gene might be associated with an adult-onset milder form of VWM, and the genetic and clinical spectrum of VWM was extended. Further research on how the heterozygous R446H variant contributes to VWM is required in the future.

DATA AVAILABILITY STATEMENT

The original contributions presented in the study are included in the article/**Supplementary Material**; further inquiries can be directed to the corresponding author.

ETHICS STATEMENT

This study involving human participants was reviewed and approved by the Ethics Committee of Xiangya Hospital of Central South University in China. Written informed consent was obtained from all participants.

AUTHOR CONTRIBUTIONS

YT carried out most of the clinical assessment, data analysis, and manuscript writing. QL carried out the *in vitro* experiments and participated in manuscript writing. YZ contributed to clinical assessment and data analysis. XC performed the data analysis. YP, HX, and LS helped in the experimental design. ZY contributed to experimental design and manuscript revising.

FUNDING

This work was funded by the Natural Science Foundation of Hunan Province (Grant 2020JJ5923) and Scientific Research Projects of Health Commission of Hunan Province (Grant 202104090550).

ACKNOWLEDGMENTS

We would like to thank the participants for permitting us to publish this information in this study.

SUPPLEMENTARY MATERIAL

The Supplementary Material for this article can be found online at: https://www.frontiersin.org/articles/10.3389/fbioe.2022.901452/full#supplementary-material

REFERENCES

Adzhubei, I. A., Schmidt, S., Peshkin, L., Ramensky, V. E., Gerasimova, A., Bork, P., et al. (2010). A Method and Server for Predicting Damaging Missense Mutations. *Nat. Methods* 7, 248–249. doi:10.1038/nmeth0410-248

Alanazi, M., Abduljaleel, Z., Khan, W., Warsy, A. S., Elrobh, M., KhanFAU - Al Amri, Z. A., et al. (2011). In Silico Analysis of Single Nucleotide Polymorphism (SNPs) in Human β-Globin Gene. *PloS One* 6 (10), e25876. doi:10.1371/journal.pone.0025876

Bugiani, M., Boor, I., Powers, J. M., Scheper, G. C., and Van Der Knaap, M. S. (2010). Leukoencephalopathy with Vanishing White Matter: A Review. *J. Neuropathol. Exp. Neurol.* 69, 987–996. doi:10.1097/nen.0b013e3181f2eafa

Di Tommaso, P., Moretti, S., Xenarios, I., OROBITG, M., Montanyola, A., Chang, J.-M., et al. (2011). T-coffee: a Web Server for the Multiple Sequence Alignment of Protein and RNA Sequences Using Structural Information and Homology Extension. *Nucleic Acids Res.* 39, W13–W17. doi:10.1093/nar/gkr245

Elsby, R., Heiber, J. F., Reid, P., Kimball, S. R., Pavitt, G. D., and Barber, G. N. (2011). The Alpha Subunit of Eukaryotic Initiation Factor 2B (eIF2B) Is Required for eIF2-Mediated Translational Suppression of Vesicular Stomatitis Virus. *J. Virol.* 85, 9716–9725. doi:10.1128/jvi.05146-11

Fogli, A., Rodriguez, D., Eymard-Pierre, E., Bouhour, F., Labauge, P., Meaney, B. F., et al. (2003). Ovarian Failure Related to Eukaryotic Initiation Factor 2B Mutations. *Am. J. Hum. Genet.* 72, 1544–1550. doi:10.1086/375404

Fogli, A., Schiffmann, R., Bertini, E., Ughetto, S., Combes, P., Eymard-Pierre, E., et al. (2004). The Effect of Genotype on the Natural History of eIF2B-Related Leukodystrophies. *Neurology* 62, 1509–1517. doi:10.1212/01.wnl.0000123259.67815.db

Hamilton, E. M. C., Van Der Lei, H. D. W., Vermeulen, G., Gerver, J. A. M., Lourenço, C. M., Naidu, S., et al. (2018). Natural History of Vanishing White Matter. *Ann. Neurol.* 84, 274–288. doi:10.1002/ana.25287

Hinnebusch, A. G. (2011). Molecular Mechanism of Scanning and Start Codon Selection in Eukaryotes. *Microbiol. Mol. Biol. Rev.* 75, 434–467. doi:10.1128/mmbr.00008-11

Kanbayashi, T., Saito, F., Matsukawa, T., Oba, H., Hokkoku, K., Hatanaka, Y., et al. (2015). Adult-onset Vanishing White Matter Disease with Novel Missense Mutations in a Subunit of Translational regulator,EIF2B4. *Clin. Genet.* 88, 401–403. doi:10.1111/cge.12554

Kashiwagi, K., Yokoyama, T., Nishimoto, M., Takahashi, M., Sakamoto, A., Yonemochi, M., et al. (2019). Structural Basis for eIF2B Inhibition in Integrated Stress Response. *Science* 364, 495–499. doi:10.1126/science.aaw4104

Kelley, L. A., Mezulis, S., Yates, C. M., Wass, M. N., and Sternberg, M. J. E. (2015). The Phyre2 Web Portal for Protein Modeling, Prediction and Analysis. *Nat. Protoc.* 10, 845–858. doi:10.1038/nprot.2015.053

Kimball, S. R., Fabian, J. R., Pavitt, G. D., Hinnebusch, A. G., and Jefferson, L. S. (1998). Regulation of Guanine Nucleotide Exchange through Phosphorylation of Eukaryotic Initiation Factor eIF2α. *J. Biol. Chem.* 273, 12841–12845. doi:10.1074/jbc.273.21.12841

Kyrpides, N. C., and Woese, C. R. (1998). Archaeal Translation Initiation Revisited: The Initiation Factor 2 and Eukaryotic Initiation Factor 2B α-β-δ Subunit Families. *Proc. Natl. Acad. Sci. U.S.A.* 95, 3726–3730. doi:10.1073/pnas.95.7.3726

Labauge, P., Horzinski, L., Ayrignac, X., Blanc, P., Vukusic, S., Rodriguez, D., et al. (2009). Natural History of Adult-Onset eIF2B-Related Disorders: a Multi-Centric Survey of 16 Cases. *Brain* 132, 2161–2169. doi:10.1093/brain/awp171

Leegwater, P. A. J., Vermeulen, G., Könst, A. A. M., Naidu, S., Mulders, J., Visser, A., et al. (2001). Subunits of the Translation Initiation Factor eIF2B Are Mutant in Leukoencephalopathy with Vanishing White Matter. *Nat. Genet.* 29, 383–388. doi:10.1038/ng764

Leng, X., Wu, Y., Wang, X., Pan, Y., Wang, J., Li, J., et al. (2011). Functional Analysis of Recently Identified Mutations in Eukaryotic Translation Initiation Factor 2Bε (eIF2Bε) Identified in Chinese Patients with Vanishing White Matter Disease. *J. Hum. Genet.* 56, 300–305. doi:10.1038/jhg.2011.9

Li, M. M., Datto, M., Duncavage, E. J., Kulkarni, S., Lindeman, N. I., Roy, S., et al. (2017). Standards and Guidelines for the Interpretation and Reporting of Sequence Variants in Cancer. *J. Mol. Diagnostics* 19, 4–23. doi:10.1016/j.jmoldx.2016.10.002

Lorsch, J. R., and Dever, T. E. (2010). Molecular View of 43 S Complex Formation and Start Site Selection in Eukaryotic Translation Initiation. *J. Biol. Chem.* 285, 21203–21207. doi:10.1074/jbc.r110.119743

Ohlenbusch, A., Henneke, M., Brockmann, K., Goerg, M., Hanefeld, F., Kohlschütter, A., et al. (2005). Identification of Ten Novel Mutations in Patients with eIF2B-Related Disorders. *Hum. Mutat.* 25, 411. doi:10.1002/humu.9325

Pavitt, G. D. (2005). eIF2B, a Mediator of General and Gene-specific Translational Control. *Biochem. Soc. Trans.* 33 (Pt 6), 1487–1492. doi:10.1042/BST20051487

Pavitt, G. D., Yang, W., and Hinnebusch, A. G. (1997). Homologous Segments in Three Subunits of the Guanine Nucleotide Exchange Factor eIF2B Mediate Translational Regulation by Phosphorylation of eIF2. *Mol. Cell Biol.* 17, 1298–1313. doi:10.1128/mcb.17.3.1298

Pronk, J. C., van Kollenburg, B., Scheper, G. C., and Van Der Knaap, M. S. (2006). Vanishing White Matter Disease: a Review with Focus on its Genetics. *Ment. Retard. Dev. Disabil. Res. Rev.* 12 (2), 123–128. doi:10.1002/mrdd.20104

Scali, O., Di Perri, C., and Federico, A. (2006). The Spectrum of Mutations for the Diagnosis of Vanishing White Matter Disease. *Neurol. Sci.* 27, 271–277. doi:10.1007/s10072-006-0683-y

Sonenberg, N., and Hinnebusch, A. G. (2009). Regulation of Translation Initiation in Eukaryotes: Mechanisms and Biological Targets. *Cell* 136, 731–745. doi:10.1016/j.cell.2009.01.042

Van Der Knaap, M. S., Barth, P. G., Gabreëls, F. J., Franzoni, E., Begeer, J. H., Stroink, H., et al. (1997). A New Leukoencephalopathy with Vanishing White Matter. *Neurology* 48 (4), 845–855. doi:10.1212/wnl.48.4.845

Van Der Knaap, M. S., Breiter, S. N., Naidu, S., Hart, A. A. M., and Valk, J. (1999). Defining and Categorizing Leukoencephalopathies of Unknown Origin: MR Imaging Approach. *Radiology* 213, 121–133. doi:10.1148/radiology.213.1.r99se01121

Van Der Knaap, M. S., Leegwater, P. A. J., Könst, A. A. M., Visser, A., Naidu, S., Oudejans, C. B. M., et al. (2002). Mutations in Each of the Five Subunits of Translation Initiation Factor eIF2B Can Cause Leukoencephalopathy with Vanishing White Matter. *Ann. Neurol.* 51, 264–270. doi:10.1002/ana.10112

Van Der Knaap, M. S., van Berkel, C. G. M., Herms, J., van Coster, R., Baethmann, M., Naidu, S., et al. (2003). eIF2B-Related Disorders: Antenatal Onset and Involvement of Multiple Organs. *Am. J. Hum. Genet.* 73, 1199–1207. doi:10.1086/379524

Wu, Y., Pan, Y., Du, L., WangFAU - Gu, J. Q., GuFAU - Gao, Q. Z., GaoFAU - Li, Z. J., et al. (2009). Identification of Novel EIF2B Mutations in Chinese Patients with Vanishing White Matter Disease. *J. Hum. Genet.* 54 (2), 74–77. doi:10.1038/jhg.2008.10

Zhang, H., Dai, L., Chen, N., Zang, L., Leng, X., Du, L., et al. (2015). Fifteen Novel EIF2B1-5 Mutations Identified in Chinese Children with Leukoencephalopathy with Vanishing White Matter and a Long Term Follow-Up. *PloS One* 10 (3), e0118001. doi:10.1371/journal.pone.0118001

Conflict of Interest: The authors declare that the research was conducted in the absence of any commercial or financial relationships that could be construed as a potential conflict of interest.

frontiers | Frontiers in Bioengineering and Biotechnology

TYPE Review
PUBLISHED 26 August 2022
DOI 10.3389/fbioe.2022.920882

OPEN ACCESS

EDITED BY
Michele Iafisco,
National Research Council (CNR), Italy

REVIEWED BY
Sergio Baldari,
University of Messina, Italy
Sophia Sarpaki,
BIOEMTECH, Greece

*CORRESPONDENCE
Hui Zeng,
androps2011@hotmail.com
Lu Wang,
l_wang1009@jnu.edu.cn

SPECIALTY SECTION
This article was submitted to Nanobiotechnology, a section of the journal Frontiers in Bioengineering and Biotechnology

RECEIVED 15 April 2022
ACCEPTED 29 July 2022
PUBLISHED 26 August 2022

CITATION
Zhang S, Shang J, Ye W, Zhao T, Xu H, Zeng H and Wang L (2022), Recent developments on the application of molecular probes in multiple myeloma: Beyond [^{18}F]FDG.
Front. Bioeng. Biotechnol. 10:920882.
doi: 10.3389/fbioe.2022.920882

Recent developments on the application of molecular probes in multiple myeloma: Beyond [^{18}F]FDG

Shaojuan Zhang[1], Jingjie Shang[1], Weijian Ye[1], Tianming Zhao[2], Hao Xu[1], Hui Zeng[2]* and Lu Wang[1]*

[1]Center of Cyclotron and PET Radiopharmaceuticals, Department of Nuclear Medicine and PET/CT-MRI Center, The First Affiliated Hospital of Jinan University, Guangzhou, China, [2]Department of Hematology, The First Affiliated Hospital of Jinan University, Guangzhou, China

Multiple myeloma (MM) is a neoplastic plasma cell proliferative disorder characterized by various osteolytic bone destruction as a radiological morphological marker. Functional imaging, particularly nuclear medicine imaging, is a promising method to visualize disease processes before the appearance of structural changes by targeting specific biomarkers related to metabolism ability, tumor microenvironment as well as neoplastic receptors. In addition, by targeting particular antigens with therapeutic antibodies, immuno-PET imaging can support the development of personalized theranostics. At present, various imaging agents have been prepared and evaluated in MM at preclinical and clinical levels. A summary overview of molecular functional imaging in MM is provided, and commonly used radiotracers are characterized.

KEYWORDS

multiple myeloma, biomarkers, molecular functional imaging, positron emission tomography (PET), radiotracers

1 Introduction

Multiple myeloma (MM) is caused by abnormal plasma cell infiltration in the bone marrow and is a final presentation of a range of monoclonal gammopathies, characterized by clinical symptomatic CRAB features including hypercalcemia, renal insufficiency, anemia, and bone lesions. In the light of the amount of clonal bone marrow plasma cells and serum monoclonal protein, monoclonal gammopathy of undetermined significance (MGUS) and smoldering multiple myeloma (SMM) are defined as its asymptomatic and premalignant stages (Rajkumar et al., 2014; Kumar et al., 2017). The potential risk of SMM (10% per year) (Kyle et al., 2007) and MGUS (1%–1.5% per year) for progression to symptomatic MM, emphasizing the importance of early monitoring and management initiation for high-risk patients (Kyle et al., 2010). On the other hand, MM is not only a highly heterogeneous disease but is also relapsing-remitting cancer, which means MM is treatable but incurable (Yang et al., 2020). Additionally, due to underlying molecular variation, the clinical disease course and optimal treatment or re-treatment strategy vary from person to person (Hideshima et al., 2007). Thus, early. Accurate assessment of

residual MM-associated intramedullary and (or) extramedullary lesions is desirable for guiding further management. In 2016, the International Myeloma Working Group (IMWG) incorporated minimal residual disease (MRD) as a standard criterion in the evaluation of treatment response (Kumar et al., 2016). Recently, the utility of MRD negativity as an important prognostic marker for long-term survival in MM patients was confirmed by a large meta-analysis (Munshi et al., 2020).

New imaging techniques have come into being a part of the new Durie/Salmon PLUS staging system, considering anatomic and functional imaging for myeloma staging (Durie, 2006). Currently, modern recommended imaging technologies include whole-body low-dose computed tomography (WBLWCT), positron emission tomography/computed tomography (PET/CT), or whole-body magnetic resonance imaging (WB-MRI) (Mosebach et al., 2019; Terao and Matsue, 2022). A good detailed comparison of those imaging techniques have been reported by Zamagni, et al. (2019) In general, WBLDCT is a practical tool in the preliminary assessment of myeloma bone disease, considering its availability. For the differentiation between MGUS and SMM, which is warranted for serological and biopsy data, CT-guided biopsy is the gold standard (Mosebach et al., 2019). Combining with anatomical information from WBLWCT, PET/CT, imaged with radionuclides and WB-MRI tracked with hydrogen atom signal intensity with no radiation exposure, are recommended as reliable techniques for diagnostic workup and assessment and monitoring of therapy response in MM patients (Pawlyn et al., 2016; Ormond Filho et al., 2019). Due to the high spatial resolution of bone marrow, WB-MRI is highly recommended over [^{18}F]fluorodeoxyglucose ([^{18}F]FDG) PET/CT for the detection of the early and diffuse type of bone marrow infiltration, thus plays a key role in detecting small bone marrow infiltrations (~5 mm) in the clinical diagnosis of suspected SMM patients (Dimopoulos et al., 2015), also helping re-identify MRD negativity (Zamagni et al., 2020). In particular, MRI functional approaches, like dynamic contrast-enhanced imaging (DCE) and diffusion weight imaging (DWI). As a functional alternative to WB-MRI, PET/CT with [^{18}F]FDG can be used to depict contemporary lytic bone lesions along with glucose metabolism. More important, bone marrow signal in MRI scans (including DWI MRI) is greatly affected by individual age and treatment conditions and thus is suboptimal for early assessment of treatment response, but based on the ability of [^{18}F]FDG PET/CT to distinguish between metabolically active and inactive diseases, as well as the "self-pop out" of avid lesions, which has great advantages in detecting extramedullary disease (EMD) and defines the imaging MRD-negative response to therapy (Cavo et al., 2017). Hybrid PET/MRI, it should be noted, is a promising "double" functional imaging technique, combining the advantages of MRI in the detection of bone marrow involvement and [^{18}F]FDG PET in the prediction of both prognosis and treatment response (Mulé et al., 2020; Rama et al., 2022), systematic clinical data is required for proving the benefit of its sound added-value.

Functional imaging can objectively measure levels of pathogenic related-biomarker, making biomarker-targeted imaging a promising strategy to promote biologically personalized treatments for MM patients (Pawlyn and Davies, 2019), by enabling the identification of disease activity from different *in vivo* molecular perspectives such as metabolic activities, neoplastic microenvironment, and some specific receptors (Sachpekidis et al., 2019). Currently, [^{18}F]FDG PET/CT in nuclear imaging, as the main type of functional imaging modalities, however, [^{18}F]FDG is just an index reflecting glucose consumption, can't help but wonder if there is a better imaging probes with better performance ability than [^{18}F]FDG to assess and monitor MM lesions, especially, with increasing treatments with an immunotherapeutic agent by targeting specific receptors (Nadeem et al., 2020). This issue not only has spurred the use of "old" (originally mainly used for other tumors) imaging probes in MM, but inspired "new" imaging probes been developing for imaging MM (shown in Figure 1). (de Waal et al., 2017) Among these, immuno-PET which uses therapeutic antibodies to identify specific surface antigens has shown great promise in radio-immunotherapy and treatment monitoring, including detection of MRD (Pandit-Taskar, 2018). In perspective of different mechanisms of medical imaging, this review discusses the applications of variously reported imaging probes, mainly PET radiotracers, for their potential further use compared to [^{18}F]FDG in MM.

2 Mechanism of medical imaging

2.1 Metabolic activity

2.1.1 Glucose

[^{18}F]FDG, a glucose analog, is subjected to the glucose metabolism pathway after intravenous injection. High retention of [^{18}F]FDG is associated with active energy metabolism in myeloma cells and is related to increased numbers of glucose transporters (GLUT), mainly GLUT-1 and GLUT-3 (Pauwels et al., 1998). Subsequent phosphorylation of [^{18}F]FDG by hexokinase makes it unable to escape cells or follow the glucose pathway, trapping it intracellularly (Kanazawa et al., 1986). To obtain optimal imaging qualities, some pre-scan patient preparations, including fasting, confirmation of normal blood glucose levels and a post-injection rest period, are required. In most clinical cases, PET is combined with CT to allow precise anatomical localization of the area of high tracer accumulation, and data is quantified as a standardized uptake value (SUV), traditionally SUVmax, SUVmean, and SUVratio (commonly indexed to liver values) (Huang, 2000). Under normal physiological states, homogeneous uptake of [^{18}F]FDG in the

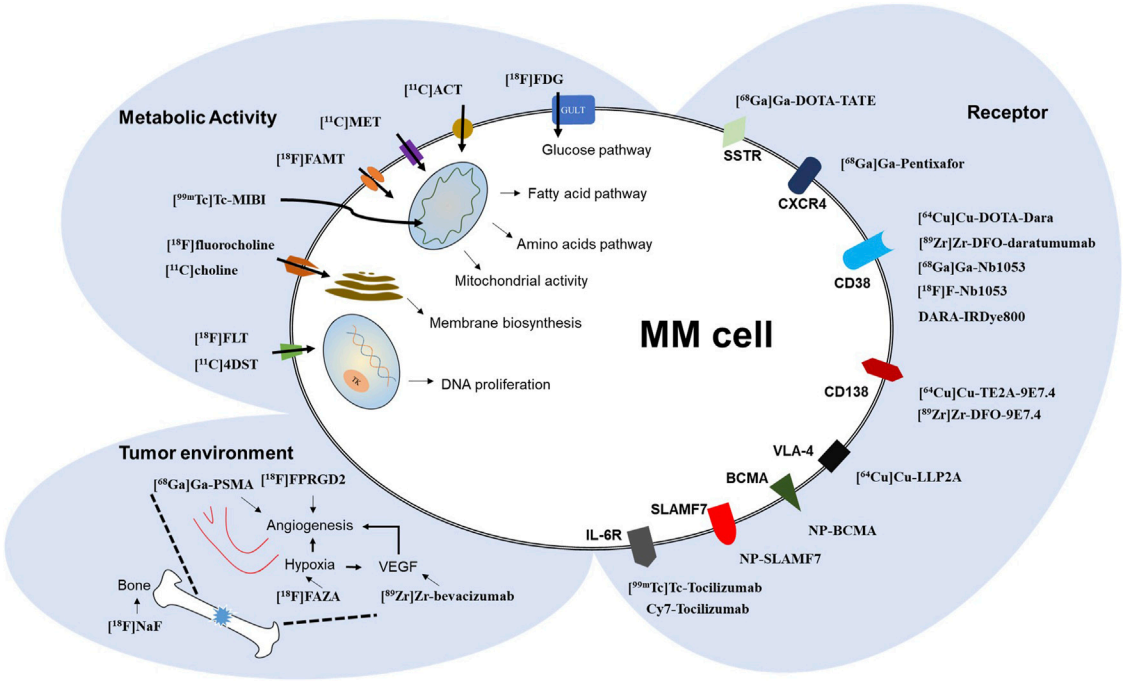

FIGURE 1
Schematic diagram of MM molecular imaging targets and associated imaging probes.

TABLE 1 Proposed refinement of the PET response criteria after therapy.

PET response after therapy	Response criteria
complete metabolic response	Uptake ≤ liver activity in bone marrow sites and focal lesion(s) previously involved (including extra-medullary and para-medullary disease) (DS1–3)
partial metabolic response	Decrease in the number and/or activity of bone marrow/focal lesion(s) present at baseline, but persistence of lesion(s) with uptake > liver activity (DS 4 or 5)
stable metabolic disease	No significant change in bone marrow/focal lesion(s) compared to baseline
progressive metabolic disease	New focal lesion(s) compared to baseline consistent with myeloma

bone marrow is low and less intense than that in the liver. A positive scan result with focal or diffuse active bone marrow uptake indicates that the disease is at an active and advanced stage, while a negative scan means a remission stage (van Lammeren-Venema et al., 2012). Evidence has shown that the number of abnormal avid lesions and associated changes in metabolic uptake after treatment are highly related to patient outcome, and can serve as an independent prognostic factor (Zamagni et al., 2016). For newly diagnosed MM patients receiving therapy, the uptake of bone lesions at levels lower than liver uptake can be thought of as a complete metabolic response, as referenced in the PET response criterion (shown in Table 1), (Zamagni et al., 2021) and is intertwined with MRD negativity.

Many factors can cause false-positive or negative results, including 1) patients lacking the hexokinase enzyme (10%–15%) critical to trapping [^{18}F]FDG in cells (Rasche et al., 2017); 2) changes in bone marrow uptake after therapy (e.g., recent chemotherapeutic drugs or use of cell growth factors) (Sugawara et al., 1998); 3) non-myeloma-associated high uptake (e.g., benign bone inflammation changes). Dynamic tracking can be combined with clinical patient information to reduce misinterpretation. However, more sensitive and specific imaging probes represent preferable alternative approaches for improving MM detection accuracy, which is complementary to the values of [^{18}F]FDG imaging (shown in Tables 2, 3).

2.1.2 Fatty acid

Lipogenesis is a shared feature of a variety of malignant cells, and increased fatty acid synthase (FAS) expression has been

TABLE 2 Reported MM related imaging probe at clinical evaluation level.

Study index; Ref	Imaging probe	Clinical MM setting	Characteristic/Compared to [^{18}F]FDG PET results
Ho CL 2014; Ho et al. (2014)	[^{11}C]ACT	35 untreated patients (26 with MM, 5 with SMM, and 4 with MGUS)	1. MM patients: higher sensitivity (84.6% vs. 57.7%) and specificity (100% vs. 93.1%) compared to MRI 2. SMM and MGUS patients: negative in [^{11}C]ACT, but 2 MGUS positive in [^{18}F]FDG
Lin C 2014; Lin et al. (2014)	[^{11}C]ACT	15 MM patients	1. Diffuse lesions: higher detection rate (100% vs. 60%) with higher SUVmax (7.4 ± 3.9 vs. 3.3 ± 1.7) 2. Focal lesions: higher detection ability (59 lesions vs. 29 lesions) with higher SUVmax (11.4 ± 3.3 vs. 6.6 ± 3.1) 3. Response assessment: diffuse bone marrow uptake reduction of SUVmax (52% vs. 22%)
Nanni C 2007; Nanni et al. (2007)	[^{11}C]choline	10 MM patients	bone lesions: comparable detection ability (37 lesions vs. 22 lesions) with higher SUVmax (5.0 vs. 3.8)
Cassou-Mounat T 2016; Cassou-Mounat et al. (2016)	[^{18}F]fluorocholine	21 MM patients	bone lesions: higher detection ability (121–124 lesions vs. 69–71 lesions) with higher SUVmax (in 71%–73% lesions)
Meckova Z 2018; Meckova et al. (2018)	[^{18}F]fluorocholine	5 MM patients	bone lesions: higher detection ability (134 lesions vs. 64 lesions) with comparable SUVmax (6.6 ± 1.6 vs. 6.5 ± 1.8)
Nakamoto Y 2013; Nakamoto et al. (2013)	[^{11}C]MET	20 patients (15 with MM and 5 with plasmacytoma)	bone lesions: comparable detection ability (156 lesions vs. 58 lesions) with higher SUVmax (10.3 ± 5.6 vs. 3.4 ± 2.7)
Okasaki M 2015; Okasaki et al. (2015)	[^{11}C]MET	46 patients with MM and 3 with MGUS (21 previously untreated, 43 restaged after treatment)	1. Bone lesions: higher detection ability (39 lesions vs. 33 lesions) with higher SUVmax 5.19 ± 2.40 vs. 3.35 ± 1.70) 2. Lesion activity: higher sensitivity (86.7% *vs.* 60.0%) and equal specificity (76.1% vs. 76.1%) compared to marrow plasma cells cytology
Lapa C 2017; Lapa et al. (2017)	[^{11}C]MET	78 patients (4 with solitary plasmacytoma, 5 with SMM and 69 with symptomatic MM)	1. MM patients: higher detection rate (75.6% vs. 60.3%) 2. EMD: higher detection rate (72 foci vs. 44 foci) 3. The first evidence of histologically proven [^{18}F]FDG negative MM detectable by [^{11}C]MET
Lapa C 2019; Lapa et al. (2019)	[^{11}C]MET [^{11}C]choline	19 patients (18 with MM and 1 with solitary bone plasmacytoma)	Bone lesions: higher detection rate in 42.1% patients of [^{11}C]MET than [^{11}C]choline
Isoda A 2012; Isoda et al. (2012)	[^{18}F]FAMT	11 MM patients (3 with newly diagnosed and 8 with relapsed)	bone lesions: comparable detection ability with lower SUVmax (2.0 ± 1.0 vs. 3.1 ± 1.2)
Luthra K 2014; Luthra et al. (2014)	[^{99m}Tc]Tc-MIBI	84 patients (24 with newly diagnosed MM; 35 with treated MM, 2 with SMM, 4 cwith plasmacytoma, 13 with MGUS and 3 with suspected MM)	1. [^{99m}Tc]Tc-MIBI uptake earlier than CT 2. Follow-up patients: the presence or absence of [^{99m}Tc]Tc-MIBI uptake could differentiate active from old burnt-out lesions
Mosci C 2020; Mosci et al. (2020)	[^{99m}Tc]Tc-MIBI	62 newly diagnosed MM patients	1. Diffuse lesions: higher detection rate (78% vs. 58%) 2. Focal lesions: lower detection rate (54% vs. 81%)
Sachpekidis C 2018; Sachpekidis et al. (2018)	[^{18}F]FLT	8 myeloma patients (4 symptomatic MM and 4 with SMM)	bone lesions: lower detection ability (17 lesions vs. 48 lesions)
Okasaki M 2015; Okasaki et al. (2015)	[^{11}C]4DST	46 patients with MM and 3 with MGUS (21 previously untreated, 43 restaged after treatment)	1. Bone lesions: higher detection ability (40 lesions vs. 33 lesions) with higher SUVmax (8.30 ± 6.24 vs. 3.35 ± 1.70) 2. Lesion activity: higher sensitivity (93.3% vs. 60.0%) and lower specificity (71.4 % vs. 76.1%) compared to marrow plasma cells cytology
Withofs N 2017; Withofs et al. (2017)	[^{18}F]FPRGD2	4 MM patients (2 with newly diagnosed and 2 with relapsed)	bone lesions: lower detection rate than WBCT (44 lesions vs. 80 lesions) and [^{18}F]NaF/[^{18}F]FDG PET/CT (44 lesions vs. 56 lesions)
de Waal EG 2015; de Waal et al. (2015)	[^{18}F]FAZA	5 relapsed MM patients	bone lesions: negative scan
de Waal EG 2015; de Waal et al. (2017)	[^{89}Zr]Zr-bevacizumab	5 relapsed MM patients	bone lesions: negative scan

(Continued on following page)

TABLE 2 (*Continued*) Reported MM related imaging probe at clinical evaluation level.

Study index; Ref	Imaging probe	Clinical MM setting	Characteristic/Compared to [^{18}F]FDG PET results
Alabed YZ 2020; Alabed (2020)	[^{68}Ga]Ga-PSMA	1 patient with multiple solitary plasmacytomas	bone lesions: positive scan
Dyrberg E 2017; Dyrberg et al. (2017)	[^{18}F]NaF	14 patients newly diagnosed MM	1. Bone lesions: higher detection ability (41 lesions vs. 13 lesions) 2. EMD: not recommended
Sonmezoglu K 2017; Sonmezoglu et al. (2017)	[^{68}Ga]Ga-DOTA-TATE	19 MM patients	bone lesions: comparable detection ability (108 lesions vs. 112 lesions)
Pan Q 2020; Pan et al. (2020)	[^{68}Ga]Ga-Pentixafor	30 patients with newly diagnosed MM	1. MM patients: higher detection rate (93.3% vs. 53.3%) 2. Diffuse lesions: higher detection rate (88.2% vs. 29.4%) with higher SUVmax (7.8 ± 3.5 vs. 2.5 ± 0.9) 3. Focal lesions: higher detection rate (92.3% vs. 69.2%) with higher SUVmax (20.4 ± 17.4 vs. 8.9 ± 5.6) 4. [^{68}Ga]Ga-Pentixafor uptake values related to tumor burden
Ulaner GA 2020; Ulaner et al. (2020)	[^{89}Zr]Zr-DFO-daratumumab	10 MM patients	1. MM patients: 50% detection rate 2. Identify lesions in one patient not seen at [^{18}F]FDG PET/CT.

TABLE 3 Reported MM related imaging probe at pre-clinical evaluation level.

Study index; Ref	Imaging probe	Pre-clinical MM setting	Characteristic/Compared to [^{18}F]FDG PET results
Soodgupta D 2016; Soodgupta et al. (2016)	[^{64}Cu]Cu-LLP2A	5TGM1-GFP cells bearing mice	1. High specificity 2. Comparable SUVmax with [^{18}F]FDG
Bailly C 2019; Bailly et al. (2019)	[^{64}Cu]Cu-TE2A-9E7.4 [^{89}Zr]Zr-DFO-9E7.4	5T33-MM cells bearing mice	higher tumor to background ratio of [^{64}Cu]Cu-TE2A-9E7.4 than [^{89}Zr]Zr-DFO-9E7.4 at 24 h post-injection (4.08 ± 1.09 %ID/g vs. 1.42 ± 0.24 %ID/g)
Caserta E 2018; Caserta et al. (2018)	[^{64}Cu]Cu-DOTA-Dara	MM.1S GFP$^+$/Luc$^+$ cells bearing mice	higher resolution and specificity than [^{18}F]FDG
Ulaner GA 2020; Ulaner et al. (2020)	[^{89}Zr]Zr-DFO-daratumumab	CD38$^+$ OPM2 cells bearing mice	with and without blocking bone marrow uptake (5.4% ID/g vs. 16.2% ID/g)
Wang C 2021; Wang et al. (2021)	[^{68}Ga]Ga-NOTA-Nb1053	MM.1S cells bearing mice	higher tumor to background ratio than [^{18}F]FDG
Wei W 2021; Wei et al. (2021)	[^{18}F]F-Nb1053	MM.1S cells bearing mice	high specificity through daratumumab premedication
Cho N 2021; Cho et al. (2021)	DARA-IRDye800	MM.1S GFP$^+$/Luc$^+$ cells bearing mice	1. High tumor to background ratio (5- and 18-fold) 2. High specificity (11-fold decrease) after therapeutic doses of daratumumab
Detappe A 2019; Detappe et al. (2019)	NP-BCMA NP-SLAMF7	MM.1S GFP$^+$/Luc$^+$ cells bearing mice	higher sensitivity and specificity of NP-BCMA than NP-SLAMF7
Ghai A 2021; Ghai et al. (2021)	[^{89}Zr]Zr-DFO-elotuzumab	MM.1S cells bearing mice	higher sensitivity and specificity than [^{18}F]FDG
Camacho X 2021; Camacho et al. (2021)	[^{99m}Tc]Tc-Tocilizumab Cy7-Tocilizumab	MM.1S cells bearing mice	longer tumor uptake time of Cy7-Tocilizumab than [^{99m}Tc]Tc-Tocilizumab

observed in MM samples and human myeloma cell lines (Wang et al., 2008). [^{11}C]acetate ([^{11}C]ACT), an exogenous acetate, can be rapidly taken up by cells and metabolized to produce acetyl CoA, a carbon source for fatty acid synthesis. In a heterogeneous group of MM patients, [^{11}C]ACT PET/CT exhibited better overall sensitivity and specificity than [^{18}F]FDG. Furthermore, [^{11}C]ACT PET/CT imaging, but not [^{18}F]FDG imaging, was negative for indolent plasma cell neoplasms (SMM and MUGS) (Ho et al., 2014). A similar study also showed that, for newly diagnosed MM patients, [^{11}C]ACT imaging has a higher detection rate for a focal or infiltrated myeloma lesions than [^{18}F]FDG. Moreover, this positive treatment response was

visualized via [^{11}C]ACT PET/CT as a significant decrease in SUVmax (listed in Table 2). (Lin et al., 2014)

2.1.3 Membrane biosynthesis

Choline, which can be phosphorylated by choline kinase into phosphatidylcholine, is involved in cell membrane biosynthesis. The use of [^{11}C]choline for MM patients can be justified based on the increase in proliferating malignant plasma cells with high demands related to membrane metabolism and growth. For MM patients, [^{11}C]choline imaging was performed similarly to [^{18}F]FDG imaging for lesion detection, treatment evaluation, and monitoring (Nanni et al., 2007). Subsequent PET imaging studies of choline were performed with labeled fluorine-18. In relapsing MM patients, [^{18}F]fluorocholine PET/CT indicated that a significantly higher number of lesions were detected compared to [^{18}F]FDG (Cassou-Mounat et al., 2016). Another study that applied [^{18}F]fluorocholine to the detection of skeletal involvement showed that [^{18}F]fluorocholine PET/CT detected about twice as many bone lesions as [^{18}F]FDG, particularly on the skull bone (listed in Table 2). (Meckova et al., 2018) These results are likely due to higher background metabolic level noise for [^{18}F]FDG.

2.1.4 Amino acids

Amino acids are important substrates in the biosynthesis of lipid and protein molecules. [^{11}C]methionine ([^{11}C]MET) possesses a higher specificity than [^{18}F]FDG for the detection of original and recurrent brain tumors and, due to its low physiological background, can also delimit surgical boundaries (Ogawa et al., 1987). Extensive MET is required for the unrestricted proliferation of plasma cells, along with the excessive synthesis of monoclonal immunoglobulins. Cellular transport of [^{11}C]MET is determined by the sodium-independent L-type amino acid transporter (LAT). The physiological uptake of [^{11}C]MET is distributed in the bone marrow and liver. High expression of LAT1 has been identified as a relevant prognostic factor associated with overall poor long-term survival (Isoda et al., 2014). Regarding patients, a study showed that more abnormal lesions were identified by [^{11}C]MET PET/CT than by [^{18}F]FDG, making it useful in grading disease stage (Nakamoto et al., 2013). Another study indicated that [^{11}C]MET PET/CT detected a greater number of positive uptake lesions with more clarity than [^{18}F]FDG, especially with 10–30% plasma cells in the bone marrow (Okasaki et al., 2015). In a study of 78 patients, the largest so far, [^{11}C]MET PET/CT was shown to have higher sensitivity than [^{18}F]FDG in detecting myeloma infiltrated lesions within or outside of bone marrow, as confirmed by histological biopsy. [^{11}C]MET can be potentially applied to disease staging and re-staging with higher accuracy than [^{18}F]FDG (Lapa et al., 2017). In addition, the same group also compared [^{11}C]MET to [^{11}C]choline, and the advantages of [^{11}C]MET were supported by a higher detection rate of MM bone lesions in approximately 40% of patients, as well as higher SUVmax (listed in Table 2). (Lapa et al., 2019)

^{18}F α-methyl tyrosine ([^{18}F]FAMT), a fluorine-18 labeled version of the unnatural amino acid methyltyrosine, can also be transported into cells through LAT-1. Likewise, the uptake of [^{18}F]FAMT by lesions is positively correlated with the expression of LAT-1. In MM patients, a comparable detection rate was observed for [^{18}F]FAMT and [^{18}F]FDG imaging, but uptake discrepancies were evident in several presented lesions (listed in Table 2). (Isoda et al., 2012)

2.1.5 Mitochondrial activity

Technetium 99 m sestamibi ([^{99m}Tc]Tc-MIBI) is a typical radiotracer used in single-photon emission computed tomography (SPECT) to investigate myocardial perfusion (Alexander and Oberhausen, 1995). Generally, the spatial resolution of SPECT is much lower than that of PET. The high lipid solubility of [^{99m}Tc]Tc-MIBI allows it to enter the mitochondria along with the negative membrane potential difference formed by membrane electrophysiological activities. The lesion concentration reflects the high energy metabolism levels found within active malignant plasma cells. A study with 112 [^{99m}Tc]Tc-MIBI SPECT was performed in 84 myeloma-associated patients, scan results indicated that the concentration of MIBI in myeloma lesions, corresponds with unchanged and changed radiological changes in CT, could expose earlier ongoing disease activity or old treated lesions (Luthra et al., 2014). In newly diagnosed MM patients, diffuse involvement of bone marrow was better visualized by [^{99m}Tc]Tc-MIBI SPECT scan than by [^{18}F]FDG PET/CT scan but was less efficient for focal lesions (listed in Table 2). (Mosci et al., 2020) [^{99m}Tc]Tc-MIBI seems to be particularly useful in evaluating the existence of extensive infiltration to avoid underestimation of disease status, meanwhile, the low spatial resolution of SPECT limits the identification of small lesions.

2.1.6 DNA proliferation

Pyrimidine 3-deoxy-3- (Mulé et al., 2020)F-fluorothymidine ([^{18}F]FLT) and the newer tracer 4′-methyl- (Terao and Matsue, 2022)C-thiothymidine ([^{11}C]4DST) can participate in DNA synthesis as thymidine analogs and have been used to image high DNA proliferation activity in cells (Toyohara et al., 2011; Peck et al., 2015). After being phosphorylated by thymidine kinase 1 (TK1), both compounds become metabolically trapped within cells. Due to the structures, [^{11}C]4DST is more stable than [^{18}F]FLT, and de-phosphorylation occurs relatively rarely. Like [^{11}C]MET, [^{11}C]4DST PET/CT can detect more bone lesions per patient than [^{18}F]FDG in patients with low levels of plasma cell infiltration (10–30%) (Okasaki et al., 2015). However, [^{11}C]4DST also tends to accumulate in active hematopoietic marrow, and has to be associated with the patient background to distinguish from diffuse MM lesions. In contrast, preliminary data indicate that [^{18}F]FLT is not suitable for initial MM

diagnostics due to the interference of background bone marrow activity in the cell compartment (Sachpekidis et al., 2018). Otherwise, [^{18}F]FLT can be used to obtain updated information on the distribution of normal bone marrow tissue during therapy (listed in Table 2). (Hayman et al., 2011)

2.2 Tumor microenvironment

2.2.1 Angiogenesis & hypoxia

Oxygen consumption is increased with the proliferation of malignant MM cells, resulting in a relatively hypoxic cellular environment that ultimately activates the vascular endothelial growth factor (VEGF) signaling pathway (Apte et al., 2019), leading to tumor angiogenesis. ^{18}F-FB-NH-mini-PEG-E [c(RGDyK)]$_2$ ([^{18}F]FPRGD2) is a standard PET tracer for imaging integrin $\alpha_v\beta_3$, a type of integrin highly expressed by vascular endothelial cells, and can be used to image tumor angiogenesis (Wu et al., 2007). However, in relapsed MM patients, [^{18}F]FPRGD2 PET/CT is not particularly helpful and was dependent on the presence of obvious lytic bone lesions found by CT (listed in Table 2). (Withofs et al., 2017)

1-α-D:-(5-deoxy-5-^{18}F-fluoroarabinofuranosyl)-2-nitroimidazole ([^{18}F]FAZA) is a PET tracer used to identify hypoxic conditions associated with tumor metabolism (Wuest and Wuest, 2013). When cells are oxygen-deficient, nitroimidazole reduction products will bind to intracellular biomacromolecules and remain in cells. One report indicated that no increased uptake of [^{18}F]FAZA was found for any of five relapsing MM patients, while numerous focal uptakes presented on [^{18}F]FDG PET/CT (de Waal et al., 2015). Likely due to the hypoxic nature of the whole bone marrow compartment, no differences were observed between MM lesions and their surroundings. Bevacizumab, the first humanized nanoantibody (mAb) approved by the Food and Drug Administration (FDA) to inhibit tumor angiogenesis, targets the VEGF receptor. Unfortunately, like [^{18}F]FAZA, PET imaging with zirconium-89 labeled bevacizumab failed to detect significant abnormalities in all patients (listed in Table 2). (de Waal et al., 2017)

Prostate-specific membrane antigen (PSMA) is a characteristic biomarker for prostate cancer cells (Wester and Schottelius, 2019), and enhanced expression has also been observed in tumor vasculature. A case report indicated that ^{68}Ga-prostate-specific membrane antigen-targeted ligand PET imaging can be used to visualize multiple lytic bone lesions throughout the spine (listed in Table 2), (Alabed, 2020) but the definite application in MM is still unclear.

2.2.2 Osteoclastic lesions

Osteoclastic lesions result from increased plasma cell infiltration in the bone marrow microenvironment, which stimulates bone resorption and impedes bone formation (Mukkamalla and Malipeddi, 2021). The PET tracer [^{18}F]NaF is 'bone-depositing', reflecting bone osteoblastic reactions related to regional blood flow. Thus, the typical accumulation of [^{18}F]NaF around lesions can be explained by a secondary osteoblastic reaction, indicating that [^{18}F]NaF is suitable for comprehensive evaluation of bone injury in late stages (listed in Table 2). (Dyrberg et al., 2017) And, [^{18}F]NaF cannot detect EMD logically.

2.3 Receptor targeted imaging

2.3.1 Somatostatin receptors

Somatostatin receptor scintigraphy (SRS) using [^{111m}In]In-pentetreotide has been applied in the workup of neuroendocrine tumors (NETs) for visualizing somatostatin receptors (SSTR), particularly subtypes 2 and 5. Due to the advantages of PET regarding spatial resolution, ^{68}Ga-tetraazacyclododecane-tetraacetic acid-octreotate ([^{68}Ga]Ga-DOTA-TATE) PET/CT has largely replaced SRS for staging NET (Ambrosini et al., 2010). *In vitro* studies have shown that functional SST is expressed by all MM cell lines, predominantly SSTR5 (Georgii-Hemming et al., 1999). No significant difference was observed between [^{18}F]FDG PET/CT, but diffuse bone marrow uptake can be better shown with [^{68}Ga]Ga-DOTA-TATE (listed in Table 2). (Sonmezoglu et al., 2017)

2.3.2 Very late antigen-4

Very late antigen-4 (VLA-4), a transmembrane adhesion receptor expressed on normal plasma cells, is an important contributor to interactions between plasma cells and the extracellular matrix and bone marrow stromal cells (Schlesinger and Bendas, 2015). Upregulated expression of VLA-4 has been confirmed for myeloma cells and surrounding tissues. With a high binding affinity, N-[[4-[[[(2-ethylphenyl)amino]carbonyl]amino]phenyl]acetyl]-N (epsilon)-6-[(2E)-1-oxo-3-(3-pyridinyl-2-propenyl)]-L-lysyl-L-2-aminohexanedioyl-(1-amino-1-cyclohexane)carboxamide (LLP2A) is a peptidomimetic ligand for VLA-4. LLP2A was conjugated to 1,4,8,11-tetraazacyclotetradecane-1-(methane phosphonic acid)-8-(methane carboxylic acid) (CB-TE1A1P) chelators for cuprum-64 labelling. Favorable pre-clinical results regarding the biodistribution and dosimetry of [^{64}Cu]Cu-LLP2A imaging have been reported for MM mice models, suggesting that this approach is a promising candidate for further imaging of activated VLA-4 in humans (listed in Table 3). (Soodgupta et al., 2016)

2.3.3 Chemokine receptor-4

A member of the G-protein-coupled chemokine receptor family, chemokine receptor-4 (CXCR4) is mainly expressed in bone marrow primitive hematopoietic cells and is involved in the survival of myeloma cells (Philipp-Abbrederis et al., 2015). Plerixafor (Wang et al., 2020), an exogenous

CXCR4 antagonist with high binding affinity, can disrupt adhesive tumor-stroma interactions and achieve treatment goals. [^{68}Ga]Ga-pentixafor PET/CT has been proposed as a theranostics tracer targeting CXCR4 for directed radio-targeted treatment with [^{177}Lu]Lu-pentixafor (or [^{90}Y]Y-pentixafor). In newly diagnosed MM patients, [^{68}Ga]Ga-pentixafor exhibited superior detection ability for myeloma lesions compared to [^{18}F]FDG (93.3% vs. 53.3%). What's more, quantitative analysis results indicated that the uptake of [^{68}Ga]Ga-pentixafor in bone marrow is a promising biomarker for tumor burden assessment, as it is positively correlated with serum β2-microglobulin and other clinical tumor burden parameters (Pan et al., 2020). A profound therapeutic impact was observed on two heavily pretreated patients following CXCR4-directed lutetium-177 or yttrium-90 endo-radiotherapy, with patients exhibiting a remarkable [^{18}F]FDG uptake reduction in intra and extra-medullary lesions despite the ultimately limited 3–6 months progression-free survival (listed in Table 2). (Herrmann et al., 2016)

2.3.4 Cluster of differentiation 138 and 38

Cluster of differentiation (CD) 138, or syndecan-1, is a type of transmembrane proteoglycan found at high levels on the surface of myeloma cells (Sanderson and Yang, 2008). It has been used as a positive sorting marker in the preconcentration of plasma cells for efficient cytogenetic analysis of bone marrow samples. In this respect, CD138 may be an important and potentially beneficial target for imaging and mAbs-based immunotherapy. Cuprum-64 or zirconium-89 labeled anti-CD138 antibodies were realized by incorporating 1,4,8,11-tetraazabicyclo [6.6.2]hexadecane (TE2A) or defetoxamine (DFO) chelator into the antibodies, thus delivering the immuno-PET tracers [^{64}Cu]Cu-TE2A-9E7.4 and [^{89}Zr]Zr-DFO-9E7.4, respectively. In the bone lesions of MM-bearing mice, higher uptake was observed during both PET imaging for [^{64}Cu]Cu-TE2A-9E7.4 and [^{89}Zr]Zr-DFO-9E7.44, but not for [^{18}F]FDG. In addition, the osteophilicity of zirconium-89 resulted in undesired bone background. The higher signal-to-noise ratio of [^{64}Cu]Cu-TE2A-9E7.4 indicated a potential use as a new specific option for MM imaging diagnosis (listed in Table 3). (Bailly et al., 2019) What's more, mouse models and dosimetry results corroborated the feasibility of radioimmunotherapy for the treatment of advanced-stage MM using anti-CD138 monoclonal antibody namely B-B4, which was radiolabeled with bismuth-213 to promote longer median survival (Chérel et al., 2013).

Daratumumab (Dara), a humanized IgG1K mAb approved by the FDA for use in relapsed MM (Lokhorst et al., 2015), is targeted to the receptor cluster of differentiation 38 (CD38) upregulated in malignant plasma cells but remained low-level expression by surrounding hematopoietic cells. Therefore, CD38-targeted imaging offers a novel approach to the dynamic and invasive assessment of its expression in MM. In preclinical studies, [^{64}Cu]Cu-DOTA-Dara displayed satisfactory potency for CD38 imaging on the surface of MM cell lines, primarily associated with bone infiltration foci. The higher specificity of [^{64}Cu]Cu-DOTA-Dara PET/CT compared to [^{18}F]FDG supports possible clinical applications for MRD detection (listed in Table 3). (Caserta et al., 2018) Recently, zirconium-89 labeled CD38-targeting antibodies for MM were generated using the chelator DFO, providing the first published proof-of-principle for chemical synthesis, preclinical evaluation, and Phase 0 imaging in humans (Ulaner et al., 2020). The results showed that [^{89}Zr]Zr-DFO-daratumumab has a robust ability to visualize CD38 in the murine model (listed in Table 3), and the use of this immuno-PET tracer could be a valuable diagnostic approach due to its high specificity. In addition, full antibody imaging means that a single injection can be sufficient for four PET/CT scans on different days. In humans, the dosimetry of [^{89}Zr]Zr-DFO-daratumumab was found to be acceptable and within safe limits. The Phase 0 clinical trials by [^{89}Zr]Zr-DFO-daratumumab PET/CT imaging study included 10 MM patients and half of them demonstrated avidity on osseous lesions, especially one patient who demonstrated unexpected focal tracer uptake previously undetected by ^{18}F-FDG, consistent with the lack of uptake in low CD38 expression lesions demonstrated by molecular detection approaches (listed in Table 2). By labelling a CD38-specific nanobody (Nb1053) with gallium-68 (Wang et al., 2021) or fluorine-18 (Wei et al., 2021), two preclinical studies indicated that Nb1053-based molecular imaging radiotracers may be useful for MM diagnosis and follow-up (listed in Table 3). Another imaging technique is NIR fluorescence imaging. Preclinical evaluation of DARA-IRDye800, in which DARA conjugated to the NIR fluorophore IRDye800CW, revealed a significant (~10×) reduction *in vivo* in fluorescence intensity for the treated group (listed in Table 3). (Cho et al., 2021)

2.3.5 B cell maturation antigen and signaling lymphocyte activation molecule 7

B cell maturation antigen (BCMA) is a member of the tumor necrosis factor receptor superfamily that is found almost exclusively on mature B cells. Its expression level increases significantly in MM cells, and its expression level is positively correlated with MM progression (Shah et al., 2020). In addition, signaling lymphocyte activation molecule 7 (SLAMF 7), which is expressed on immune cells including plasma cells, is a receptor involved in regulating MM cell migration within bone marrow stroma (Malaer and Mathew, 2017). By combining ultra-small sub-5 nm gadolinium-containing nanoparticles (NP) with BCMA and SLAMF 7 targeted antibodies, NP-BCMA and NP-SLAMF7 MR probes were successfully generated. Whole-body imaging of MM tumor-bearing mice showed that BCMA not only had better specificity than SLAMF 7 but also supported clearer imaging of lesions (listed in Table 3). (Detappe et al., 2019)

In terms of radiotracers, elotuzumab, a human monoclonal antibody against SLAMF7 that has been approved by the FDA for use in relapsed MM, has been labeled with zirconium-89. Micro-PET imaging with [^{89}Zr]Zr-DFO-elotuzumab in MM tumor mice indicated that it can specifically identify bone lesions with high expression of SLAMF7. SUVmax was significantly higher than that of [^{18}F]FDG, suggesting that [^{89}Zr]Zr-DFO-elotuzumab can be used to evaluate changes in tumor load after elotuzumab treatment (listed in Table 3). (Ghai et al., 2021) Regarding immunotherapy, BCMA would be a better choice due to its exclusively high expression in malignant plasma cells. Remarkable clinical effects have been witnessed in patients with relapsed/refractory multiple myeloma (RRMM) following antibody-drug conjugate (ADC) treatment, a type of BCMA-targeted therapeutics (Demel et al., 2021). Thus, further incorporation of PET radioisotopes with antibodies targeted to BCMA may be pursued to enhance sensitivity.

2.3.6 Interleukin-6 receptor

Interleukin-6 (IL-6) is a cytokine with broad functions in inflammation and immunity that has been identified as a proliferative factor for MM (Zhang et al., 1992). The results of an early preclinical imaging study using technetium-99 m labeled or fluorophore Cy7-labeled tocilizumab, a humanized Ab that binds to the IL-6 receptor, showed that both [^{99m}Tc]Tc-tocilizumab and Cy7-tocilizumab require a long time for uptake into MM engrafted tumors, with up to 72 h required for Cy7-tocilizumab (listed in Table 3), (Camacho et al., 2021) thus hampering further clinical translational application.

3 Conclusion

[^{18}F]FDG, one of the most common medical probes used in MM functional imaging, has provided valuable guidance for the management of MM patients, like standard WB-MRI. Standardized clinical care and proper imaging evaluation criteria have been promoted for wide distribution. Due to the limitations of [^{18}F]FDG in imaging MM, various probes, especially the radioisotope labeled PET tracers, have been suggested and assessed in clinical patients with related malignancies or during preclinical evaluation. Different imaging agents were used to identify various pathological features of MM; while their values are worth consideration, the primary pursuit in this review is superior performance compared to [^{18}F]FDG (Table 2). Some of these agents, including metabolic tracers such as [^{11}C]ACT, [^{11}C]MET, and [^{11}C]choline, have exhibited promising results in the detection of lesions in MM patients, and tend to have higher SUVmax than [^{18}F]FDG. Based on the data reported so far, it may be suggested that metabolic characterization of lipid and protein metabolism can be more accurate than glucose metabolism in the early diagnosis, disease staging, and treatment response monitoring of MM. Meanwhile, by its short half-life ($t_{1/2}$ = 20.4 min), carbon-11 makes a complementary PET/CT scan with [^{18}F]FDG on the same day realizable. But their use is somewhat limited by the requirement for an on-site cyclotron and the only very few nuclear medicine centers so far. For [^{11}C]choline, fluorine-18 ($t_{1/2}$ = 109.8 min) labeled choline ([^{18}F]fluorocholine) could be a good alternative. In terms of the background metabolic level noise, some metabolic PET tracers, such as [^{18}F]FLT, [^{18}F]fluorocholine, and [^{11}C] choline, has unfavorable physiological distribution, characterized by increased uptake in the bone marrow and liver. Further validation of these agents in larger patient cohorts and clinical trials is important. Limited performance of tracers related to the tumor environment is also reflected in the workups of MM patients, and these agents do not appear to be individually useful for clinical evaluation, except [^{99m}Tc]Tc-MIBI. [^{99m}Tc]Tc-MIBI can be a good alternative for [^{18}F]FDG PET/CT scan with a much lower cost, especially for late-stage MM patients.

Increasingly, MRD assessment has become a critical standard in the clinical assessment of MM, with major efforts to develop methods with sensitive detection and specific exclusion. The traditional treatment of MM has been revolutionized by the progression of immunotherapy. Meanwhile, immuno-PET imaging with radiolabeled antibodies or antibody fragments has potential for MRD assessment and optimization of personalized therapy, [^{64}Cu]Cu-DOTA-Dara might helpful. In the context of theragnostic approaches to MM, the major advantage of the PET tracer [^{68}Ga]Ga-pentixafor is its potential for use in combination with the therapeutic lutetium-177 or yttrium-90 labeled pentixafor in progressive MM patients with CXCR4-positive tumor cells, as confirmed by a [^{68}Ga]Ga-pentixafor PET scan. Likewise, [^{89}Zr]Zr-DFO-daratumumab could be used to identify MM patients who would benefit from daratumumab and thus predict the effectiveness of treatment. Additional research is needed to validate and explore the practical application indications of these novel agents in various MM clinical conditions. Most other reported probes are in very early preclinical development, but some agents, particularly the NP-BCMA have shown promising potential for further prospective studies, which also signifies the possibility and feasibility of a PET tracer for BCMA aimed at immuno-PET imaging. And zirconium-89 ($t_{1/2}$ = 78.4 h) and cuprum-64 ($t_{1/2}$ = 12.7 h) are the most common radioisotopes for antibody labelling. The “bone-seeking” nature of zirconium-89 must be considered to understand the intrinsic impact of immuno-PET imaging. Even though routine clinical use of immune-PET imaging is hindered by a lack of proper long-lived radionuclides and the availability of antibodies or corresponding fragments, mAb-based immune-PET holds the potential to maximize

patient benefits through MRD detection and the promotion of immunotherapy.

Author contributions

SZ contributed to the writing of the manuscript and constructed the figures and tables. JS and WY and TZ provided analysis and interpretation of data and constructive suggestions. HX contributed to the English language editing and revising. HZ and LW conceived the project and modified the paper for submission and publication.

Funding

The authors gratefully acknowledge the support of K.C. Wong Education Foundation (China), and the Project of Innovative Team for the Guangdong Universities (2018KCXTD001, China). This work was financially supported by the National Natural Science Foundation of China (No. 82071974 to LW) and Guangdong Basic and Applied Basic Research Foundation (2020A1515011192, China).

Conflict of interest

The authors declare that the research was conducted in the absence of any commercial or financial relationships that could be construed as a potential conflict of interest.

Publisher's note

All claims expressed in this article are solely those of the authors and do not necessarily represent those of their affiliated organizations, or those of the publisher, the editors and the reviewers. Any product that may be evaluated in this article, or claim that may be made by its manufacturer, is not guaranteed or endorsed by the publisher.

References

Alabed, Y. Z. (2020). Multiple solitary plasmacytomas with multifocal bone involvement diagnosed with ^{68}Ga-Prostate-Specific membrane antigen PET/CT. *Clin. Nucl. Med.* 45, e51–e52. doi:10.1097/rlu.0000000000002682

Alexander, C., and Oberhausen, E. (1995). Myocardial scintigraphy. *Semin. Nucl. Med.* 25, 195–201. doi:10.1016/s0001-2998(95)80026-3

Ambrosini, V., Tomassetti, P., Franchi, R., and Fanti, S. (2010). Imaging of NETs with PET radiopharmaceuticals. *Q. J. Nucl. Med. Mol. Imaging.* 54, 16–23.

Apte, R. S., Chen, D. S., and Ferrara, N. (2019). VEGF in signaling and disease: beyond discovery and development. *Cell* 176, 1248–1264. doi:10.1016/j.cell.2019.01.021

Bailly, C., Gouard, S., Guérard, F., Chalopin, B., Carlier, T., Faivre-Chauvet, A., et al. (2019). What is the best radionuclide for immuno-PET of multiple myeloma? A comparison study between ^{89}Zr- and ^{64}Cu-labeled anti-CD138 in a preclinical syngeneic model. *Int. J. Mol. Sci.* 20, 2564. doi:10.3390/ijms20102564

Camacho, X., Perroni, C., Machado, C. L., de Godoi Carneiro, C., de Souza Junqueira, M., Faria, D., et al. (2021). ^{99m}Technetium- or Cy7-labeled fab(tocilizumab) as potential multiple myeloma imaging agents. *Anticancer. Agents Med. Chem.* 21, 1883–1893. doi:10.2174/1871520621999210104181238

Caserta, E., Chea, J., Minnix, M., Poku, E. K., Viola, D., Vonderfecht, S., et al. (2018). Copper 64-labeled daratumumab as a PET/CT imaging tracer for multiple myeloma. *Blood* 131, 741–745. doi:10.1182/blood-2017-09-807263

Cassou-Mounat, T., Balogova, S., Nataf, V., Calzada, M., Huchet, V., Kerrou, K., et al. (2016). ^{18}F-fluorocholine versus ^{18}F-fluorodeoxyglucose for PET/CT imaging in patients with suspected relapsing or progressive multiple myeloma: a pilot study. *Eur. J. Nucl. Med. Mol. Imaging* 43, 1995–2004. doi:10.1007/s00259-016-3392-7

Cavo, M., Terpos, E., Nanni, C., Moreau, P., Lentzsch, S., Zweegman, S., et al. (2017). Role of ^{18}F-FDG PET/CT in the diagnosis and management of multiple myeloma and other plasma cell disorders: a consensus statement by the international myeloma working group. *Lancet Oncol.* 18, e206–e217. doi:10.1016/s1470-2045(17)30189-4

Chérel, M., Gouard, S., Gaschet, J., Sai-Maurel, C., Bruchertseifer, F., Morgenstern, A., et al. (2013). ^{213}Bi radioimmunotherapy with an anti-mCD138 monoclonal antibody in a murine model of multiple myeloma. *J. Nucl. Med.* 54, 1597–1604. doi:10.2967/jnumed.112.111997

Cho, N., Ko, S., and Shokeen, M. (2021). Preclinical development of near-infrared-labeled CD38-targeted daratumumab for optical imaging of CD38 in multiple myeloma. *Mol. Imaging Biol.* 23, 186–195. doi:10.1007/s11307-020-01542-4

de Waal, E. G., Slart, R. H., Leene, M. J., Kluin, P. M., and Vellenga, E. (2015). ^{18}F-FDG PET increases visibility of bone lesions in relapsed multiple myeloma: is this hypoxia-driven? *Clin. Nucl. Med.* 40, 291–296. doi:10.1097/rlu.0000000000000629

de Waal, E. G. M., Glaudemans, A., Schröder, C. P., Vellenga, E., and Slart, R. H. J. A. (2017). Nuclear medicine imaging of multiple myeloma, particularly in the relapsed setting. *Eur. J. Nucl. Med. Mol. Imaging* 44, 332–341. doi:10.1007/s00259-016-3576-1

Demel, I., Bago, J. R., Hajek, R., and Jelinek, T. (2021). Focus on monoclonal antibodies targeting B-cell maturation antigen (BCMA) in multiple myeloma: update 2021. *Br. J. Haematol.* 193, 705–722. doi:10.1111/bjh.17235

Detappe, A., Reidy, M., Yu, Y., Mathieu, C., Nguyen, H. V. T., Coroller, T. P., et al. (2019). Antibody-targeting of ultra-small nanoparticles enhances imaging sensitivity and enables longitudinal tracking of multiple myeloma. *Nanoscale* 11, 20485–20496. doi:10.1039/c9nr06512a

Dimopoulos, M. A., Hillengass, J., Usmani, S., Zamagni, E., Lentzsch, S., Davies, F. E., et al. (2015). Role of magnetic resonance imaging in the management of patients with multiple myeloma: a consensus statement. *J. Clin. Oncol.* 33, 657–664. doi:10.1200/jco.2014.57.9961

Durie, B. G. (2006). The role of anatomic and functional staging in myeloma: description of durie/salmon plus staging system. *Eur. J. Cancer* 42, 1539–1543. doi:10.1016/j.ejca.2005.11.037

Dyrberg, E., Hendel, H. W., Al-Farra, G., Balding, L., Logager, V. B., Madsen, C., et al. (2017). A prospective study comparing whole-body skeletal X-ray survey with ^{18}F-FDG-PET/CT, ^{18}F-NaF-PET/CT and whole-body MRI in the detection of bone lesions in multiple myeloma patients. *Acta Radiol. Open* 6, 2058460117738809. doi:10.1177/2058460117738809

Georgii-Hemming, P., Strömberg, T., Janson, E. T., Stridsberg, M., Wiklund, H. J., and Nilsson, K. (1999). The somatostatin analog octreotide inhibits growth of interleukin-6 (IL-6)-dependent and IL-6-independent human multiple myeloma cell lines. *Blood* 93, 1724–1731. doi:10.1182/blood.v93.5.1724

Ghai, A., Zheleznyak, A., Mixdorf, M., O'Neal, J., Ritchey, J., Rettig, M., et al. (2021). Development of [^{89}Zr]DFO-elotuzumab for immunoPET imaging of CS1 in multiple myeloma. *Eur. J. Nucl. Med. Mol. Imaging* 48, 1302–1311. doi:10.1007/s00259-020-05097-y

Hayman, J. A., Callahan, J. W., Herschtal, A., Everitt, S., Binns, D. S., Hicks, R. J., et al. (2011). Distribution of proliferating bone marrow in adult cancer patients determined using FLT-PET imaging. *Int. J. Radiat. Oncol. Biol. Phys.* 79, 847–852. doi:10.1016/j.ijrobp.2009.11.040

Herrmann, K., Schottelius, M., Lapa, C., Osl, T., Poschenrieder, A., Hanscheid, H., et al. (2016). First-in-Human experience of CXCR4-directed endoradiotherapy with ^{177}Lu- and ^{90}Y-labeled pentixather in advanced-stage multiple myeloma with extensive intra- and extramedullary disease. *J. Nucl. Med.* 57, 248–251. doi:10.2967/jnumed.115.167361

Hideshima, T., Mitsiades, C., Tonon, G., Richardson, P. G., and Anderson, K. C. (2007). Understanding multiple myeloma pathogenesis in the bone marrow to identify new therapeutic targets. *Nat. Rev. Cancer* 7, 585–598. doi:10.1038/nrc2189

Ho, C. L., Chen, S., Leung, Y. L., Cheng, T., Wong, K. n., Cheung, S. K., et al. (2014). ^{11}C-acetate PET/CT for metabolic characterization of multiple myeloma: a comparative study with ^{18}F-FDG PET/CT. *J. Nucl. Med.* 55, 749–752. doi:10.2967/jnumed.113.131169

Huang, S. C. (2000). Anatomy of SUV. Standardized uptake value. *Nucl. Med. Biol.* 27, 643–646. doi:10.1016/s0969-8051(00)00155-4

Isoda, A., Higuchi, T., Nakano, S., Arisaka, Y., Kaira, K., Kamio, T., et al. (2012). ^{18}F-FAMT in patients with multiple myeloma: clinical utility compared to ^{18}F-FDG. *Ann. Nucl. Med.* 26, 811–816. doi:10.1007/s12149-012-0645-9

Isoda, A., Kaira, K., Iwashina, M., Oriuchi, N., Tominaga, H., Nagamori, S., et al. (2014). Expression of L-type amino acid transporter 1 (LAT1) as a prognostic and therapeutic indicator in multiple myeloma. *Cancer Sci.* 105, 1496–1502. doi:10.1111/cas.12529

Kanazawa, Y., Momozono, Y., Ishikawa, M., Yamada, T., Yamane, H., Haradahira, T., et al. (1986). Metabolic pathway of 2-deoxy-2-fluoro-D-glucose studied by F-19 NMR. *Life Sci.* 39, 737–742. doi:10.1016/0024-3205(86)90022-6

Kumar, S., Paiva, B., Anderson, K. C., Durie, B., Landgren, O., Moreau, P., et al. (2016). International Myeloma Working Group consensus criteria for response and minimal residual disease assessment in multiple myeloma. *Lancet Oncol.* 17, e328–e346. doi:10.1016/s1470-2045(16)30206-6

Kumar, S. K., Rajkumar, V., Kyle, R. A., van Duin, M., Sonneveld, P., Mateos, M. V., et al. (2017). Multiple myeloma. *Nat. Rev. Dis. Prim.* 3, 17046. doi:10.1038/nrdp.2017.46

Kyle, R. A., Durie, B. G., Rajkumar, S. V., Landgren, O., Blade, J., Merlini, G., et al. (2010). Monoclonal gammopathy of undetermined significance (MGUS) and smoldering (asymptomatic) multiple myeloma: IMWG consensus perspectives risk factors for progression and guidelines for monitoring and management. *Leukemia* 24, 1121–1127. doi:10.1038/leu.2010.60

Kyle, R. A., Remstein, E. D., Therneau, T. M., Dispenzieri, A., Kurtin, P. J., Hodnefield, J. M., et al. (2007). Clinical course and prognosis of smoldering (asymptomatic) multiple myeloma. *N. Engl. J. Med. Overseas. Ed.* 356, 2582–2590. doi:10.1056/nejmoa070389

Lapa, C., Garcia-Velloso, M. J., Lückerath, K., Samnick, S., Schreder, M., Otero, P. R., et al. (2017). ^{11}C-Methionine-PET in multiple myeloma: a combined study from two different institutions. *Theranostics* 7, 2956–2964. doi:10.7150/thno.20491

Lapa, C., Kircher, M., Da Via, M., Schreder, M., Rasche, L., Kortum, K. M., et al. (2019). Comparison of ^{11}C-choline and ^{11}C-methionine PET/CT in multiple myeloma. *Clin. Nucl. Med.* 44, 620–624. doi:10.1097/rlu.0000000000002638

Lin, C., Ho, C. L., Ng, S. H., Wang, P. N., Huang, Y., Lin, Y. C., et al. (2014). ^{11}C-acetate as a new biomarker for PET/CT in patients with multiple myeloma: initial staging and postinduction response assessment. *Eur. J. Nucl. Med. Mol. Imaging* 41, 41–49. doi:10.1007/s00259-013-2520-x

Lokhorst, H. M., Plesner, T., Laubach, J. P., Nahi, H., Gimsing, P., Hansson, M., et al. (2015). Targeting CD38 with daratumumab monotherapy in multiple myeloma. *N. Engl. J. Med. Overseas. Ed.* 373, 1207–1219. doi:10.1056/nejmoa1506348

Luthra, K., Bhave, A., and Lele, R. D. (2014). Tc-99m sestamibi scanning in multiple myeloma-a new look with SPECT-CT. *J. Assoc. Physicians India* 62, 801–812.

Malaer, J. D., and Mathew, P. A. (2017). CS1 (SLAMF7, CD319) is an effective immunotherapeutic target for multiple myeloma. *Am. J. Cancer Res.* 7, 1637–1641.

Meckova, Z., Lambert, L., Spicka, I., Kubinyi, J., and Burgetova, A. (2018). Is fluorine-18-fluorocholine PET/CT suitable for the detection of skeletal involvement of multiple myeloma? *Hell. J. Nucl. Med.* 21, 167–168. doi:10.1967/s002449910900

Mosci, C., Pericole, F. V., Oliveira, G. B., Delamain, M. T., Takahashi, M. E., Carvalheira, J. B. C., et al. (2020). ^{99m}Tc-sestamibi SPECT/CT and ^{18}F-FDG-PET/CT have similar performance but different imaging patterns in newly diagnosed multiple myeloma. *Nucl. Med. Commun.* 41, 1081–1088. doi:10.1097/mnm.0000000000001259

Mosebach, J., Thierjung, H., Schlemmer, H. P., and Delorme, S. (2019). Multiple myeloma guidelines and their recent updates: implications for imaging. *Rofo* 191, 998–1009. doi:10.1055/a-0897-3966

Mukkamalla, S. K. R., and Malipeddi, D. (2021). Myeloma bone disease: a comprehensive review. *Int. J. Mol. Sci.* 22, 6208. doi:10.3390/ijms22126208

Mulé, S., Reizine, E., Blanc-Durand, P., Baranes, L., Zerbib, P., Burns, R., et al. (2020). Whole-body functional MRI and PET/MRI in multiple myeloma. *Cancers (Basel)* 12 (11), 3155. doi:10.3390/cancers12113155

Munshi, N. C., Avet-Loiseau, H., Anderson, K. C., Neri, P., Paiva, B., Samur, M., et al. (2020). A large meta-analysis establishes the role of MRD negativity in long-term survival outcomes in patients with multiple myeloma. *Blood Adv.* 4, 5988–5999. doi:10.1182/bloodadvances.2020002827

Nadeem, O., Tai, Y. T., and Anderson, K. C. (2020). Immunotherapeutic and targeted approaches in multiple myeloma. *Immunotargets Ther.* 9, 201–215. doi:10.2147/itt.s240886

Nakamoto, Y., Kurihara, K., Nishizawa, M., Yamashita, K., Nakatani, K., Kondo, T., et al. (2013). Clinical value of ^{11}C-methionine PET/CT in patients with plasma cell malignancy: comparison with ^{18}F-FDG PET/CT. *Eur. J. Nucl. Med. Mol. Imaging* 40, 708–715. doi:10.1007/s00259-012-2333-3

Nanni, C., Zamagni, E., Cavo, M., Rubello, D., Tacchetti, P., Pettinato, C., et al. (2007). ^{11}C-choline vs. ^{18}F-FDG PET/CT in assessing bone involvement in patients with multiple myeloma. *World J. Surg. Oncol.* 5, 68. doi:10.1186/1477-7819-5-68

Ogawa, T., Kanno, I., Shishido, F., Inugami, A., Higano, S., Fujita, H., et al. (1987). Clinical value of PET with ^{18}F-fluorodeoxyglucose and L-methyl-11C-methionine for diagnosis of recurrent brain tumor and radiation injury. *Acta Radiol.* 32, 197–202. doi:10.3109/02841859109177547

Okasaki, M., Kubota, K., Minamimoto, R., Miyata, Y., Morooka, M., Ito, K., et al. (2015). Comparison of ^{11}C-4'-thiothymidine, ^{11}C-methionine, and ^{18}F-FDG PET/CT for the detection of active lesions of multiple myeloma. *Ann. Nucl. Med.* 29, 224–232. doi:10.1007/s12149-014-0931-9

Ormond Filho, A. G., Carneiro, B. C., Pastore, D., Silva, I. P., Yamashita, S. R., Consolo, F. D., et al. (2019). Whole-body imaging of multiple myeloma: diagnostic criteria. *Radiographics* 39, 1077–1097. doi:10.1148/rg.2019180096

Pan, Q., Cao, X., Luo, Y., Li, J., Feng, J., and Li, F. (2020). Chemokine receptor-4 targeted PET/CT with ^{68}Ga-pentixafor in assessment of newly diagnosed multiple myeloma: comparison to ^{18}F-FDG PET/CT. *Eur. J. Nucl. Med. Mol. Imaging* 47, 537–546. doi:10.1007/s00259-019-04605-z

Pandit-Taskar, N. (2018). Functional imaging methods for assessment of minimal residual disease in multiple myeloma: current status and novel ImmunoPET based methods. *Semin. Hematol.* 55, 22–32. doi:10.1053/j.seminhematol.2018.02.009

Pauwels, E. K., Ribeiro, M. J., Stoot, J. H., McCready, V., Bourguignon, M., and Maziere, B. (1998). FDG accumulation and tumor biology. *Nucl. Med. Biol.* 25, 317–322. doi:10.1016/s0969-8051(97)00226-6

Pawlyn, C., and Davies, F. E. (2019). Toward personalized treatment in multiple myeloma based on molecular characteristics. *Blood* 133, 660–675. doi:10.1182/blood-2018-09-825331

Pawlyn, C., Fowkes, L., Otero, S., Jones, J. R., Boyd, K. D., Davies, F. E., et al. (2016). Whole-body diffusion-weighted MRI: a new gold standard for assessing disease burden in patients with multiple myeloma? *Leukemia* 30, 1446–1448. doi:10.1038/leu.2015.338

Peck, M., Pollack, H. A., Muzi, M., Friesen, A., Shoner, S. C., Shankland, E. G., et al. (2015). Applications of PET imaging with the proliferation marker ^{18}F-FLT. *Q. J. Nucl. Med. Mol. Imaging.* 59, 95–104.

Philipp-Abbrederis, K., Herrmann, K., Knop, S., Schottelius, M., Eiber, M., Luckerath, K., et al. (2015). *In vivo* molecular imaging of chemokine receptor CXCR4 expression in patients with advanced multiple myeloma. *EMBO Mol. Med.* 7, 477–487. doi:10.15252/emmm.201404698

Rajkumar, S. V., Dimopoulos, M. A., Palumbo, A., Blade, J., Merlini, G., Mateos, M. V., et al. (2014). International Myeloma Working Group updated criteria for the diagnosis of multiple myeloma. *Lancet Oncol.* 15, e538–548. doi:10.1016/s1470-2045(14)70442-5

Rama, S., Suh, C. H., Kim, K. W., Durieux, J. C., Ramaiya, N. H., and Tirumani, S. H. (2022). Comparative performance of whole-body MRI and FDG PET/CT in evaluation of multiple myeloma treatment response: systematic review and meta-analysis. *Am. J. Roentgenol.* 218, 602–613. doi:10.2214/ajr.21.26381

Rasche, L., Angtuaco, E., McDonald, J. E., Buros, A., Stein, C., Pawlyn, C., et al. (2017). Low expression of hexokinase-2 is associated with false-negative FDG-positron emission tomography in multiple myeloma. *Blood* 130, 30–34. doi:10.1182/blood-2017-03-774422

Sachpekidis, C., Goldschmidt, H., and Dimitrakopoulou-Strauss, A. (2019). Positron emission tomography (PET) radiopharmaceuticals in multiple myeloma. *Molecules* 25, 134. doi:10.3390/molecules25010134

Sachpekidis, C., Goldschmidt, H., Kopka, K., Kopp-Schneider, A., and Dimitrakopoulou-Strauss, A. (2018). Assessment of glucose metabolism and cellular proliferation in multiple myeloma: a first report on combined ^{18}F-FDG and ^{18}F-FLT PET/CT imaging. *EJNMMI Res.* 8, 28. doi:10.1186/s13550-018-0383-7

Sanderson, R. D., and Yang, Y. (2008). Syndecan-1: a dynamic regulator of the myeloma microenvironment. *Clin. Exp. Metastasis* 25, 149–159. doi:10.1007/s10585-007-9125-3

Schlesinger, M., and Bendas, G. (2015). Contribution of very late antigen-4 (VLA-4) integrin to cancer progression and metastasis. *Cancer Metastasis Rev.* 34, 575–591. doi:10.1007/s10555-014-9545-x

Shah, N., Chari, A., Scott, E., Mezzi, K., and Usmani, S. Z. (2020). B-cell maturation antigen (BCMA) in multiple myeloma: rationale for targeting and current therapeutic approaches. *Leukemia* 34, 985–1005. doi:10.1038/s41375-020-0734-z

Sonmezoglu, K., Vatankulu, B., Elverdi, T., Akyel, R., Erkan, M. E., Halac, M., et al. (2017). The role of ^{68}Ga-DOTA-TATE PET/CT scanning in the evaluation of patients with multiple myeloma: preliminary results. *Nucl. Med. Commun.* 38, 76–83. doi:10.1097/mnm.0000000000000610

Soodgupta, D., Zhou, H., Beaino, W., Lu, L., Rettig, M., Snee, M., et al. (2016). *Ex vivo* and *in vivo* evaluation of overexpressed VLA-4 in multiple myeloma using LLP2A imaging agents. *J. Nucl. Med.* 57, 640–645. doi:10.2967/jnumed.115.164624

Sugawara, Y., Fisher, S. J., Zasadny, K. R., Kison, P. V., Baker, L. H., and Wahl, R. L. (1998). Preclinical and clinical studies of bone marrow uptake of fluorine-1-fluorodeoxyglucose with or without granulocyte colony-stimulating factor during chemotherapy. *J. Clin. Oncol.* 16, 173–180. doi:10.1200/jco.1998.16.1.173

Terao, T., and Matsue, K. (2022). Progress of modern imaging modalities in multiple myeloma. *Int. J. Hematol.* 115, 778–789. doi:10.1007/s12185-022-03360-6

Toyohara, J., Nariai, T., Sakata, M., Oda, K., Ishii, K., Kawabe, T., et al. (2011). Whole-body distribution and brain tumor imaging with ^{11}C-4DST: a pilot study. *J. Nucl. Med.* 52, 1322–1328. doi:10.2967/jnumed.111.088435

Ulaner, G. A., Sobol, N. B., O'Donoghue, J. A., Kirov, A. S., Riedl, C. C., Min, R., et al. (2020). CD38-targeted immuno-PET of multiple myeloma: from xenograft models to first-in-human imaging. *Radiology* 295, 606–615. doi:10.1148/radiol.2020192621

van Lammeren-Venema, D., Regelink, J. C., RiphagenII, Zweegman, S., Hoekstra, O. S., and Zijlstra, J. M. (2012). 18F-fluoro-deoxyglucose positron emission tomography in assessment of myeloma-related bone disease: a systematic review. *Cancer* 118, 1971–1981. doi:10.1002/cncr.26467

Wang, C., Chen, Y., Hou, Y. N., Liu, Q., Zhang, D., Zhao, H., et al. (2021). ImmunoPET imaging of multiple myeloma with [^{68}Ga]Ga-NOTA-Nb1053. *Eur. J. Nucl. Med. Mol. Imaging* 48, 2749–2760. doi:10.1007/s00259-021-05218-1

Wang, J., Tannous, B. A., Poznansky, M. C., and Chen, H. (2020). CXCR4 antagonist AMD3100 (plerixafor): From an impurity to a therapeutic agent. *Pharmacol. Res.* 159, 105010. doi:10.1016/j.phrs.2020.105010

Wang, W. Q., Zhao, X. Y., Wang, H. Y., and Liang, Y. (2008). Increased fatty acid synthase as a potential therapeutic target in multiple myeloma. *J. Zhejiang Univ. Sci. B* 9, 441–447. doi:10.1631/jzus.b0740640

Wei, W., Zhang, D., Wang, C., Zhang, Y., An, S., Chen, Y., et al. (2021). Annotating CD38 expression in multiple myeloma with [^{18}F]F-Nb1053. *Mol. Pharm.* doi:10.1021/acs.molpharmaceut.1c00733

Wester, H. J., and Schottelius, M. (2019). PSMA-targeted radiopharmaceuticals for imaging and therapy. *Semin. Nucl. Med.* 49, 302–312. doi:10.1053/j.semnuclmed.2019.02.008

Withofs, N., Cousin, F., De Prijck, B., Bonnet, C., Hustinx, R., Gambhir, S. S., et al. (2017). A first report on ^{18}F-FPRGD(2) PET/CT imaging in multiple myeloma. *Contrast Media Mol. Imaging* 2017, 6162845. doi:10.1155/2017/6162845

Wu, Z., Li, Z. B., Cai, W., He, L., Chin, F. T., Li, F., et al. (2007). ^{18}F-labeled mini-PEG spacered RGD dimer (^{18}F-FPRGD2): synthesis and microPET imaging of alphavbeta3 integrin expression. *Eur. J. Nucl. Med. Mol. Imaging* 34, 1823–1831. doi:10.1007/s00259-007-0427-0

Wuest, M., and Wuest, F. (2013). Positron emission tomography radiotracers for imaging hypoxia. *J. Label. Comp. Radiopharm.* 56, 244–250. doi:10.1002/jlcr.2997

Yang, Y., Li, Y., Gu, H., Dong, M., and Cai, Z. (2020). Emerging agents and regimens for multiple myeloma. *J. Hematol. Oncol.* 13, 150. doi:10.1186/s13045-020-00980-5

Zamagni, E., Nanni, C., Dozza, L., Carlier, T., Bailly, C., Tacchetti, P., et al. (2021). Standardization of ^{18}F-FDG-PET/CT according to deauville criteria for metabolic complete response definition in newly diagnosed multiple myeloma. *J. Clin. Oncol.* 39, 116–125. doi:10.1200/jco.20.00386

Zamagni, E., Nanni, C., Gay, F., Pezzi, A., Patriarca, F., Bello, M., et al. (2016). ^{18}F-FDG PET/CT focal, but not osteolytic, lesions predict the progression of smoldering myeloma to active disease. *Leukemia* 30, 417–422. doi:10.1038/leu.2015.291

Zamagni, E., Tacchetti, P., Barbato, S., and Cavo, M. (2020). Role of imaging in the evaluation of minimal residual disease in multiple myeloma patients. *J. Clin. Med.* 9, 3519. doi:10.3390/jcm9113519

Zamagni, E., Tacchetti, P., and Cavo, M. (2019). Imaging in multiple myeloma: how? when? *Blood* 133, 644–651. doi:10.1182/blood-2018-08-825356

Zhang, X. G., Bataille, R., Widjenes, J., and Klein, B. (1992). Interleukin-6 dependence of advanced malignant plasma cell dyscrasias. *Cancer* 69, 1373–1376. doi:10.1002/1097-0142(19920315)69:6<1373::aid-cncr2820690612>3.0.co;2-1

Glossary

[^{11}C]4DST 4′-methyl-^{11}C-thiothymidine

[^{11}C]ACT [^{11}C]acetate

[^{11}C]MET [^{11}C]methionine

[^{18}F]FAMT ^{18}F α-methyl-tyrosine

[^{18}F]FAZA 1-α-D: -(5-deoxy-5-^{18}F-fluoroarabinofuranosyl)-2-nitroimidazole

[^{18}F]FDG [^{18}F]fluorodeoxyglucose

[^{18}F]FLT Pyrimidine 3-deoxy-3-^{18}F-fluorothymidine

[^{18}F]FPRGD2 ^{18}F-FB-NH-mini-PEG-E[c(RGDyK)]$_2$

[^{64}Cu]Cu-LLP2A ^{64}Cu-CB-TE1A1P-PEG4-LLP2A

[^{68}Ga]Ga-DOTA-TATE ^{68}Ga-tetraazacyclododecane-tetraacetic acid-octreotate

[^{99m}Tc]Tc-MIBI Technetium 99 m sestamibi

ADC antibody-drug conjugate

BCMA B cell maturation antigen

CB-TE1A1P 1,4,8,11-tetraazacyclotetradecane-1-[methane phosphonic acid]-8-[methane carboxylic acid]

CD cluster of differentiation

CXCR4 chemokine receptor-4

Dara Daratumumab

DCE dynamic contrast-enhanced

DFO Defetoxamine

DWI diffusion weight imaging

FAS fatty acid synthase

FDA Food and Drug Administration

GLUT glucose transporters

IL-6 Interleukin-6

IMWG International Myeloma Working Group

LAT L-type amino acid transporter

LLP2A N-[[4-[[[(2-ethylphenyl)amino]carbonyl]amino]phenyl] acetyl]-N(epsilon)-6-[(2E)-1-oxo-3-(3-pyridinyl-2-propenyl)]-L-lysyl-L-2-aminohexanedioyl-(1-amino-1-cyclohexane) carboxamide

mAb humanized nanoantibody

MGUS monoclonal gammopathy of undetermined significance

MM multiple myeloma

MRD minimal residual disease

NETs neuroendocrine tumors

NIR near-infrared

NOTA 1,4,7-triazacyclononane-N,N′,N″-triacetic acid

NP nanoparticles

PET/CT positron emission tomography/computed tomography

PSMA prostate-specific membrane antigen

RRMM relapsed/refractory multiple myeloma

SLAMF 7 signaling lymphocyte activation molecule 7

SMM smoldering multiple myeloma

SRS somatostatin receptor scintigraphy

SSTR somatostatin receptors

SUV standardized uptake value

TE2A 1,4,8,11-tetraazabicyclo[6.6.2]hexadecane

TK1 thymidine kinase 1

VEGF vascular endothelial growth factor

VLA-4 very late antigen-4

WBLWCT whole-body low-dose computed tomography

WB-MRI whole-body magnetic resonance imaging

EMD extramedullary disease

frontiers | Frontiers in Bioengineering and Biotechnology

TYPE Original Research
PUBLISHED 06 September 2022
DOI 10.3389/fbioe.2022.983488

OPEN ACCESS

EDITED BY
Shaobo Yao,
First Affiliated Hospital of Fujian Medical University, China

REVIEWED BY
Jianguo Lin,
Jiangsu Institute of Nuclear Medicine, China
Jianing Wang,
Brigham and Women's Hospital and Harvard Medical School, United States

*CORRESPONDENCE
Lu Wang,
l_wang1009@jnu.edu.cn
Jinghao Wang,
wangjinghao@jnu.edu.cn
Zhiyong Dong,
dongzy2008@jnu.edu.cn

†These authors have contributed equally to this work

SPECIALTY SECTION
This article was submitted to Nanobiotechnology, a section of the journal Frontiers in Bioengineering and Biotechnology

RECEIVED 01 July 2022
ACCEPTED 01 August 2022
PUBLISHED 06 September 2022

CITATION
Wei H, Wei J, Zhang S, Dong S, Li G, Ran W, Dong C, Zhang W, Che C, Luo W, Xu H, Dong Z, Wang J and Wang L (2022), Easily automated radiosynthesis of [^{18}F]P10A-1910 and its clinical translation to quantify phosphodiesterase 10A in human brain. *Front. Bioeng. Biotechnol.* 10:983488. doi: 10.3389/fbioe.2022.983488

Easily automated radiosynthesis of [^{18}F]P10A-1910 and its clinical translation to quantify phosphodiesterase 10A in human brain

Huiyi Wei[1†], Junjie Wei[1†], Shaojuan Zhang[1†], Shiliang Dong[2], Guocong Li[1], Wenqing Ran[1], Chenchen Dong[1], Weibin Zhang[3], Chao Che[3], Wenzhao Luo[4], Hao Xu[1], Zhiyong Dong[2,5]*, Jinghao Wang[5,6]* and Lu Wang[1,5]*

[1]Center of Cyclotron and PET Radiopharmaceuticals, Department of Nuclear Medicine, The First Affiliated Hospital of Jinan University, Guangzhou, China, [2]Center of Bariatric Surgery, Department of Gastrointestinal Surgery, The First Affiliated Hospital of Jinan University, Guangzhou, China, [3]State Key Laboratory of Chemical Oncogenomics, Key Laboratory of Chemical Genomics, Peking University Shenzhen Graduate School, Shenzhen, China, [4]Institute of Analysis, Guangdong Academy of Sciences (China National Analytical Center), Guangzhou, China, [5]The Guangzhou Key Laboratory of Basic and Translational Research on Chronic Diseases, The First Affiliated Hospital of Jinan University, Guangzhou, China, [6]Department of Pharmacy, The First Affiliated Hospital of Jinan University, Guangzhou, China

Our previous work showed that [^{18}F]P10A-1910 was a potential radioligand for use in imaging phosphodiesterase 10A (PDE10A). Specifically, it had high brain penetration and specific binding that was demonstrated in both rodents and non-human primates. Here, we present the first automatic cGMP-level production of [^{18}F]P10A-1910 and translational PET/MRI study in living human brains. Successful one-step radiolabeling of [^{18}F]P10A-1910 on a GE TRACERlab FX2N synthesis module was realized via two different methods. First, formulated [^{18}F]P10A-1910 was derived from heating spirocyclic iodonium ylide in a tetra-*n*-butyl ammonium methanesulfonate solution. At the end of synthesis, it was obtained in non-decay corrected radiochemical yields (n.d.c. RCYs) of 12.4 ± 1.3%, with molar activities (MAs) of 90.3 ± 12.6 μmol (n = 7) (*Method I*). The boronic pinacol ester combined with copper and oxygen also delivered the radioligand with 16.8 ± 1.0% n. d.c. RCYs and 77.3 ± 20.7 GBq/μmol (n = 7) MAs after formulation (*Method II*). The radiochemical purity, radionuclidic purity, solvent residue, sterility, endotoxin content and other parameters were all validated for human use. Consistent with the distribution of PDE10A in the brain, escalating uptake of [^{18}F]P10A-1910 was observed in the order of cerebellum (reference region), substantial nigra, caudate and putamen. The non-displaceable binding potential (BP_{ND}) was estimated by simplified reference-tissue model (SRTM); linear regressions demonstrated that BP_{ND} was well correlated with the most widely used semiquantitative parameter SUV. The strongest correlation was observed with $SUV_{(50-60\ min)}$ (R^2 = 0.966, p < 0.01). Collectively, these results indicated that a static scan protocol could be easily performed for PET imaging of

PDE10A. Most importantly, that [^{18}F]P10A-1910 is a promising radioligand to clinically quantify PDE10A.

KEYWORDS

phosphodiesterase 10A, positron emission tomography, automatic radiosynthesis, translational PET/MRI, human brain

Introduction

Phosphodiesterases (PDEs) are widely present in various cells and catalyze the hydrolysis and inactivation of cyclic adenosine monophosphate (cAMP) and/or cyclic guanosine monophosphate (cGMP). Moreover, they synergize with both ATP and GTP to regulate the content of these second messengers (Charbonneau et al., 1990; Beavo, 1995; Francis et al., 2011). Therefore, PDEs play a critical role in various physiological processes involving cyclic nucleotide signaling (Bender and Beavo, 2006). In mammals, different cell types express different PDEs, which can be divided into 11 different subtypes according to their distribution and respective base sequences (Omori and Kotera, 2007). One-PDE10A-is expressed less in peripheral system, however, abundantly in striatum and substantia nigra in the central nervous system (CNS) (Loughney et al., 1999; Coskran et al., 2006; Xie et al., 2006). Medium spiny neurons in the striatum are the primary input point to the basal ganglia and they integrate both dopaminergic and glutaminergic signals with cortical reception. Ultimately, this leads to the performance of associated motor and cognitive activities (Kötter, 1994; Girault, 2012). Therefore, abnormal expression and dysfunction of PDE10A would affect the signal transmission in basal ganglia circuit. This would lead to nigrostriatal neuronal pathway-related mental and functional disorders, such as schizophrenia, Huntington's disease (HD), Parkinson's disease (PD) and Alzheimer's disease (AD) (Geerts et al., 2017; Pagano et al., 2019). Thus, PDE10A is considered an attractive biomarker for the diagnosis and treatment of these diseases (Wilson et al., 2017).

As a non-invasive medical evaluation method, positron emission tomography (PET) can provide valuable, *in vivo* information for exploring a host of physiological and pathological mechanisms. As a result, PET is useful in assessing the progression of related diseases, as well as help accelerate the development of targeted drugs (Gulyás et al., 1996; Cecchin et al., 2021). Given the clinical significance of PDE10A and increasing interest in PET applications, several radioligands targeted PDE10A have been reported (Laere et al., 2013; Barret et al., 2014; Russell et al., 2014; Marques et al., 2016; Mori et al., 2019; Xiao et al., 2022). In particular, a PET ligand named [^{18}F]MNI659 ([^{18}F]**1**, Figure 1) has been explored in healthy human volunteers and has shown high brain binding specificity in the brain as well as good pharmacokinetics. It has also been shown to have a non-displaceable binding potential (BP_{ND}) ranging from 3.0 to 5.0 in healthy people aged 29–47 years (Barret et al., 2014). Clinical PET studies using [^{18}F]**1** were further conducted on patients with HD (Russell et al., 2014; Russell et al., 2016). However, the [^{18}F] fluoroethoxyl structure in [^{18}F]**1** is peculiarly prone to metabolism by cytochrome-P450 monooxygenase system, resulting in unexpected radioactive aggregation in the brain and skull that interferes with imaging quantification (Russell et al., 2014). To compensate for metabolic deficiency, the side chain [^{18}F]fluoroethoxy was replaced by [^{18}F]fluoromethoxy-d_2. The modified radioligand [^{18}F]2 (Figure 1) was more stable *in vivo*, and its corresponding BP_{ND} was also improved (Mori et al., 2019). Nevertheless, the difficulty and complexity of radiolabeling prevented its further development (Stepanov et al., 2018; Mori et al., 2019).

Our previous work revealed the successful radiosynthesis of [^{18}F]P10A-1910 ([^{18}F]**3**, Figure 1) with satisfying manual labeling

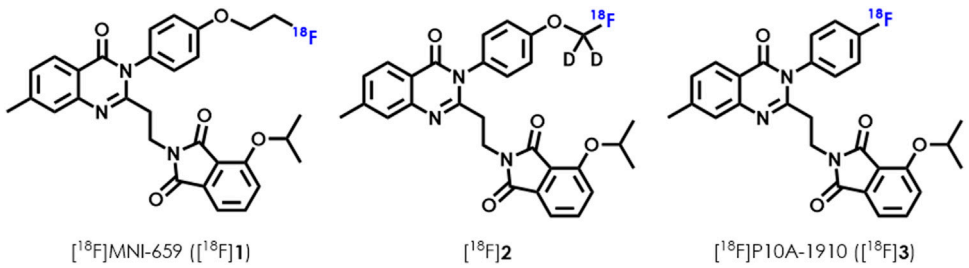

FIGURE 1
Representative PET ligands for imaging PDE10A: [^{18}F]MNI-659 and their derivatives.

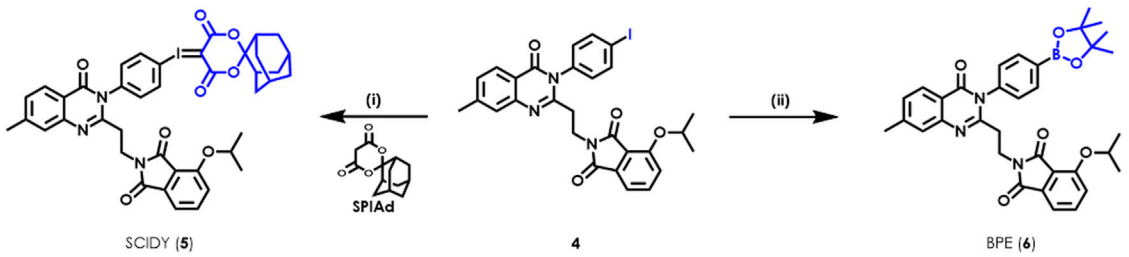

SCHEME 1
Syntheses of radiolabeling precursors SCIDY **5** and BPE **6**. Reagents and conditions: (i) oxone, TFA/$CHCl_3$, room temperature, 1 h; then SPIAd, 10% Na_2CO_3 (aq), EtOH, room temperature, 1 h, 69% for **5**; (ii) Bis(pinacolato)diboron, $Pd(dppf)_2Cl_2$, KOAc, DMSO, 80°C, 16 h, 62% for **6**.

radiochemical yields. Its high binding specificity, good pharmacokinetics and improved metabolic stability owing to an intrinsic aryl-^{18}F bond (Joong-Hyun and Pike, 2012) indicated that it was a promising radioligand for further clinical translation (Xiao et al., 2022). Here, we report a fully automated synthesis of [^{18}F]**3** in a commonly used commercial GE TRACERlab FX2N radiofluorination module based on two different types of precursors. These included *i.e.*, the spirocyclic iodonium ylide (SCIDY) 2-(2-(3-(4-(((1*R*,5*S*)-4′,6′-dioxospiro [adamantane-2,2′- (Charbonneau et al., 1990; Francis et al., 2011)dioxan]-5′-ylidene)-λ^3-iodaneyl)phenyl)-7-methyl-4-oxo-3,4-dihydroquinazolin-2-yl)ethyl)-4-isopropoxyisoindoline-1,3-dione (**5**), and the boronic pinacol ester (BPE) 4-isopropoxy-2-(2-(7-methyl-4-oxo-3-(4-(4,4,5,5-tetramethyl-1,3,2-dioxaborolan-2-yl)phenyl)-3,4-dihydroquinazolin-2-yl)ethyl) isoindoline-1,3-dione (**6**). A comprehensive quality control of [^{18}F]**3** derived from these two methods was then performed to validate it for human use. Finally, a PET imaging study on healthy volunteers demonstrated that PDE10A expression in substantial nigra, caudate and putamen was sensitively quantified by [^{18}F]**3** via the static scan protocol. Taken together, this work will pave the way for routine radioligand production and widespread application, as well as facile clinical translation for further diagnosis of PDE10A-related neurological disorders.

Results and discussion

Chemical syntheses of precursors

As shown in Scheme 1, the radiolabeling precursors SCIDY **5** and BPE **6** were prepared from the common intermediate aryl iodide **4**, which was obtained efficiently in gram scale according to our previously reported synthetic procedures (Xiao et al., 2022). Particularly, oxone was used to oxidize **4** into the corresponding iodo (III) intermediate in a solution of TFA/$CHCl_3$. After evaporation of the acid solvent, the crude mixture was directly dissolved in ethanol, then coupled with SPIAd under basic conditions to deliver the desired SCIDY **5** as a colorless powder in 69% yield. Additionally, BPE **6**, a baby pink solid, was synthesized via Pd-catalyzed cross-coupling with bis(pinacolato)diboron at a comparable yield of 62%. When maintained at −78°C, both precursors remained stable radiolabeling efficiency for at least 6 months.

Radiofluorination optimization in a GE TRACERlab FX2N module

We set out the automatic radiolabeling with SCIDY **5** according to our previously reported method (Xiao et al., 2022), resulting in only trace to low non-decay corrected radiochemical yield (n.d.c. RCY, 1~3.2%). This was not enough to meet our demand for clinical use. This unexpected difference in outcomes between manual operation and automated performance inspired us to re-optimize the radiolabeling conditions directly on a GE TRACERlab FX2N module equipped in our facility. As shown in Figure 2A, after adjusting the type of solvent, we found that 0.5 ml MeCN gave the highest yields (8%). Reaction temperatures were then screened and 110°C was found to be stable at the tube sealing condition in the module (Figure 2B). Our continuous efforts into researching the best SCIDY strategy revealed that basic conditions may play a critical role in the balance between precursor stability and radiolabeling efficiency (Rotstein et al., 2016; Wang et al., 2017; Liang et al., 2019; Wang et al., 2020; Xiao et al., 2022). Given this, two commonly used quaternary alkylammonium salts tetraethylammonium bicarbonate (TEAB) and tetrabutylammonium methanesulfonate (TBAOMs) (Christopher et al., 2012; Inkster et al., 2016; Shi et al., 2016) were further evaluated in automation with different amounts. After, the latter was elected as the best additive at a loading of 12 mg (Figure 2C). Collectively, we identified that the combination of 12 mg TBAOMs and 2 mg SCIDY **5** in CH_3CN at

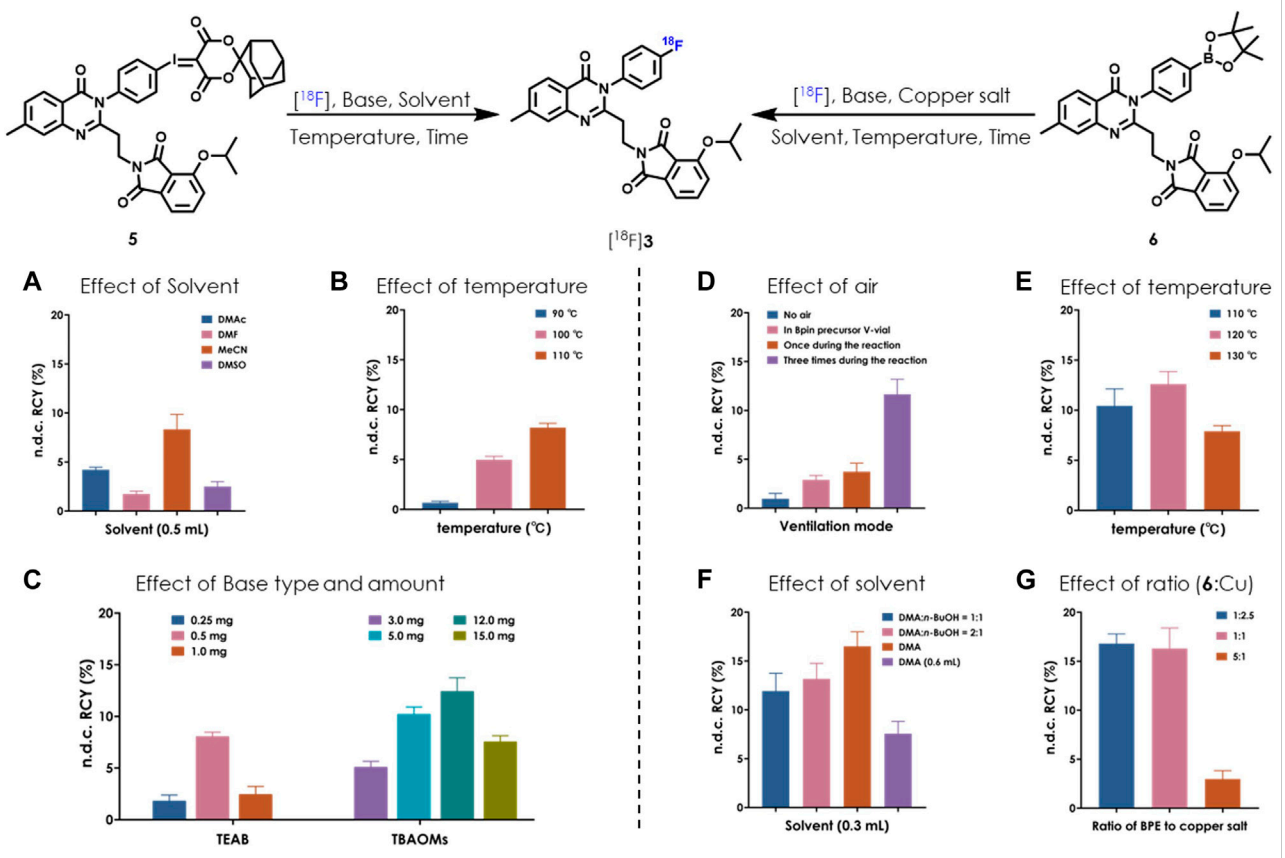

FIGURE 2
Optimization of automatic radiolabeling conditions for [^{18}F]**3** based on SCIDY **5 (A–C)** and BPE **6 (D–G)** (n = 3). [^{18}F]fluoride (14.8–18.5 GBq; 400–500 mCi) was delivered from the cyclotron to a GE TRACERlab FX2N module in each test. **(A) 5** (2 mg), TEAB (0.5 mg), 110°C, 10 min; **(B) 5** (2 mg), MeCN (0.5 ml), heated for 10 min; **(C) 5** (2 mg), MeCN (0.5 ml), 110°C, 10 min; **(D) 6** (4.25 μmol), Cu(OTf)$_2$(py)$_4$ (10.5 μmol), DMA:n-BuOH (300 μL, v/v = 2/1), TEAB (0.5 mg), 120°C, 20 min; **(E) 6** (4.25 μmol), Cu(OTf)$_2$(py)$_4$ (10.5 μmol), DMA:n-BuOH (300 μL, v/v = 2/1), TEAB (0.5 mg), heated for 20 min. Air was bubbled into the reaction three times; **(F) 6** (4.25 μmol), Cu(OTf)$_2$(py)$_4$ (10.5 μmol), solvent, TEAB (0.5 mg), 120°C, 20 min. Air was bubbled into the reaction three times; **(G) 6** (4.25 μmol), Cu(OTf)$_2$(py)$_4$ (indicated molar ratio), DMA (300 μL), TEAB (0.5 mg), 120°C, 20 min. Air was bubbled into the reaction three times.

110°C for 10 min provided the desired radioligand [^{18}F]**3** with stable and high enough automatic labeling efficiencies.

Copper-induced nucleophilic ^{18}F labeling, which was developed by Gouverneur's (Tredwell et al., 2014; Taylor et al., 2017) and Scott's group (Chu and Qing, 2014), is another strategy for radiofluorination of a non-active aromatic ring. There is easy access to the precursor BPE via Miyaura boration (Ishiyama et al., 1995), which would be complementary to SCIDY synthesis (Rong et al., 2021). Because of this, we also systemically evaluated BPE radiolabeling feasibility in our FX2N module. A big challenge in this process was controlling air bubbling; thus, we tested the effect of air and found that the highest RCYs were obtained when the mixture was ventilated three times during the radiolabeling process (Figure 2D). Heating the reaction at 120°C was also shown to be optimal (Figure 2E). By elevating the ratio of *N*, *N*-dimethylacetamide (DMA) from 50% to 100%, n.d.c. RCYs were improved to 16.5%, while increasing the solvent volume decreased RCYs dramatically (Figure 2F). Finally, the molar ratios of BPE **6** and copper salt were optimized. Although low RCYs were observed when decreasing the amount of copper salt to *ca.* 20%, comparable yields were obtained with the ratio ranging from 1:2.5 to 1:1 (Figure 2G). Together with the above results and considering efforts to minimize consumption of the precursor, we determined that marriage of 2.5 mg BPE **6**, 7 mg copper salt (molar ratio was 1:2.5), 0.5 mg TEAB and 0.3 ml DMA at 120°C for 20 min would allow for the best automatic labeling of [^{18}F]**3** with the assistance of three-times air bubbling.

In summary, after conducting more than 100 tests in the FX2N module, we realized stable and highly efficient automatic radiolabeling of [^{18}F]**3** from either SCIDY **5** (*Method I*) or BPE **6** (*Method II*). The semipreparative HPLC purification chromatography of these two methods is shown in Figure 3. The indicated radioactive peak was collected and formulated via a

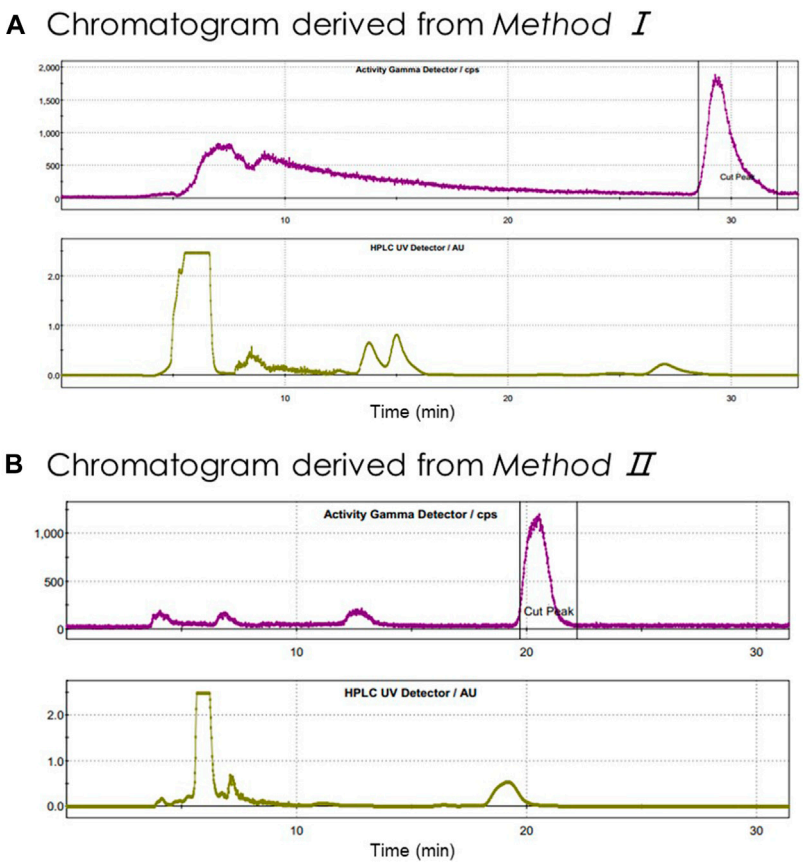

FIGURE 3
Semipreparative HPLC chromatography of crude radioligand [^{18}F]**3**. Units on *y*-axis are arbitrary. Column: OS□K□ SOD□, CAPCELL PAK C18, UG80 5 μm, 250 × 10 mm; **(A)** mobile phase: CH_3CN/H_2O = 55/45 (v/v); flow rate: 5 ml/min; Gamma (t_R = 29 min; purple) and UV (λ = 254 nm; yellow); **(B)** mobile phase: CH_3CN/H_2O = 60/40 (v/v); flow rate: 3.5 ml/min; Gamma (t_R = 21.8 min; purple) and UV (λ = 254 nm; yellow).

C18 Sep-Pak with 1.5 ml ethanol and 15.5 ml saline containing 1.55 mg ascorbic acid. The final solution was filtered by a Millex®-GV filter and collected in a 25 ml sterile vial. The n.d.c. RCYs obtained by these two different labeling methods were 12.4 ± 1.3% and 16.8 ± 1.0%, respectively, both of which met our requirements for further clinical application.

Quality control and acceptance criteria for human use

According to the USP General Chapter <823> and ChP General Chapter <2321>, we conducted a comprehensive and meticulous validation and quality control for the six consecutive batches of [^{18}F]**3**, three of them prepared from *Method I* and all others obtained via *Method II*. The acceptance criteria and detection results are depicted in Table 1. Immediately after formulation and sterile filtration, a series of real-time assessments were performed. The solution was observed through lead glass to ensure that it was either a colorless or light yellow and transparent liquid without any suspended particles. Using standard pH paper, pH values were determined to be between 5 and 6. The retention time of [^{18}F]**3** was determined to be 5.3 ± 0.2 min as measured by an analytical HPLC system equipped with a WondaSil C18-WR column (GL Science, 4.6 × 150 mm, 5 μm), and eluted with CH_3CN/H_2O (7:3, v/v) with a flow rate of 1.0 ml/min. The tandem UV (λ = 254 nm) and Gamma detectors showed that radiochemical purities were greater than 95%, and the radioligand structure was confirmed by co-injection using standard reference (Supplementary Figures S5, S6). The above system with 20 μL of injection loop was used for cold masses estimation in the formulated solution. Molar activities were determined within a range of either 77.7–104.9 GBq/μmol (*Method I*) or 56.6–98.0 GBq/μmol (*Method II*) as calculated by a standardized curve derived from the reference compounds.

By radioactivity testing every 30 min in a dose calibrator (7–8 total times), the half-life was found to range from 105–115 min. Only the 0.511 MeV and occasionally

TABLE 1 Summary of [^{18}F]3 human use validation data.

Test	Acceptance criteria	[^{18}F]3 from SCIDY (method I)	[^{18}F]3 from BPE (method II)	
Product yield	Report result at EOS	(1.5 ± 0.5 GBq at EOS)	(1.4 ± 0.3 GBq at EOS)	
Product volume	Report result at EOS	17 ml	17 ml	
Radioactive concentration	Report result at EOS	88.1 ± 29.8 MBq/ml	84.1 ± 15.4 MBq/ml	
Appearance	Clear color liquid; No suspended particles	Pass	Pass	
Radiochemical purity	≥95% at EOS	99%	99%	
Radionuclidic identity	105–115 min	109–113 min	109–113 min	
Molar activity (GBq/μmol)	Report result at EOS	88.6 ± 27.9 GBq/μmol	81.0 ± 4.3 GBq/μmol	
pH	4.0–7.5	5.0–6.0	5.0–6.0	
Solvents residue (USP/ICH Limits)	Acetone ≤ 0.5% v/v Ethanol ≤ 10% v/v DMA ≤ 0.041% v/v Acetonitrile ≤ 0.41 mg/ml	0.045 ± 0.016% pass — pass	0.052% pass Not detected pass	
Cu	Not more than 150 μg/day	—		Not detected
Sterile Filter Integrity Test	Not less than 46 psi	>50 psi	>50 psi	
Sterility	No growth observed after 14 d	Sterile	Sterile	
Bacterial Endotoxin Test	Not more than 15 EU/ml	Pass	Pass	

Abbreviations: EOS, end of synthesis.

TABLE 2 Information of volunteers and administrations of [^{18}F]3.

Number	Status	Sex	Age (years)	Weight (kg)	PET tracer administration		
					Injected dose (MBq)	Molar activity (GBq/μmol)	Cold mass (μg)
Dynamic scan (0–60 min)							
1	HV	M	33	68	260.4	43.3	3.56
2	HV	F	32	55	227.3	67.3	2.0
3	HV	M	32	63	340.7	33.7	6.0
4	HV	M	36	64	201.4	37.7	3.18
5	HV	M	37	70	286.8	19.61	8.73
6	HV	F	24	48	159.1	27.01	3.5
7	HV	F	26	51.5	196.0	18.13	6.4
8	HV	F	27	54	161.3	17.39	5.53

Abbreviations: HV, healthy volunteer; M, male; F, female.

1.022 MeV energy peaks were observed by spectrometer. No long-lived isotopes were observed by the analysis on a HPGE detector after ^{18}F-decay. The formulated product was free of pyrogens (Charles River Endosafe PTS) and sterile. No copper residue was detected using ICP-MS with detection limits of 0.1 mg/L, which ensures that the tracer injection has no effect on the physiological copper level in human body (Trumbo et al., 2001; Leong et al., 2020). Volatile organic solvent analysis was conducted using GC-FID disclosing residual acetone, acetonitrile, ethanol and DMA that were well within the limits required by the International Conference on Harmonization of Technical Requirements of Pharmaceuticals for Human Use.

Although both methods could deliver qualified radiotracer, considering the radiolabeling period, synthetic cost and quality control convenience, we chose *Method I* for routine productions in clinics.

Quantitative assessment of PDE10A in living human brains

After signing an informed consent forms, eight healthy volunteers (HVs) aged 24–37 years (women n = 4, men n = 4) underwent brain 3.0 T magnetic resonance imaging (MRI)

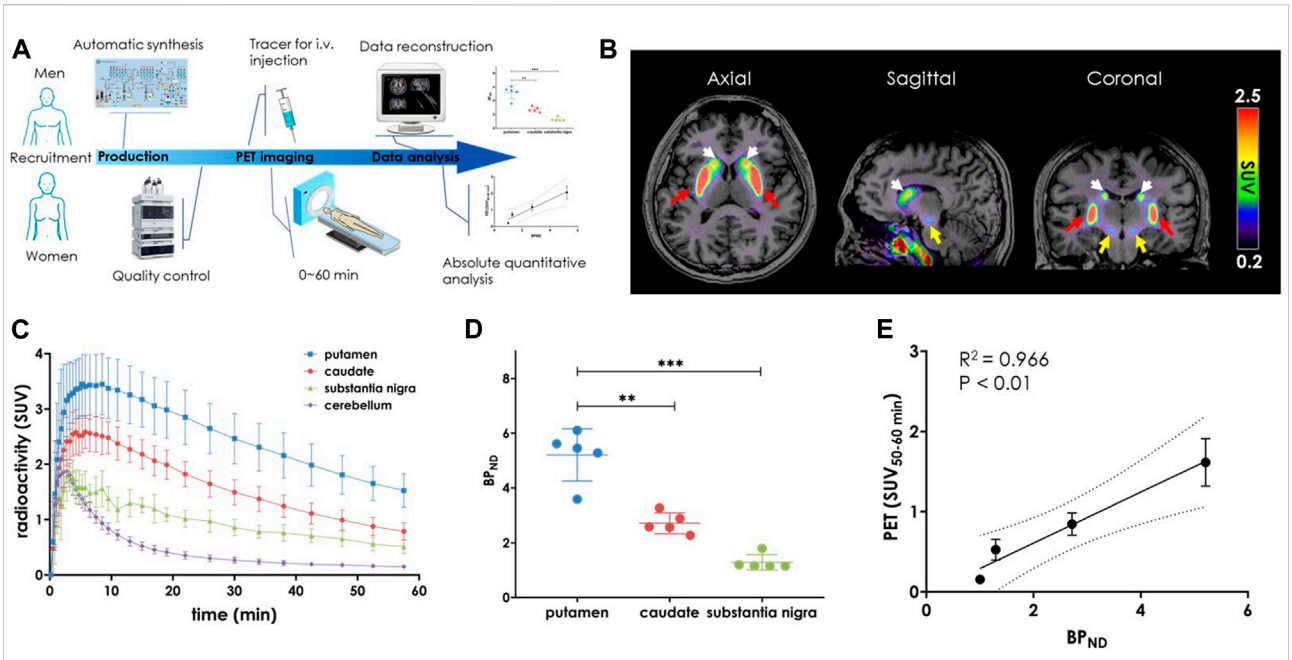

FIGURE 4
PET-MRI study of [^{18}F]**3** in the living human brain. **(A)** General flow chart of the experiment including four parts: volunteer recruitment, radioligand production, PET imaging and data processing; **(B)** Averaged PET-MRI images (0–60 min) presented in the axial, sagittal and coronal views. The layers showed high uptake of the putamen (red), caudate (white) and substantia nigra (yellow). The color scale on the right side of the picture is in SUV units; **(C)** Time activity curves (TACs) of PET imaging after injection of [^{18}F]**3** (n = 8); **(D)** BP_{ND} values in putamen, caudate and substantia nigra. Data are presented as mean ± SD (n = 8). Asterisks indicated statistical significance, ****$p < 0.0001$; **(E)** Correlation analysis of BP_{ND} with $SUV_{(50-60\ min)}$ (R^2 = 0.966, $p < 0.01$).

scan for anatomical analysis, followed by a dynamic 0–60 min PET/CT scan with injection of the radioligand [^{18}F]**3**. Demographic data and radioligand information for each study are summarized in Table 2, and the outline of this translational performance is illustrated in Figure 4A. According to our efforts on automatic radiofluorination, [^{18}F]**3** was produced on the day of the PET/CT scan using the GE TRACERlab FX2N module in a well-shielded hot cell. The reconstructed data were shown with averaged standardized uptake values ($SUV_{0-60min}$) and revealed an obvious, heterogenous radioactivity distribution pattern in the human brain. The highest accumulation was found in the caudate nucleus and putamen, followed by the substantia nigra. The lowest accumulation of tracer uptake was detected in the cerebellum, implying that this region had low PDE10A expression (Figure 4B).

To assess the binding specificity of [^{18}F]**3** to PDE10A in human brain, regional time-activity curves (TACs, Figure 4C) were used for kinetic modeling. For this modeling, the cerebellum was used as the reference region (Liu et al., 2016; Liu et al., 2018) and non-displaceable binding potential (BP_{ND}) was estimated by simplified reference-tissue model (SRTM). As shown in Figure 4D, the highest BP_{ND} were observed in the putamen, followed by the caudate nucleus (putamen vs caudate, 5.2 ± 0.9 vs. 2.7 ± 0.4, $p < 0.001$). Thus, the distribution of [^{18}F]**3** in the human brain closely matched the binding patterns that had been previously observed in both rodent and nonhuman primate (NHP) brain (Xiao et al., 2022). As expected, no skull radioactivity accumulation was detected, demonstrating that [^{18}F]**3** was more stable than [^{18}F]**1**. No defluorination occurred *in vivo*. Promisingly and despite its small size, the nucleus substantia nigra also showed good tracer accumulation with BP_{ND} of 1.3 ± 0.2. This had not been previously observed in our preclinical animal neuroimaging studies (Xiao et al., 2022). To the best of our knowledge, [^{18}F]**3** is the first radioligand capable of detecting PDE10A in substantia nigra in living human brain, which may pave the way for the exploration of the earliest pathogenesis in neurodegenerative diseases such as PD and HD (Chinta and Andersen, 2005; Koch and Raymond, 2019; Balestrino and Schapira, 2020).

In terms of clinical PET neuroimaging applications, either a dynamic or long time period scan would be challenging for patients due to physical or emotional causes and inescapable head movements. To verify a static scan with a reasonable duration, we then examined whether 10-min averaged SUV was practical for quantifying a target imaging signal. Comparisons between $SUV_{10-20min}$, $SUV_{20-30min}$, $SUV_{30-40min}$, $SUV_{40-50min}$, and $SUV_{50-60min}$ with specific binding (Supplementary Figure S8) revealed a much better relationship across the three high-uptake brain regions. Of these, the strongest relationship was observed between $SUV_{50-60min}$ and BP_{ND} (Figure 4E, R^2 = 0.966, $p < 0.01$). These results indicated that the widely used SUV PET signal derived from a 10-min static

scan after 50 min post-injection can be used as a routine protocol for *in vivo* measurement of PDE10A density using [^{18}F]**3**.

Materials and methods

General considerations and study design

All commercial reagents were purchased from commercially available vendors and used as received. Unless otherwise noted, solvents were freshly dried and degassed according to the purification handbook Purification of Laboratory Chemicals before use. Analytical thin-layer chromatography (TLC) was performed on pre-coated glass-backed plates (EMD TLC Silica gel 60 F254) and visualized using either a UV lamp (254 nm) or potassium permanganate. Silica gel for flash chromatography was 300–400 mesh. NMR spectra were recorded on Bruker 400/500 MHz on Bruker spectrometers, and resonances chemical shifts (δ) were given in parts per million (ppm) relative residual solvent. Peak multiplicities are abbreviated by the following symbols: s, singlet; d, doublet; t, triplet; hept, heptahedron; m, multiplet; dd, doublet of doublets. HRMS spectra were measured on a Thermo Scientific LTQ Qrbitrap XL using ESI+.

[^{18}F]Fluoride was produced by the GE Qilin MINITrace cyclotron via the ^{18}O(p, n)^{18}F reaction. The automatic radiolabeling was conducted in an GE TRACERlab FX2N module. Radiochemical purity and molar activity of the radioligand were determined by the HPLC (Shimadzu, Japan) with an analytical column (GL Science, WondaSil C18-WR, 4.6 × 150 mm). Radionuclide purity was tested on an energy disperse spectroscopy (Beijing Sunvic Co., Ltd.). The radioactivity of the product at the end of the synthesis was measured using a dose calibrator (Capintec CRC-55tR). The solvent and copper residue in the formulated product were tested by GC-FID (Agilent 6820) and ICP-MS (Agilent 7700x), respectively.

Clinical studies were performed in accordance with Good Clinical Practice standards, as well as in adherence with the ethical standards of the 1964 Helsinki declaration and amendments. The clinical study was approved by the Institutional Review Board (IRB) of the First Affiliated Hospital of Jinan University (Approval Letter No. KY-2022-007) (Guangdong Province Pharmaceutical Association, 2020). The healthy volunteers used in this clinical study signed informed consent forms before undergoing PET imaging with the right to know their legal guardians and welfare, as well as the nature of the study and the potential risks.

Synthesis of SCIDY (**5**) and BPE (**6**)

2-(2-(3-(4-(((2'S,3a'S,5'R)-4,6-dioxooctahydrospiro[[1,3]*dioxane-2,7'-*[2,5]*methanoinden]-5-ylidene)-l3-iodaneyl) phenyl)-7-methyl-4-oxo-3,4-dihydroquinazolin-2-yl)ethyl)-4-isopropoxyisoindoline-1,3-dione* (SCIDY, **5**). According to our previous report (Xiao et al., 2022), SCIDY **5** as obtained was a colorless powder (69% from aryl iodide **4**). ^{1}H NMR (400 MHz, DMSO-d_6) δ: 7.95 (dd, *J* = 11.7, 8.5 Hz, 3H), 7.70 (t, *J* = 7.8 Hz, 1H), 7.61 (d, *J* = 8.3 Hz, 2H), 7.43 (d, *J* = 8.4 Hz, 1H), 7.33 (dd, *J* = 11.1, 7.5 Hz, 3H), 4.79 (*p*, *J* = 6.1 Hz, 1H), 3.88 (t, *J* = 7.1 Hz, 2H), 2.63 (t, *J* = 6.8 Hz, 2H), 2.43 (s, 3H), 2.35 (s, 2H), 1.94 (d, *J* = 11.9 Hz, 4H), 1.77 (s, 2H), 1.72–1.57 (m, 6H), 1.28 (s, 3H), 1.27 (s, 3H).

4-isopropoxy-2-(2-(7-methyl-4-oxo-3-(4-(4,4,5,5-tetramethyl-1,3,2-dioxaborolan-2-yl)phenyl)-3,4-dihydroquinazolin-2-yl) ethyl)isoindoline-1,3-dione (BPE, **6**). To the solution of compound **4** (300 mg, 1.0 eq) in 5 ml of DMSO was added KOAc (149 mg, 3.0 eq), bis(pinacolato)diboron (141 mg, 1.1 eq), Pd (dppf)$_2$Cl$_2$ (11 mg, 0.03 eq), and the reaction mixture was then stirred under N_2 atmosphere at 80°C for 16 h. After cooling, the reaction mixture was diluted with EtOAc (50 ml) and washed with water (30 ml) and brine (30 ml). The organic layer was dried over Na_2SO_4 and concentrated to provide the crude residue which was purified by column chromatography (Hexane: EtOAc = 4:1) to deliver the desired product **6** as a baby pink solid in 62% yield. ^{1}H NMR (500 MHz, $CDCl_3$) δ 8.11 (d, *J* = 8.1 Hz, 1H), 7.95 (d, *J* = 8.1 Hz, 2H), 7.58–7.52 (m, 1H), 7.35–7.27 (m, 4H), 7.25–7.21 (m, 1H), 7.13 (d, *J* = 8.5 Hz, 1H), 4.67 (h, *J* = 6.0 Hz, 1H), 4.05 (t, *J* = 7.3 Hz, 2H), 2.67 (t, *J* = 7.3 Hz, 2H), 2.44 (s, 3H), 1.36 (d, *J* = 6.1 Hz, 6H), 1.33 (s, 12H) (Supplementary Figure S1); ^{13}C NMR (100 MHz, $CDCl_3$) δ 169.4, 168.1, 163.6, 157.0, 154.7, 148.8, 146.7, 141.1, 137.9, 137.1, 136.1, 129.7, 129.2, 128.4, 128.3, 122.3, 120.0, 116.9, 85.6, 76.5, 74.2, 36.3, 35.1, 26.4, 23.4 (Supplementary Figure S2); HRMS (m/z, ESI) calcd for $C_{34}H_{37}BN_3O_6$ (+) 594.2775, found 594.2768 (Supplementary Figure S3).

Automatic radiolabeling of [^{18}F]P10A-1910

A schematic diagram of the GE TRACERlab FX2N radiosynthesis module used for the production of [^{18}F]P10A-1910 is shown in Supplementary Figure S4. It should be noted that there was no SPE cartridges in the positions 1, 2, and 3, where the lines were connected directly. Automated radiolabeling involved the following: 1) receiving [^{18}F]fluoride in REACTOR 1 and trapping on the QMA cartridge in position 4, 2) azeotropic drying of [^{18}F]fluoride in REACTOR 2, 3) radiofluorination of SCIDY **5** (*Method I*) or BPE **6** (*Method II*) in REACTOR 2, and 4) HPLC purification followed by solid-phase formulation of the final product. Radiofluorination was performed using the sequential operations indicated in the schematic diagram (Supplementary Figure S4) as follows:

Vial 6: 12 mg TBAOMs in 300 μL H_2O and 700 μL CH_3CN (*Method I*); 0.5 mg TEAB in 1 ml CH_3OH (*Method II*)

Vial 7: 1 ml CH_3CN

Vial 8: 2 mg SCIDY **5** dissolved in 1 ml CH_3CN (*Method I*); 2.5 mg BPE **6** and 7 mg $Cu(OTf)_2$ $(py)_4$ dissolved in 300 μL DMA (*Method II*)

Vial 9: 1.5 ml mixed solvent (CH_3CN: H_2O = 3:2, v/v)

Vial 12: 10 ml H_2O

Vial 13: 1.5 ml EtOH.

Vial 14: 15.5 ml Vc aqueous solution (100 mg/L)

Vessel 2: 80 ml sterile water

C18 1 (position 4): Sep-Pak QMA Carbonate Plus (Part No. 186004540) preconditioned with 2 ml 7.5% $NaHCO_3$ aqueous solution, followed by 10 ml sterile water and 10 ml air.

C18 2 (position 5): Sep-Pak Plus Light C18 (Part No. WAT023501) activated with 5 ml EtOH, 10 ml sterile water and 10 ml air.

1) $^{18}F^-$ in Vessel 1 was transferred to REACTOR 1 by vacuum pump, then passed through the QMA installed in position 4 by helium flow, where the $^{18}F^-$ was trapped. The basic solution in Vial 6 was used for eluting $^{18}F^-$ from QMA to REACTOR 2, where the radioactive solution was heated to 85°C for 5 min. The mixture in REACTOR 2 was again dried azeotropically by addition of 1 ml anhydrous CH_3CN, preloaded into Vial 7, at 85°C for 3 min, then at 110°C for 5 min under helium flow and vacuum.
2) After REACTOR 2 was cooled down to room temperature, the precursor solution in Vial 8 was added. The mixture in REACTOR 2 was heated at 110°C for 10 min (*Method I*), or at 120°C for 20 min (*Method II*) during which REACTOR 2 was pumped into negative pressure and the air was passed through V25 and V37 three times.
3) The mixture was cooled to 40°C, then transferred to TUBE 2 through valves V16, VZ2, and V33. The liquid in Vial 9 was added, washing the radioactive residues from REACTOR 2 to TUBE 2 through the pipeline.
4) The crude mixture in TUBE 2 was injected into HPLC equipped with a semi-preparative column (OS∧K∧ SOD∧, CAPCELL PAK C18, UG80 5 μm, 250 × 10 mm) and eluted with CH_3CN/H_2O (55/45, v/v, *Method I*; 60/40, v/v, *Method II*) in Eluent 1 at a flow rate of 5 ml/min (*Method I*) or 3.5 ml/min (*Method II*) for radioligand purification. The semi-preparative HPLC chromatograms for both Methods are shown in Figure 3.
5) The indicated product portion was collected and diluted in the bottle of Vessel 2, then captured by Light C18 SPE in position 5. The cartridge was washed with 10 ml sterile water preloaded in Vial 12 to remove HPLC mobile phase and $^{18}F^-$.
6) The radioligand on Light C18 cartridge was eluted with 1.5 ml EtOH in Vial 13 into collection Vessel 3, followed by 15.5 ml Vc aqueous sodium chloride solution for injection preloaded into Vial 14. The solution was transferred, via V16a, and passed through a Millipore GV vented filter (0.22 μm, SLGVR13SL) connected to a 16-gauge hypodermic needle into a sterile 25-ml dose vial (ABX) fitted with a Millex sterile filtered venting needle (0.2 μm, 25 mm, Merck).

Quality control and analysis

An analytical HPLC (SHIMADZU, SPD-16) was performed on the system using a UV detector (λ = 254 nm), a gamma detector (Eckert & Ziegler, BGO Detector, B-FC-4100) and analysis software (LabSolutions Essentia). The radiochemical purity and molar activity were determined by an analytical column (GL Science, WondaSil C18-WR, 4.6 × 150 mm) with CH_3CN: H_2O = 7:3 (v/v) at a flow rate of 1.0 ml/min. Refer to the Supporting Information for the standard curve and calculation of molar activity (Supplementary Figure S7).

The formula for calculating injected cold mass was as follows: Injected mass dose (μg) = molecular weight (g/mol) × injected radioactivity (mCi/1000)/molar activity (Ci/μmol).

Solvent residual testing: Either the FFAP column (30 m, 0.25 mm, 0.5 μm) or INNOWAX column (30 m, 0.53 mm, 0.5 μm) was used with a constant hydrogen flow rate of 1.5 ml/min. Oven temperature was ramped up starting from 50°C and the front inlet was set to 240°C. A split ratio of 10:1 was used. The elution time for ethanol was approximately 1.63 min, acetonitrile was approximately 1.95 min, acetone was approximately 1.39 min, and DMA was approximately 2.23 min.

Determination of copper residue: Sample processing including the following: 0.5 ml was diluted to 50 ml with 2% nitric acid. Instrument conditions: RF power: 1.55 kW; Feedback power < 10 W; Sampling depth: 10 mm; Nebulizer: MicroMist; Nebulizer chamber temperature: 2°C; Argon gas flow: plasma gas 15.0 L/min, auxiliary gas 0.8 L/min, carrier gas 0.8 L/min, compensation gas 0.4 L/min; collision gas: helium, 4.3 ml/min; scanning mode: peak skipping; online internal standard element Ge, concentration 0.5 mg/L. According to these methods, the limit of quantification was determined to be 0.1 mg/L (data in house).

PET-MRI study in living human brain

Each volunteer participating in this study signed an informed consent form. All participants underwent a complete physical exam before the study, including medical history, electrocardiogram (ECG), blood routine and chemical tests. The volunteer first underwent a brain magnetic resonance imaging examination (GE Discovery 750, Milwaukee, United States), including 3D Bravo T1 (repetition time (TR), 8.24 ms; echo time (TE), 3.24 ms; slice thickness = 1.1 mm; matrix size = 256 × 256; flip

angle, 12), 3D Cor T2 Cube (TR, 3002 ms; TE, 95.328 ms; slice thickness = 1.0 mm; matrix size = 256 × 256; flip angle, 90), T2 FLAIR (TR, 5002 ms; TE, 127.316 ms; slice thickness = 1.0 mm; matrix size = 256 × 256; flip angle, 90), diffusion weighted imaging (DWI) (TR, 3000 ms; TE, 90.6 ms; slice thickness = 3.0 mm; matrix size = 128 × 128; flip angle, 90), cerebrovascular imaging (MRA) (TR, 22 ms; TE, 2.7 ms; slice thickness = 1.2 mm; matrix size = 384 × 256; flip angle, 20). Preliminary judgement from the anatomical level was conducted by two senior radiologists to make sure only healthy volunteers (HV) with normal brain function and structures were enrolled in the study.

HVs were placed in a supine position on a GE Discovery 690 PET/CT Elite scanner [^{18}F]P10A-1910 (*ca*. 0.12 mCi/kg, mass dose < 10 μg) was injected into the body from the cubital vein within 20 s, followed by dynamic brain PET collection in a 3D list mode for 60 min. Reconstruction of PET raw data was 32 frames (6 × 20 s, 8 × 30 s, 4 × 1 min, 5 × 2 min, 5 × 4 min, 4 × 5 min). A specialist monitored the volunteers' electrocardiograms (ECG) and blood pressure throughout the entire scan. After the scan, all HVs were advised to stay away from people, especially children and pregnant women, and to drink plenty of water to facilitate radioactivity excretion.

Individual MRI and PET image co-registration, and dynamic PET data processing were analyzed by PMOD (version 4.105, The First Affiliated of Jinan University). According to the biological expression of PDE10A, the caudate, putamen and substantia nigra were selected as regions of interest. Time radioactivity curves (TACs) from 0 to 60 min were generated. A simplified reference-tissue model (SRTM) was used to calculate their non-displaceable binding potential (BP_{ND}) with the cerebellum as the reference brain region. PET signal was presented as standardized uptake value (SUV) averaged from 0–60 min (SUV_{0-60}), 10–20 min (SUV_{10-20}), 20–30 min (SUV_{20-30}), 30–40 min (SUV_{30-40}), 40–50 min (SUV_{40-50}), or from 50–60 min (SUV_{50-60}) post injection. SUV data were analyzed by correlating with binding potentials.

Statistical analyses

Continuous variables were presented as mean ± standard deviation (SD). Student's *t* test and one way analysis of variance (one-way ANOVA) tests were used for group comparisons of continuous variables. Strength and direction of associations were assessed by Spearman's rank-order correlation. Linear regressions were performed as appropriate. A *p*-value was considered the significance level of the statistical analysis results, with $p < 0.05$ representing statistical significance. All statistical data were analyzed using GraphPad Prism (version 8.0.1).

Conclusion

We have realized the first automatic radiolabeling of a novel PDE10A PET tracer [^{18}F]**3** (designated [^{18}F]P10A-1910). Using the GE TRACERlab FX2N as our operation module, either the spirocyclic iodonium ylide tailing with an adamantyl auxiliary (**5**, *Method I*) or the boronic pinacol ester (**6**) coupled with copper salt and oxygen (*Method II*) delivered the product with comparable radiolabeling yields and molar activities. Moreover, the quality control of both was fully validated for human use. A subsequent imaging study in the living human brain revealed that the radioactivity accumulated in the caudate, putamen, as well as the substantia nigra. BP_{ND} was strongly correlated with the PET signal indicated by $SUV_{50-60min}$. This easy, automatic radiolabeling, good *in vivo* stability and binding potential, as well as practical protocols for use in imaging scan in clinics would facilitate widespread use of [^{18}F]**3**. Critically, its use would contribute to future exploration of PDE10A-related CNS pathologies in large-scale, multicenter trials.

Data availability statement

The original contributions presented in the study are included in the article/SupplementaryMaterial, further inquiries can be directed to the corresponding authors.

Ethics statement

The studies involving human participants were reviewed and approved by IRB of the First Affiliated Hospital of Jinan University (KY-2022-007). The patients/participants provided their written informed consent to participate in this study. Written informed consent was obtained from the individual(s) for the publication of any potentially identifiable images or data included in this article.

Author contributions

All the authors contributed to this manuscript and have approved its final version. LW and JW proposed the study and conceived the project. HW, JW, and LW wrote the manuscript. HX and LW modified the paper. HW, JW, and SZ synthesized the radioligand. HW, JW, SZ, SD, GL, WR, CD, WZ, CC, and WL carried out experiments. ZD, JW, and LW designed and guided experiments.

Funding

This work was financially supported by the National Natural Science Foundation of China (No. 82071974, 81871383, China), Guangdong Basic and Applied Basic Research Foundation (2020A1515011192, China), Guangzhou Science and

Technology Program (202206010106, China), and Shenzhen Basic Research Project (JCYJ20180503182116931, China).

Acknowledgments

We gratefully acknowledge the support of K.C. Wong Education Foundation (China).

Conflict of interest

The authors declare that the research was conducted in the absence of any commercial or financial relationships that could be construed as a potential conflict of interest.

Publisher's note

Supplementary material

The Supplementary Material for this article can be found online at: https://www.frontiersin.org/articles/10.3389/fbioe.2022.983488/full#supplementary-material

References

Balestrino, R., and Schapira, A. H. V. (2020). Parkinson disease. *Eur. J. Neurol.* 27, 27–42. doi:10.1111/ene.14108

Barret, O., Thomae, D., Tavares, A., Alagille, D., Papin, C., Waterhouse, R., et al. (2014). *In vivo* assessment and dosimetry of 2 novel PDE10A PET radiotracers in humans: ^{18}F-MNI-659 and ^{18}F-MNI-654. *J. Nucl. Med.* 55, 1297–1304. doi:10.2967/jnumed.113.122895

Beavo, J. A. (1995). Cyclic nucleotide phosphodiesterases: Functional implications of multiple isoforms. *Physiol. Rev.* 75, 725–748. doi:10.1152/physrev.1995.75.4.725

Bender, A. T., and Beavo, J. A. (2006). Cyclic nucleotide phosphodiesterases: Molecular regulation to clinical use. *Pharmacol. Rev.* 58, 488–520. doi:10.1124/pr.58.3.5

Cecchin, D., Garibotto, V., Law, I., and Goffin, K. (2021). PET imaging in neurodegeneration and neuro-oncology: Variants and pitfalls. *Semin. Nucl. Med.* 51, 408–418. doi:10.1053/j.semnuclmed.2021.03.003

Charbonneau, H., Prusti, R. K., LeTrong, H., Sonnenburg, W. K., Mullaney, P. J., Walsh, K. A., et al. (1990). Identification of a noncatalytic cGMP-binding domain conserved in both the cGMP-stimulated and photoreceptor cyclic nucleotide phosphodiesterases. *Proc. Natl. Acad. Sci. U. S. A.* 87, 288–292. doi:10.1073/pnas.87.1.288

Chinta, S. J., and Andersen, J. K. (2005). Dopaminergic neurons. *Int. J. Biochem. Cell Biol.* 37, 942–946. doi:10.1016/j.biocel.2004.09.009

Christopher, D., Guillaume, G. R., Michael, A. L., and Carroll, M. (2012). Evaluation of tetraethylammonium bicarbonate as a phase-transfer agent in the formation of [^{18}F]fluoroarenes. *J. Fluor. Chem.* 143, 231–237. doi:10.1016/j.jfluchem.2012.07.015

Chu, L., and Qing, F. L. (2014). Oxidative trifluoromethylation and trifluoromethylthiolation reactions using (trifluoromethyl)trimethylsilane as a nucleophilic CF3 source. *Acc. Chem. Res.* 47, 1513–1522. doi:10.1021/ar4003202

Coskran, T. M., Morton, D., Menniti, F. S., Adamowicz, W. O., Kleiman, R. J., Ryan, A. M., et al. (2006). Immunohistochemical localization of phosphodiesterase 10A in multiple mammalian species. *J. Histochem. Cytochem.* 54, 1205–1213. doi:10.1369/jhc.6A6930.2006

Francis, S. H., Blount, M. A., and Corbin, J. D. (2011). Mammalian cyclic nucleotide phosphodiesterases: Molecular mechanisms and physiological functions. *Physiol. Rev.* 91, 651–690. doi:10.1152/physrev.00030.2010

Geerts, H., Spiros, A., and Roberts, P. (2017). Phosphodiesterase 10 inhibitors in clinical development for CNS disorders. *Expert Rev. Neurother.* 17, 553–560. doi:10.1080/14737175.2017.1268531

Girault, J. A. (2012). Integrating neurotransmission in striatal medium spiny neurons. *Adv. Exp. Med. Biol.* 970, 407–429. doi:10.1007/978-3-7091-0932-8_18

Guangdong Province Pharmaceutical Association (2020). Consensus on phase 0 clinical trial application for positron radiopharmaceuticals. *Pharm. Today (Chinese)* 30, 793–798. Available at: https://yaxu.cbpt.cnki.net/WKE3/WebPublication/paperDigest.aspx?paperID=2b4207a7-5d76-4f85-9af1-c058de9bdd03. doi:10.12048/j.issn.1674-229X.2020.12.001

Gulyás, B., Trón, L., Csiba, L., Esik, O., Pálinkás, J., and Szabó, Z. (1996). Positron emission tomography: Foundations and applications. *Orv. Hetil.* 137, 731–738. doi:10.1556/650.1996.04.07

Inkster, J., Akurathi, V., Chen, Y., Sromek, A., Neumeyer, J., and Packard, A. (2016). ^{18}F chemistry without azeotropic distillations: Tetraethylammonium salts as combined anion exchange reagents and phase transfer catalysts. *JNM* 57, 328. Available at: https://jnm.snmjournals.org/content/57/supplement_2/328.

Ishiyama, T., Murata, M., and Miyaura, N. (1995). Palladium(0)-catalyzed cross-coupling reaction of alkoxydiboron with haloarenes: A direct procedure for arylboronic esters. *J. Org. Chem.* 60, 7508–7510. doi:10.1021/jo00128a024

Joong-Hyun, C., and Pike, V. W. (2012). Single-step radiosyntheses of '^{18}F-labeled click synthons' from azide-functionalized diaryliodonium salts. *Eur. J. Org. Chem.* 24, 4541–4547. doi:10.1002/ejoc.201200695

Koch, E. T., and Raymond, L. A. (2019). Dysfunctional striatal dopamine signaling in Huntington's disease. *J. Neurosci. Res.* 97, 1636–1654. doi:10.1002/jnr.24495

Kötter, R. (1994). Postsynaptic integration of glutamatergic and dopaminergic signals in the striatum. *Prog. Neurobiol.* 44, 163–196. doi:10.1016/0301-0082(94)90037-x

Laere, K. V., Ahmad, R. U., Hudyana, H., Celen, S., Dubois, K., Schmidt, M. E., et al. (2013). Human biodistribution and dosimetry of ^{18}F-JNJ42259152, a radioligand for phosphodiesterase 10A imaging. *Eur. J. Nucl. Med. Mol. Imaging* 40, 254–261. doi:10.1007/s00259-012-2270-1

Leong, F., Hua, X., Wang, M., Chen, T., Song, Y., Tu, P., et al. (2020). Quality standard of traditional Chinese medicines: Comparison between European pharmacopoeia and Chinese pharmacopoeia and recent advances. *Chin. Med.* 15, 76. doi:10.1186/s13020-020-00357-3

Liang, S. H., Wang, L., Stephenson, N. A., Rotstein, B. H., and Vasdev, N. (2019). Facile ^{18}F labeling of non-activated arenes via a spirocyclic iodonium(III) ylide method and its application in the synthesis of the mGluR5 PET radiopharmaceutical [^{18}F]FPEB. *Nat. Protoc.* 14, 1530–1545. doi:10.1038/s41596-019-0149-3

Liu, H., Jin, H., Luo, Z., Yue, X., Zhang, X., Flores, H., et al. (2018). *In vivo* Characterization of two ^{18}F-labeled PDE10A PET radioligands in nonhuman primate brains. *ACS Chem. Neurosci.* 9, 1066–1073. doi:10.1021/acschemneuro.7b00458

Liu, H., Jin, H., Yue, X., Han, J., Yang, H., Flores, H., et al. (2016). Comparison of [^{11}C]TZ1964B and [^{18}F]MNI659 for PET imaging brain PDE10A in nonhuman primates. *Pharmacol. Res. Perspect.* 4, e00253. doi:10.1002/prp2.253

Loughney, K., Snyder, P. B., Uher, L., Rosman, G. J., Ferguson, K., and Florio, V. A. (1999). Isolation and characterization of PDE10A, a novel human 3', 5'-cyclic nucleotide phosphodiesterase. *Gene* 234, 109–117. doi:10.1016/s0378-1119(99)00171-7

Marques, T. R., Natesan, S., Niccolini, F., Politis, M., Gunn, R. N., Searle, G. E., et al. (2016). Phosphodiesterase 10A in schizophrenia: A PET study using [^{11}C]IMA107. *Am. J. Psychiatry.* 173, 714–721. doi:10.1176/appi.ajp.2015.15040518

Mori, W., Yamasaki, T., Fujinaga, M., Ogawa, M., Zhang, Y., Hatori, A., et al. (2019). Development of 2-(2-(3-(4-([^{18}F]Fluoromethoxy-d_2)phenyl)-7-methyl-4-oxo-3, 4-dihydroquinazolin-2-yl)ethyl)-4-isopropoxyisoindoline-1, 3-dione for Positron-Emission-Tomography imaging of phosphodiesterase 10A in the brain. *J. Med. Chem.* 62, 688–698. doi:10.1021/acs.jmedchem.8b01366

Omori, K., and Kotera, J. (2007). Overview of PDEs and their regulation. *Circ. Res.* 100, 309–327. doi:10.1161/01.RES.0000256354.95791.f1

Pagano, G., Niccolini, F., Wilson, H., Yousaf, T., Khan, N. L., Martino, D., et al. (2019). Comparison of phosphodiesterase 10A and dopamine transporter levels as markers of disease burden in early Parkinson's disease. *Mov. Disord.* 34, 1505–1515. doi:10.1002/mds.27733

Rong, J., Mori, W., Xia, X., Schafroth, M. A., Zhao, C., Van, R. S., et al. (2021). Novel reversible-binding PET ligands for imaging monoacylglycerol lipase based on the piperazinyl azetidine scaffold. *J. Med. Chem.* 6, 14283–14298. doi:10.1021/acs.jmedchem.1c00747

Rotstein, B. H., Wang, L., Liu, R. Y., Patteson, J., Kwan, E. E., Vasdev, N., et al. (2016). Mechanistic studies and radiofluorination of structurally diverse pharmaceuticals with spirocyclic iodonium(III) ylides. *Chem. Sci.* 7, 4407–4417. doi:10.1039/C6SC00197A

Russell, D. S., Barret, O., Jennings, D. L., Friedman, J. H., Tamagnan, G. D., Thomae, D., et al. (2014). The phosphodiesterase 10 positron emission tomography tracer, [^{18}F]MNI-659, as a novel biomarker for early Huntington disease. *JAMA Neurol.* 71, 1520–1528. doi:10.1001/jamaneurol.2014.1954

Russell, D. S., Jennings, D. L., Barret, O., Tamagnan, G. D., Carroll, V. M., Caillé, F., et al. (2016). Change in PDE10 across early Huntington disease assessed by [^{18}F] MNI-659 and PET imaging. *Neurology* 86, 748–754. doi:10.1212/WNL.0000000000002391

Shi, H., Braun, A., Wang, L., Liang, S. H., Vasdev, N., and Ritter, T. (2016). Synthesis of ^{18}F-difluoromethylarenes from aryl (pseudo) halides. *Angew. Chem. Int. Ed.* 55, 10786–10790. doi:10.1002/anie.201604106

Stepanov, V., Takano, A., Nakao, R., Amini, N., Miura, S., Hasui, T., et al. (2018). Development of two fluorine-18 labeled PET radioligands targeting PDE10A and *in vivo* PET evaluation in nonhuman primates. *Nucl. Med. Biol.* 57, 12–19. doi:10.1016/j.nucmedbio.2017.10.004

Taylor, N. J., Emer, E., Preshlock, S., Schedler, M., Tredwell, M., Verhoog, S., et al. (2017). Derisking the Cu-mediated ^{18}F-fluorination of heterocyclic positron emission tomography radioligands. *J. Am. Chem. Soc.* 139, 8267–8276. doi:10.1021/jacs.7b03131

Tredwell, M., Preshlock, S. M., Taylor, N. J., Gruber, S., Huiban, M., Passchier, J., et al. (2014). A general copper-mediated nucleophilic ^{18}F-fluorination of arenes. *Angew. Chem. Int. Ed.* 53, 7751–7755. doi:10.1002/anie.201404436

Trumbo, P., Yates, A. A., Schlicker, S., and Poos, M. (2001). Dietary reference intakes: Vitamin A, vitamin K, arsenic, boron, chromium, copper, iodine, iron, manganese, molybdenum, nickel, silicon, vanadium, and zinc. *J. Am. Diet. Assoc.* 101, 294–301. doi:10.1016/S0002-8223(01)00078-5

Wang, L., Cheng, R., Fujinaga, M., Yang, J., Zhang, Y., Hatori, A., et al. (2017). A facile radiolabeling of [^{18}F]FDPA via spirocyclic iodonium ylides: Preliminary PET imaging studies in preclinical models of neuroinflammation. *J. Med. Chem.* 60, 5222–5227. doi:10.1021/acs.jmedchem.7b00432

Wang, L., Yao, S., Tang, R., Zhu, H., Zhang, L., Gong, J., et al. (2020). A concisely automated synthesis of TSPO radiotracer [^{18}F]FDPA based on spirocyclic iodonium ylide method and validation for human use. *J. Label. Comp. Radiopharm.* 63, 119–128. doi:10.1002/jlcr.3824

Wilson, H., Micco, R. D., Niccolini, F., and Politis, M. (2017). Molecular imaging markers to track Huntington's disease pathology. *Front. Neurol.* 8, 11. doi:10.3389/fneur.2017.00011

Xiao, Z. W., Wei, H. Y., Xu, Y., Haider, A., Wei, J. J., Yuan, S. Y., et al. (2022). Discovery of a highly specific ^{18}F-labeled PET ligand for phosphodiesterase 10A enabled by novel spirocyclic iodonium ylide radiofluorination. *Acta Pharm. Sin. B* 12, 1963–1975. doi:10.1016/j.apsb.2021.11.014

Xie, Z., Adamowicz, W. O., Eldred, W. D., Jakowski, A. B., Kleiman, R. J., Morton, D. G., et al. (2006). Cellular and subcellular localization of PDE10A, a striatum-enriched phosphodiesterase. *Neuroscience* 139, 597–607. doi:10.1016/j.neuroscience.2005.12.042

frontiers | Frontiers in Bioengineering and Biotechnology

TYPE Original Research
PUBLISHED 06 October 2022
DOI 10.3389/fbioe.2022.1010672

OPEN ACCESS

EDITED BY
Chao Zheng,
Yale University, United States

REVIEWED BY
Ruiguo Zhang,
Tianjin Medical University General Hospital, China
Yi Li,
Fox Chase Cancer Center, United States

*CORRESPONDENCE
Hao Xu,
txh@jnu.edu.cn
Guibin Qiao,
qiaoguibin@gdph.org.cn

†These authors have contributed equally to this work

SPECIALTY SECTION
This article was submitted to Nanobiotechnology, a section of the journal Frontiers in Bioengineering and Biotechnology

RECEIVED 03 August 2022
ACCEPTED 20 September 2022
PUBLISHED 06 October 2022

CITATION
Sun T, Huang S, Jiang Y, Yuan H, Wu J, Liu C, Zhang X, Tang Y, Ben X, Tang J, Zhou H, Zhang D, Xie L, Chen G, Zhao Y, Wang S, Xu H and Qiao G (2022), Dynamic alteration in SULmax predicts early pathological tumor response and short-term prognosis in non-small cell lung cancer treated with neoadjuvant immunochemotherapy. *Front. Bioeng. Biotechnol.* 10:1010672. doi: 10.3389/fbioe.2022.1010672

Dynamic alteration in SULmax predicts early pathological tumor response and short-term prognosis in non-small cell lung cancer treated with neoadjuvant immunochemotherapy

Taotao Sun[1,2†], Shujie Huang[3,4†], Yongluo Jiang[5,6†], Hui Yuan[2], Junhan Wu[3,4], Chao Liu[7], Xiaochun Zhang[2], Yong Tang[3], Xiaosong Ben[3], Jiming Tang[3], Haiyu Zhou[3], Dongkun Zhang[3], Liang Xie[3], Gang Chen[3], Yumo Zhao[5,6], Shuxia Wang[2], Hao Xu[1]* and Guibin Qiao[3,4,8]*

[1]Department of Nuclear Medicine and PET/CT-MRI Centre, The First Affiliated Hospital of Jinan University, Guangzhou, China, [2]Department of Nuclear Medicine, WeiLun PET Center, Guangdong Provincial People's Hospital, Guangdong Academy of Medical Sciences, Guangzhou, China, [3]Department of Thoracic Surgery, Guangdong Provincial People's Hospital, Guangdong Academy of Medical Sciences, Guangzhou, China, [4]Shantou University Medical College, Shantou, China, [5]State Key Laboratory of Oncology in South China, Collaborative Innovation Center for Cancer Medicine, Guangzhou, China, [6]Department of Nuclear Medicine, Sun Yat-sen University Cancer Center, Guangzhou, China, [7]Department of Pathology, Guangdong Provincial People's Hospital, Guangdong Academy of Medical Sciences, Guangzhou, China, [8]The Second School of Clinical Medicine, Southern Medical University, Guangzhou, China

Introduction: Biomarkers predicting tumor response to neoadjuvant immunochemotherapy in non-small cell lung cancer (NSCLC) are still lacking despite great efforts. We aimed to assess the effectiveness of the immune PET Response Criteria in Solid Tumors *via* SULmax (iPERCIST-max) in predicting tumor response to neoadjuvant immunochemotherapy and short-term survival in locally advanced NSCLC.

Methods: In this prospective cohort study, we calculated SULmax, SULpeak, metabolic tumor volume (MTV), total lesion glycolysis (TLG) and their dynamic percentage changes in a training cohort. We then investigated the correlation between alterations in these parameters and pathological tumor responses. Subsequently, iPERCIST-max defined by the proportional changes in the SULmax response (△SULmax%) was constructed and internally validated using a time-dependent receiver operating characteristic (ROC) curve and the area under the curve (AUC) value. A prospective cohort from the Sun Yat-Sen University Cancer Center (SYSUCC) was also included for external validation. The relationship between the iPERCIST-max responsiveness and event-free survival in the training cohort was also investigated.

Results: Fifty-five patients with NSCLC were included in this study from May 2019 to December 2021. Significant alterations in post-treatment SULmax ($p < 0.001$), SULpeak ($p < 0.001$), SULmean ($p < 0.001$), MTV ($p < 0.001$), TLG ($p <$

0.001), and tumor size ($p < 0.001$) were observed compared to baseline values. Significant differences in SULpeak, SULmax, and SULmean between major pathological response (mPR) and non-mPR statuses were observed. The optimal cutoff values of the SULmax response rate were −70.0% and −88.0% using the X-tile software. The univariate and multivariate binary logistic regression showed that iPERCIST-max is the only significant key predictor for mPR status [OR = 84.0, 95% confidence interval (CI): 7.84–900.12, $p < 0.001$]. The AUC value for iPERCIST-max was 0.896 (95% CI: 0.776–1.000, $p < 0.001$). Further, external validation showed that the AUC value for iPERCIST-max in the SYSUCC cohort was 0.889 (95% CI: 0.698–1.000, $p = 0.05$). Significantly better event-free survival (EFS) in iPERCIST-max responsive disease (31.5 months, 95% CI 27.9–35.1) than that in iPERCIST-max unresponsive disease (22.2 months, 95% CI: 17.3–27.1 months, $p = 0.024$) was observed.

Conclusion: iPERCIST-max could better predict both early pathological tumor response and short-term prognosis of NSCLC treated with neoadjuvant immunochemotherapy than commonly used criteria. Furthermore, large-scale prospective studies are required to confirm the generalizability of our findings.

KEYWORDS

non-small cell lung cancer, neoadjuvant immunochemotherapy, major pathological response, iPERCIST-max, 18F-FDG positron emission tomography

Introduction

Non-small cell lung cancer (NSCLC) is the most common cause of cancer-related death worldwide (Siegel et al., 2021), likely because most NSCLC patients (>70%) are diagnosed at advanced stages (Ramos-Esquivel et al., 2017). Immune checkpoint inhibitors (ICIs) have changed the landscape of advanced NSCLC treatment (Ramos-Esquivel et al., 2017; Uprety et al., 2020; Huang et al., 2021; Wang et al., 2021). It has been reported that a combination of ICIs and chemotherapy significantly improve the prognosis of NSCLC (Spicer et al., 2021; Wang et al., 2021; Zhao et al., 2021). Although previously published data showed that more than 40% of NSCLC patients achieved major pathological response after neoadjuvant immunochemotherapy (NAIC), a large proportion of patients still could not benefit from such treatment modality and developed disease progression rapidly (Jiang et al., 2022). As the clinical management strategies for responders significantly differ from nonresponders, a non-invasive method to early evaluate, or even predict the treatment response to NAIC is urgently needed.

18F-FDG PET/CT, with its ability to depict both anatomical and functional changes, has been widely applied in oncological routines. The glucometabolism within a tumor, as revealed by PET imaging, was found to correlate with the expression of immune checkpoint programmed death 1 (PD-1), and the quantitative measurement of metabolic changes was found to associate with pathological response to NAIC (Lopci et al., 2016; Tao et al., 2020). Hence, 18F-FDG PET/CT might be utilized for early response evaluation. Prior studies have proposed several response-evaluation criteria for novel immunotherapies, of which the PET Response Criteria in Solid Tumors (PERCIST) (Joo Hyun et al., 2016) and the immune PERCIST (iPERCIST) standards were the most well-known (Goldfarb et al., 2019). Despite the reasonable diagnostic and predictive performance, their clinical implementation was hindered by several drawbacks (Tao et al., 2020). Both criteria require SULpeak, a value that reveals the average SUV within a small sphere (usually 1.2 cm in diameter) around the most hypermetabolic voxel, rendering small lesions with a metabolic diameter of less than 1 cm unmeasurable. Moreover, the partial volume effect might incur considerable measuring bias (Soret et al., 2007). Compared with SULpeak, a SULmax value, which reflects the most metabolically active portion of a potentially heterogeneous mass, was applicable in most lesions, thus is routinely reported and more clinically feasible (Wahl et al., 2009; Lodge et al., 2012). Moreover, prior studies found SULmax highly reproducible and comparable with proper standardization of the scanning protocol, despite the theoretical reproducibility issues. Hence, we hypothesize that a SULmax-based protocol might be clinically practical yet robust for the response evaluation and prediction of NAIC.

In light of the above, we proposed a SULmax-based protocol, named iPERCIST-max, to evaluate and predict treatment response to NAIC and tested our model's diagnostic and

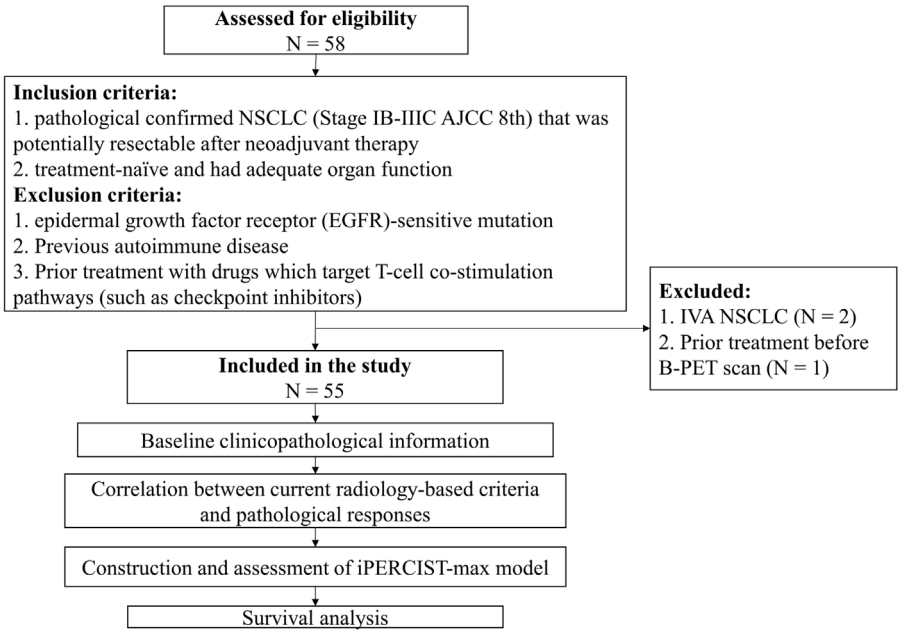

FIGURE 1
Flowchart of the study design. Fifty-eight patients were assessed for eligibility; eventually, fifty-five cases were included for subsequent analysis.

prognostic performance in a training and an independent external validation cohort.

Materials and methods

Patients and study design

This prospective study was proved by the institutional review board (The Ethics Committee of the Guangdong Provincial People's Hospital, No. GDREC2019687H). All procedures involved in this study were performed in accordance with the Declaration of Helsinki (as revised in 2013). Written informed consent was obtained from each participant in the study.

Data were collected from two prospectively maintained cohorts starting from May 2019 to December 2021: 1) A training cohort from our local institute and 2) an external validation cohort from an independent institute from Sun Yat-sen University Cancer Center.

The included patients met the following criteria: 1) Pathologically confirmed as NSCLC (Stage IB-IIIC AJCC 8th edition) that was potentially resectable after neoadjuvant therapy; 2) treatment-naïve and adequate organ function. Exclusion criteria were as follows: 1) Epidermal growth factor receptor (EGFR)-sensitive mutation; 2) previous autoimmune disease; 3) prior treatment with drugs that target T-cell co-stimulation pathways (such as checkpoint inhibitors).

A flowchart describing the study design is presented in Figure 1. All patients underwent baseline ^{18}F-FDG PET/CT (B-PET) examination within 14 days before neoadjuvant therapy incorporating PD-1 inhibitors (200 mg) plus platinum-doublet chemotherapy every 3 weeks. After 2-4 cycles of neoadjuvant therapy, a follow-up ^{18}F-FDG PET/CT (F-PET) was performed. When F-PET showed progressive disease, a second F-PET was performed after 4–8 weeks (Goldfarb et al., 2019).

Image acquisition and analysis

All patients in our training cohort were scanned using the same scanner (Biograph HI-REZ 16; Siemens Healthcare, Henkestr, Germany), following the criteria of the uniform protocols for imaging in clinical trials (UPICT) (Graham et al., 2015). Supplementary File S1 describing the details of the imaging protocol was provided. All images were evaluated using a commercial medical image-processing workstation (uWS-MI, United Imaging Healthcare, Shanghai, China). Two experienced nuclear medicine physicians (TT S & YL J) who were blinded to the patients' clinical information independently analyzed the PET/CT images, resolving disagreements through consensus. Metabolic parameters including SULmax, SULpeak, SULmean, MTV in mL, and TLG were recorded on a lesion basis. Additionally, thoracic CECT images were reviewed by two

board-certified radiologists (H Y & XC Z) who were blinded to the PET/CT study.

Response evaluation

We proposed the iPERCIST-max criteria based on the proportional changes in the SULmax response (△SULmax%) using the following formula:

$$\frac{Subsequent\ SULmax - baseline\ SULmax}{baseline\ SULmax} \times 100\%. \quad (1)$$

The patients were divided into the following three groups based on tumor responses assessed by △SULmax%: iPERCIST-max complete metabolic responsive disease (imCMRD), responsive metabolic disease (imRMD), and unresponsive metabolic disease (imUMD). The optimal cutoff values for grouping were determined using a X-tile software (Camp et al., 2004).

Additionally, as references, metabolic and morphological responses were also evaluated using iPERCIST and iRECIST criteria (Goldfarb et al., 2019). Specifically, iPERCIST categorized patients into: Immune complete metabolic response (iCMR), partial metabolic response (iPMR), stable disease (iSMD), unconfirmed progressive metabolic disease PMD (iUPMD), and confirmed PMD (iCPMD); whereas iRECIST (Ayati et al., 2021) classified patients into: immune-complete response (iCR), immune-partial response (iPR), immune-stable disease (iSD), immune-confirmed progressive disease (iCPD), and unconfirmed PD (iUPD). Responsive diseases were defined as either metabolically (iCMR & iPMR per iPERCIST or imCMRD & imRMD per IPERCIST-max as mRD) or morphologically (iCR & iPR, as RD) alterations. Likewise, metabolic and morphological unresponsive disease were diagnosed as mUD (iSMD & iCPMD per iPERCIST or imUMD per iPERCIST-max) and UD (iSD & iCPD), respectively. Notably, upon the diagnosis of iUPMD or iUPD, a second F-PET/CECT study was performed 4–8 weeks later to verify the diagnosis (Eisenhauer et al., 2009; Seymour et al., 2017). (Supplementary Table S1 for a comparison of the iPERCIST, iRECIST, and iPERCIST-max criteria).

Outcome evaluation

Two experienced pathologists independently performed pathological assessments according to the current standard protocol. Pathological complete response (pCR) was defined as no evidence of residual viable tumor after neoadjuvant treatment. The major pathological response (mPR) was defined as less than 10% residual viable tumor following neoadjuvant treatment. Event-free survival (EFS) was calculated from the date of treatment initiation to the date of the first progression (local recurrence of tumor or distant metastasis) or death from any cause (Zheng et al., 2021). Censored data included those who were lost to follow-up or at the time of the final analysis.

Statistical analysis

Comparisons of intergroup continuous variables were performed using the Student's t-test or the Mann-Whitney method whenever suitable. Categorical variables were compared using the chi-squared test or Fisher's exact test, where suitable. The intraclass correlation coefficient (ICC) was calculated for quantification of the agreement between proportion changes in SULmax (△SULmax%) and in SULpeak (△SULpeak%). Notably, an ICC value between 0.81 and 1.00 suggests an excellent agreement (Zhao et al., 2015). Univariate followed by multivariate binary logistic regressions were used to identify independent predictors of mPR, following a three-step approach (Zhou et al., 2022). The power of prediction models was assessed by the area under the curve (AUC) value acquired from the Time-dependent receiver operating characteristic (ROC) curves. All tests were two-tailed, and $p < 0.05$ denotes statistical significance. All statistical analyses were performed using SPSS v26 software (IBM Corporation, Armonk, NY, United States) and R 4.0.0 (R Core Team 2020).

Results

Patient characteristics

Fifty-five patients (males: $n = 50$; females: $n = 5$) with a median age of 66 [Interquartile range (IQR) 58–69] years were enrolled in the training cohort, while 13 patients were enrolled in the external validation cohort. Detailed patient characteristics were tabulated in Table 1.

Treatment responses to NAIC

In the training cohort, 36 patients were deemed surgical candidates after the treatment, and the post-surgical histological studies confirmed that 13 (36.1%) patients achieved pCR while 23 (63.9%) achieved mPR. Likewise, in the independent validation cohort, 12 patients underwent surgery and 9 (75%) patients achieved mPR status.

PET imaging parameters in mPR and pCR patients

Significant alterations in post-treatment SULmax ($p < 0.001$), SULpeak ($p < 0.001$), SULmean ($p < 0.001$), MTV

TABLE 1 Patient characteristics. Values are presented as n (%) or median (interquartile range).

Characteristics	Training cohort	Validation cohort	*p* Value
Sex			0.265
Male	50 (91)	13 (100)	
Female	5 (9)	0 (0)	
Age (yrs)			0.001
Median (IQR)	66 (58–69)	57 (47–59)	
Smoking history			0.036
Yes	29 (52.7)	11 (84.6)	
No	26 (47.3)	2 (15.4)	
Lesion location			0.370
Right upper lobe	18 (32.7)	5 (38.5)	
Right middle lobe	3 (5.5)	1 (7.7)	
Right lower lobe	8 (14.5)	2 (15.4)	
Left upper lobe	20 (36.4)	2 (15.4)	
Left lower lobe	6 (10.9)	3 (23.1)	
Pathological subtypes			0.241
Adenocarcinoma	17 (30.9)	4 (30.8)	
Squamous cell carcinoma	35 (63.6)	7 (53.8)	
Others	3 (5.5)	2 (15.4)	
Clinical stage			0.345
IB	2 (3.6)	0 (0)	
IIA	5 (9.1)	0 (0)	
IIB	8 (14.5)	1 (7.7)	
IIIA	17 (30.9)	6 (46.2)	
IIIB	19 (34.5)	6 (46.2)	
IIIC	4 (7.3)	0 (0)	
Pathological stage			0.650
0	13 (36.1)	8 (66.7)	
IA	9 (25)	0 (0)	
IB	4 (11.1)	1 (8.3)	
IIB	5 (13.9)	1 (8.3)	
IIIA	5 (13.9)	2 (16.7)	
Lymphovascular invasion			0.553
Negative	35 (97.2)	12 (100)	
Positive	1 (2.8)	0 (0)	
Perineural invasion			1
Negative	36 (100)	12 (100)	
R0			0.553
R0	35 (97.2)	12 (100)	
R1	1 (2.8)	0 (0)	

($p < 0.001$), TLG ($p < 0.001$), and tumor size ($p < 0.001$) were observed compared with baseline values (Supplementary Figure S1) for all patients. Specifically, mPR patients presented with significantly lower SULpeak, SULmax, and SULmean than non-mPR ($p < 0.05$, as shown in Figures 2A–C). The median response rates of SULmax, SULpeak, and SULmean were significantly higher in the pCR cohort than in the non-pCR cohort (Figures 2D–F).

Comparison of iRECIST and iPERCIST evaluation

At the first radiological evaluation, 4 of 55 (7.3%) patients were evaluated as iUPD, 20 (36.4%) as iSD, and 31 (56.4%) as iPR. All the iUPD patients were identified as iCPD after the second evaluation. Based on the iRECIST criteria, none of the patients achieved iCR despite 13 pCR cases. Meanwhile, 5 of the

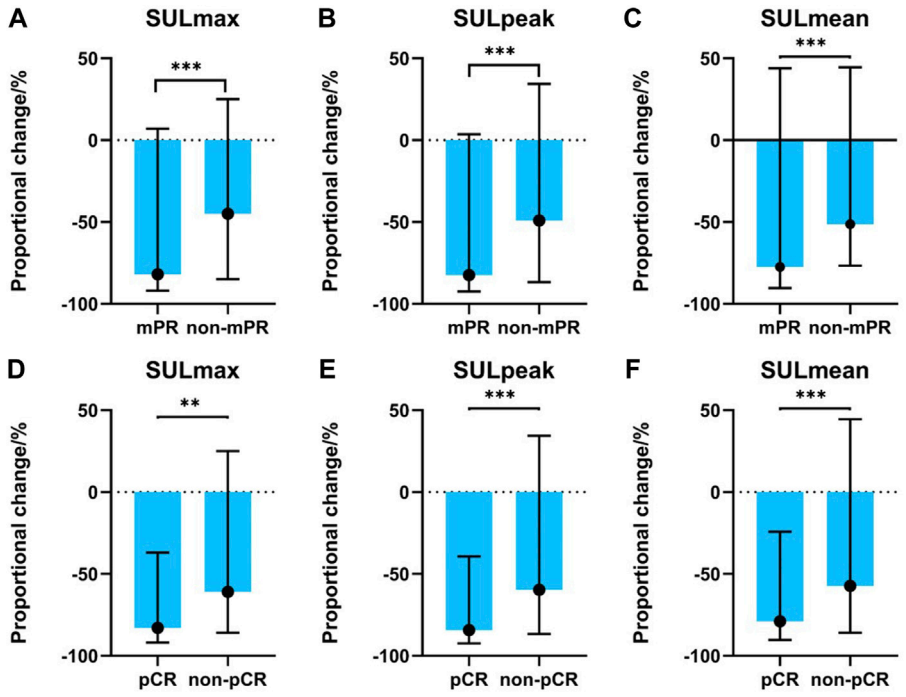

FIGURE 2
Association between PET-related parameters and pathological responses. **(A)** SULmax between mPR and non-mPR cohorts; **(B)** SULpeak between mPR and non-mPR cohorts; **(C)** SULmean between mPR and non-mPR cohorts; **(D)** SULmax between pCR and non-pCR cohorts; **(E)** SULpeak between pCR and non-pCR cohorts; **(F)** SULmean between pCR and non-pCR cohorts.

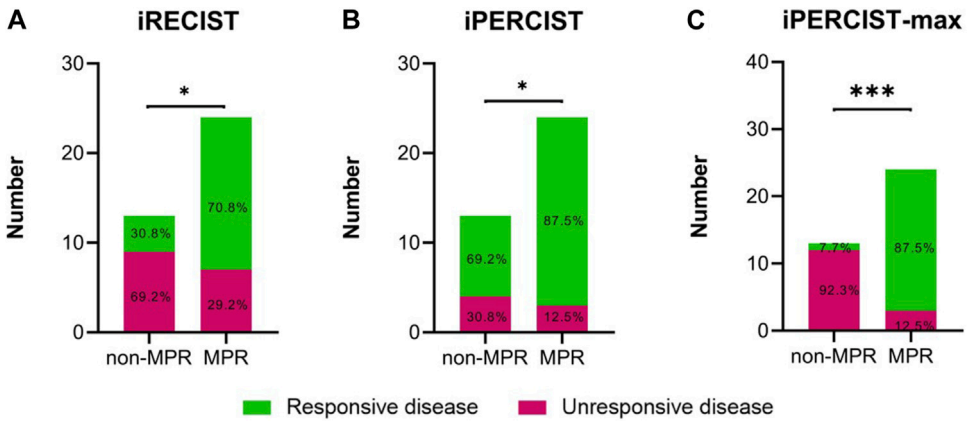

FIGURE 3
Differences in radiological disease responsiveness between mPR and non-mPR status based on iRECIST/iPERCIST/iPERCIST-max. **(A)** iRECIST; **(B)** iPERCIST; **(C)** iPERCIST-max. Green color represents responsive disease, while red color represents unresponsive disease.

55 (9.1%) patients were classified as iUPMD, seven (12.7%) as iSMD, 38 (69.1%) as iPMR, and five (9.1%) as iCMR based on the iPERCIST criteria. Subsequent PET-scan verified that four out of the five iUPMD cases were iCPMD, and one patient presented with pseudoprogressive disease. Three of the five iCMR patients underwent surgery, and all achieved pCR status. Despite the

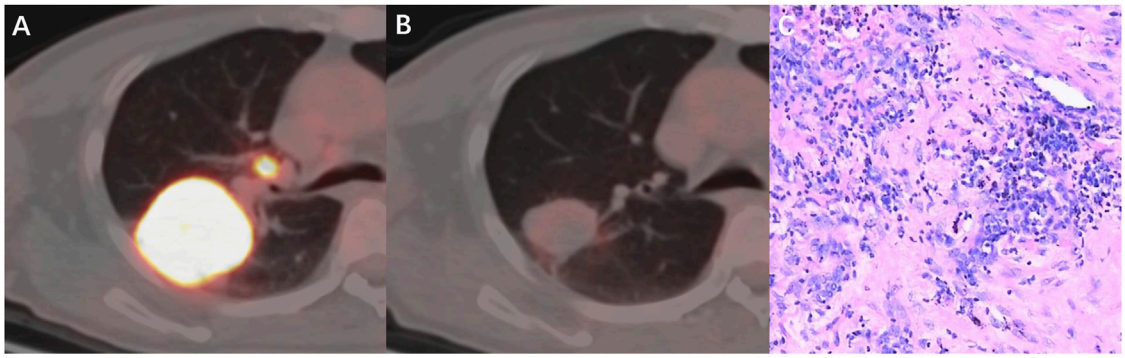

FIGURE 4
A 53-year-old man with squamous cell carcinoma, who had marked metabolic changes on PET scanning after two cycles of neoadjuvant immunochemotherapy and was classified as responder per iPERCIST-max. **(A)** Baseline PET-CT fusion image of the primary tumor and lymph nodes; **(B)** Follow-up PET-CT fusion image showed markedly reduced metabolic activity of the tumor. **(C)** pathological examination revealed this patient had mPR disease. mPR, major pathological response.

above stated differences, a significant association was observed in mPR status vs. iRECIST responsiveness (Figure 3A, $p = 0.019$) and iPERCIST responsiveness (Figure 3B, $p = 0.025$). Comparisons in diagnostic indicators among different criteria were shown in Supplementary Table S2.

Diagnostic performance of the proposed iPERCIST-max method

The ICC used to establish the agreement between the SULmax and SULpeak response rates was 0.994 (95% CI 0.990-0.997). The optimal cutoff values of the SULmax response rate were -70.0% and -88.0% using the X-tile software. Subsequently, tumor response represented by △SULmax% higher than -70% was defined as imUMD, those whose SULmax response rate was lower than -70.0% as imRMD, and those whose SULmax response rate was lower than -88.0% as imCMRD. All imCMRD patients who underwent surgery achieved pCR status. Moreover, a significantly higher proportion of imRMD was observed in the mPR cohort than in the non-mPR cohort ($\chi2 = 12.17$, $p < 0.001$) (Figure 3C). Figure 4 showed a typical case who achieved imRMD after two cycles of NAIC and had mPR status after surgery. Furthermore, the univariate and multivariate binary logistic regression showed that iPERCIST-max was the only significant key predictor for mPR status [OR = 84.0, 95% confidence interval (CI): 7.84–900.12, $p < 0.001$] (Table 2).

We utilized ROC and AUC values to better quantify the overall discriminatory power of various prediction models in predicting the mPR status. ROC analyses for comparisons in mPR status among iRECIST, iPERCIST, and iPERCIST-max were shown in Supplementary Figure S2. The AUC values for iRECIST responsiveness, iPERCIST responsiveness, and iPERCIST-max were 0.688 (95% CI: 0.498–0.877, $p = 0.070$), 0.625 (95% CI: 0.419–0.831, $p = 0.227$), and 0.896 (95% CI: 0.776–1.000, $p < 0.001$), respectively.

Furthermore, the Sun Yat-Sen University Cancer Center (SYSUCC) cohort was used to externally validate the robustness of iPERCIST-max. AUC value for iPERCIST-max predicting mPR status was 0.889 (95% CI: 0.698–1.000, $p = 0.05$).

The relationship between the iPERCIST-max responsiveness and event-free survival

The longest and median follow-up time was 35.5 and 21.0 months, respectively. iRECIST, iPERCIST, and iPERCIST-max can stratify patients into distinctive survival groups. Interestingly, no events (recurrence, metastasis, death, etc.) occurred in the imCMRD group at the last follow-up. The imCMRD group exhibited superior EFS compared to the other groups classified by iPERCIST-max ($p < 0.001$). Significantly better EFS in iPERCIST-max mRD (31.5 months, 95% CI: 27.9–35.1) than that in iPERCIST-max mUD (22.2 months, 95% CI: 17.3–27.1 months, $p = 0.024$) was observed (Figure 5A). Moreover, the 1-year survival AUC was 0.776 (95% CI: 0.575–0.976; $p < 0.001$) (Figure 5B). Significant differences in EFS were also seen between the UD and RD cohorts when classified using the iRECIST responsiveness ($p = 0.033$) and iPERCIST responsiveness ($p = 0.004$).

Discussion

Although the NSCLC treatment is profoundly shifting in the treatment paradigm due to recent advances in immunotherapy

TABLE 2 Univariate and multivariate binary logistic regression analyses. RD: responsive disease; UD: unresponsive disease; MRD: metabolic responsive disease; MUD: metabolic unresponsive disease; cT: clinical T stage; cN: clinical N stage; cTNM: clinical Tumor-nodal-metastasis stage.

Variables	Univariate		Multivariate	
	Odds ratio (95% CI)	*p* value	Odds ratio (95% CI)	*p* value
Sex	0.5 (0.062–4.04)	0.516	—	
Age	1.079 (0.984–1.184)	0.104	—	
cT	1.106 (0.703–1.741)	0.663	—	
cN	1.106 (0.703–1.741)	0.663	—	
cTNM	1.046 (0.611–1.789)	0.87	—	
Histological		—	—	
Adenocarcinoma (ref)	—	—	—	
Squamous cell carcinoma	1.143 (0.257–5.087)	0.861	—	
Others	0.571 (0.028–11.849)	0.718	—	
Smoking status	1.379 (0.356–5.341)	0.642	—	
iRECIST (RD vs. UD)	5.464 (1.256–23.774)	0.024	—	
iPERCIST (RD vs. UD)	3.111 (0.575–16.833)	0.188	—	
iPERCIST max (MRD vs. MUD)	73.333 (6.789–792.167)	<0.001	84 (7.839–900.116)	<0.001

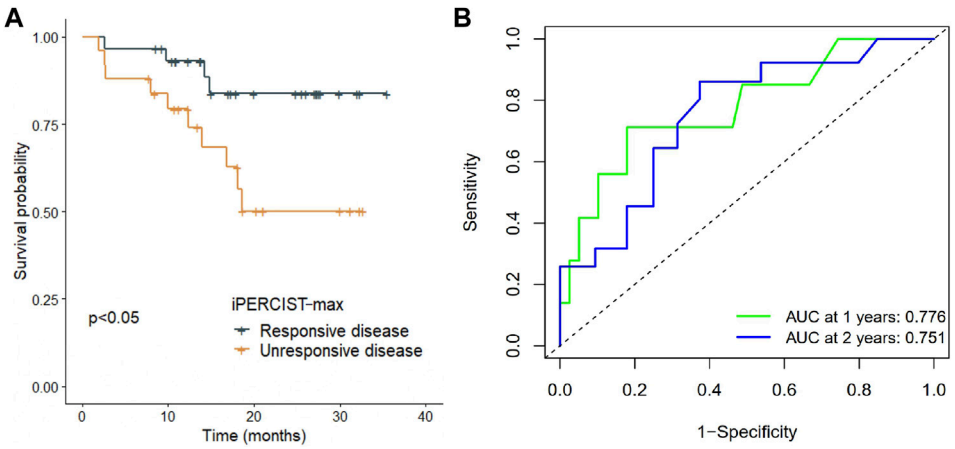

FIGURE 5
Survival difference in iPERCIST-max groups and internal validation of the robustness of iPERCSIT-max. **(A)** Kaplan-Meier estimated event-free survival between the responsive disease group and unresponsive disease group stratified by iPERCIST-max. **(B)** Time-dependent receiver-operating-characteristics (ROC) analysis for assessment of iPERCIST-max.

(Spicer et al., 2021; Zhao et al., 2021), it is clinically challenged by the lack of a robust and easy-to-use method to distinguish responders from non-responders. Hence, we proposed an iPERCIST-max model to predict the treatment response to NAIC. We found this method non-inferior to iPERCIST and iRECIST criteria in terms of robustness (Figure 3) but outperformed the latter in feasibility due to more straightforward clinical applications. Thus, the iPERCIST-max model might better suit the response evaluation to NAIC in NSCLC patients than iPERCIST and iRECIST criteria.

iPERCIST has been validated in multiple studies for its performance in assessing treatment responses to immunotherapies, using proportional changes in SULpeak values (Tao et al., 2020). However, as shown in our research, its clinical application was significantly challenged by its inability to index small lesions, mainly nodal and pulmonary metastasis [21 of 132 (15.6%) at baseline and 56 of 132 (42.2%) at follow-up]. Interestingly, SULmax, which was believed to be affected by multiple factors such as quanton noises, thus lacks the reproducibility for a quantitative study, was found effective in

the treatment evaluation in this study. We hypothesize that with the modern advancement of novel PET hardware and proper standardization of the imaging acquisition protocol, the variation of SULmax has been minimized, evidenced by a high agreement between the SULpeak and SULmax measurement in this study [ICC = 0.994 (95% CI 0.990-0.997)] and in others (Kumar et al., 2013).

Owing to the broader clinical applicability of SULmax, we decided to develop iPERCIST-max based on △SULmax%. Using −70.0% as the cutoff value calculated from the X-tile, the iPERCIST-max divided patients into imCMRD, imRMD and imUMD.

Subsequent binary logistic regression and ROC curve analysis demonstrated the ability of iPERCIST-max to predict the mPR status. Furthermore, external validation using an independent SYSUCC cohort further enhanced the applicability of iPERCIST-max.

The difference in the mPR prediction power between iPERCIST-max and iPERCIST is mainly due to the choice of the optimal cutoff value. The cutoff value for the iPERCIST responsiveness-based model was 30%, the selection of which could falsely include patients with non-mPR status. Tao et al. reported that an increase in △SULmax% and △SULpeak% was positively associated with the degree of pathological regression, which indicated that pathological responses that achieved mPR were significantly associated with a −90% proportional change in metabolism. From this aspect, it is reasonable to locate a cut-off value higher than 30%.

Beer et al. and Ayati et al. reported better overall survival (OS) and progression-free survival in the RD cohort than in the UD cohort classified by the PERCIST and RECIST cohorts (Beer et al., 2019; Ayati et al., 2021). Similarly, our study revealed that both CT-based and PET-based criteria could stratify the survival difference between radiological/metabolic responders and nonresponders. In contrast to these findings, Rossi et al. showed no significant difference in OS prediction ability between morphological- and metabolic-based criteria (Rossi et al., 2020), indicating that PERCIST or iPERCIST may have limited clinical applicability in certain cohorts. In the present study, further survival analysis showed that the iPERCIST-max model could not only predict mPR status but could also stratify patients into ordinal survival groups (Figure 5A). The AUC value at 1 year and 2 years reached 0.776 (95% CI, 0.575–0.976; $p < 0.001$) and 0.751 (95% CI, 0.637–0.957) respectively, suggesting the robustness of the iPERCIST-max model.

Pseudo-progression might challenge the treatment evaluation, leading to premature termination of a potentially effective treatment; however, our data showed a low incidence of pseudo-progression (1 in 55,1.8%), which is in accordance with published data (Chiou and Burotto, 2015; Katz et al., 2018; Lee et al., 2018).

Despite these promising results, this study has several limitations. The sample size is small, and we excluded patients with EGFR-mutant adenocarcinoma, resulting in a biased disease population, which might prohibit the direct generalization of our conclusion into other cohorts. Further large-scale prospective studies with an unbiased disease population (without exclusion of adenocarcinoma) are needed to validate our proposal.

Conclusion

iPERCSIT-max based on temporal changes in PET metabolic parameters, particularly △SULmax% could better predict both early pathological tumor response and prognosis of NSCLC treated with NAIC than commonly used criteria.

Data availability statement

The raw data supporting the conclusion of this article will be made available by the authors, without undue reservation.

Ethics statement

This prospective study was proved by the institutional review board (The Ethics Committee of the Guangdong Provincial People's Hospital, No. GDREC2019687H). All procedures involved in this study were performed in accordance with the Declaration of Helsinki (as revised in 2013). Written informed consent was obtained from each participant in the study.

Author contributions

TS, SH, and YJ: Conceptualization; Data curation; Formal analysis; Project administration; Resources; Software; Validation; Visualization; Roles/Writing—original draft; Writing—review and editing. HY, JW, CL, XZ, YT, XB, JT, HZ, DZ, LX, GC, YZ, and SW: Methodology; Project administration; Resources; Roles/Writing—original draft; Writing—review and editing. HX and GQ: Conceptualization; Funding acquisition; Investigation; Supervision; Roles/Writing—original draft; Writing—review and editing.

Funding

This work was supported by a grant from the 2020–2021 Popularization of Science and Technology Innovation Special Project of Guangdong Province of China (2020A1414070007); the Science and Technology Program of Guangzhou, China (202206010103); and Natural Science Foundation of Guangdong Province (2022A1515012469), and

the Foundation of Medical Science and Technology Research of Guangdong Province (B2022075).

Acknowledgments

We would like to thank Editage (www.editage.com/) for English language editing.

Conflict of interest

The authors declare that the research was conducted in the absence of any commercial or financial relationships that could be construed as a potential conflict of interest.

Publisher's note

All claims expressed in this article are solely those of the authors and do not necessarily represent those of their affiliated organizations, or those of the publisher, the editors and the reviewers. Any product that may be evaluated in this article, or claim that may be made by its manufacturer, is not guaranteed or endorsed by the publisher.

Supplementary material

The Supplementary Material for this article can be found online at: https://www.frontiersin.org/articles/10.3389/fbioe.2022.1010672/full#supplementary-material

SUPPLEMENTARY FIGURE S1
Paired sample test for PET-associated metabolic characteristics. **(A)** SULmax. **(B)** SULpeak; **(C)** SULmean; **(D)** MTV; **(E)** TLG; **(F)** size. Blue dots represent patients at baseline PET-CT evaluation, while red dots represents patients at the final time of tumor response evaluation. *, $p < 0.05$; **, $p < 0.01$, ***, $p < 0.001$. MTV, metabolic tumor volume; TLG, total lesion glycolysis; PreT: pretreatment; PostT: posttreatment.

SUPPLEMENTARY FIGURE S2
Receiver-operating-characteristics (ROC) analysis for assessment of iRECIST, iPERCIST and iPERCIST-max in predicting major pathological response status. **(A)** iRECIST; **(B)** iPERCIST; **(C)** iPERCIST-max.

References

Ayati, N., Lee, S. T., Zakavi, S. R., Cheng, M., Lau, W. F. E., Parakh, S., et al. (2021). Response evaluation and survival prediction after PD-1 immunotherapy in patients with non-small cell lung cancer: Comparison of assessment methods. *J. Nucl. Med.* 62, 926–933. doi:10.2967/jnumed.120.254508

Beer, L., Hochmair, M., Haug, A. R., Schwabel, B., Kifjak, D., Wadsak, W., et al. (2019). Comparison of RECIST, iRECIST, and PERCIST for the evaluation of response to PD-1/PD-L1 blockade therapy in patients with non-small cell lung cancer. *Clin. Nucl. Med.* 44, 535–543. doi:10.1097/rlu.0000000000002603

Camp, R. L., Dolled-Filhart, M., and Rimm, D. L. (2004). X-Tile. *Clin. Cancer Res.* 10, 7252–7259. doi:10.1158/1078-0432.ccr-04-0713

Chiou, V. L., and Burotto, M. (2015). Pseudoprogression and immune-related response in solid tumors. *J. Clin. Oncol. official J. Am. Soc. Clin. Oncol.* 33, 3541–3543. doi:10.1200/jco.2015.61.6870

Eisenhauer, E. A., Therasse, P., Bogaerts, J., Schwartz, L. H., Sargent, D., Ford, R., et al. (2009). New response evaluation criteria in solid tumours: Revised RECIST guideline (version 1.1). *Eur. J. Cancer* 45, 228–247. doi:10.1016/j.ejca.2008.10.026

Goldfarb, L., Duchemann, B., Chouahnia, K., Zelek, L., and Soussan, M. (2019). Monitoring anti-PD-1-based immunotherapy in non-small cell lung cancer with FDG PET: Introduction of iPERCIST. *EJNMMI Res.* 9, 8. doi:10.1186/s13550-019-0473-1

Graham, M. M., Wahl, R. L., Hoffman, J. M., Yap, J. T., Sunderland, J. J., Boellaard, R., et al. (2015). Summary of the UPICT protocol for 18F-FDG PET/CT imaging in Oncology clinical trials. *J. Nucl. Med.* 56, 955–961. doi:10.2967/jnumed.115.158402

Huang, S., Gao, Z., and Qiao, G. (2021). Immunochemotherapy as first-line treatment for locally advanced or metastatic squamous non-small cell lung cancers. *JAMA Oncol.* 7, 1580. doi:10.1001/jamaoncol.2021.3372

Jiang, J., Wang, Y., Gao, Y., Sugimura, H., Minervini, F., Uchino, J., et al. (2022). Neoadjuvant immunotherapy or chemoimmunotherapy in non-small cell lung cancer: A systematic review and meta-analysis. *Transl. Lung Cancer Res.* 11, 277–294. doi:10.21037/tlcr-22-75

Katz, S. I., Hammer, M., Bagley, S. J., Aggarwal, C., Bauml, J. M., Thompson, J. C., et al. (2018). Radiologic pseudoprogression during anti-PD-1 therapy for advanced non-small cell lung cancer. *J. Thorac. Oncol.* 13, 978–986. doi:10.1016/j.jtho.2018.04.010

Kumar, V., Nath, K., Berman, C. G., Kim, J., Tanvetyanon, T., Chiappori, A. A., et al. (2013). Variance of SUVs for FDG-PET/CT is greater in clinical practice than under ideal study settings. *Clin. Nucl. Med.* 38, 175–182. doi:10.1097/rlu.0b013e318279ffdf

Lee, J. H., Long, G. V., Menzies, A. M., Lo, S., Guminski, A., Whitbourne, K., et al. (2018). Association between circulating tumor DNA and pseudoprogression in patients with metastatic melanoma treated with anti-programmed cell death 1 antibodies. *JAMA Oncol.* 4, 717–721. doi:10.1001/jamaoncol.2017.5332

Lodge, M. A., Chaudhry, M. A., and Wahl, R. L. (2012). Noise considerations for PET quantification using maximum and peak standardized uptake value. *J. Nucl. Med.* 53, 1041–1047. doi:10.2967/jnumed.111.101733

Lopci, E., Toschi, L., Grizzi, F., Rahal, D., Olivari, L., Castino, G. F., et al. (2016). Correlation of metabolic information on FDG-PET with tissue expression of immune markers in patients with non-small cell lung cancer (NSCLC) who are candidates for upfront surgery. *Eur. J. Nucl. Med. Mol. Imaging* 43, 1954–1961. doi:10.1007/s00259-016-3425-2

Joo Hyun, O., Lodge, M. A., and Wahl, R. L. (2016). Practical PERCIST: A simplified Guide to PET response criteria in solid tumors 1.0. *Radiology* 280, 576–584. doi:10.1148/radiol.2016142043

Ramos-Esquivel, A., Van Der Laat, A., Rojas-Vigott, R., Juárez, M., and Corrales-Rodríguez, L. (2017). Anti-PD-1/anti-PD-L1 immunotherapy versus docetaxel for previously treated advanced non-small cell lung cancer: A systematic review and meta-analysis of randomised clinical trials. *ESMO Open* 2, e000236. doi:10.1136/esmoopen-2017-000236

Rossi, G., Baucknehtt, M., Genova, C., Rijavec, E., Biello, F., Mennella, S., et al. (2020). Comparison between (18)F-FDG PET-based and CT-based criteria in non-small cell lung cancer patients treated with nivolumab. *J. Nucl. Med.* 61, 990–998. doi:10.2967/jnumed.119.233056

Seymour, L., Bogaerts, J., Perrone, A., Ford, R., Schwartz, L. H., Mandrekar, S., et al. (2017). iRECIST: guidelines for response criteria for use in trials testing immunotherapeutics. *Lancet Oncol.* 18, e143–e152. doi:10.1016/s1470-2045(17)30074-8

Siegel, R. L., Miller, K. D., Fuchs, H. E., and Jemal, A. (2021). Cancer statistics, 2021. *Ca. A Cancer J. Clin.* 71, 7–33. doi:10.3322/caac.21654

Soret, M., Bacharach, S. L., and Buvat, I. (2007). Partial-volume effect in PET tumor imaging. *J. Nucl. Med.* 48, 932–945. doi:10.2967/jnumed.106.035774

Spicer, J., Wang, C., Tanaka, F., Saylors, G. B., Chen, K.-N., Liberman, M., et al. (2021). Surgical outcomes from the phase 3 CheckMate 816 trial: Nivolumab (NIVO) + platinum-doublet chemotherapy (chemo) vs chemo alone as

neoadjuvant treatment for patients with resectable non-small cell lung cancer (NSCLC). *J. Clin. Oncol.* 39, 8503. doi:10.1200/jco.2021.39.15_suppl.8503

Tao, X., Li, N., Wu, N., He, J., Ying, J., Gao, S., et al. (2020). The efficiency of (18) F-FDG PET-CT for predicting the major pathologic response to the neoadjuvant PD-1 blockade in resectable non-small cell lung cancer. *Eur. J. Nucl. Med. Mol. Imaging* 47, 1209–1219. doi:10.1007/s00259-020-04711-3

Uprety, D., Mandrekar, S. J., Wigle, D., Roden, A. C., and Adjei, A. A. (2020). Neoadjuvant immunotherapy for NSCLC: Current concepts and future approaches. *J. Thorac. Oncol.* 15, 1281–1297. doi:10.1016/j.jtho.2020.05.020

Wahl, R. L., Jacene, H., Kasamon, Y., and Lodge, M. A. (2009). From RECIST to PERCIST: Evolving Considerations for PET response criteria in solid tumors. *J. Nucl. Med.* 50 (1), 122s–150s. doi:10.2967/jnumed.108.057307

Wang, J., Lu, S., Yu, X., Hu, Y., Sun, Y., Wang, Z., et al. (2021). Tislelizumab plus chemotherapy vs chemotherapy alone as first-line treatment for advanced squamous non-small-cell lung cancer: A phase 3 randomized clinical trial. *JAMA Oncol.* 7, 709–717. doi:10.1001/jamaoncol.2021.0366

Zhao, H., Wang, J., Liu, X., Zhao, X., Hippe, D. S., Cao, Y., et al. (2015). Assessment of carotid artery atherosclerotic disease by using three-dimensional fast black-blood MR imaging: Comparison with DSA. *Radiology* 274, 508–516. doi:10.1148/radiol.14132687

Zhao, Z. R., Yang, C. P., Chen, S., Yu, H., Lin, Y. B., Lin, Y. B., et al. (2021). Phase 2 trial of neoadjuvant toripalimab with chemotherapy for resectable stage III non-small-cell lung cancer. *Oncoimmunology* 10, 1996000. doi:10.1080/2162402x.2021.1996000

Zheng, Y., Liu, X.-B., Sun, H.-B., Xu, J., Shen, S., Ba, Y.-F., et al. (2021). Written on Henan Cancer Hospital Thoracic Oncology, GA phase III study on neoadjuvant chemotherapy versus neoadjuvant toripalimab plus chemotherapy for locally advanced esophageal squamous cell carcinoma: Henan Cancer Hospital Thoracic Oncology Group 1909 (HCHTOG1909). *Ann. Transl. Med.* 9, 73. doi:10.21037/atm-20-5404

Zhou, Z., Huang, S., Ben, X., Zhuang, W., Hong, L., Xie, Z., et al. (2022). A novel prognostic model: Which group of esophageal squamous cell carcinoma patients could benefit from adjuvant chemotherapy. *Ann. Transl. Med.* 10, 182. doi:10.21037/atm-22-46

Glossary

AUC area under the curve

B-PET baseline 18F-FDG PET/CT

EFS event-free survival

EGFR epidermal growth factor receptor

F-PET follow-up PET/CT

ICC intraclass correlation coefficient

ICIs Immune checkpoint inhibitors

iPERCIST-max the immune PET Response Criteria in Solid Tumors *via* SULmax

iPERCIST the immune PERCIST

imCMRD iPERCIST-max complete metabolic responsive disease

imRMD iPERCIST-max responsive metabolic disease

imUMD iPERCIST-max unresponsive metabolic disease

iCMR immune complete metabolic response

iPMR immune partial metabolic response

iSMD immune stable disease

iUPMD immune unconfirmed progressive metabolic disease

iCR immune-complete response

iPR immune-partial response

iSD immune-stable disease

i(C/U)PD immune (confirmed/unconfirmed) progressive disease

mPR major pathological response

NSCLC non-small cell lung cancer

MTV metabolic tumor volume

NAIC neoadjuvant immunochemotherapy

PD-1 programmed death 1

pCR pathological complete response

PERCIST PET Response Criteria in Solid Tumors

SYSUCC Sun Yat-Sen University Cancer Center

△SULmax% proportional changes in the SULmax response

TLG total lesion glycolysis

UPICT uniform protocols for imaging in clinical trials

frontiers | Frontiers in Bioengineering and Biotechnology

TYPE Original Research
PUBLISHED 07 October 2022
DOI 10.3389/fbioe.2022.1021499

OPEN ACCESS

EDITED BY
Lu Wang,
First Affiliated Hospital of Jinan University, China

REVIEWED BY
Dawei Jiang,
Huazhong University of Science and Technology, China
Chunfu Zhang,
Shanghai Jiao Tong University, China

*CORRESPONDENCE
Qingyun Bai,
110623@jxycu.edu.cn
Xiao Li,
lixiao_nm@smmu.edu.cn

†These authors have contributed equally to this work

SPECIALTY SECTION
This article was submitted to Nanobiotechnology, a section of the journal Frontiers in Bioengineering and Biotechnology

RECEIVED 17 August 2022
ACCEPTED 13 September 2022
PUBLISHED 07 October 2022

CITATION
Tong Q, Li R, Wang R, Zuo C, Li D, Jia G, Peng Y, Li X, Yang J, Xue S, Bai Q and Li X (2022), The inhibiting effect of alpha-based TARE on embolized vessels and neovascularization.
Front. Bioeng. Biotechnol. 10:1021499.
doi: 10.3389/fbioe.2022.1021499

The inhibiting effect of alpha-based TARE on embolized vessels and neovascularization

Qianqian Tong[1,2†], Rou Li[2†], Ruizhi Wang[3†], Changjing Zuo[2], Danni Li[2], Guorong Jia[2], Ye Peng[2], Xiaohong Li[2], Jian Yang[2], Shuai Xue[1], Qingyun Bai[1]* and Xiao Li[2,4]*

[1]School of Chemistry and Bioengineering, Yichun University, Yichun, Jiangxi, China, [2]Department of Nuclear Medicine, Changhai Hospital, Naval Medical University, Shanghai, China, [3]Department of Radiology, Huadong Hospital, Fudan University, Shanghai, China, [4]Institute of Applied Physics, Chinese Academy of Sciences, Shanghai, China

Transarterial embolization (TAE) is a personalized technology that offers precise delivery of chemotherapeutic drugs or selective internal radiation therapy for hepatocellular carcinoma (HCC). Beta-emitting radionuclide embolisms for TAE (β-based TARE) are commonly used in the clinic *via* inducing biochemical lethality on tumor cells, while alpha-emitting radionuclides-based embolisms for TAE (α-based TARE) are still under study. The feeding artery plays a key role in tumor growth, metastasis, and recurrence. In this research, the auricular central arteries (ACAs) of rabbits were embolized with silk fibroin-based microspheres (SFMs) or SFMs integrated with α (Ra-223) or β (I-131) radionuclides to investigate the influence on vessels. TARE-induced tissue necrosis and the following neovascularization were measured by pathological analysis and ^{68}Ga-DOTA-RGD PET/CT. The results showed that, compared to I-131, Ra-223 enhanced the growth inhibition of human hepatoma cells Huh-7 and induced more DNA double-strand breaks in vascular smooth muscle cells. Unlike β-based TARE, which mainly led to extensive necrosis of surrounding tissues, α-based TARE induced irreversible necrosis of a limited area adjacent to the embolized vessels. RGD PET revealed the inhibition on neovascularization in α-based TARE (SUV_{max} = 0.053 ± 0.004) when compared with normal group (SUV_{max} = 0.099 ± 0.036), the SFMs-lipiodol group (SUV_{max} = 0.240 ± 0.040), and β-based TARE (SUV_{max} = 0.141 ± 0.026), owing to the avoidance of the embolism-induced neovascularization. In conclusion, α-based TARE provided a promising strategy for HCC treatments *via* destroying the embolized vessels and inhibiting neovascularization.

KEYWORDS

hepatocellular carcinoma, transarterial radioembolization, α radionuclides, Ra-223, neovascularization, silk fibroin, necrosis

1 Introduction

Liver cancer is a major global health challenge, and hepatocellular carcinoma (HCC) is the most common (90%) type of primary liver cancer (Llovet et al., 2021). As a treatment with precise delivery of radioactive nuclides to the tumorous feeding artery, transarterial radioembolization (TARE) delivers therapeutic isotopes targeting the tumor in patients with unresectable hepatic malignancy (Habib et al., 2015; Bruix et al., 2016). Recently, with the development of nuclear technology and innovation of theranostic equipment, a number of radioactive microspheres and particles for TARE have become available.

So far, three types of beta-emitting radionuclide embolisms for TARE (β-based TARE) have been applied in the clinic. These β-emitting radionuclides generate β-rays with linear energy (0.1–2.2 MeV) to produce reactive oxygen species (ROS), leading to the mitochondria-related cellular apoptosis or damage to the single-strand DNA of cells (Aghevlian et al., 2017; King et al., 2021). The range of β-emitting is over 1 mm, an effective range to cover most solid tumors when beads are embolized in the peripheral artery. In the clinic, yttrium-90 (Y-90) microspheres, including TheraSpheres and SIR-Spheres, have already been applied in unresectable HCC or unresectable liver metastases of colorectal cancer (Edeline et al., 2015). Recently, a type of holmium-166 (Ho-166) microspheres named QuiremSpheres, which were developed with biodegradable poly-l-lactic acid-based microspheres containing Ho-166, have been approved to treat unresectable liver cancer (Reinders et al., 2019). Another extensively used β-emitting radionuclide is iodine-131 (I-131), which has several advantages, including economic feasibility and easy securement (Fujiwara, 2016). In detail, I-131 has a half-life of 8.06 d ($t_{1/2}$ = 8.06 d) and emits β particles of maximum energy of 0.6 MeV with a 2.3 mm maximum range in tissue (Mies et al., 1981), which could penetrate the embolized arterial walls and reach the boundary of tumorous tissues (Li et al., 2021). Hence, β-emitting radionuclides like Y-90, Ho-166, and I-131 are commonly developed or being developed for β-based TARE.

Different from β-emitting radionuclides, α-emitting radionuclides are among the most radiotoxic of all radionuclides. Although the radionuclides (such as iodine-125) with Auger electrons are of nuclear toxicity, the requirements for entrance into cells and approaching the cell nucleus limit the opportunity to translate these properties into clinical therapies. Usually, α nuclides permit a short range of radiation of less than 100 μm (Kratochwil et al., 2014), but the linear energy is 100–1,000 times greater than conventional β-emitting radionuclides (Sgouros, 2008). Along the emitting track *in vivo*, α-particles could emit thousands of ion pairs with radiation from enormously higher linear energy (4–9 MeV) to deposit on and break the double-strand DNA (Heskamp et al., 2017). Therefore, α-emitting radionuclides irreversibly accelerate the death of the exposed cells. For example, radium-223 (Ra-223) has a half-life of 11.43 d ($t_{1/2}$ = 11.43 d), and four emissions of α-particles are generated during each decay. These particles predominately break double-strand DNA, which accounts for the irreversible cell damage (Pandit-Taskar et al., 2014; Roobol et al., 2020). In addition to cellular death, embolization-induced neovascularization is the first concern in controlling recurrence and metastasis. However, in the application of alpha-emitting radionuclide-based embolisms for transarterial embolization (α-based TARE), the systemic influence of the α-emitter in the whole procedure of embolization, especially its effect on the embolized vessels and the following vascular remodeling, was not understood.

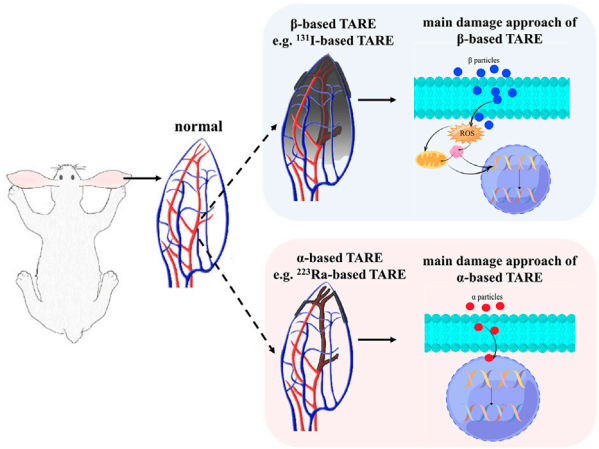

FIGURE 1
The schematic radiation process and the main damage approaches of β-based TARE and α-based TARE. The shaded area represents the radiation coverage area.

Until now, fewer α-emitting radionuclides have been used in TARE. This present study aims to determine the principles of α-based TARE, especially the effect of radiation on the embolized artery and surrounding tissues. Ra-223 was chosen as the representative radionuclide in exploring α-based TARE, and I-131 served as a comparison with definite therapeutic effects (Figure 1). Silk fibroin microspheres (SFMs) offer the characteristics of relatively good dispersion stability, biodegradability, biocompatibility, and low cytotoxicity (Sun et al., 2018; He et al., 2020), and the feasibility of radionuclide-labeled SFMs for TARE to treat HCC has been proven (Wu et al., 2022). In this study, we compared the ability of I-131 and Ra-223 to induce apoptosis at the cellular level, the inhibition effects on tumor cell growth, and the induction of γ-H2AX in vascular smooth muscle cells (VSMCs). SFMs combined with Ra-223 or I-131 were injected into the auricular central artery (ACA) of rabbits, where the radionuclides served as the unique variable. Single photon planar imaging was used to quantify the efficiency of

embolization, and the subsequent damage to the appearance and pathological section of the ear were recorded. Functional imaging of neovascularization was performed using positron emission tomography/computed tomography (PET/CT) imaging with gallium-68-labeled 1,4,7,10-tetraazacyclododecane-1,4,7,10-tetraacetic acid conjugated with arginine-glycine-aspartate (^{68}Ga-DOTA-RGD) post TARE, and the specific findings were verified with pathological analysis.

2 Materials and methods

2.1 Materials and animals

$Na^{131}I$ was purchased from Shanghai XinKe Pharmaceutical Co., Ltd. $^{223}RaCl_2$ was purchased from the Institute for Energy Technology. The operation related to the above agents was performed in a hot cell. Ethiodized poppyseed oil injection was purchased from Jiangsu HengRui Medicine Co., Ltd. Silk fibroin microspheres (about 150.61 ± 10.39 μm in diameter, controlled by steel screens) were purchased from Suzhou Meilun Biotechnology Co., Ltd. The TdT-mediated dUTP Nick-End Labeling (TUNEL) kit was purchased from KeyGEN Biotechnology Co., Ltd. The annexin V-fluorescein isothiocyanate (FITC)/propidium iodide (PI) apoptosis kit was purchased from BD Bioscience. A cell counting kit-8 (CCK-8) was purchased from the Beyotime Institute of Biotechnology. A γ-H2AX ELISA kit was purchased from Jiangsu Meimian Industrial Co., Ltd.

A human hepatocyte carcinoma cell line (Huh-7) was purchased from the Cell Bank of the Type Culture Collection of the Chinese Academy of Sciences, Shanghai Institute of Cell Biology, Chinese Academy of Sciences. The New Zealand white rabbits (male, weighing 2.5 ± 0.5 kg) were purchased from Ailingfei Biotechnology Co., Ltd., and kept under a specific pathogen-free condition at the laboratory animal center. This research was approved and guided by the Ethics Committee of Naval Medical University (Approval No. 1207050662).

2.2 Cell culture

Primary mouse VSMCs were isolated from C57BL/6 mice as previously described (Chamley-Campbell et al., 1979). VSMCs were grown to confluence in DMEM medium supplemented with 10% FBS and 1% penicillin-streptomycin. Huh-7 cells were cultured in DMEM containing 10% FBS at 37°C in 5% CO_2.

2.3 Flow cytometry

VSMCs and Huh-7 cells at a density of 10^5 cells per sample were incubated with I-131 (1 mCi) or Ra-223 (1 μCi) for 24 h at 37°C, respectively. Post incubation, the cells were washed twice with cold PBS and then stained using the annexin V-FITC/PI apoptosis kit, followed by flow cytometric analysis. The percentage of apoptosis was corrected for background levels found in the corresponding untreated controls. The percentage of cells undergoing apoptosis was defined as the sum of early apoptosis (annexin V-positive and PI-negative) and late apoptosis (annexin V-positive and PI-positive) cells. Necrotic cells of VSMCs and Huh-7 cells were defined as the percentage of annexin V-negative and PI-positive cells. Three independent experiments were performed, and the values of apoptotic percentages were presented as the mean ± SD.

2.4 Cell viability and γ-H2AX activation assays

The cell viability assay was performed on tumor cells using CCK-8. Huh-7 cells were seeded into 96-well culture plates at a density of 1×10^4 cells per well in 100 μl culture medium and cultured overnight at 37°C. Three duplicate wells were set up for each group. The cells were then exposed to I-131 (100 μCi) or Ra-223 (0.1 μCi) for 24 h, then 10 μl CCK-8 solution was added to each well. After incubating for 4 h at 37°C in 5% CO_2, absorbance at 450 nm was measured using a microplate reader.

For the γ-H2AX assay, VSMCs were seeded into 96-well culture plates at a density of 1×10^4 cells per well and incubated overnight at 37°C. VSMCs were treated with I-131 (100 μCi) or Ra-223 (0.1 μCi) for 24 h. Subsequently, the treated VSMCs were fixed, permeabilized, and stained with anti-γ-H2AX following the γ-H2AX ELISA kit protocol. The induced concentration of γ-H2AX was quantified on the basis of absorbance at 450 nm.

2.5 Preparation of embolism and radiopharmaceuticals

To make SFMs-lipiodol TAE, 50 μg SFMs were added into 1 ml 0.9% saline to obtain an SFMs suspension. Afterward, 2 ml ethiodized poppyseed oil injection was added to the SFMs suspension. The SFMs-lipiodol suspension was further aspirated and blown with a pipette and then sonicated for 1 minute to ensure the homogeneous dispersion of microspheres.

To make ^{131}I-SFMs-lipiodol TARE, 1 ml $Na^{131}I$ (6.6 MBq) was mixed with 50 μg SFMs and vibrated for 10 min to increase physical adsorption between I-131 and SFMs. The adsorption rate was evaluated with thin-layer chromatography (TLC) with a radioactive detector. Glass microfiber chromatography paper impregnated with silica gel was used as the stationary phase, and saline was used as the mobile phase. The free I-131 was removed by centrifugation if the adsorption rate was less than 90%. Then, 2 ml ethiodized poppyseed oil was added to ^{131}I-SFMs to obtain the suspension of ^{131}I-SFMs-lipiodol. The

β-based TARE of each ACA used 1.1 MBq/0.5 ml ^{131}I-SFMs-lipiodol.

To make ^{223}Ra-SFMs-lipiodol TARE, 1 ml Ra-223 (6.6 kBq) was mixed with 50 μg SFMs and vibrated for 10 min to increase the physical adsorption of Ra-223 to SFMs. The quality control and purification were the same as I-131. After that, 2 ml ethiodized poppyseed oil was added to the mixture and mixed as described above. The ^{223}Ra-SFMs-lipiodol was suspended, and 1.1 kBq/0.5 ml was used for the α-based TARE of each ACA.

$^{68}Ga^{3+}$ was acquired in the form of $^{68}GaCl_3$ from a $^{68}Ge/^{68}Ga$ generator by elution with 0.1 M HCl and then labeled to the integrin-targeted DOTA-RGD in house following the protocols. Quality control of ^{68}Ga-DOTA-RGD was performed to guarantee the radiochemical purity >90%. The injected dosage of each rabbit was set as 7.4 MBq/kg body weight.

2.6 Radioembolization of auricular central arteries

In consideration of the visibility of ACAs, the strategy of ACA embolization was chosen to verify α-TARE (Li et al., 2021). ACA embolization of 12 rabbits was performed to evaluate the differential radiation damage to the artery and surrounding tissues. Before embolization, the ears of New Zealand rabbits were shaved and cleaned. Afterward, the rabbits (n = 3 for each group) were divided into four groups: a normal group, an SFMs-lipiodol group, a ^{131}I-SFMs-lipiodol group, and a ^{223}Ra-SFMs-lipiodol group. The rabbits were anesthetized under 3% (v/v) isoflurane. The suspension was emulsified before injection to prevent delamination. Subsequently, a 500 μl suspension of the embolism was slowly injected along the flow of blood into the ACA. The injection site was pressed for 5 min to control the bleeding and backflow. By virtue of α-particles depositing energy 100 to 1,000 times higher than β-particles, the activity of Ra-223 was adjusted to 1.1 kBq per ear, while the activity of I-131 was set as 1.1 MBq. Rabbits were excluded from the study if the recanalization of the ACA occurred after the backflow of blood in the arteries. The changes in the ear appearance were photographed at 1, 3, 5 and 7 days after the embolization.

2.7 Single photon planer imaging on embolization and radiation inspection

Single photon planar imaging was performed to record the distribution of SFMs-lipiodol. A SPECT/CT (Symbia T16, Siemens) scanner was utilized, and scans were performed immediately after the TARE and at 48 h post-injection to detect the distribution of ^{131}I-SFMs-lipiodol *in vivo*. I-131 possesses an energetic spectrum of gamma radiation (Eγ = 0.364 MeV), and the ^{131}I-SFMs-lipiodol group was chosen as the representative one.

During scan acquisition, rabbits were anesthetized under 3% (v/v) isoflurane. In addition, ears were stretched away from the body to avoid signal interference from other organs. The SPECT/CT scanner was equipped with a high-resolution collimator, and the acquisition of planar pictures was performed in 5 min with matrix = 256 × 256 and zoom = 1.

Radiation from ^{131}I-SFMs-lipiodol was measured by a Radiation Alert® inspector to quantify the embolization efficiency. The radiation from the whole body and the body except for the embolized ear was measured at 0, 36, 72, and 120 h post embolization. Embolized dosage (ED) was used in this study to represent the results, which was similar to "ID" in SPECT/CT. The time-dependent residuals in the embolized ear were calculated, and the ratio of the embolization in the ear to the whole body and the residual percentage of embolization in the ear are presented as line charts.

2.8 ^{68}Ga-DOTA-RGD PET/CT imaging

^{68}Ga-labeled arginine-glycine-aspartate peptides were regarded as PET tracers for angiogenesis imaging because RGD is specific toward the integrin $\alpha_v\beta_3$ that is excessively expressed during neovascularization (Parihar et al., 2020). To compare the state of the neovascularization of ears after embolization in each group, a ^{68}Ga-DOTA-RGD PET/CT scan was performed at 4 days post-embolization. About 7.4 MBq/kg of ^{68}Ga-DOTA-RGD were administrated through the ear vein, and PET/CT images were acquired 45 min later. The spatial resolution of the PET/CT scanner (Biograph 64; Siemens) was 1 mm with CT (120 kV, 35 mA). In addition, the reconstruction resolution of CT was 1 mm by the postprocessing workstation TureD system. The tracer uptake of ^{68}Ga-DOTA-RGD was presented as the maximum standardized uptake value (SUV_{max}).

2.9 Histopathological examination

After 7 days post-embolization, all rabbits were sacrificed with excessive anesthesia. All ears were harvested, and the selected tissues mainly included the auricular artery and surrounding tissues, which were fixed and preserved in 10% neutral buffered formalin for 48 h. Thereafter, the fixed tissues were dehydrated, transparentized, embedded in paraffin, and longitudinally cut into 4-μm thick slices. Slices were stained with hematoxylin-eosin (H&E) and TUNEL and then photographed under a microscope equipped with optical and fluorescent lenses.

2.10 Statistical analysis

The values of SUV_{max} were described as the mean ± standard deviation (SD). Comparisons were performed using an unpaired

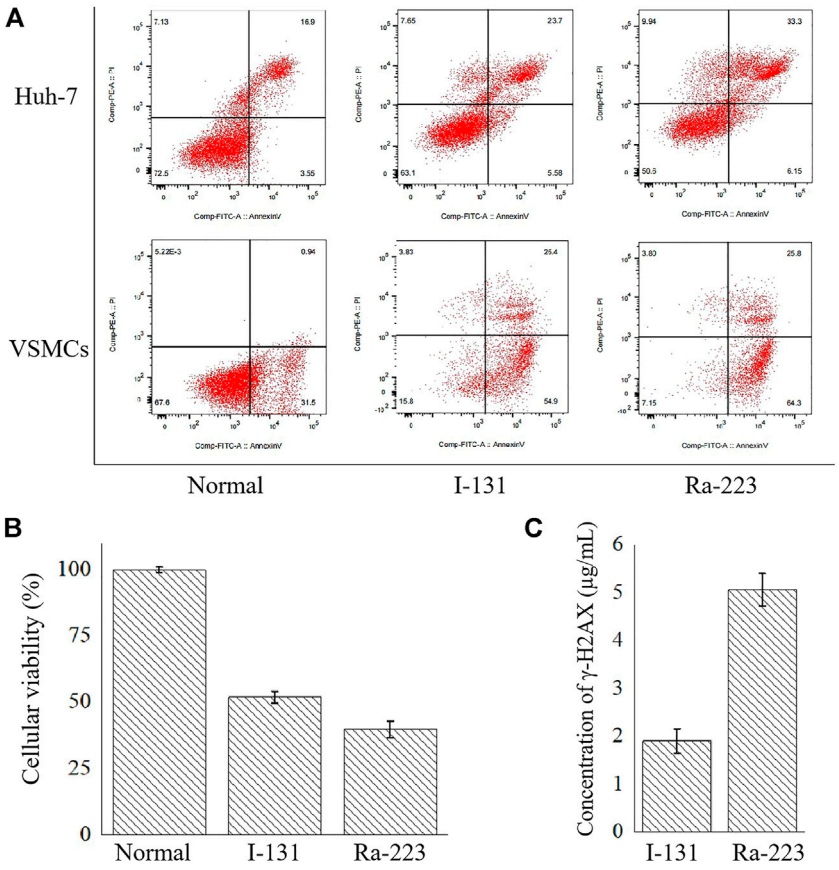

FIGURE 2
The comparison between I-131 and Ra-223 on the cellular level, including the apoptosis induction **(A)**, the inhibition of the cellular viability of Huh-7 cells **(B)**, and the induction of γ-H2AX on VSMCs **(C)**.

t-test. The analyses of histopathological examination were performed using ImageJ software.

3 Results

3.1 Cell damage by radiation

Apoptosis and necrosis were the main consequence of radiation. The effects of 24 h radiation of radionuclides on Huh-7 and VSMCs were examined using flow cytometry on apoptosis. As shown in Figure 2A, compared with the normal group, apoptotic percentages were elevated in Huh-7 cells and VSMCs after the treatment of I-131 and Ra-223. Compared with normal Huh-7 cells (20.20% ± 0.70%), the percentage of apoptotic Huh-7 cells increased to 29.33% ± 0.08% after treatment with I-131 and 39.93% ± 0.03% after treatment with Ra-223. Compared with normal VSMCs (31.15% ± 1.38%), the percentage of apoptotic VSMCs increased to 79.41% ± 1.41% after treatment with I-131 and 88.88% ± 0.29% after treatment with Ra-223. Although I-131 and Ra-223 both induced apoptosis, the effects of Ra-223 in Huh-7 cells at the late stage of apoptosis and in VSMCs at the early stage of apoptosis were more obvious than I-131. In addition, the percentage of necrotic Huh-7 cells increased to 7.81% ± 0.26% after treatment with I-131 and 9.87% ± 0.21% after treatment with Ra-223. The percentage of necrotic VSMCs increased to 4.22% ± 0.31% after treatment with I-131 and 4.13% ± 0.30% after treatment with Ra-223.

In order to determine the influences of treatment on tumorous cell viability, the cellular viability of Huh-7 cells co-incubated with I-131 or Ra-223 for 24 h was examined *via* the CCK-8. Compared to the control group, treatments with I-131 and Ra-223 signally inhibited Huh-7 cell viability (Figure 2B), and treatment with Ra-223 was more effective in inhibiting Huh-7 cell proliferation.

10.3389/fbioe.2022.1021499

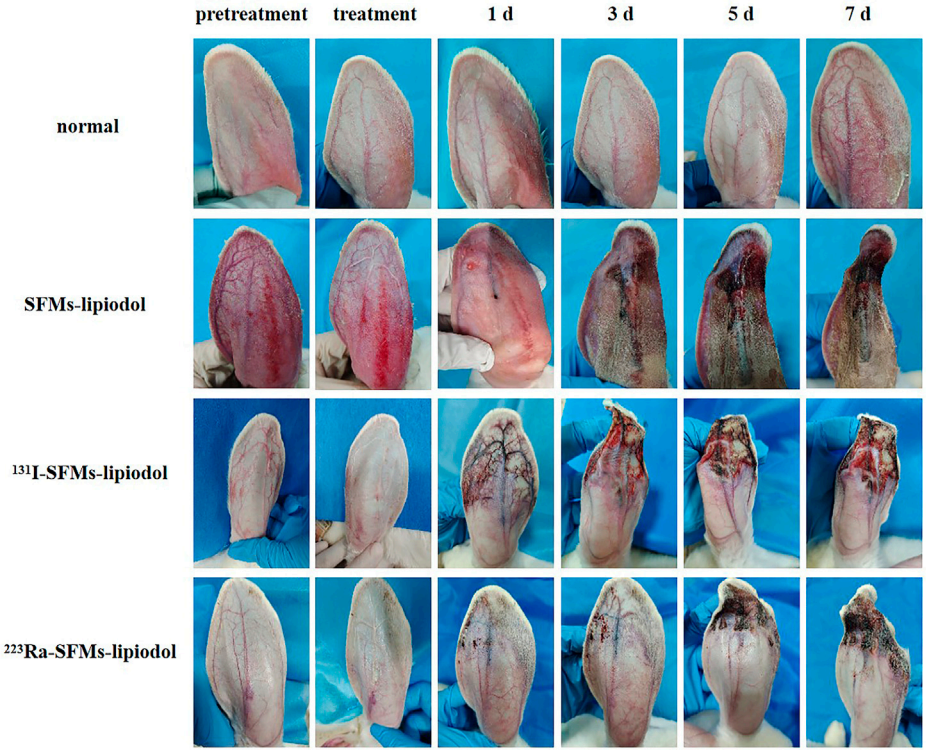

FIGURE 3
The appearance of pre-embolization rabbit ears, immediately post treatment with SFMs-lipiodol, ^{131}I-SFMs-lipiodol and ^{223}Ra-SFMs-lipiodol, and at 1, 3, 5, and 7 days post-embolization.

Compared to the DNA strand breakage caused by the I-131-induced γ-H2AX (1.89 ± 0.05 μg/ml), the treatment of Ra-223 further increased γ-H2AX expression levels (5.05 ± 0.05 μg/ml) (Figure 2C), creating a more thorough lethality.

3.2 Radioembolization of auricular central arteries

^{131}I-SFMs and ^{223}Ra-SFMs were successfully synthesized *via* the adsorption capacity of protein in silk fibrin. Although the physical adsorption was of relatively low stability, this approach was the most effective way of establishing the unbiased protocol to only evaluate the influence of nuclides, regardless of confounding factors, such as the chemical modification and labeling method. In addition, the ^{68}Ga-DOTA-RGD synthesized in house met the quality control criteria of acid-base property (pH = 4), radiochemical purity (>95%), and solubility (clear and no undissolved substance). The specificity activity was adjusted to around 37 MBq/μg precursor.

As time progressed, progressive changes in skin color and appearance of the rabbit ears were observed in the embolization groups. As shown in Figure 3, the ACAs, auricular veins, and terminal branches of vessels were immediately pale after injection, owing to the blockage of blood flow. After embolization for 1 day, the vascular color in the ACA changed to purple in the embolization groups (the SFMs-lipiodol group, the ^{131}I-SFMs-lipiodol group, and the ^{223}Ra-SFMs-lipiodol group). Distal vessels and tissues around the embolized arteries became maroon in the ^{131}I-SFMs-lipiodol group. By comparison, the surrounding tissues remained normal during the super early period of embolization in the ^{223}Ra-SFMs-lipiodol group. On the third day after embolization, the congestive edema of ears in the SFMs-lipiodol group emerged, and then necrosis occurred in a portion of the tissue. Extensive necrosis and shrinkage of ears were observed in the ^{131}I-SFMs-lipiodol group. Comparably, no recanalization of the ACA occurred, and tissues around arteries only slightly turned purple in the ^{223}Ra-SFMs-lipiodol group at 3 days post-embolization. Significant changes could be seen in the ^{223}Ra-SFMs-lipiodol group from the fifth to the seventh day post-embolization. The distal tissue supplied by the embolized vessel became black, stiff, and twisted, while the adjacent and proximal tissues showed no damage. Conversely, some

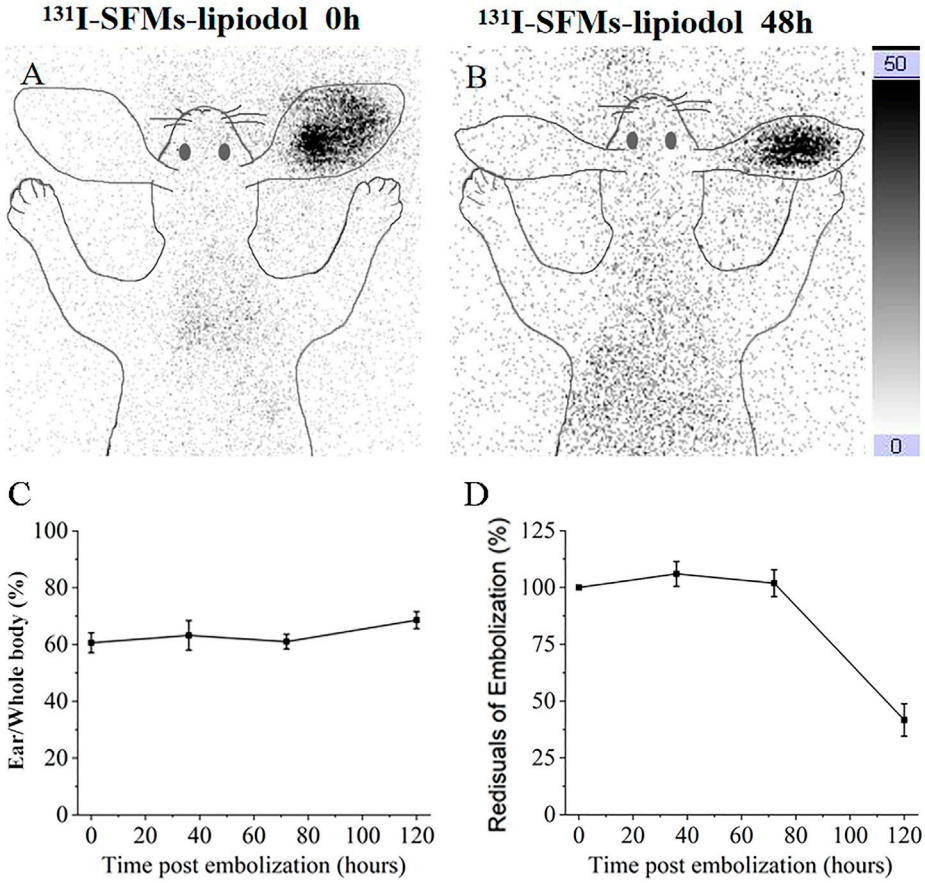

FIGURE 4
Planar images of rabbit at 0 h **(A)** and 48 h **(B)** after embolization with ^{131}I-SFMs-lipiodol. Ear to whole body radioactivity ratios were measured at 0, 36, 72, and 120 h **(C)**. Residual radioactivity ratios of embolization (decay corrected) were measured at 0, 36, 72, and 120 h **(D)**.

normal non-necrotic tissues were scattered throughout the extensive necrosis in the ^{131}I-SFMs-lipiodol group at 7 days post-embolization. The progressive changes in ears indicated that ^{223}Ra-SFMs-lipiodol TARE induced restricted and thorough damage, which resulted from the shorter radiation range and higher energy of α-particles than β-particles.

3.3 Distribution of SFMs-lipiodol in TARE

Because there was no γ radiation in the normal and the SFMs-lipiodol groups and a low dose of γ radiation in the ^{223}Ra-SFMs-lipiodol group, the ^{131}I-SFMs-lipiodol group was examined at 0 and 48 h after embolization. Because the same embolism procedure was used in other groups, except for the radionuclides, planar imaging of the ^{131}I-SFMs-lipiodol group revealed the distribution of embolism in all groups. Compared with the surrounding tissue, an embolism in the tip of the ear was distinguishable in the ^{131}I-SFMs-lipiodol group after injection, as presented in Figure 4A. The anchored radioactivity in the ACAs increased to 60.21% embolized dosage (ED) after the primary distribution. At 48 h after embolization, the leaked ^{131}I-SFMs was distributed *in vivo* without a specific target, as shown in Figure 4B. Meanwhile, 16.37% of the SFMs-lipiodol was excreted from the rabbit. Illustrated data visually demonstrated that ^{131}I-SFMs-lipiodol deposited in the ACA and provided continuous radiation to the ACA and its surroundings. Images confirmed that SFMs-lipiodol could potentially be used as the base of TARE.

In terms of quantification, ear-to-whole-body radioactivity ratios were maintained at a high level (60%–70%) at 0, 36, 72, and 120 h (Figure 4C). Results confirmed ^{131}I-SFMs-lipiodol demonstrated occlusion in the ACA and had a favorable *in vivo* distribution. The residual radioactivity ratio of decay-corrected embolization decreased between 72 and 120 h (Figure 4D), consistent with the timeline of extensive necrosis in ^{131}I-SFMs-lipiodol group shown in Figure 3.

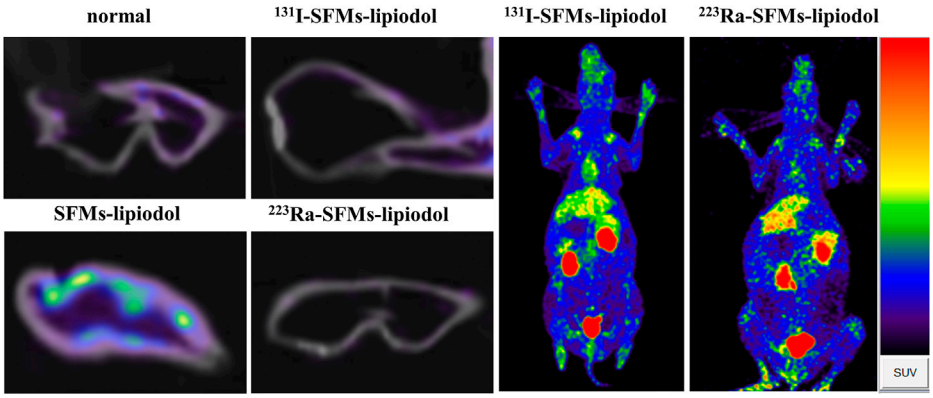

FIGURE 5
^{68}Ga-DOTA-RGD PET/CT images of rabbit ears were captured at 4 days after embolization with ^{131}I-SFMs-lipiodol.

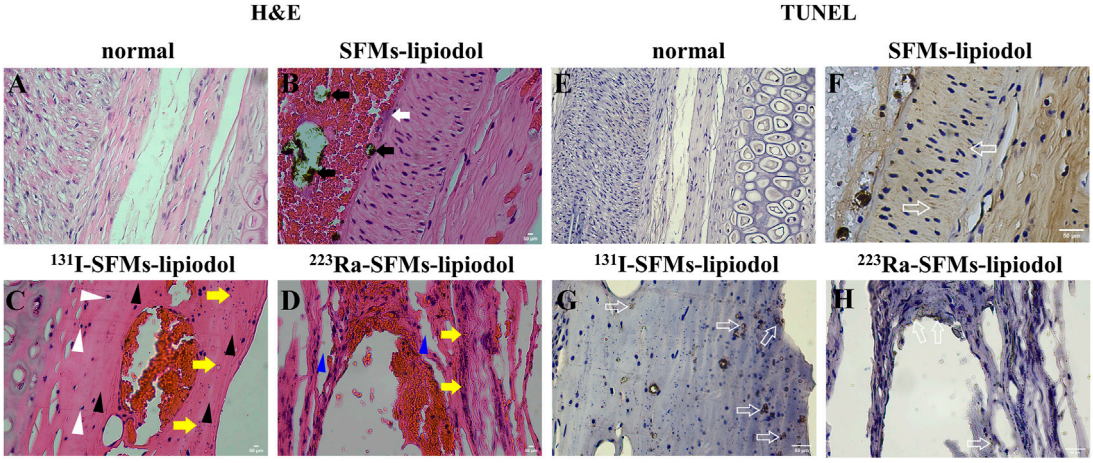

FIGURE 6
H&E staining of the longitudinal sections of the auricular central artery, normal **(A)**, 7 days after embolization with SFMs-lipiodol **(B)**, ^{131}I-SFMs-lipiodol **(C)** and ^{223}Ra-SFMs-lipiodol **(D)** (× 400). Black arrows indicate SFMs-lipiodol, white arrows indicate inflammatory cells, white triangular arrows indicate acidophilic bodies, yellow arrows cell indicate fragments, black triangular arrows indicate disappeared nuclei, blue triangular arrows indicate intercellular space; TUNEL staining of the longitudinal sections of the auricular central artery, normal **(E)**, after injection with SFMs-lipiodol **(F)**, ^{131}I-SFMs-lipiodol **(G)** and ^{223}Ra-SFMs-lipiodol **(H)** at 7 days post-embolization (× 400), hollow arrows indicate positive apoptotic cells.

3.4 The inhibition of neovascularization

To explore the influence of embolization on neovascularization, ^{68}Ga-DOTA-RGD PET/CT was conducted at 4 days post-embolization. The uptake of ^{68}Ga-DOTA-RGD was at the highest level in the SFMs-lipiodol group (SUV_{max} = 0.240 ± 0.040), confirming the inductive effect of embolization; the SUV_{max} of ^{68}Ga-DOTA-RGD PET/CT in the normal group was 0.099 ± 0.036. In comparison, Figure 5 displayed that the tracer uptake increased in the ACA in the ^{131}I-SFMs-lipiodol group (SUV_{max} = 0.141 ± 0.026), which indicated that new blood vessels or a new blood supply existed. In contrast, the uptake of ^{68}Ga-DOTA-RGD in the ^{223}Ra-SFMs-lipiodol group was at a low level (SUV_{max} = 0.053 ± 0.004), even lower than the normal group, manifesting a strong inhibition on neovascularization, which contributed to the accelerated necrosis shown in Figure 3. The results of ^{68}Ga-DOTA-RGD PET/CT in each group were consistent with changes in the appearance of the rabbit ears.

3.5 The destruction of embolized vessels

3.5.1 H&E staining

The longitudinal sections of ACAs stained by H&E are displayed in Figure 6. In the normal group (Figure 6A), vascular endothelial cells and vascular smooth muscle cells were arranged in regular order. In Figure 6B, SFMs-lipiodol is indicated by black arrows in the lumen of the ACA at 7 days post-embolization. The SFMs-lipiodol group showed signs of moderate inflammation, indicating the post-treatment inflammatory cells, such as neutrophils and lymphocytes in the inside tissue of the vascular wall, which are indicated by a white arrow.

The organization structure of the vascular wall was changed in the H&E stained sections of the ^{223}Ra-SFMs-lipiodol group (Figure 6D). In addition, nuclear atrophy and acidophilic bodies were found throughout the adjacent vascular tissues (white arrows). The majority of cell fragments were next to the lining of blood vessels (yellow arrows), and many nuclei disappeared in the lining of the ACA (black arrows). Compared with the ^{131}I-SFMs-lipiodol group (Figure 6C), the rupture of the blood vessel wall was more distinct and thorough, and the normal vascular structures were difficult to discern in the ^{223}Ra-SFMs-lipiodol group. The existence of intercellular space is indicated by blue arrows in Figure 6D, and some platelets entered the inner vessel wall, manifesting that Ra-223 could break the intercellular space.

3.5.2 TUNEL staining

Only small amounts of cell apoptosis existed in normal tissues (Figure 6E). As exhibited in Figures 6F–H, cell apoptosis was detected in the inside of the ACAs in embolization groups by TUNEL staining (hollow arrows). In comparison with the normal group, the positive apoptotic cells were confined to the vascular endothelium in the ^{223}Ra-SFMs-lipiodol group, while the involved range of cell apoptosis was wider in the ^{131}I-SFMs-lipiodol group.

4 Discussion

This research aimed to establish the α-based TARE, which was first proved effective in inhibiting the proliferation of tumorous cells and VSMCs. Because the ability to proliferate independently of signals from other cell types is a fundamental characteristic of tumor cells (Kenny and Bissell, 2007), the direct break of vessels was meaningful in cutting off the blood supply of tumorous tissues. Thus, α-based TARE was an alternative to treating HCC, especially for a tumor close to the distal blood vessel.

Previous studies have confirmed that TARE is a safe technology with an objective response in phase 3 trials (Chauhan et al., 2018). The effect of TARE mainly relies on cutting the arterial supply and the radiation from radionuclides (Li et al., 2020). α particles have higher linear energy transfer than β particles (Lee et al., 2020). β particles require several hundred traversals through the nucleus to induce cell death, while less than ten α particles achieve the same efficacy (King et al., 2021). Compared to β particles, the high LET and short range mean that α radiation treatments are more suitable for small-volume or residual micro-tumors, potentially offering more efficient and specific killing of tumors and avoiding damage to surrounding normal cells. However, this shorter range limits the long-range "cross-fire" effect of α particles, which is advantageous in β particle therapies for large-volume tumors (Song et al., 2017). Hence, although there are great differences between the embolization influences of these two kinds of radionuclides, α particles have great potential as an alternative for personalized treatment, and the principle needs to be further explored.

This study preliminarily established a new direction of TARE on HCC treatment, titled α-based TARE. Although TARE was based on the hepatic artery embolization for unresectable HCC (Habib et al., 2015; Chen et al., 2022), the adjacent tissues of the hepatic artery need protection from scattered rays. In this consideration, Ra-223-based TARE, which has a short radiation range, could effectively kill the tumor and avoid radiation damage to the surrounding normal tissues. This research revealed that Ra-223-based TARE could lead to complete necrosis, and the properly confined radiation range minimized the occurrence of adverse effects. In addition, the short range of α particles makes it easier to carry out radiation protection even though the therapy nuclides have a relatively long half-life.

Most HCCs are highly vascularized. The upregulation of hypoxia-inducible factor proteins enhances the expression of proangiogenic factors, including vascular endothelial growth factor (VEGF), which promotes angiogenesis in HCC tumors (Morse et al., 2019). Consequently, inhibition of angiogenesis in tumors is expected to improve the effects of TARE treatment. The results of ^{68}Ga-DOTA-RGD PET/CT indicated that new blood flow was gradually established to compensate for embolization in the ^{131}I-SFMs-lipiodol group. When compared with the ^{131}I-SFMs-lipiodol group, tracer uptake in the ^{223}Ra-SFMs-lipiodol group was at a low level, even lower than the normal group (0.053 ± 0.004 vs. 0.099 ± 0.036, $p < 0.01$). These results showed that the Ra-223 radiation strongly inhibits angiogenesis, which is beneficial for patients with advanced HCC. ^{223}Ra-SFMs-lipiodol could potentially inhibit the growth of a carcinoma and decrease the recurrence of the tumor.

Hence, the development of α-based TARE is of great significance, and α-emitting radionuclides are promising candidates for TARE with their short range of radiation and high-energy α-particles.

The destruction of embolized vessels was another finding in this research. According to the analysis of H&E and TUNEL staining slides, the Ra-233 α radionuclides could break the intercellular space. Currently, resistance to targeted chemotherapeutic agents poses a huge challenge (Ma et al., 2021). This feature of breaking the intercellular space is far-reaching not only for cutting the artery feeding the tumor but also for the release of a drug to surrounding tissues. Thus, the use of chemotherapeutic drugs in TAE may decline when integrated with α-based TARE. For instance, the development of α-emitting radionuclides TAE together with chemotherapy drugs Sorafenib is a win-win option for the design of drugs for HCC treatment. Synergistic therapy could achieve the desired effect for HCC patients.

Several known challenges limit the wide application of α nuclides in the clinic (Marcu et al., 2018). For example, several low-dose radiation treatments over an extended period can improve effectiveness and reduce radiation toxicity. However, α-emitters are relatively scarce and are typically produced on a strict schedule, and it is critical that the supply of radionuclides is able to meet the clinical trial demand. In addition, although Ra-223 has the ability to be imaged *via* SPECT, the relatively low activity of the administered nuclides and the long acquisition time for SPECT produce blurred images. It is to be hoped that improving the quality and quantity of radionuclide production, combined with increasingly available tools, will make α nuclides suitable for clinical use in the future. In a word, α-based TARE has an application prospect for HCC therapy.

5 Conclusion

In this study, we primarily explored the effects of α-based TARE on the ACA as structural destruction of embolized vessels and inhibition of neovascularization. The embolization results of ^{223}Ra-SFMs-lipiodol provided evidence for the therapeutic effects of α-based TARE and provided a reference for HCC treatments in the setting of a personalized TARE protocol.

Data availability statement

The original contributions presented in the study are included in the article/Supplementary Material; further inquiries can be directed to the corresponding authors.

Ethics statement

The animal study was reviewed and approved by the Ethics Committee of Naval Medical University.

Author contributions

QT, XiL, QB, and CZ were responsible for the conceptualization of the study; RL, RW, and XiL were responsible for chemical synthesis; QT, RL, RW, YP, XiL, and SX carried out the animal studies; DL, GJ, YP, XiaL, and JY were responsible for data analysis and interpretation; XiaL, QB, and CZ provided the guidance and supervision for the execution of experiments; QT, RL, RW, and XiL prepared the draft of the manuscript. All the authors have read and agreed to the final version of the manuscript.

Funding

This work was funded by the National Natural Science Foundation of China (81960748 and 81871390).

Conflict of interest

The authors declare that the research was conducted in the absence of any commercial or financial relationships that could be construed as a potential conflict of interest.

Publisher's note

All claims expressed in this article are solely those of the authors and do not necessarily represent those of their affiliated organizations or those of the publisher, the editors and the reviewers. Any product that may be evaluated in this article, or claim that may be made by its manufacturer, is not guaranteed or endorsed by the publisher.

References

Aghevlian, S., Boyle, A. J., and Reilly, R. M. (2017). Radioimmunotherapy of cancer with high linear energy transfer (LET) radiation delivered by radionuclides emitting α-particles or auger electrons. *Adv. Drug Deliv. Rev.* 109, 102–118. doi:10.1016/j.addr.2015.12.003

Bruix, J., Reig, M., and Sherman, M. (2016). Evidence-based diagnosis, staging, and treatment of patients with hepatocellular carcinoma. *Gastroenterology* 150, 835–853. doi:10.1053/j.gastro.2015.12.041

Chamley-Campbell, J., Campbell, G. R., and Ross, R. (1979). The smooth muscle cell in culture. *Physiol. Rev.* 59, 1–61. doi:10.1152/physrev.1979.59.1.1

Chauhan, N., Bukovcan, J., Boucher, E., Cosgrove, D., Edeline, J., Hamilyon, B., et al. (2018). Intra-arterial theraSphere yttrium-90 glass microspheres in thetreatment of patients with unresectable hepatocellular carcinoma: Protocol for theSTOP-HCC phase 3 randomized controlled trial. *Jmir. Res. Protoc.* 7, e11234. doi:10.2196/11234

Chen, H., Nan, G., Wei, D., Zhai, R. Y., Huang, M., Yang, W. W., et al. (2022). Hepatic artery injection of ^{131}I-metuximab combined with transcatheter arterial chemoembolization for unresectable hepatocellular carcinoma: A prospective nonrandomized, multicenter clinical trial. *J. Nucl. Med.* 63, 556–559. doi:10.2967/jnumed.121.262136

Clarke, L. P., Qadir, F., Al-Sheikh, W., Sfakianakis, G., and Serafini, A. N. (1983). Comparison of the physical characteristics of I-131 and I-123, with respect to differentiating the relative activity in the kidneys. *J. Nucl. Med.* 24, 683–688.

Edeline, J., Gilabert, M., Garin, E., Boucher, E., and Raoul, J. L. (2015). Yttrium-90 microsphere radioembolization for hepatocellular carcinoma. *Liver Cancer* 4, 16–25. doi:10.1159/000343878

Fujiwara, H. (2016). Observation of radioactive iodine ((131)I, (129)I) in cropland soil after the Fukushima nuclear accident. *Sci. Total Environ.* 566-567, 1432–1439. doi:10.1016/j.scitotenv.2016.06.004

Habib, A., Desai, K., Hickey, R., Thornburg, B., Lewandowski, R., and Salem, R. (2015). Transarterial approaches to primary and secondary hepatic malignancies. *Nat. Rev. Clin. Oncol.* 12, 481–489. doi:10.1038/nrclinonc.2015.78

He, F., You, X., Gong, H., Yang, Y., Bai, T., Wang, W., et al. (2020). Stretchable, biocompatible, and multifunctional silk fibroin-based hydrogels toward wearable strain/pressure sensors and triboelectric nanogenerators. *ACS Appl. Mat. Interfaces* 12, 6442–6450. doi:10.1021/acsami.9b19721

Heskamp, S., Hernandez, R., Molkenboer-Kuenen, J. D. M., Essler, M., Bruchertseifer, F., Morgenstern, A., et al. (2017). α- versus β-emitting radionuclides for pretargeted radioimmunotherapy of carcinoembryonic antigen-expressing human colon cancer xenografts. *J. Nucl. Med.* 58, 926–933. doi:10.2967/jnumed.116.187021

Kenny, P. A., and Bissell, M. J. (2007). Targeting TACE-dependent EGFR ligand shedding in breast cancer. *J. Clin. Invest.* 117, 337–345. doi:10.1172/JCI29518

King, A. P., Lin, F. I., and Escorcia, F. E. (2021). Why bother with alpha particles? *Eur. J. Nucl. Med. Mol. Imaging* 49, 7–17. doi:10.1007/s00259-021-05431-y

Kratochwil, C., Giesel, F. L., Bruchertseifer, F., Mier, W., Apostolidis, C., Boll, R., et al. (2014). ^{213}Bi-DOTATOC receptor-targeted alpha-radionuclide therapy induces remission in neuroendocrine tumours refractory to beta radiation: A first-in-human experience. *Eur. J. Nucl. Med. Mol. Imaging* 41, 2106–2119. doi:10.1007/s00259-014-2857-9

Lee, H., Riad, A., Martorano, P., Mansfield, A., Samanta, M., Batra, V., et al. (2020). PARP-1-targeted auger emitters display high-LET cytotoxic properties *in vitro* but show limited therapeutic utility in solid tumor models of human neuroblastoma. *J. Nucl. Med.* 61, 850–856. doi:10.2967/jnumed.119.233965

Li, R., Li, D., Jia, G., Li, X., Sun, G., and Zuo, C. (2020). Diagnostic performance of theranostic radionuclides used in transarterial radioembolization for liver cancer. *Front. Oncol.* 10, 551622. doi:10.3389/fonc.2020.551622

Li, X., Ji, X., Chen, K., Ullah, M. W., Li, B., Cao, J., et al. (2021). Immobilized thrombin on X-ray radiopaque polyvinyl alcohol/chitosan embolic microspheres for precise localization and topical blood coagulation. *Bioact. Mat.* 6, 2105–2119. doi:10.1016/j.bioactmat.2020.12.013

Llovet, J. M., Kelley, R. K., Villanueva, A., Singal, A. G., Pikarsky, E., Roayaie, S., et al. (2021). Hepatocellular carcinoma. *Nat. Rev. Dis. Prim.* 7, 6. doi:10.1038/s41572-020-00240-3

Ma, L., Xu, A., Kang, L., Cong, R., Fan, Z., Zhu, X., et al. (2021). LSD1-demethylated LINC01134 confers oxaliplatin resistance through SP1-induced p62 transcription in HCC. *Hepatology* 74, 3213–3234. doi:10.1002/hep.32079

Marcu, L., Bezak, E., and Allen, B. J. (2018). Global comparison of targeted alpha vs targeted beta therapy for cancer: *In vitro*, *in vivo* and clinical trials. *Crit. Rev. Oncol. Hematol.* 123, 7–20. doi:10.1016/j.critrevonc.2018.01.001

Mies, G., Niebuhr, I., and Hossmann, K. A. (1981). Simultaneous measurement of blood flow and glucose metabolism by autoradiographic techniques. *Stroke* 12, 581–588. doi:10.1161/01.str.12.5.581

Morse, M. A., Sun, W., Kim, R., He, A. R., Abada, P. B., Mynderse, M., et al. (2019). The Role of angiogenesis in hepatocellular carcinoma. *Clin. Cancer Res.* 25, 912–920. doi:10.1158/1078-0432.CCR-18-1254

Pandit-Taskar, N., Larson, S. M., and Carrasquillo, J. A. (2014). Bone-seeking radiopharmaceuticals for treatment of osseous metastases, part 1: α therapy with ^{223}Ra-dichloride. *J. Nucl. Med.* 55, 268–274. doi:10.2967/jnumed.112.112482

Parihar, A. S., Mittal, B. R., Kumar, R., Shukla, J., and Bhattacharya, A. (2020). ^{68}Ga-DOTA-RGD$_2$ positron emission tomography/computed tomography in radioiodine refractory thyroid cancer: Prospective comparison of diagnostic accuracy with ^{18}F-fdg positron emission tomography/computed tomography and evaluation toward potential theranostics. *Thyroid* 30, 557–567. doi:10.1089/thy.2019.0450

Reinders, M. T. M., Smits, M. L. J., van Roekel, C., and Braat, A. J. A. T. (2019). Holmium-166 microsphere radioembolization of hepatic malignancies. *Semin. Nucl. Med.* 49, 237–243. doi:10.1053/j.semnuclmed.2019.01.008

Roobol, S. J., Van den Bent, I., Van Cappellen, W. A., Abraham, T. E., Paul, M. W., Kanaar, R., et al. (2020). Comparison of high- and low-LET radiation-induced DNA double-strand break processing in living cells. *Int. J. Mol. Sci.* 21, 6602. doi:10.3390/ijms21186602

Sgouros, G. (2008). Alpha-particles for targeted therapy. *Adv. Drug Deliv. Rev.* 60, 1402–1406. doi:10.1016/j.addr.2008.04.007

Song, G., Cheng, L., Chao, Y., Yang, K., and Liu, Z. (2017). Emerging nanotechnology and advanced materials for cancer radiation therapy. *Adv. Mat.* 29, 1700996. doi:10.1002/adma.201700996

Sun, G., Wang, T., Li, X., Li, D., Peng, Y., Wang, X., et al. (2018). Sub-micrometer Au@PDA-^{125}I particles as theranostic embolism beads for radiosensitization and SPECT/CT monitoring. *Adv. Healthc. Mat.* 7, e1800375. doi:10.1002/adhm.201800375

Wu, X., Ge, L., Shen, G., He, Y., Xu, Z., Li, D., et al. (2022). ^{131}I-labeled silk fibroin microspheres for radioembolic therapy of rat hepatocellular carcinoma. *ACS Appl. Mat. Interfaces* 14, 21848–21859. doi:10.1021/acsami.2c00211

frontiers | Frontiers in Neurology

TYPE Original Research
PUBLISHED 08 February 2023
DOI 10.3389/fneur.2023.1045644

OPEN ACCESS

EDITED BY
Jie Lu,
Xuanwu Hospital, Capital Medical University, China

REVIEWED BY
Yuhei Takado,
National Institutes for Quantum and Radiological Science and Technology, Japan
Bin Ji,
Fudan University, China

*CORRESPONDENCE
Zhengxin Cai
✉ Jason.cai@yale.edu

SPECIALTY SECTION
This article was submitted to Dementia and Neurodegenerative Diseases, a section of the journal Frontiers in Neurology

RECEIVED 16 September 2022
ACCEPTED 17 January 2023
PUBLISHED 08 February 2023

CITATION
Zheng C, Toyonaga T, Chen B, Nicholson L, Mennie W, Liu M, Spurrier J, Deluca K, Strittmatter SM, Carson RE, Huang Y and Cai Z (2023) Decreased synaptic vesicle glycoprotein 2A binding in a rodent model of familial Alzheimer's disease detected by [18F]SDM-16. *Front. Neurol.* 14:1045644. doi: 10.3389/fneur.2023.1045644

Decreased synaptic vesicle glycoprotein 2A binding in a rodent model of familial Alzheimer's disease detected by [^{18}F]SDM-16

Chao Zheng[1], Takuya Toyonaga[1], Baosheng Chen[1], LaShae Nicholson[2], William Mennie[1], Michael Liu[1], Joshua Spurrier[2], Kristin Deluca[2], Stephen M. Strittmatter[2], Richard E. Carson[1], Yiyun Huang[1] and Zhengxin Cai[1]*

[1]Department of Radiology and Biomedical Imaging, PET Center, Yale School of Medicine, New Haven, CT, United States, [2]Program in Cellular Neuroscience, Neurodegeneration, and Repair, Departments of Neuroscience and Neurology, Yale University School of Medicine, New Haven, CT, United States

Introduction: Synapse loss is one of the hallmarks of Alzheimer's disease (AD) and is associated with cognitive decline. In this study, we tested [^{18}F]SDM-16, a novel metabolically stable SV2A PET imaging probe, in the transgenic APPswe/PS1dE9 (APP/PS1) mouse model of AD and age-matched wild-type (WT) mice at 12 months of age.

Methods: Based on previous preclinical PET imaging studies using [^{11}C]UCB-J and [^{18}F]SynVesT-1 in the same strain animals, we used the simplified reference tissue model (SRTM), with brain stem as the pseudo reference region to calculate distribution volume ratios (DVRs).

Results: To simplify and streamline the quantitative analysis, we compared the standardized uptake value ratios (SUVRs) from different imaging windows to DVRs and found that the averaged SUVRs from 60–90 min post-injection (*p.i.*) are most consistent with the DVRs. Thus, we used averaged SUVRs from 60–90 min for group comparisons and found statistically significant differences in the tracer uptake in different brain regions, e.g., hippocampus ($p = 0.001$), striatum ($p = 0.002$), thalamus ($p = 0.003$), and cingulate cortex ($p = 0.0003$).

Conclusions: In conclusion, [^{18}F]SDM-16 was used to detect decreased SV2A levels in the brain of APP/PS1 AD mouse model at one year old. Our data suggest that [^{18}F]SDM-16 has similar statistical power in detecting the synapse loss in APP/PS1 mice as [^{11}C]UCB-J and [^{18}F]SynVesT-1, albeit later imaging window (60–90 min *p.i.*) is needed when SUVR is used as a surrogate for DVR for [^{18}F]SDM-16 due to its slower brain kinetics.

KEYWORDS

[^{18}F]SDM-16, APP/PS1, SV2A, PET, brain, SRTM, DVR, SUVR

1. Introduction

Synaptic loss is considered as one of the most robust and consistent neuropathological biomarkers of Alzheimer's disease (AD). The loss of synapses and several presynaptic proteins is observed at the earliest stages of AD (1). Synaptic vesicle glycoprotein 2A (SV2A) is an essential protein expressed in all presynaptic terminals and is involved in the regulation of synaptic exocytosis and endocytosis (2). Thus, SV2A positron emission tomography (PET) tracers may be used to measure changes of synaptic density, and facilitate early AD diagnosis (3) and the development of AD treatments at preclinical and clinical stages (4–6). With the lead SV2A PET tracer, [^{11}C]UCB-J (7), the preclinical and clinical quantitative assessment of SV2A changes in AD has been achieved. Compared to control subjects, statistically significant reduction of SV2A in the hippocampus of AD patients was identified (8, 9). [^{18}F]UCB-H was also used to

evaluate patients with mild cognitive impairment (MCI) or AD (10). In addition to studying AD pathophysiology, repeated [^{11}C]UCB-J PET was used to monitor the treatment effects of saracatinib in the APP/PS1 mouse model of familial AD (11). For example, [^{11}C]UCB-J binding was shown to be 9.8% lower in the hippocampus of APP/PS1 mice than WT mice (11). Similarly, hippocampal binding of [^{18}F]SynVesT-1, a newer ^{18}F-labeled SV2A tracer, was found to be 7.4% less in APP/PS1 mice than their littermate controls (12, 13). Recently, we synthesized and evaluated [^{18}F]SDM-16, a novel SV2A PET tracer with high binding affinity and metabolic stability in non-human primates (14, 15). The objective of this study is to assess the brain kinetics of [^{18}F]SDM-16 in mice and identify a simplified method for its quantification in APP/PS1 and control mice. We also compared the performance of [^{18}F]SDM-16 in detecting synapse loss in APP/PS1 mice with that of [^{11}C]UCB-J and [^{18}F]SynVesT-1. *In vivo* assessments of [^{18}F]SDM16 binding to mouse SV2A is an important validation step toward its application in mouse disease models to investigate synaptic density dynamics following drug treatment or other interventions.

2. Materials and methods

2.1. Radiochemistry

Instrumentation for radiochemistry procedures and production of (*R*)-4-(3-fluoro-5-(fluoro-^{18}F)phenyl)-1-((2-methyl-1*H*-imidazol-1-yl)methyl)pyrrolidin-2-one ([^{18}F]SDM-16) have been described previously (15). In brief, radiosynthesis of [^{18}F]SDM-16 was achieved *via* copper (II) catalyzed reaction of the corresponding tin precursor, (*R*)-4-(3-fluoro-5-(trimethylstannyl)phenyl)-1-((2-methyl-1*H*-imidazol-1-yl)methyl)pyrrolidin-2-one, with $^{18}F^-$ in the presence of pyridine and potassium carbonate. Chemical purity, radiochemical purity, and molar activity were determined by high-performance liquid chromatography (HPLC) analysis of the final product solution. Identity of the labeled compound was confirmed by co-injection of the product solution with the unlabeled reference standard.

2.2. Animals and PET imaging experimental set-up

All animal experiments were approved by the Yale Institutional Animal Care and Use Committee for compliance with National Institutes of Health requirements on the use of laboratory animals. WT C57/B6J mice and amyloid precursor protein and presenilin 1 double-transgenic [APPswe/PS1*D*E9 (APP/PS1)] mice were purchased from Jackson Laboratories and maintained on a C57/B16J background as described previously (16). For PET scanning, mice (53 ± 2 weeks) were kept on a heating pad and anesthetized with 0.75∼2.5 % isoflurane. Mice were administered with 150 μL of [^{18}F]SDM-16 (8.9 ± 6.7 MBq, molar activity of 286 GBq/μmol at the end of synthesis, $n = 2$) formulated with saline containing <10% *v*/*v* EtOH, *via* intravenous (*i.v.*) tail-vein injection. Dynamic PET data were acquired on the Siemens Focus 220 scanners for a total of 90 min post-radiotracer injection (*p.i.*, $n = 9$ per group).

2.3. Image analysis

PET images were reconstructed with 3D ordered subset expectation maximization method (OSEM3D; 2 iterations, 16 subsets) with maximum a posteriori probability algorithm (MAP; 25 iterations). Corrections for decay, attenuation, scatter, normalization and randoms were applied. An empirically determined system calibration factor (in units of Bq/cps) combined with the decay corrected administered activity and the animals' weights were used to calculate the standardized uptake value (SUV). An averaged PET image for each measurement (mean of all frames) was co-registered to a representative PET image of [^{18}F]SDM-16 resliced in the Ma-Benveniste-Mirrione mouse brain atlas space. Registration was performed with a 6 degree-of-freedom linear registration using FMRIB's Linear Image Registration Tool in FSL. Regions of interest (ROIs) were extracted from the brain atlas and regional time activity curves (TACs) were obtained by applying template ROIs to the PET images. The following ROIs were included: brain stem (BS), cerebellum (CB), cingulate cortex (CCX), cortex (CX), hippocampus (HC), inferior colliculi (IC), mid brain (MB), striatum (ST), superior colliculi (SC), thalamus (TH), and whole brain (WB).

2.4. Quantitative analysis

In a cohort of three WT and three APP/PS1 mice, the simplified reference tissue model (SRTM) (17, 18) was used to estimate distribution volume ratios (DVRs), using 90 min dynamic PET scan data and brain stem (BS) as the pseudo reference region. SUVs of brain regions averaged from 40 to 70, 50 to 80, and 60 to 90 min *p.i.* were normalized with BS to generate SUV ratios (SUVRs). SUVRs from different time windows were correlated with DVRs to determine the optimal static imaging window. The SUVRs from the optimal imaging window was used in subsequent data analysis.

2.5. Statistical analysis

The primary target region was the hippocampus. All variables are presented as mean ± SD. For group differences, unpaired *t* tests were applied. $P < 0.05$ without correction for multiple comparisons were considered statistically significant. Sample sizes were analyzed by G*Power, a free statistical program for power analysis (http://www.gpower.hhu.de/en.html; Heinrich Heine University, Düsseldorf, Germany software) (19).

3. Results

3.1. Radiochemistry

The SV2A PET tracer [^{18}F]SDM-16 was synthesized using its enantiopure trimethyltin precursor following published procedures (15), with >99% radiochemical and enantiomeric purity, as determined by reverse phase C18 and chiral HPLC analysis. Molar activity at the end of synthesis (EOS) was 286 GBq/μmol ($n = 2$). Total synthesis time including purification and formulation was around 90 min.

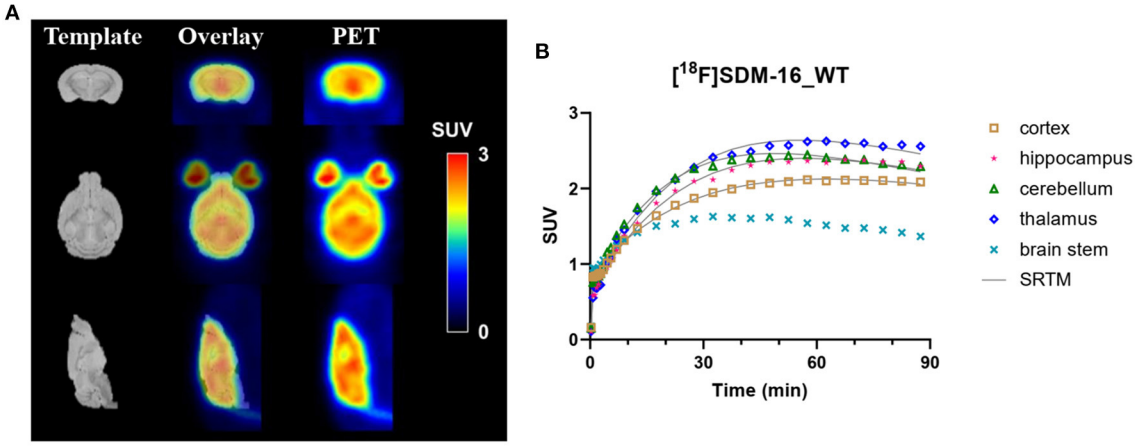

FIGURE 1
(A) Representative summed SUV (0–60 min) images of [^{18}F]SDM-16 in a wild-type (WT) mouse brain and the overlaid images with an MR template. **(B)** The time-activity curves of [^{18}F]SDM-16 in selected brain regions (cortex, hippocampus, cerebellum, thalamus, and brain stem) of a WT mouse. Solid lines are SRTM-fitted curves, using brain stem as the reference region.

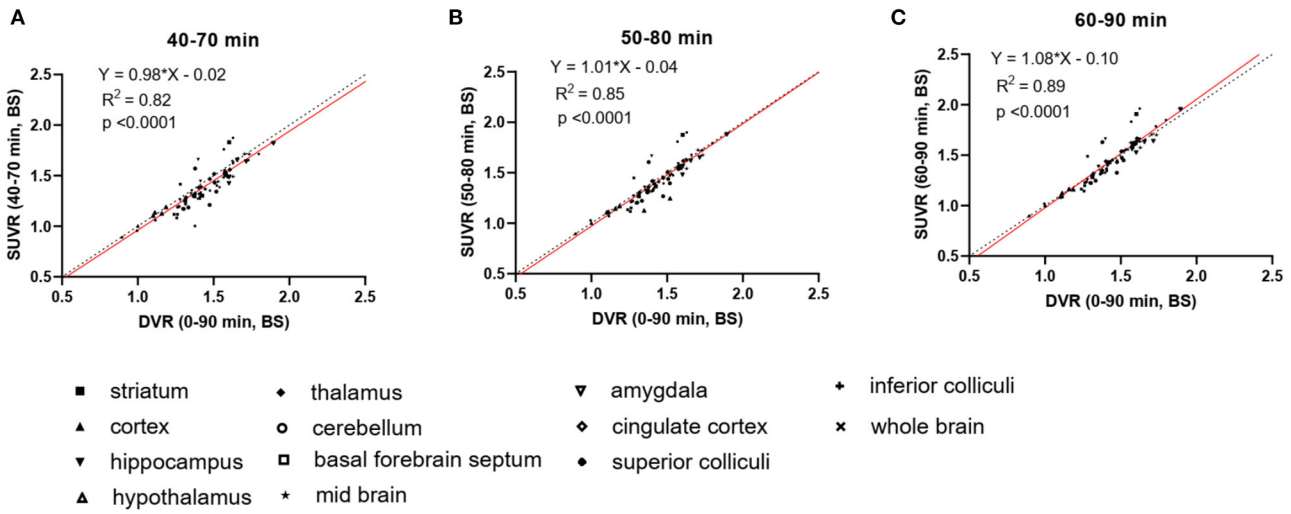

FIGURE 2
Linear regression analysis of DVR and SUVR using averaged SUVs from three different imaging windows, i.e., **(A)** 40–70 min p.i., **(B)** 50–80 min p.i., and **(C)** 60–90 min p.i. DVRs are calculated through SRTM using 90-min dynamic scan data and brain stem as reference region, $N = 3$ for each genotype. Dashed lines are lines of identity.

3.2. Rodent PET imaging and data analysis

The rodent brain PET images showed ubiquitous [^{18}F]SDM-16 uptake in gray matter (Figure 1A). Representative TACs of [^{18}F]SDM-16 in a WT mouse brain were shown in Figure 1B. The TACs indicated efficient brain penetration (SUV up to 2.4 after 30 min *p.i.*), and a steady increase in uptake over 30–60 min *p.i.*, followed by a relatively slow washout phase. The highest uptake was in the inferior colliculi among the brain regions analyzed, and the lowest uptake in the BS, which is consistent with our previous results using [^{11}C]UCB-J and [^{18}F]SynVesT-1 (12). Therefore, we chose BS as the pseudo reference region in the SRTM analysis. Satisfyingly, the TACs were well-described by SRTM (Figure 1B). The regional SUVRs of [^{18}F]SDM-16 correlated well with those of [^{11}C]UCB-J and [^{18}F]SynVesT-1 (Supplementary Figure 1, $R^2 = 0.66$, $p < 0.0001$ with [^{11}C]UCB-J; $R^2 = 0.68$, $p < 0.0001$ with [^{18}F]SynVesT-1).

To increase the throughput of PET scanning and simplify the quantification method, we compared the averaged SUVRs from different imaging windows (40–70, 50–80, and 60–90 min) with the DVRs calculated using the complete 90 min data set to identify a suitable static imaging window for [^{18}F]SDM-16 in mouse brain PET (Figure 2). The SUVRs at all time intervals correlated well with DVRs ($R^2 = 0.82$, 0.85, and 0.89, for imaging windows 40–70, 50–80, and 60–90 min, respectively). The averaged SUVRs from 60 to 90 min *p.i.* were most consistent with the DVRs (Figure 2C, $Y = 1.08*X-0.10$, $R^2 = 0.89$, $p < 0.0001$), compared with the other imaging windows. As expected, the SUVRs from earlier time windows underestimated the DVRs. The percentage differences between SUVR and DVR

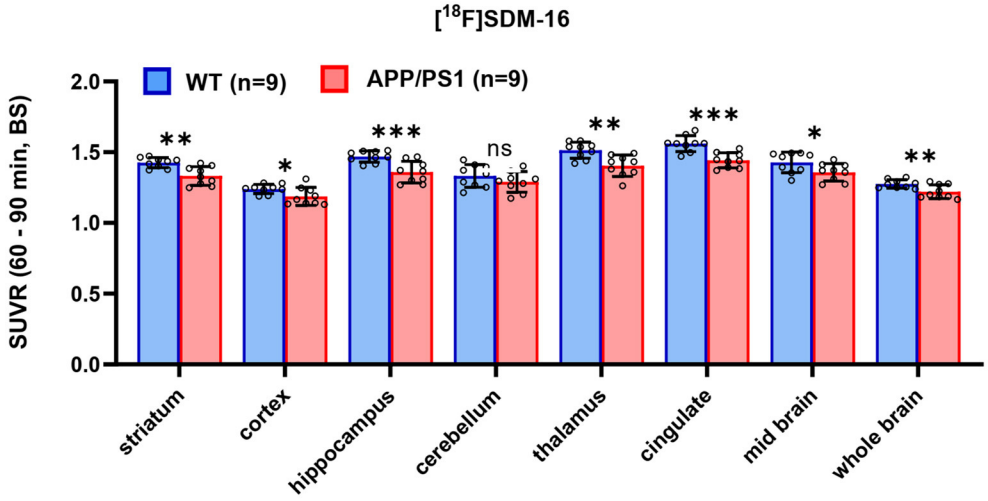

FIGURE 3
Comparison of SUVR in selected brain regions for WT and APP/PS1 mice ($n = 9$ for each group, ***$p < 0.001$; **$p < 0.01$; $0.01 <^{*} p \leq 0.05$; ns, statistically non-significant).

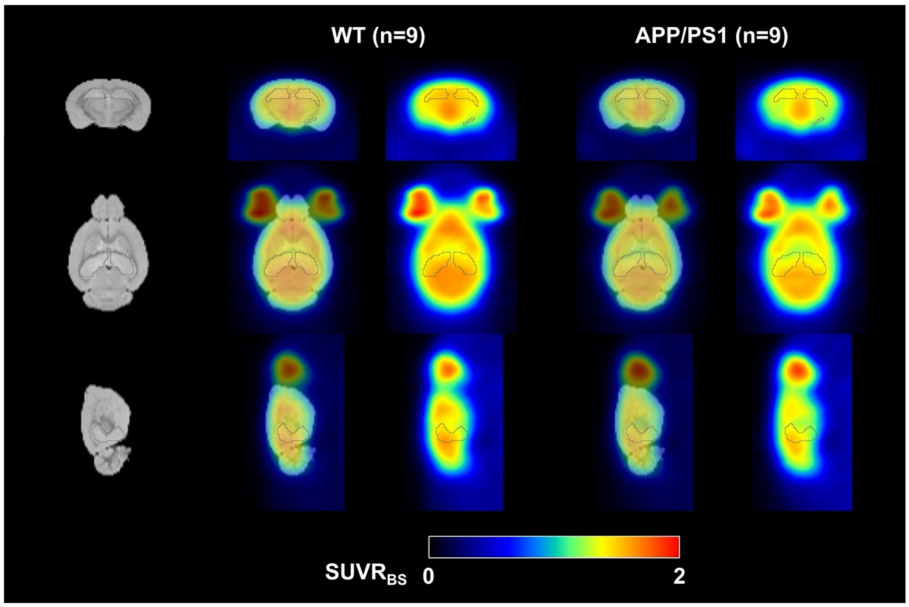

FIGURE 4
Averaged [18F]SDM-16 SUVR images for WT ($n = 9$) and APP/PS1 ($n = 9$) mouse brains. Color scale represents SUVR, averaged from 60 to 90 min p.i. and normalized to brain stem.

decreased from 5.2 ± 3.3% (40–70 min) and 4.2 ± 2.8% (50–80 min) to 3.8 ± 2.4% (60–90 min) (Supplementary Table 1). Therefore, the 60–90 min *p.i.* was identified as a suitable static imaging window to allow for the use of SUVR as a surrogate of DVR for [18F]SDM-16 in the mouse brain.

After identifying the best static imaging time window, we compared the SUVR (60–90 min) of [18F]SDM-16 in APP/PS1 and WT mice. The whole brain SUVR (60–90 min) was 4.3% lower in 12-month-old APP/PS1 mice ($n = 9$) than in age-matched WT controls ($n = 9$). The most profound differences were found in hippocampus (7.5%, $p = 0.001$), cingulate cortex (7.6%, $p = 0.0003$), thalamus (7.2%, $p = 0.003$), followed by striatum (6.6%, $p = 0.001$), mid brain (4.9%, $p = 0.04$), cortex (4.2%, $p = 0.04$), and cerebellum (3.2%, $p = 0.2$) (Figure 3 and Supplementary Table 2). These results are consistent with previously published SUVR (30–60 min) results using [11C]UCB-J and [18F]SynVesT-1. With [11C]UCB-J ($n = 9$), the averaged whole brain SUVR (30–60 min) in APP/PS1 mice was 6.9% ($p = 0.015$) lower than age-matched WT controls, with the most profound differences found in hippocampus (9.8%, $p = 0.017$), thalamus 9.6%, $p = 0.028$), striatum (9.1%, $p = 0.023$), and cingulate cortex (6.8%, $p = 0.024$) (Supplementary Figure 2 and Supplementary Table 3). With [18F]SynVesT-1, the averaged whole brain SUVR (30–60 min) was 3.5% lower in 12-month-old APP/PS1 mice ($n = 24$) than age-matched WT controls. The most

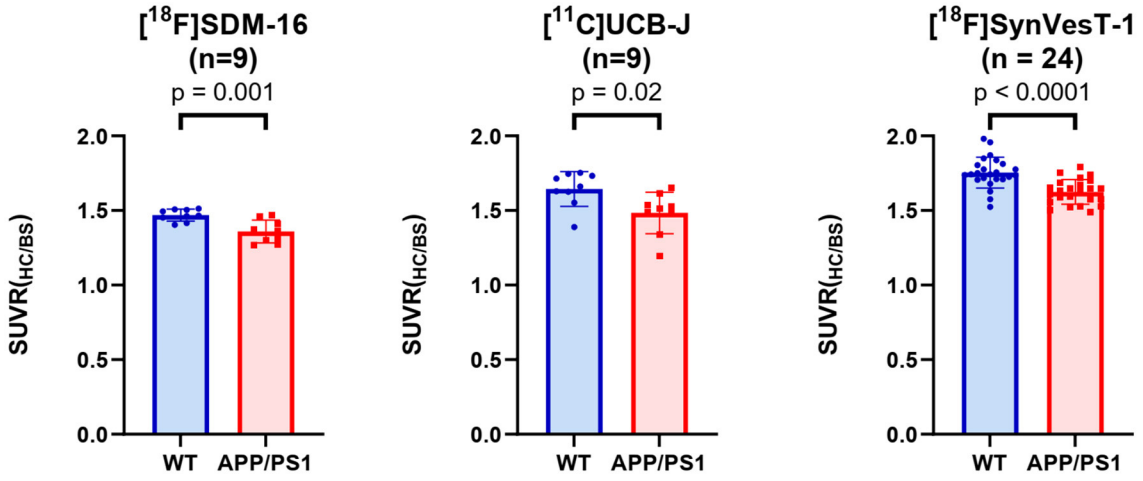

FIGURE 5
Group comparisons of hippocampal SUVRs in APP/PS1 mice and WT mice, using [^{18}F]SDM-16, [^{11}C]UCB-J, and [^{18}F]SynVesT-1 and the corresponding optimal imaging windows, i.e., 60–90, 30–60, and 30–60 min, for [^{18}F]SDM-16, [^{11}C]UCB-J and [^{18}F]SynVesT-1, respectively.

TABLE 1 Power analysis based on hippocampal SUVR of [^{18}F]SDM-16 (60–90 min), [^{11}C]UCB-J (30–60 min), and [^{18}F]SynVesT-1 (30–60 min) in APP/PS1 and WT mice.

Tracer	SUVR			*N* number (one-tail)		*N* number (two-tail)	
	WT (*n*, Mean ± SD)	APP/PS1 (*n*, Mean ± SD)	Mean difference	80% power	90% power	80% power	90% power
[^{18}F]SDM-16	9, 1.47 ± 0.04	9, 1.36 ± 0.08	0.11	5	7	7	9
[^{11}C]UCB-J	9, 1.64 ± 0.12	9, 1.48 ± 0.14	0.16	9	13	12	15
[^{18}F]SynVesT-1	24, 1.75 ± 0.10	24, 1.62 ± 0.08	0.13	7	10	9	12

profound differences were found in hippocampus (7.4%, $p < 0.0001$), followed by thalamus (5.5%, $p < 0.0001$), cingulate cortex (5.1%, $p < 0.0001$), striatum (4.4%, $p = 0.004$), and cortex (3.6%, $p = 0.012$) (Supplementary Figure 2 and Supplementary Table 4).

In this study, the injected mass of SDM-16 was (0.55 ± 0.75) μg/kg, with no significant group difference (Supplementary Figure 3A, $p = 0.98$). We do not expect to see any significant mass effect on binding, as there is no statistically meaningful correlation between the brain SUVs and the administered tracer mass (Supplementary Figure 3B, $p = 0.24$ for hippocampus; $p = 0.27$ for whole brain). Voxel-based parametric statistical analysis also showed a global decrease in tracer uptake in the APP/PS1 mouse brain, with the most significant decrease in hippocampus, which is consistent with the results from ROI-based analysis (Figure 4).

3.3. Results of the power analysis

Because the synapse loss in hippocampus is the most significant in APP/PS1 mice (Figure 5), we used the G*Power to estimate the reasonable sample sizes for different SV2A radioligands at predefined statistical power levels (Table 1). In context, studies with [^{11}C]UCB-J require sample sizes of 13 (power = 0.9), and 9 (power = 0.8) for a one-tailed test. For a two-tailed test, sample sizes of 15 (power = 0.9) and 12 (power = 0.8) were required for [^{11}C]UCB-J. For studies using [^{18}F]SynVesT-1, we found sample size requirements dropped to 10 (power = 0.9) and 7 (power = 0.8) for a one-tailed test, 12 (power = 0.9) and 9 (power = 0.8) for a two-tailed test.

The required sample sizes per genotype were reduced even further for [^{18}F]SDM-16: $n = 7$ (power = 0.9), and $n = 5$ (power = 0.8) for one-tailed test; $n = 9$ (power = 0.9) and n = 7 (power = 0.8) for a two-tailed test. This finding indicated that studies with [^{18}F]SDM-16 requires less animals to achieve the same statistical power for future experiments. Under two-tailed (power = 0.9) conditions, the reasonable sample sizes were calculated for other brain regions for [^{18}F]SDM-16, [^{11}C]UCB-J, and [^{18}F]SynVesT-1 (Supplementary Table 5).

4. Discussion

Synapse loss is a robust pathology in AD (20). Non-invasive measurement of synaptic density provided a method to track synaptic alterations *in vivo* during the AD pathogenesis, and to objectively monitor therapeutic effects. As a sensitive and quantitative imaging modality, SV2A PET has been used in clinical neuroimaging studies of a variety of neuropsychiatric disorders (5). As new interventions are emerging to treat AD at different stages (21), the application of SV2A PET at the preclinical phase will facilitate the evaluations of these new treatments in relevant animal models. However, the accurate quantification of synapse loss in small rodent brains poses seemingly formidable challenges, mainly due to the intrinsic spatial

resolution of small animal PET scanners and the partial volume effects (PVE) (22). Previous work from our group proved for the first time that it is possible to detect synapse loss in the hippocampus of APP/PS1 mice relative to their WT controls using [^{11}C]UCB-J (11). Glorie et al. performed longitudinal SV2A PET studies and detected synaptic density changes in the brain of a transgenic animal model of obsessive-compulsive disorder using [^{11}C]UCB-J (23). Decreases of 2.5 and 5.7% in [^{11}C]UCB-J binding was detected in the ipsilateral striatum of rats at 15- and 22-weeks post injection of alpha synuclein fibrils, respectively (24). Using [^{18}F]UCB-H, progressive synapse loss was detected in a rat model of epilepsy (25, 26). Our group evaluated [^{18}F]SynVesT-1, an ^{18}F-labeled 3,5-difluorobenzyl analog of UCB-J, in APP/PS1 mice and simplified the quantification method by using SUVR from 30 to 60 min *p.i.* (12). [^{18}F]SynVesT-1 turned out to be comparable to [^{11}C]UCB-J in terms of brain kinetics and specific binding signals in mouse brain, but more practical to use in rodent PET imaging studies due to the longer half-life of ^{18}F (110 min) than ^{11}C (20 min). To image the synapse dynamics beyond the brain and in the whole CNS (27), we recently developed [^{18}F]SDM-16 as an SV2A ligand with improved binding affinity and metabolic stability, which showed high specific binding signals in non-human primate brains, with relatively slow kinetics. Interestingly, in mouse brains, we observed lower uptake and faster kinetics for [^{18}F]SDM-16 than seen in non-human primates (Figure 1). However, in the same species, the kinetics of [^{18}F]SDM-16 remains slower than that of [^{11}C]UCB-J and [^{18}F]SynVesT-1.

Although the apparent kinetics of [^{18}F]SDM-16 in the non-human primate brain is relatively slow, the time-activity curves are well-described with the simple one-tissue compartment (1TC) model, which produced volume of distribution values reliably with low standard errors (15). Due to the lack of arterial input function in the mouse PET imaging study, we applied SRTM to calculate the DVR in selected brain subregions, with brain stem as the pseudo reference region, because there is no absolute reference region for SV2A PET data analysis (28) and the SV2A PET tracers uptake in the brain stem appears to be the lowest among all the ROIs. As SRTM assumes 1TC characteristics of the kinetics in the target brain regions, we performed reference Logan analysis to check the 1TC nature of the kinetics and cross-validated the DVRs estimated by both methods (Supplementary Figure 4). We found that the reference Logan derived DVRs ($t^* = 0$ min) are consistent with DVRs estimated with $t^* = 10$ min (Supplementary Figure 4A, $Y = 0.80 \times X + 0.20$, $R^2 = 0.95$). Also, the reference Logan DVRs correlated well with SRTM-derived DVRs (Supplementary Figure 4B, $Y = 0.94 \times X - 0.10$, $R^2 = 0.95$) and SUVR (60–90 min) (Supplementary Figure 4C, $Y = 1.21 \times X - 0.13$, $R^2 = 1.00$).

In previous studies using [^{11}C]UCB-J and [^{18}F]SynVesT-1 in the same rodent model (APP/PS1 and C57BL/6J littermate control), BS was used as a pseudo reference region to calculate the binding potential (BP_{ND}), and SUVR-1 as a surrogate for BP_{ND}. Presumably, because of the better signal statistics of [^{18}F]SynVesT-1, BS showed lower variability in our rodent PET imaging study (12). The optimal static imaging window for [^{11}C]UCB-J and [^{18}F]SynVesT-1 is from 30 to 60 min *p.i.* As expected, the appropriate static imaging window for [^{18}F]SDM-16 in mouse brain (60–90 min *p.i.* in Figure 2) is later than that of [^{11}C]UCB-J and [^{18}F]SynVesT-1 (30–60 min *p.i.*), reflecting its slower brain kinetics than [^{11}C]UCB-J and [^{18}F]SynVesT-1.

As there is likely a certain extent of synapse loss in BS of APP/PS1 mice (29, 30), we are likely underestimating the group differences by using BS as the pseudo reference region. We did not observe any statistically significant difference in cerebellum ($p = 0.25$) (Figure 3 and Supplementary Table 2), which suggests that the changes in SV2A level in cerebellum is similar to BS in 1-year-old APP/PS1 mice. The SPM analysis showed global decrease in tracer uptake in the APP/PS1 mice, with the most significant decrease in the hippocampus, corroborating the ROI-based analysis. These imaging results are consistent with previous histological staining analysis of SV2A and PSD-95 in the dentate gyrus and cortex of 1-year old APP/PS1 mice (13), where a 24% decrease in SV2A expression was observed in dentate gyrus, and a 20% decrease in cortex. The relatively lesser group differences we observed in SV2A PET could be due to partial volume effects in small animal PET imaging as discussed in a recent review article (31).

Using SUVR as the readout, we performed statistical power analysis for [^{18}F]SDM-16, [^{11}C]UCB-J, and [^{18}F]SynVesT-1 (Table 1) and found that these tracers share similar effect sizes and sample sizes to achieve the same level of statistical power to detect the synapse loss in the hippocampi of APP/PS1 mice, though [^{18}F]SDM-16 requires slightly smaller sample sizes (Table 1). This is due to the slightly lower variability in [^{18}F]SDM-16 SUVRs. Nonetheless, it should be noted that these comparisons were based on results from studies using different cohorts of animals.

5. Conclusions

In summary, we demonstrated that the radioligand [^{18}F]SDM-16 had high uptake in mouse brain, and APP/PS1 mice showed lower tracer uptake than WT mice, supporting the use of [^{18}F]SDM-16 in preclinical AD drug discovery and development. We applied a simplified quantification method in APP/PS1 mice and WT controls using [^{18}F]SDM16 and small animal PET, supporting further evaluation and validation of this tracer in other disease models. SUVR from 60 to 90 min *p.i.* using BS as reference region provides reliable estimation of DVR. Using this simplified quantification method, [^{18}F]SDM16 could be used to estimate SV2A levels in rodent models, providing a translational method for tracking disease progression and testing treatment effects.

Data availability statement

The original contributions presented in the study are included in the article/Supplementary material, further inquiries can be directed to the corresponding author.

Ethics statement

The animal study was reviewed and approved by Yale Institutional Animal Care and Use Committee.

Author contributions

CZ, BC, and ZC designed research. CZ synthesized the radiotracer and wrote the manuscript. CZ, TT, BC, LN, ML, WM, and JS conducted research and oversaw collection of imaging data. CZ and TT analyzed imaging data. KD arranged experiment animals. CZ, ZC, SS, RC, and YH edited the final manuscript. All authors have read and approved the final manuscript.

Funding

This work was supported by NIH grants (R01AG058773, R01AG069921, R01NS123183, R01AG066165, RF1AG070926, and R01AG034924), Alzheimer's Association Research Fellowship (AARF-22-919976) and Yale Alzheimer's Disease Research Center Research Grant (P30AG066508).

Acknowledgments

The authors thank Yale PET Center staff for their professional technical assistance in the cyclotron operation and PET imaging study.

Conflict of interest

The authors declare that the research was conducted in the absence of any commercial or financial relationships that could be construed as a potential conflict of interest.

Publisher's note

All claims expressed in this article are solely those of the authors and do not necessarily represent those of their affiliated organizations, or those of the publisher, the editors and the reviewers. Any product that may be evaluated in this article, or claim that may be made by its manufacturer, is not guaranteed or endorsed by the publisher.

Supplementary material

The Supplementary Material for this article can be found online at: https://www.frontiersin.org/articles/10.3389/fneur.2023.1045644/full#supplementary-material

References

1. Colom-Cadena M, Spires-Jones T, Zetterberg H, Blennow K, Caggiano A, DeKosky ST, et al. The clinical promise of biomarkers of synapse damage or loss in Alzheimer's disease. *Alzheimers Res Ther.* (2020) 12:21. doi: 10.1186/s13195-020-00588-4

2. Madeo M, Kovács AD, Pearce DA. The human synaptic vesicle protein, SV2A, functions as a galactose transporter in *Saccharomyces cerevisiae*. *J Biol Chem.* (2014) 289:33066–71. doi: 10.1074/jbc.C114.584516

3. Mecca AP, O'Dell RS, Sharp ES, Banks ER, Bartlett HH, Zhao W, et al. Synaptic density and cognitive performance in Alzheimer's disease: a PET imaging study with [11C]UCB-J. *Alzheimers Dement.* (2022) 18:2527–36. doi: 10.1002/alz.12582

4. Cai Z, Li S, Matuskey D, Nabulsi N, Huang Y. PET imaging of synaptic density: a new tool for investigation of neuropsychiatric diseases. *Neurosci Lett.* (2019) 691:44–50. doi: 10.1016/j.neulet.2018.07.038

5. Finnema SJ, Li S, Cai Z, Naganawa M, Chen MK, Matuskey D, et al. (2021). PET Imaging of synaptic vesicle protein 2A. In: Dierckx R, Otte A, de Vries EF, van Waarde A, Lammertsma AA, editors. *PET and SPECT of Neurobiological Systems*. Cham: Springer International Publishing. p. 993–1019.

6. Finnema SJ, Nabulsi NB, Eid T, Detyniecki K, Lin SF, Chen MK, et al. Imaging synaptic density in the living human brain. *Sci Transl Med.* (2016) 8:348ra96. doi: 10.1126/scitranslmed.aaf6667

7. Nabulsi NB, Mercier J, Holden D, Carré S, Najafzadeh S, Vandergeten MC, et al. Synthesis and preclinical evaluation of ^{11}C-UCB-J as a PET tracer for imaging the synaptic vesicle glycoprotein 2A in the brain. *J Nuclear Med.* (2016) 57:777. doi: 10.2967/jnumed.115.168179

8. Chen MK, Mecca AP, Naganawa M, Finnema SJ, Toyonaga T, Lin SF, et al. Assessing synaptic density in Alzheimer disease with synaptic vesicle glycoprotein 2A positron emission tomographic imaging. *JAMA Neurol.* (2018) 75:1215–24. doi: 10.1001/jamaneurol.2018.1836

9. Mecca AP, Chen MK, O'Dell RS, Naganawa M, Toyonaga T, Godek TA, et al. *In vivo* measurement of widespread synaptic loss in Alzheimer's disease with SV2A PET. *Alzheimer's Dementia.* (2020) 16:974–82. doi: 10.1002/alz.12097

10. Bastin C, Bahri MA, Meyer F, Manard M, Delhaye E, Plenevaux A, et al. *In vivo* imaging of synaptic loss in Alzheimer's disease with [18F]UCB-H positron emission tomography. *Eur J Nucl Med Mol Imaging.* (2020) 47:390–402. doi: 10.1007/s00259-019-04461-x

11. Toyonaga T, Smith LM, Finnema SJ, Gallezot JD, Naganawa M, Bini J, et al. *In vivo* synaptic density imaging with [^{11}C]-UCB-J detects treatment effects of saracatinib in a mouse model of Alzheimer disease. *J Nuclear Med.* (2019) 60:1780–6. doi: 10.2967/jnumed.118.223867

12. Sadasivam P, Fang XT, Toyonaga T, Lee S, Xu Y, Zheng MQ, et al. Quantification of SV2A binding in rodent brain using [18F]SynVesT-1 and PET imaging. *Mol Imaging Biol.* (2021) 23:372–81. doi: 10.1007/s11307-020-01567-9

13. Spurrier J, Nicholson L, Fang XT, Stoner AJ, Toyonaga T, Holden D, et al. Reversal of synapse loss in Alzheimer mouse models by targeting mGluR5 to prevent synaptic tagging by C1Q. *Sci Transl Med.* (2022) 14:eabi8593. doi: 10.1126/scitranslmed.abi8593

14. Zheng C, Holden D, Pracitto R, Wilcox K, Felchner Z, Fowles K, et al. Synthesis and preclinical characterization of a metabolically stable SV2A PET imaging probe: [^{18}F]SDM-16. *J Nuclear Med.* (2021) 62(supplement 1):5.

15. Zheng C, Holden D, Zheng MQ, Pracitto R, Wilcox KC, Lindemann M, et al. A metabolically stable PET tracer for imaging synaptic vesicle protein 2A: synthesis and preclinical characterization of [(18)F]SDM-16. *Eur J Nucl Med Mol Imaging.* (2022) 49:1482–96. doi: 10.1007/s00259-021-05597-5

16. Jankowsky JL, Fadale DJ, Anderson J, Xu GM, Gonzales V, Jenkins NA, et al. Mutant presenilins specifically elevate the levels of the 42 residue β-amyloid peptide *in vivo*: evidence for augmentation of a 42-specific γ secretase. *Hum Mol Genet.* (2003) 13:159–70. doi: 10.1093/hmg/ddh019

17. Lammertsma AA, Hume SP. Simplified reference tissue model for PET receptor studies. *Neuroimage.* (1996) 4:153–8. doi: 10.1006/nimg.1996.0066

18. Salinas CA, Searle GE, Gunn RN. The simplified reference tissue model: model assumption violations and their impact on binding potential. *J Cereb Blood Flow Metab.* (2015) 35:304–11. doi: 10.1038/jcbfm.2014.202

19. Chiuzan C, West EA, Duong J, Cheung KYK, Einstein AJ. Sample size considerations for clinical research studies in nuclear cardiology. *J Nuclear Cardiol.* (2015) 22:1300–13. doi: 10.1007/s12350-015-0256-7

20. Selkoe DJ. Alzheimer's disease is a synaptic failure. *Science.* (2002) 298:789–91. doi: 10.1126/science.1074069

21. Scheltens P, De Strooper B, Kivipelto M, Holstege H, Chételat G, Teunissen CE, et al. Alzheimer's disease. *Lancet.* (2021) 397:1577–90. doi: 10.1016/S0140-6736(20)32205-4

22. Herfert K, Mannheim JG, Kuebler L, Marciano S, Amend M, Parl C, et al. Quantitative rodent brain receptor imaging. *Mol Imag Biol.* (2020) 22:223–44. doi: 10.1007/s11307-019-01368-9

23. Glorie D, Verhaeghe J, Miranda A, De Lombaerde S, Stroobants S, Staelens S. Sapap3 deletion causes dynamic synaptic density abnormalities: a longitudinal [(11)C]UCB-J PET study in a model of obsessive-compulsive disorder-like behaviour. *EJNMMI Res.* (2020) 10:140. doi: 10.1186/s13550-020-00721-2

24. Thomsen MB, Ferreira SA, Schacht AC, Jacobsen J, Simonsen M, Betzer C, et al. PET imaging reveals early and progressive dopaminergic deficits after intra-striatal injection of preformed alpha-synuclein fibrils in rats. *Neurobiol Dis.* (2021) 149:105229. doi: 10.1016/j.nbd.2020.105229

25. Serrano ME, Bahri MA, Becker G, Seret A, Germonpré C, Lemaire C, et al. Exploring with [(18)F]UCB-H the *in vivo* variations in SV2A expression through the kainic acid rat model of temporal lobe epilepsy. *Mol Imaging Biol.* (2020) 22:1197–207. doi: 10.1007/s11307-020-01488-7

26. Serrano ME, Bahri MA, Becker G, Seret A, Mievis F, Giacomelli F, et al. Quantification of [18F]UCB-H binding in the rat brain: from kinetic modelling to standardised uptake value. *Mol Imag Biol.* (2019) 21:888–97. doi: 10.1007/s11307-018-1301-0

27. Xie Q, Zhao WJ, Ou GY, Xue WK. An overview of experimental and clinical spinal cord findings in Alzheimer's disease. *Brain Sci.* (2019) 9:168. doi: 10.3390/brainsci9070168

28. Rossano S, Toyonaga T, Finnema SJ, Naganawa M, Lu Y, Nabulsi N, et al. Assessment of a white matter reference region for (11)C-UCB-J PET quantification. *J Cereb Blood Flow Metab.* (2020) 40:1890–901. doi: 10.1177/0271678X19879230

29. Gordon MN, Holcomb LA, Jantzen PT, DiCarlo G, Wilcock D, Boyett KW, et al. Time course of the development of Alzheimer-like pathology in the doubly transgenic PS1+APP mouse. *Exp Neurol.* (2002) 173:183–95. doi: 10.1006/exnr.2001.7754

30. Radde R, Bolmont T, Kaeser SA, Coomaraswamy J, Lindau D, Stoltze L, et al. Aβ42-driven cerebral amyloidosis in transgenic mice reveals early and robust pathology. *EMBO Rep.* (2006) 7:940–6. doi: 10.1038/sj.embor.7400784

31. Toyonaga T, Fesharaki-Zadeh A, Strittmatter SM, Carson RE, Cai Z. PET imaging of synaptic density: challenges and opportunities of synaptic vesicle glycoprotein 2A PET in small animal imaging. *Front Neurosci.* (2022) 16:787404. doi: 10.3389/fnins.2022.787404

Frontiers in
Bioengineering and Biotechnology

Accelerates the development of therapies, devices, and technologies to improve our lives

A multidisciplinary journal that accelerates the development of biological therapies, devices, processes and technologies to improve our lives by bridging the gap between discoveries and their application.

Discover the latest Research Topics

See more →

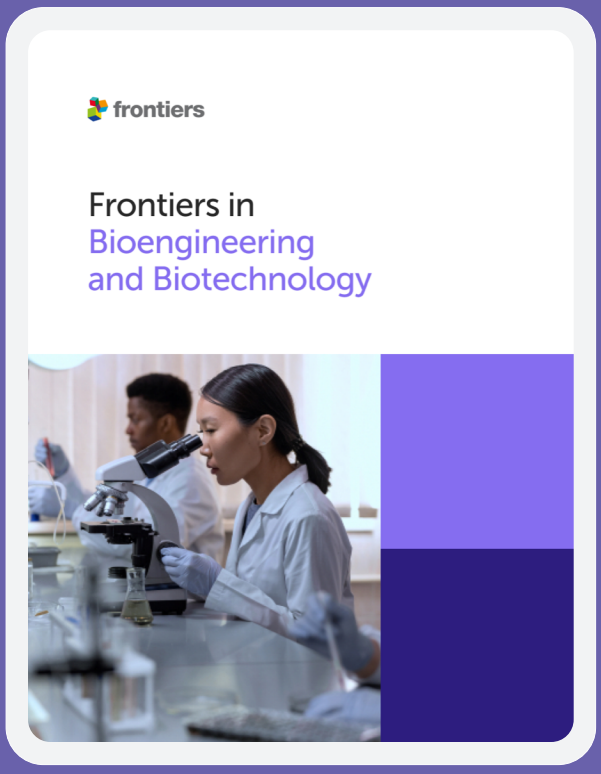

Frontiers

Avenue du Tribunal-Fédéral 34
1005 Lausanne, Switzerland
frontiersin.org

Contact us

+41 (0)21 510 17 00
frontiersin.org/about/contact